UNIVERSITAT POLITÈCNICA
DE CATALUNYA
BARCELONATECH

MPM modelling of landslides in brittle and unsaturated soils

Author
Alba Yerro Colom

Thesis Advisors
Eduardo Alonso Pérez de Ágreda
Núria Pinyol Puigmartí

A thesis submitted to the Universitat Politècnica de Catalunya (UPC)
in partial fulfillment of the requirements for the degree of
DOCTOR OF PHILOSOPHY

Ph.D. program on Geotechnical Engineering and Geo-Sciences
Department of Geotechnical Engineering and Geo-Sciences
Barcelona, September 2015

Thesis written by Alba Yerro Colom

This work has been supported by FPI/UPC Research Fellowship Program, ref. BES-2009-018300 under the project BIA2008-06614

Cover Picture: Cecil Lake road landslide, Peace River. Photo by R. Couture, Geological Survey of Canada.

A la meva família,

Acknowledgments

En primer lugar, me gustaría expresar mi sincero agradecimiento a mi tutor, Eduardo Alonso, por apoyarme y orientarme a lo largo de estos años. De él he aprendido muchísimo y sigo aprendiendo cada día, de su rigor científico y de sus explicaciones que hacen fácil lo difícil.

També vull donar les gràcies a la meva co-tutora, la Núria Pinyol, per donar-me la seva visió crítica la qual sempre m'ha motivat per seguir millorant.

I want to extend my gratitude to Professor Pieter Vermeer for his guidance during my stage in Deltares (Delft, The Netherlands) and for giving me the opportunity to be a member of the MPM group.

Vull agrair al professor Jordi Corominas que em descobrís el món de la recerca durant la realització de la meva tesina de final de carrera. Probablement, sense aquesta bona experiència, no hagués iniciat un doctorat.

També vull donar les gràcies als professors del departament que desinteressadament han dedicat part del seu temps als meus dubtes: l'Ignasi Carol, l'Antonio Lloret, el Josep Suriol, l'Antonio Gens, l'Alberto Ledesma i el Marcel Hürlimann. En especial al Sebastià Olivella, pels seus consells, per escoltar-me i ajudar-me des del principi. También a Jean Vaunat, por sus ánimos y por estar siempre predispuesto a ayudar.

Agraeixo al personal de secretaria del Departament d'Enginyeria del Terreny: l'Eva Martínez, l'Óscar Rubio, la M. Carmen Rodríguez i la Mar Obrador, per facilitar els tràmits administratius. També a l'Albert Marquès, pel seu suport informàtic.

Aquesta tesis s'ha pogut realitzar, principalment, gràcies al suport econòmic del Ministerio de Ciencia e Innovación i la Universitat Politècnica de Catalunya a través de la beca FPI BES-2009-018300. Durant els dos primers anys, el Col·legi d'Enginyers de Camins Canals i Pots també hi ha contribuït econòmicament.

I would like to express my gratitude to my colleges from Deltares and the MPM Research Community: Lars Beuth, Shuhong Tan, Alex Rohe, Mario Martinelli, James Fern, Francesca Ceccato, Issam Jassim, Phuong Nguyen, and Fursam Hamad, for their collab-

oration and friendly support.

M'agradaria agrair als meus companys de doctorat, de despatx i de congressos: el Guillem Domènech, l'Olga Mavrouli, el Mauricio Tapias, l'Ivan Puig, la Natàlia Climent, el Mauricio Albarado, el Víctor Serri, la M. Teresa Yubero, el Crístian De Santos, el Dani Garolera, el Joaquín Liaudad, l'Héctor Marín, el Jubert Pineda, la Joanna Butlanska, la Claudia González i l'Héctor Levatti, per tots els bons moments compartits i per ajudar-me sempre que ho he necessitat. Especialment a la Clàudia Abancó i a l'Anna Ramon, per la confiança i els seus consells sobre la tesis i la vida.

També vull recordar als dos estudiants que han realitzat les seves tesines dins el marc d'aquest treball, l'Helena Castellví i el Francesc Mirada.

Gràcies també al grup de "telecos": el Dani Monells, el Rubén Iglesias, el Giuseppe Centolanza, l'Edu Makhoul, el Marc Imbert i l'Alberto Alonso, per la vostra amistat i les converses animades que m'han dibuixat un somriure cada matí.

I would also like to thank my iranian housemates of *kikkerweg*, Sepehr Eslami and Nima Sharif, you did my stay in The Netherlands unbelievable.

Vull estendre el meu agraïment a l'Arnau Clot pel seu suport i les incomptables discussions enriquidores. I, molt sincerament, al Pau Pujadas per ajudar-me tant i motivar-me quan més ho he necessitat.

Deixo pel final als més importants, la meva família i a la meva parella. Els hi vull donar les gràcies per estar al meu costat i per encoratjar-me en els moments més difícils. Per la seva comprensió, per ensenyar-me a gaudir de les petites coses i a viure intensament. Sense vosaltres hagués sigut impossible.

Abstract

Landslides and slope instabilities represent one of the most important problems in geotechnics causing significant damages around the world every year. Understanding the mechanics of the whole deformation process is of particular importance for risk assessment. First, it is important to determine what areas may be susceptible to landsliding. In addition, it is essential to estimate the travelled distance and the velocity of the unstable mass in order to prevent severe damage. The need to develop solution schemes capable of simulating failure initiation as well as post-failure dynamics is also required in most geotechnical analyses. For instance the design of dams, tunnels, pipes or foundations.

The numerical modelling of such events presents several challenges due to the complexity of simulating large deformations and real soil behaviour. In addition, coupled formulations are needed to model solid-fluid interaction in saturated and unsaturated soils.

Traditional geotechnical analysis, such as Limit Equilibrium Methods (LEM) and the well-known standard lagrangian Finite Element Methods (FEM) are very useful to study the failure initiation, but they provide limited information on the post-failure behaviour. In order to overcome such difficulties, modern numerical approaches are being developed. This is the case of the Material Point Method (MPM), which offers an interesting alternative. MPM discretises the media into a set of lagrangian material points which move attached to the material carrying the soil properties. Governing equations are solved incrementally at the nodes of a computational grid that remains fixed through the calculation. This dual description of the media is capable of modelling large deformations and prevents mesh tangling.

This thesis focusses on studying brittle failures and slope instabilities, from static conditions to run-out by means of the MPM framework. It is proved to be a very useful tool to analyse relevant aspects for the interpretation of landslides such as the development of progressive failure mechanism, the role played by internal shearing in compound slides, and the effect of brittleness on the onset of failure and run-out. The MPM is successfully applied to solve several slope instability problems caused by pore pressure changes. First, the Selborne slope experiment is simulated. This case, well identified with laboratory data, has been an opportunity to perform a validation of the MPM formulation, since a good agreement is obtained between numerical results and experimental data. In a second example, a simplified geometry of the Vajont landslide is analysed. It has shown that a kinematically admissible failure mechanism requires internal degradation of the mobilised

mass controlled by the geometry of the basal sliding surface. In a third analysis, a parametric study varying peak and residual strength is presented, and run-out is found to be directly related with brittleness index.

Moreover, a step forward in the application of MPM to solve multi-phase problems in porous media has been achieved. A coupled 3-phase 1-point MPM formulation is derived and implemented in a software code in order to model problems involving large deformations in unsaturated soils. In this way, the interaction of three different phases (solid, liquid and gas) is taken into account within each material point. This approach is validated with a benchmark problem and it is applied to study the behaviour of an embankment slope instability induced by heavy rain.

Finally, two constitutive models are derived and implemented: a brittle model with strain softening for saturated soils, and a Mohr-Coulomb elastoplastic model for unsaturated materials formulated in terms of net stress and suction.

Resum

Les esllavissades representen un dels problemes més destacats en el camp de la geotècnia ja que cada any causen danys importants arreu. L'estudi d'aquests procesos és fonamental per l'avaluació de riscos. En primer lloc, és important determinar les zones susceptibles a lliscaments o inestabilitats, i per altra banda, és essencial estimar la velocitat i la distància recorreguda per la massa desestabilitzada. El desenvolupament de tècniques numèriques amb la capacitat de simular de forma unificada des de l'inici de la trencada fins a l'estabilització final són claus en problemes d'estabilitat de talussos, així com també en altres anàlisis geotècnics, com per exemple, en estudis d'estabilitat de preses, túnels, canalitzacions o fonamentacions.

La predicció d'aquest tipus d'episodis catastròfics presenta diversos reptes a causa de la dificultat de modelar problemes que impliquen grans deformacions del terreny. A més, el comportament real del sòl és complex i, en molts casos, es requereix la implementació de formulacions hidro-mecàniques per tal de tenir en compte l'efecte de fluids (líquid i/o gas) en terrenys saturats i parcialment saturats.

Les tècniques més tradicionals, com ara els Mètodes d'Equilibri Límit (LEM) i la formulació clàssica del Mètode dels Elements Finits (FEM), són molt útils per estudiar l'inici de la trencada, però proporcionen informació molt limitada del comportament de la massa involucrada un cop ha trencat.

Actualment, s'estan desenvolupant eines numèriques per tal de de simular tot el procés (trencament i post-trencada), com per exemple el Mètode del Punt Material (MPM) el qual ofereix una alternativa interessant. El MPM discretitza el medi continu mitjançant un conjunt de punts lagrangians (punts materials) que es mouen units al material i transporten les seves propietats. Per altra banda, les equacions de govern es resolen de forma incremental als nodes d'una malla computacional que roman fix durant tot el càlcul. Aquesta doble discretització permet la simulació de grans deformacions i evita problemes de distorsió de malla, típics en el FEM.

Aquesta Tesi es centra en la simulació d'inestabilitats de talussos mitjançant el MPM. Es demostra que el MPM és una eina molt potent per analizar tant les condicions estàtiques inicials, com la formació del mecanisme de trencament i el comportament post-trencada. A més, es descriuen diferents aspectes rellevants per a la interpretació de les esllavissades: el desenvolupament del mecanisme de trencada progressiva, l'efecte de la fragilitat i la

degradació interna del material. El MPM s'ha aplicat amb èxit en diferents problemes d'estabilitat de talussos causats per canvis de la pressió intersticial. En primer lloc, es presenta l'experiment de Selborne. Aquest exemple ha servit per validar la formulació del MPM ja que s'ha aconseguit un bon ajust entre resultats numèrics i dades experimentals. En un segon model, s'analitza una geometria simplificada de l'esllavissada de Vajont, amb la qual es demostra que un mecanisme de trencada cinemàticament admissible requereix de la degradació interna de la massa mobilitzada depenent de la geometria de la superfície basal de lliscament. En tercer lloc, per mitjà d'un estudi paramètric variant les resistències pic i residual, s'ha determinat que l'abast està directament relacionat amb la fragilitat del terreny.

Un objectiu important de la tesis ha estat donar un pas endavant en l'aplicació del MPM per tal de resoldre problemes multi-fàsics en medis porosos. Es presenta un esquema hidro-mecànic acoplat per simular el comportament de sòls no saturats que té en compte la interacció de sòlid, líquid i gas en cada punt material. Aquest formulació s'ha validat mitjançant un problema d'infiltració, i s'ha aplicat per estudiar la inestabilitat d'un terraplè induïda per fortes pluges.

Finalment, s'han presentat i implementat dos models constitutius: un model amb reblaniment per sòls saturats, i un model elastoplàstic Mohr-Coulomb per a sòls no saturats formulat en termes de tensió neta i succió.

Resumen

Los deslizamientos constituyen una de las amenazas naturales más relevantes en el campo de la geotecnia ya que cada año causan daños importantes en todo el planeta. El conocimiento de la mecánica del proceso de inestabilidad del deslizamiento es fundamental en la evaluación de riesgos. En primer lugar, es importante determinar las zonas que pueden ser susceptibles a estos fenómenos. Además, es esencial estimar la velocidad y la distancia recorrida por la masa inestable. El desarrollo de técnicas numéricas capaces de simular de forma unificada desde el inicio de la rotura hasta el equilibrio final son claves en problemas de estabilidad de taludes así como también en otros análisis geotécnicos, tales como estudios de estabilidad de presas, túneles, canalizaciones o cimentaciones.

La predicción de este tipo de episodios catastróficos presenta varios retos debido a la dificultad de modelar grandes deformaciones. Además, el comportamiento real del suelo es complejo y la implementación de formulaciones hidro-mecánicas es determinante para tener en cuenta el efecto de fluidos (líquido y/o gas) en terrenos saturados y parcialmente saturados.

Los análisis geotécnicos tradicionales, tales como los Métodos de Equilibrio Límite (LEM) y la formulación clásica del Método de los Elementos Finitos (FEM) son muy útiles para estudiar el inicio de la rotura. Sin embargo, estos métodos proporcionan información muy limitada de la post-rotura y del comportamiento de la masa movilizada.

Actualmente, se están desarrollando herramientas numéricas capaces de simular de forma unificada todo el proceso (rotura y post-rotura), como por ejemplo el Método del Punto Material (MPM) que ofrece una alternativa interesante. El MPM discretiza el medio continuo mediante un conjunto de puntos lagrangianos (puntos materiales) que se mueven unidos al material y transportan sus propiedades. Por otra parte, las ecuaciones de gobierno se resuelven de forma incremental en los nodos de una malla computacional que permanece fija durante todo el cálculo. Esta doble discretización permite simular grandes deformaciones y evita los problemas de distorsión de malla típicos en el FEM.

Esta Tesis se centra en la simulación de inestabilidades de taludes mediante el MPM. Se ha demostrado que el MPM es una herramienta muy útil para analizar tanto las condiciones estáticas iniciales, como la formación del mecanismo de rotura y el comportamiento post-rotura. Además, se describen diferentes aspectos relevantes para la interpretación de los deslizamientos: el mecanismo de rotura progresiva, el efecto de la fragilidad y la

degradación interna del material. El MPM se ha aplicado con éxito para resolver diversos problemas de inestabilidad de taludes causados por cambios de presión intersticial. En primer lugar, se simula el experimento de Selborne. Este ejemplo ha servido para llevar a cabo la validación de la formulación MPM ya que se ha conseguido un buen ajuste entre resultados numéricos y los datos experimentales. En un segundo modelo, se considera una geometría simplificada del deslizamiento de Vajont en el que se analiza la degradación interna de la roca movilizada debido a esfuerzos cortantes. En tercer lugar, por medio de un estudio paramétrico variando las resistencias pico y residual, se determina la relación entre el alcance del deslizamiento y la fragilidad del material.

Uno de los objetivos de la Tesis ha sido dar un paso adelante en la aplicación del MPM para resolver problemas multi-fásicos en medios porosos. Se presenta un esquema hidro-mecánico acoplado para simular el comportamiento de suelos no saturados que tiene en cuenta la interacción de sólido, líquido y gas en cada punto material. Esta formulación se ha validado mediante un problema de infiltración, y se ha aplicado para estudiar la inestabilidad de un terraplén causada por fuertes lluvias.

Finalmente, se han presentado e implementado dos modelos constitutivos: un modelo con reblandecimiento para suelos saturados, y un modelo elastoplástico Mohr-Coulomb para suelos no saturados formulado en términos de tensión neta y succión.

Contents

1

Chapter 1
Introduction

In this first Chapter, the motivation of this work is presented in order to justify its raison d'être. Then, the main goal as well as several specific objectives are stated. Finally, the organisation of the document is also outlined.

1.1 Motivation

Landsliding represents one of the most important problems in geotechnics causing significant damages around the world every year (see Figures 1.1 and 1.2). Understanding the mechanics of the whole process is of particular importance for risk assessment. First, it is important to determine what areas may be susceptible to landsliding. Second, it is essential to estimate the travelled distance and the velocity of the unstable mass in order to prevent severe damage. For instance, when reservoirs, lakes or fjords are potentially affected by landslides on their margins, the calculation of tsunami effects require information on the soil/rock mass run-out and its expected velocity.

The need to develop solution schemes capable of simulating failure initiation as well as post-failure dynamics is also required in most geotechnical analyses. For instance the design of dams, tunnels, pipes, foundations or embankments. Ensuring the stability of these constructions is the most important issue. Despite the probability of failure at the initiation stage is often small, soil and rock as natural geological materials exhibit spatial variability and the uncertainty is always existent. Therefore, in these cases, it is

Figure 1.1: La Conchita landslide, coastal area of southern California. Occurred in the spring of 1995. People were evacuated and the houses nearest the slide were completely destroyed. Photo by R.L. Schuster, U.S. Geological Survey.

Figure 1.2: Cecil Lake road landslide, Peace River. Photo by R. Couture, Geological Survey of Canada.

also important to understand the post-failure behaviour so that the risk of catastrophic damage can be minimised.

The prediction of such catastrophic episodes presents several challenges due to the complexities of real soil behaviour. In addition, since many geotechnical problems often involve seepage forces, the consideration of the coupled behaviour of soil and pore fluids is essential by means coupled hydromechanical formulations.

Rain-induced instabilities are very common especially in partially saturated soils. Natural or cut slopes may remain stable for long times under unsaturated conditions due to the positive effect of the suction on the strenght, and then they fail during heavy rainstorms or after a long period of rain. Often, they are shallow failures that involve large deformations of the mobilised mass. Other applications associated with unsaturated soils involve large deformations in history-dependent constitutive models. This is the case of swelling problems in expansive clays or collapse behaviour of low density materials.

There is much to learn about the evolution of failure in landslide systems, and in particular about the ways in which fracture initiation allows the development of the final failure surface. When examined in detail, one of the factors causing the acceleration of landslides is the loss of strength of the soil involved in a potential unstable mechanism. This typically occurs in brittle materials such as overconsolidated plastic clays and cemented soils, which are characterised with a strain softening behaviour. In these cases, a progressive failure mechanism is developed. During the failure process, slope deformations tend to be small because of the stiff nature of brittle clays. However, the subsequent motion, controlled by Newton law, can involve rapid movements. The consequences of the instability depend on many aspects, typically related to the strength of the failure surface and to the geometry of the site at a larger scale.

Except for simple sliding motions, the stability of a slope not only depends on the resistance of the basal failure surface. For instance, it is also affected by the distortion of the moving mass in compound slides. Internal shearing plays an important role on the stability and post-failure behaviour of a landslide (Fell et al., 2007; Glastonbury and Fell, 2010).

Traditional geotechnical analysis, such as Limit Equilibrium Methods (LEM), are very useful to estimate the failure initiation, but these simple solutions can not provide information on movements and are unable of simulating real soil (or rock) behaviour. The well-known lagrangian Finite Element Methods (FEM) can model complex geometries and they are well suited to integrate advanced constitutive models. However FEM provides limited information on the post-failure behaviour due to mesh tangling problems when large displacements are involved.

Modern numerical algorithms are being developed in order to provide an integrated tool capable of simulating the entire instability process in a unified calculation: the static stability associated to small deformations, the failure triggering and the large displacements during the subsequent run-out. This is the case of the Material Point Method (MPM).

MPM has been applied to a number of geotechnical problems and it has been extended to solve coupled flow-deformation problems in saturated conditions. It is considered as a Particle-based method with some features from Finite Element analysis. It uses two different spatial discretisation schemes to describe the continuum: a set of lagrangian material points that move with the material and carry all the information, and a fixed computational mesh in which the governing equations are solved. The dynamic formulation and the dual description of the media provide the MPM the capabilities of handling problems involving large displacements and deformations.

1.2 Objectives

This Thesis focuses on developing the Material Point Method with the aim of modelling geotechnical problems involving large deformations, such as the whole instability process of a landslide, in brittle and unsaturated soils. In order to achieve such general purpose, the following specific objectives are formulated.

Regarding numerical improvements:

- To extend MPM to analyse problems in unsaturated soils by means a 3-phase (solid, liquid and gas) dynamic coupled hydromechanic formulation
- To implement elastoplastic constitutive models capable of simulating brittle soil behaviour and effects in strength due to suction changes
- To study the numerical stability of explicit schemes and to propose a criterion to calculate critical time step increments

Regarding geotechnical knowledge:

- To test the capability of MPM to model large deformations by simulating a real slope instability case, from initiation and failure propagation to final geometry and run-outs.
- To understand the development of progressive failure mechanisms in brittle materials
- To determine the influence of brittleness in landslide run-out and kinematics of the motion
- To examine the effect of internal shearing in the stability conditions and the post-failure behaviour of compound landslides

- To model unsaturated soil behaviour under rainfall conditions

1.3 Thesis layout

The Thesis is organised in 8 chapters. The main contents are introduced here:

In Chapter 2, a general review of the most important numerical methods used in geotechnics is presented. These are divided in Mesh-based and Particle-based methods. MPM is briefly described, and the main reasons why it has been preferred against others are outlined.

Chapter 3 begins with a literature review regarding the origins and applications of MPM. Then, the basis of the method are presented in a general framework of mechanical problems. The 1-phase MPM formulation and its explicit numerical implementation are detailed. The dynamic formulation is validated through the analysis of a wave propagation problem and a blasting example is presented.

In Chapter 4, the 2-phase 1-point MPM formulation is describedfor fully saturated soil and several numerical issues are discussed. A stability analysis of the integration scheme is carried out and a practical criterion to determine the critical time step size is proposed. The damping of the solution and boundary conditions are also outlined. This approach is validated by means of the one-dimensional consolidation problem.

Chapter 5 focuses on modelling landslide initiation and post-failure evolution in brittle materials. The progressive failure phenomenon is described and the non-associated Mohr-Coulomb is extended by introducing strain softening plasticity. Afterwards, three slope instabilities triggered by the increase of pore water pressure are analysed. First, the Selborne failure experiment is modelled. Then, the effect of internal shearing in a compound slide based on Vajont landslide is discussed. Remarkable consistent and accurate results are achieved. Additionally, the influence of the brittleness is evaluated on the triggering of instability and run-out for a typical slope geometry by means a parametric study.

In Chapter 6, the MPM formulation is extended to model problems involving unsaturated soil. From a computational point of view, the soil is understood as a unique medium integrated by three distinct phases (solid, liquid and gas). After a short discussion of which are the possible MPM strategies capable of simulating such solid-fluid interaction problems, a 3-phase 1-point MPM formulation is presented. The implementation of this approach is validated with a benchmark problem against an analytical solution.

In Chapter 7 the instability of an unsaturated slope subjected to rain infiltration is solved and discussed. A suction-dependent elastoplastic Mohr-Coulomb model is presented in order to simulate strength changes due to wetting effects. The development of the initial failure surface, the evolution of stress and suction states, and the dynamics of the motion

are presented.

Finally, in Chapter 8, the general conclusions are summarised and future works are outlined.

To give a complete understanding of this work, additional Appendices are included.

2

Chapter 2
Introduction to Computational Mechanics

The purpose of this Chapter 2 is to present an outline of the existing numerical methods in geotechnics (Sec.2.1). These are divided into Mesh-based and Particle-based methods, depending on the discretisation approach. Each technique is briefly described and the main features are introduced. The capability of modelling large displacements is discussed. Finally, in Section 2.2, the main reasons why the Material Point Method is the preferred tool in this Thesis are presented.

2.1 Numerical methods in soil and fluid mechanics

Analytical solutions are very useful to understand the behaviour of simple mathematical models. However, most of real processes involved in many engineering areas and applied sciences are much more complex. To find analytical expressions capable of describing such problems is practically impossible. Since 50 years ago, the exponential improvement of computer technologies allowed the development of numerical methods and advanced techniques capable of modelling wide range of problems. Such methods apply numerical approximations in order to convert mathematical problems into systems of discrete equations that can be solved with sufficient accuracy. Because the type of problems in the engineering field involve a large variety of mathematical phenomena, many numerical approaches are also being developed.

The geotechnical field comprises all applications concerning the study of earth materials. Many problems involve the ground in some way, for example cut slopes, earth embankments, tunnels, dikes and offshore constructions. In all cases, understanding the soil (or rock) behaviour is essential to establish the functionality of such structures. Many investigations also include the assessment of the risk from natural hazards such as landslides, soil liquefaction and debris flows.

Traditionally, simplified models and empirical approaches have been used to determine the ultimate conditions that ensures the stability of a problem. For instance, in slope stability, Limit Equilibrium analysis (LEM) assume an arbitrary failure surface and the equilibrium is considered imposing that the ultimate strength criterion holds everywhere along the failure. Only the global equilibrium of the mobilised blocks between failure surfaces is considered. Because of their simplicity and ease of use, these kind of methods have been widely applied (Cascini et al., 2010; Cooper et al., 1998; Cuomo et al., 2013; Ling et al., 2009) and they are very useful to obtain first estimations at early stages of the design. However, these simple solutions can not provide information on movements. Moreover, geotechnical problems in reality are much more complicated due to nonlinearities that characterise the constitutive behaviour of soil (and rock), and the difficulty of determining stress field conditions, interaction between different phases (solid, liquid and gas) and heterogeneities at micro and macro scales. Several numerical methods are being developed to analyse and predict the behaviour of complex field situations, simulating realistic soil constitutive models and boundary conditions. The most important limitation of these full numerical analysis is their high computational cost.

There are different numerical approaches to describe the soil. Most of them consider the material as a continuum, but in other cases, such as in granular flows, it can be analysed as a discontinuous medium formed by a set of particles. Moreover, often, soils consist of a heterogeneous mixture of solid (such as particles of clay, silt or sand) with fluids (liquid and gas), hence soil mechanics and fluid mechanics are closely related in the geotechnical field.

In the literature there exist many different numerical methods. Each one has its own features, with advantages and limitations. Taking into account the large variability of problems, it is very important to chose what kind of method is more convenient depending on the expected results. Thereby, a better numerical approximation will lead to a better understanding of the problem.

The purpose of this Thesis is the analysis of problems that involve large deformations such landslides. Therefore, a numerical tool capable to achieve a realistic transition between static and dynamic conditions is required in order to provide, in a unified calculation, the entire instability process (the static stability, the failure triggering and the subsequent run-out). In addition, it is also important to have the capability of including the hydromechanical coupling.

In the following sections, an outline of the existing numerical methods in geotechnics is presented. These are divided into Mesh-based and Particle-based methods, depending on

the discretisation approach.

2.1.1 Mesh-based methods

Mesh-based methods have been the starting point for most of the advanced numerical techniques, generally based in continuum mechanics. They have been used in many fields for over thirty years. Its main feature is that they divide the domain of the problem into a collection of subdomains, so-called elements, thus forming a mesh. Each element has several nodes, with a fixed number of predefined neighbours. This connectivity is used to define mathematical operators like the derivative and to ensure compatibility of numerical interpolation. In this way, the required equations describing the boundary value problem can be discretised and solved.

The relationship between the deforming continuum and the mesh determines the ability of the numerical method to deal with large distortions and provide an accurate resolution of material interfaces and mobile boundaries. The algorithms of continuum mechanics usually make use of two classical descriptions of motion: the lagrangian description and the eulerian description (Malvern, 1969).

Lagrangian algorithms, in which each individual node of the computational mesh follows the associated material particle during motion, are mainly used in geotechnical engineering (see Figure 2.1). The lagrangian description allows an easy tracking of free surfaces and interfaces between different materials. It also facilitates the treatment of materials with history dependent constitutive relations. Its weakness is its inability to follow large distortions of the computational domain (Armero and Love, 2003).

Eulerian algorithms are widely used in fluid dynamics. Here, as shown in Figure 2.1, the computational mesh is fixed and the continuum moves with respect to the grid. In the eulerian description large distortions in the continuum motion can be handled with relative ease, but generally at the expense of precise interface definition. Numerical difficulties arise to calculate convective terms, which appear due to the relative motion between the deforming material and the computational grid. In addition, serious limitations are now found in following deforming material interfaces and mobile boundaries (Armero and Love, 2003).

The three classical mesh-based methods are the Finite Difference Method, the Finite Element Method, and the Finite Volume Method.

The Finite Difference Method (FDM) is the oldest numerical analysis of partial differential equations. Standard references on finite difference methods are the textbooks of Collatz (1955), Forsyth and Wasow (1960) and Richtmyer and Morton (1967). It uses a square network of lines to construct the discretisation of the strong form of the governing equations. The lack of flexibility in determining the shape of the network is the bottleneck of the method when handling complex geometries.

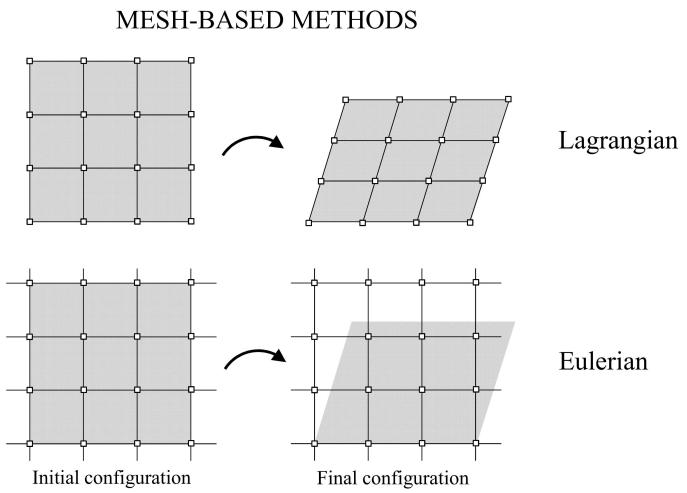

Figure 2.1: Spatial discretisation scheme of lagrangian and eulerian mesh-based methods.

The Finite Element Method (FEM) originated in the engineering literature and it is the most used technique in geotechnics for finding approximate solutions to boundary value problems (Zienkiewicz, 1977). The material geometry is replaced by an equivalent lagrangian finite element mesh. The shape of the elements can be very diverse and even can have curved edges depending on the integration order. State variables are determined at the nodes of the mesh by interpolation functions. This method is well suited to solve couped hydromechanical problems, however, despite being a valuable tool in the field of modelling, the standard lagrangian FEM has serious limitations in problems involving large deformations of the material. This is due to distortions suffered by the mesh and that in some cases they lead to large inaccuracies (Armero and Love, 2003).

In the field of computational fluid dynamics, the Finite Volume Method (FVM) is used (Eymard et al., 2000). Typically, it uses an eulerian description to describe the continuum. Each element of the computational grid represents a control volume in which the balance equations are solved in it, hence conservation principles are imposed element by element. The determination of input and output flows through the contour of each cell is the main purpose of the calculation.

One attempt to modelling large deformations maintaining well defined the boundaries arises from the arbitrary Lagrangian-Eulerian (ALE) methods (Donea et al., 1977, 2004). These make use of the two classical kinematical descriptions of motion, lagrangian and eluerian, by taking the advantages of both. Here, the nodes of the computational mesh may be moved with the continuum, or be held fixed. Therefore, to keep the computational mesh as regular as possible and to avoid mesh entanglement during the calculation, remeshing algorithms are used. However, this requires greater computational time.

2.1.2 Particle-based methods

In order to avoid the difficulties of mesh-based methods, during recent years the particle-based methods, also called meshless or mesh-free methods, have been developed. According to Li and Liu (2002), these are the new generation of computational methods. They do not require the definition of a mesh connecting points storing data. On the contrary, they are based on the generation of free particles, without given relationships one to each other, that move attached with the domain (lagrangian description). Within this framework, continuum and also discrete domains, such as granular materials, can be modelled (see Figure 2.2). Some of the most common techniques used in the field of soil mechanics and fluid dynamics are presented below.

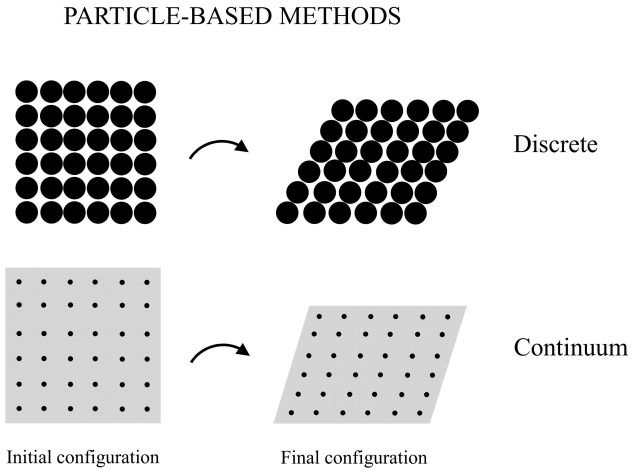

Figure 2.2: Spatial discretisation of particle-based methods, representing discrete or continuum media.

One of the most accepted particle-based methods, is the Discrete Element Method (DEM) proposed by Cundall and Strack (1979). DEM assumes the soil as a discontinuous medium and takes into account the individual existence of each discrete grain forming the medium. Therefore, it consists on computing the motion of a large number of particles that interact one with each other through the calculation of forces in their contacts. One feature of the method is that it incorporates the concept of friction and bounding so that slip and breakage can occur between two particles when the contact forces between them exceeds a critical value. DEM is a very useful tool in the study of granular materials (Radjaï and Dubais, 2011). However, it is difficult to jump from contact properties to a common understanding of constitutive behaviour. Despite some limitations, the applications of DEM have been proven successful in simulating landslides with high movement speed and long travel distance (Li et al., 2012, 2011; Liu and Koyi, 2012; Okura et al., 2000; Zhao et al., 2015).

The Smoothed Particle Hydrodynamics (SPH) method is the oldest particle-based method. It was developed by Lucy (1977) and Gingold and Monaghan (1977) and initially was ap-

plied to astrophysical problems. More recently, it is increasingly used for modelling in fluid dynamics. The considered domain is divided into a set of particles that move attached to the material and carry the most fundamental characteristics of the material portion that represent. Each particle has a spatial distance, known as the smoothing length, over which the properties are smoothed by a kernel function. SPH is well adapted to solve flow problems, but they struggle apply boundary conditions. SPH has been applied in geomechanics for solving large deformations problems, such as Bui and Fukagawa (2008, 2013); Bui et al. (2011).

The most modern particle-based methods take advantage of the experience gained during more that 30 years form FEM by using a support finite element mesh. These methods are computationally more expensive. One of these is the Particle Finite Element Method (PFEM) (Aubry et al., 2005). It discretises the media by means a cloud of nodes. After recognising the distribution of these points, the boundaries are detected and a computational mesh is constructed by connecting the nodes belonging to the same material domain. As in FEM, the governing equations are solved at the nodes of the computational grid and the nodes move fixed to the material carrying all properties. In problems involving large deformations, a frequent re-meshing effort is required. PFEM is being developed for the study of fluid-structure interaction (Oñate et al., 2011).

The Material Point Method (MPM) was developed by Sulsky et al. (1994). This method is based on the Particle-In-Cell method (PIC) (Harlow, 1964). The state variables are carried by a set of lagrangian material points that move with the material and carry all the information. The governing equations are solved at the nodes of a computational background grid that remains fixed through the calculation and covers the whole domain (Figure 2.3). This dual description of the media provides to MPM the capabilities of handling problems involving large displacements without remeshing requirements, moreover, contact between different bodies is automatically solved. The computational effort of this method lies in transferring information from both discretisations. Recently, it has been applied to a number of geotechnical problems (see Section 3.2) and it has been extended to coupled flow-deformation formulations.

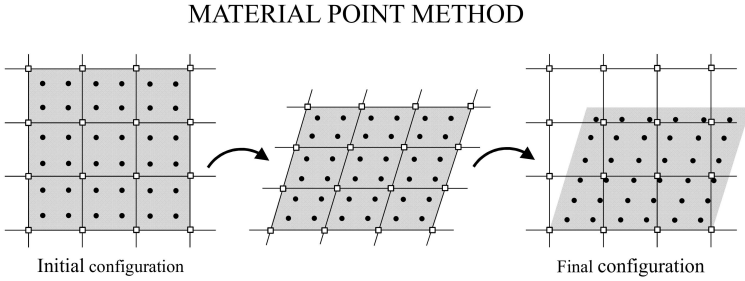

Figure 2.3: Discretisation scheme of MPM.

Finally, FEM Lagrangian Interpolation Points (FEMLIP) was originally formulated by Dufour et al. (2001) and Moresi et al. (2001). It is also based on the PIC method and its formulation is very close to the MPM. Typically it has been used for geophysical

modelling and simulation of viscous flows (Moresi et al., 2003). It has been applied on slope stability analysis and mudflow analysis in Cuomo et al. (2013) and Prime et al. (2014) respectively.

2.2 Why MPM?

Most of the methods described above present some attractive features. In this Thesis, MPM has been the chosen for modelling problems involving large deformations within the geotechnical framework. The main reasons for this decision are the following:

- It is well suited to simulate large deformation problems without mesh tangling.
- The soil is modelled as a continuum and a common understanding of constitutive behaviour can be implemented.
- A lagrangian description of the motion, by means a set of material points, allows the incorporation of advanced history-dependent constitutive models.
- The definition of a background computational mesh, totally detached from the material domain, allows applying the boundary conditions relatively easily.
- Contact between different bodies is automatically solved when these share elements of the mesh.
- MPM resembles classical FEM in many aspects, because governing equations are solved at the nodes of the computational mesh. Therefore, much of the knowledge and research of FEM can be directly transferred to MPM.
- Coupled hydromechanical formulations are well suited within the MPM framework.
- The implementation is intuitive for users familiarised with the FEM.
- Transferring information from material points to the nodes of the grid increases the computational cost of the method, but remeshing is not required.

3

Chapter 3

Basis of the Material Point Method

As it has been mentioned, the aim of this work is to solve geotechnical problems by means the Material Point Method (MPM). Taking into account that the soil is formed by a solid skeleton and a set of connected pores (voids), a mechanical 1-phase formulation is very useful whether the voids are totally empty (for dried conditions), or fully filled with fluid for undrained conditions (in which fluid and solid skeleton move attached one to each other). In both cases, one single velocity field is enough to describe the entire problem.

In this Chapter 3, the basis of the method are presented in a general framework of mechanical problems. In Sections 3.1 and 3.2, the origins of MPM and its applications in multiple fields are presented. Afterwards, the most general 1-phase MPM formulation is widely explained in Section 3.3. This approach consists of considering the material as a continuum comprised of one single phase. Governing equations of the problem are presented as well as its discretisation in space and time. Here, the numerical implementation is described in detail and the stability of the method is discussed. Finally, the dynamic formulation is validated through the analysis of a wave propagation problem (Sec.3.4).

3.1 Origin of MPM

The origin of MPM was the work developed by Harlow et al. (1964) in Los Alamos National Laboratory. The basis of that method, called initially Particle-In-Cell method (PIC), was to represent fluid flow by a set of material points moving through a background fixed mesh. Later, in 1994 in the New Mexico University, Sulsky and Schreyer (Sulsky et al., 1994; Sulsky and Schreyer, 1996; Sulsky et al., 1995) extended the approach for modelling problems of solid mechanics, where basically the equation of dynamic momentum balance is discretised.

MPM is considered as a method in between the particle-based methods and the Finite Element Method (FEM) because it discretises the media in two different frames. First, the continuum is divided into a set of material points. Each material point represents a portion of the domain and the mass of such subdomain, assumed to be fixed during all the calculation (to ensure mass conservation). In the classical MPM, it is considered to be concentrated at the corresponding material point. Other quantities such as velocities, strains and stresses, are also initialised and carried by the material points. Each material point moves attached with the solid skeleton and these provide the lagrangian description of the media.

The second frame is a computational mesh. It is the same as the one used in the conventional FEM and it is built to cover the full domain of the problem. In the nodes of the mesh is where the discrete governing equations are solved. The variables required to solve the equations in the mesh at any step of the analysis are transferred from the material points to the nodes of the mesh by using mapping functions. For instance, the typical linear shape functions used in the FEM. Boundary conditions can be imposed at the mesh nodes or at the material points and the governing equations are solved by using an incremental scheme. Then the quantities carried by the material points are updated through the interpolation of the mesh results, using the same mapping functions. The information associated with the mesh is not required for the next step of the analysis; therefore it can be discarded avoiding any mesh distortion.

Figure 3.1 is a typical problem setup. The material domain is represented by a set of material points. The computational mesh covers all the computational domain.

3.2 Applications of MPM

Since MPM was developed by Sulsky et al. (1994) considering the basis of PIC method Harlow et al. (1964), it has been extended to deal with advanced features and many engineering problems. A literature review of that published works have been carried out and the most significant developments and applications of the method are presented below. In order to be as clear as possible, the references are grouped by topics and are presented trying to keep a chronological order.

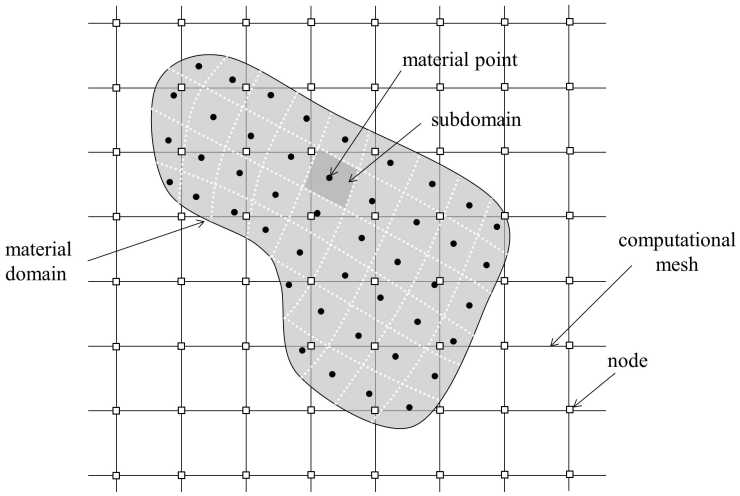

Figure 3.1: Space discretisation. Nodes of the computational mesh and material points

3.2.1 Thin membranes

York II (1997) presented the modifications necessary to simulate thin membranes. Each membrane is discretised by a collection of unconnected material points and a projection of the strains onto a local normal-tangential coordinate system is required for each material point. In this work, the MPM formulation is also extended to simulate interaction between thin membranes and compressible fluids, and the non-slip contact is handled naturally by the classic MPM formulation. Some simulations of the interaction of an impacting probe with an inflated airbag were also performed.

3.2.2 Contact problems

In 1999, York II et al. (1999) presented the modelling of several engineering problems involving contact. They showed that two bodies stick together nonphysically when they should separate. In this work, a first contact-release algorithm is presented. The velocity of each body is calculated separately at grid nodes. The contact may occur if the material points of different bodies are projected on to the same nodes of the background mesh. The contact force is associated with the velocity of the centre of mass. At the same time, Wieckowski et al. (1999) studied the flow of a granular material during the process of discharging a silo. The formulation of a frictional contact algorithm is developed in order to simulate the relative movement between grains and fixed boundaries.

Later on, Bardenhagen et al. (2000) extend the MPM formulation with a contact algorithm that allows separation, sliding and rolling with friction between different solid bodies. This approach was improved in Bardenhagen et al. (2001) in order to apply the MPM to stress propagation in granular material. Hu and Chen (2003) proposed a multi-mesh mapping scheme to simulate contact between spur gears, where each material lies in an individual background mesh rather than in the common one. In 2008, Xiao-Fei et al. (2008) presented a contact algorithm in which the criterion of contact condition is similar to BardenhagenŠs but the multi-mesh is used to calculate the normal and tangential velocities of different bodies. More recently, Huang et al. (2011) presented two methods to implement the contact algorithm to solve problems involving penetration.

3.2.3 Decohesion and delamination

In 2002 and 2004, an extension of the MPM to solve problems with decohesion and delamination where presented by Schreyer et al. (2002) and Sulsky and Schreyer (2004) respectively. The material failure is approached as a strong discontinuity in displacement. This type of failure can occur in layered composites and the definition of discrete constitutive equations is required.

3.2.4 Explicit cracks

Conventional MPM is not capable of handling explicit cracks due to the nature of a single velocity field on the background. In 2003, Nairn (2003) and Guo and Nairn (2004) derived a modified MPM labelled as CRAMP for "CRAcks" with "Material Points" that extended MPM to handle two-dimensional dynamic explicit cracks. Multiple velocity fields represent velocities above and below cracks that enable representation of discontinuities which are necessary for description of explicit cracks. Several calculations, including crack propagation, are presented in Nairn and Guo (2005). Later, Guo and Nairn (2006) adapted the dynamic fracture algorithms to three-dimensional cracks and three-dimensional crack-front parameter calculations. In 2009, it was extended to include cohesive zones to model fracture process zones behind the crack tip (Nairn and Matsumoto, 2009). This work was focused on modelling static fracture processes for cracks with bridging zones, particularly useful in the modelling of materials such as wood. Finally, in 2011, Bardenhagen et al. (2011) presented an extension of the CRAMP algorithm in the MPM framework simulating dynamic fracture processes, which allows fracture propagation in arbitrary directions and in three dimensions.

3.2.5 Engineering problems in geomechanics

Several geotechnical problems have been solved using MPM formulation. In 1999, Wieckowski et al. (1999) presented some simulations of granular flow. The entire process of

discharging a silo is analysed and some results are compared with experimental ones. Other problems such as silo filling, retaining wall failures, and cutting processes are analysed in Wieckowski (2004), Vermeer et al. (2008) and Beuth (2012). Coetzee et al. (2005) presented a modelling of anchors placed in soil. Coetzee et al. (2007) and Mackenzie-Helnwein et al. (2010) studied excavation procedures and dragging interactions. Simulation of landslides and slopes have also been carried out by several authors, in which the development of shear bands within the soil can be observed (Andersen and Andersen, 2008, 2010; Andersen, 2009; Vermeer et al., 2008; Yerro et al., 2013). Simulations of cone penetration testing are presented in Beuth (2012) and Ceccato (2014). In 2013, Al-Kafaji (2013) showed the capabilities of MPM to simulate the dynamic collapse of tunnel face, an slope instability case, the installation of dynamic anchor and a pile driving in dry sand. The modelling of avalanches and its interactions with structures have been recently presented by Mast (2013). It is important to highlight that in most of the geotechnical problems the soil is considered as a single-phase material.

3.2.6 Saturated porous media

More recently, the interaction between solid skeleton and pore fluid has been taken into account. For coupled hydro-mechanical saturated problems the continuum can be considered as a saturated soil-fluid mixture. Two different formulations have been recently developed.

In the first one, it is assumed that material points carry the pore pressure as an associated variable (Al-Kafaji, 2013; Jassim et al., 2013; Zabala and Alonso, 2011; Zhang et al., 2009). Therefore, 2 phases are represented in each material point (2-Phase 1-Point MPM formulation). In 2009, Zhang et al. (2009) studied the dynamic analysis of saturated soil in three different examples: a shallow foundation, a retaining wall and an impact problem between saturated porous media and solid bodies. In Zabala (2010); Zabala and Alonso (2011, 2012) the MPM is applied to the simulation of the historical failure case of Aznalcóllar dam and two other dams that are under high seismic hazard. In 2013 Jassim et al. (2013) studied the wave attack on sea dike. More recently, the progressive failure mechanism in slopes and post-failure analysis of run-out and velocities has been studied by Yerro et al. (2014a,b). Finally, Muller and Vargas (2014) modelled openings and impact problems in saturated porous media.

The second approximation to solve coupled fluid-mechanical problems with the MPM is a multi-point formulation (2-Phase 2-Point MPM formulation). In this case, the solid-fluid mixture is modelled by using two distinct layers of lagrangian material points, one for each phase. Different approaches have been published in Abe et al. (2014); Bandara and Soga (2015); Bandara (2013). The deformation of a river levee embankment after seepage failure is simulated and the numerical results are compared with experimental ones.

3.2.7 Other applications

MPM has been applied to many different fields. For instance, Mostazo (2004) modelled grain growth in polycrystalline materials with an Hybride Montecarlo algorithm, and Zou and Zhang (2004) simulated the penetration of multi-bodies such as a weapon-target interaction. In 2005, Ionescu et al. (2005) simulated biological soft tissues subjected to penetrating trauma using the membrane MPM formulation (York II, 1997). Brydon et al. (2005) studied the densification of real open-celled foam microstructures. In 2006, Hu and Chen (2006) presented some examples of fragmentation on concrete walls. Schreyer et al. (2006), Sulsky et al. (2007) and Peterson (2008) modelled sea ice dynamics based on the representative research on decohesion models. Guilkey et al. (2007) developed a multi-material hydrodynamic MPM code which has been applied in Banerjee (2004) for the simulation of the deformation and failure of a steel container that expands under the effect of gases produced by an explosively reacting high energy material contained inside. In 2010 Tran et al. (2010) undertook MPM in the context of model problems from gas dynamics. More recently, Lian et al. (2011) and Banerjee et al. (2012) present some simulations of impact, penetration, and fragmentation of metals; Wang et al. (2012) studied the mechanical behaviour of composites; Zhou et al. (2013) simulated human head impacts. Finally, Stomakhin et al. (2013) used the method in the graphics community for the animation of snow dynamics.

3.2.8 Implicit integration algorithms

Most of the MPM developments consider the dynamics in the formulation and use an explicit integration scheme to discretise the time (Al-Kafaji, 2013; Bardenhagen et al., 2000; Coetzee et al., 2007; Nairn, 2003; Schreyer et al., 2002; Sulsky and Schreyer, 1996; Wieckowski et al., 1999; Zabala, 2010; Zhang et al., 2009). However, when problems to be solved involve very slow processes, an implicit time integration scheme has been used by some authors in order to reduce the computational cost. Guilkey and Weiss (2001, 2003) used an incremental iterative solution strategy based on Newton method to solve the equations of motion, and Newmark integration to update the kinematic variables. Cummins and Brackbill (2002) describe an implicit algorithm for granular materials under low strain rates which incorporates a model for contact among grains with friction. It considers a Newton−Krylov equation solver in order to improve energy conservation. A similar implicit algorithm is also presented by Sulsky and Kaul (2004), which proves that it can be made unconditionally stable, thus the time step is only restricted by the desired accuracy of the computed results. Other authors have examined the implicit MPM formulation, such as Love and Sulsky (2006a,b).

Moreover, some quasi-static MPM codes with an implicit solver have been presented in order to study static and low-rate dynamic loading conditions. Guilkey et al. (2006) were the first authors who applied the quasi-static formulation to model multicellular constructs, followed by Beuth et al. (2007).

3.2.9 MPM variations

Different studies have been carried out in order to identify the caveats and to improve the accuracy and efficiency of the MPM.

The Material Point Method for solid mechanics conserves mass and momentum by construction, but energy conservation is not explicitly enforced. In 2002, Bardenhagen (2002) found that the energy conservation on the material points strongly depends on whether updating strain and stress rates first (USF) or later (USL) within a numerical time step. Meanwhile USL algorithm is dissipative, the USF algorithm is conservative. It suggested that the dissipative algorithm is a better choice in general, as the damping is consistent with the accuracy of the solution.

In 2004, Bardenhagen and Kober (2004) presented the generalised MPM procedure for computational solid mechanics by using a variational form and a Petrov-Galerkin discretisation scheme. This results in a family of methods named the Generalised Interpolation Material Point (GIMP) methods. To avoid some computational instabilities (cell crossing noise) inherent to the original method (MPM), the interpolation functions are in C^1 (as opposed to MPM, for which they are in C^0). Wallstedt and Guilkey (2008) studied the stability and accuracy of the method and several time integration schemes were compared.

In 2008, Buzzi et al. (2008) posed some caveats during the implementation of both MPM and GIMP algorithms. For instance, the setting up of boundary conditions and the steps for the computation of values at nodes and material points were discussed. Steffen et al. (2008a) presented an analysis of the quadrature errors found in the computation of internal force in MPM and proposed some improvements, such as the use of a quadratic B-spline basis for representing solutions on the grid.

In 2010, Shin et al. (2010) proposed strategies for dynamically creating, managing and removing mesh cells during computations. It was developed to model problems involving motion of a finite size body in unbounded domains in which the extent of material travel and deformation is unknown a priory, such as in landslides and debris flows. The key idea is to initialise the mesh efficiently and to search only that cells containing material points, thereby avoiding unneeded storage and computation.

Other extensions of the MPM are the convected particle domain interpolation methods (CPDI1 and CPDI2) (Kamojjala et al., 2013; Sadeghirad et al., 2011, 2013). These are capable of tracking material point domains more accurately, especially for problems involving extremely large tensile deformations and rotations.

3.3 Single-phase MPM formulation

The MPM formulation for mechanical problems (1-phase MPM formulation) is presented in this Section. It is based on Sulsky et al. (1995), in which only a single phase is considered. Because the MPM can be viewed as an extension of the FEM procedure, is important to note that they have much in common. For instance, the weak form of the governing equations as well as the final system of equations posed at the nodes of the computational mesh are identical in both schemes. The most distinguishing feature between them is the calculation of the numerical integrations over the volume of a finite element. Meanwhile in FEM the integrations are carried out using Gaussian quadrature, in MPM they are calculated at the corresponding material points.

The domains are three-dimensional in any case. Vectors and tensors are identified with bold type.

3.3.1 Governing equations

From a mathematical point of view, the continuum can be described by a set of differential governing equations. This includes conservation of mass, conservation of momentum, balance of energy and the corresponding boundary conditions. Furthermore, constitutive equations such as stress-strain relationship, which are characteristic of the material forming the continuum, are needed.

One of the features of the MPM formulation for a 1-phase material is that the mass of each material point m_p remains constant during all calculation. This fact implies that mass conservation is automatically satisfied. Moreover, it has been assumed that thermal effects are very small hence they have been neglected in all the document.

3.3.1.1 Momentum balance equation

The momentum conservation of the continuum can be written with the differential equation (3.1). A dynamic formulation is considered, which means that the acceleration therm is taken into account.

$$\rho \mathbf{a} = \nabla \cdot \boldsymbol{\sigma} + \rho \mathbf{b} \tag{3.1}$$

The density of the continuum is represented by ρ, $\mathbf{a}$ is the acceleration, $\boldsymbol{\sigma}$ is the Cauchy stress tensor, and $\mathbf{b}$ is the body force vector.

Two kind of boundary conditions are defined: prescribed traction (Eq.3.2) and prescribed displacements (Eq.3.3). Each one is applied on the corresponding domain, $\partial\Omega^{\mathbf{t}}$ and $\partial\Omega^{\mathbf{u}}$ respectively.

$$\boldsymbol{\sigma}(\mathbf{x}, t) \cdot \mathbf{n} = \widehat{\mathbf{t}}(t) \tag{3.2}$$

$$\mathbf{u}(\mathbf{x}, t) = \widehat{\mathbf{u}}(t) \tag{3.3}$$

$\mathbf{x}$ is the position vector, $\mathbf{u}$ is the displacement vector and t is time.

3.3.1.2 Constitutive equation

The constitutive equation of a mechanical problem defines the relationship between stress and strain. The stress tensor and the strain tensor both can be represented in a vector form, respectively as follows,

$$\boldsymbol{\sigma} = (\sigma_{xx}, \sigma_{yy}, \sigma_{zz}, \sigma_{xy}, \sigma_{yz}, \sigma_{xz})^T$$

$$\boldsymbol{\varepsilon} = (\varepsilon_{xx}, \varepsilon_{yy}, \varepsilon_{zz}, 2\varepsilon_{xy}, 2\varepsilon_{yz}, 2\varepsilon_{xz})^T$$

being x, y and z the Cartesian coordinates. Taking into account the stress and strain rate vectors (Eq.3.4 and Eq.3.5), the general form of a suitable stress-strain relationship is written incrementally as equation (3.6), in which $\mathbf{D}$ is the tangent matrix defined by means of the constitutive model.

$$\dot{\boldsymbol{\sigma}}(\mathbf{x}, t) = \frac{d}{dt}\boldsymbol{\sigma}(\mathbf{x}, t) \tag{3.4}$$

$$\dot{\boldsymbol{\varepsilon}}(\mathbf{x}, t) = \frac{d}{dt}\boldsymbol{\varepsilon}(\mathbf{x}, t) \tag{3.5}$$

$$\dot{\boldsymbol{\sigma}} = \mathbf{D} \cdot \dot{\boldsymbol{\varepsilon}} \tag{3.6}$$

3.3.2 Numerical implementation

The differential form of the governing equation (3.1) must be integrated and discretised in space and time. In the current Section, the spatial discretisation, to the nodes and to the material points, is described. Finally, the explicit time algorithm is outlined.

Hereinafter, note that subscripts i and j are refereed to the nodal index, the subscript or superscript p corresponds to the material point index, and the superscript k is refereed to the time step.

3.3.2.1 Spatial Discretisation

The computational mesh that uses MPM is the same as the one in the conventional FEM, composed by nodes and elements (Fig.3.1). The standard nodal shape functions N_j provide the relationship between the nodes and any point of the computational domain. In this thesis 4-nodded tetrahedral elements (Fig.3.2) with linear shape functions have been used. The displacement at any point of the computational domain is approximated

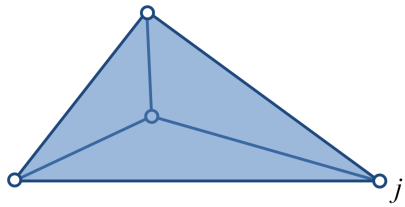

Figure 3.2: Used element: 4-nodded tetrahedral element

considering the nodal values as

$$\mathbf{u}(\mathbf{x},t) = \sum_{j=1}^{N_n} \mathbf{u}_j(t) N_j(\mathbf{x},t) \tag{3.7}$$

in which N_n is the number of active nodes in the mesh, $\mathbf{u}_j(t)$ is the displacement vector of node j. The shape functions N_j are packed in the matrix $\mathbf{N}_j$, defined below, because of three dimensions of the domain.

$$\mathbf{N}_j(\mathbf{x},t) = \begin{bmatrix} N_j & 0 & 0 \\ 0 & N_j & 0 \\ 0 & 0 & N_j \end{bmatrix} \tag{3.8}$$

Until this point, both the MPM and the FEM procedures are identical. The main difference is from now on, that MPM divides the continuum into a finite number of subdomains called material points (Fig.3.1). Each one moves attached with the solid skeleton of the continuum that represents, providing a lagrangian description of the motion and carrying all the information (displacement, velocity, stresses, etc.). From a numerical point of view, the material points can be compared with the Gaussian integration points in FEM, but in this case they can move through the computational mesh instead of being fixed within the elements. As we consider low order shape functions, only a single integration point per each finite element is the minimum to perform the numerical integration over the volume of a tetrahedra element.

Assuming the whole mass of a subdomain represented by a material point is concentrated at the corresponding material point, the density of the continuum can be expressed as

$$\rho(\mathbf{x},t) = \sum_{p=1}^{N_p} m_p \delta(\mathbf{x} - \mathbf{x}_p) \tag{3.9}$$

where m_p and $\mathbf{x}_p$ are the mass and the position of the p material point, $\delta(\mathbf{x})$ is the Dirac delta function, and N_p is the total number of material points.

Finally, the displacement of a material point can be obtained as function of the nodal displacements, particularising equation (3.7) in the corresponding material point position $\mathbf{x}_p$ as follows.

$$\mathbf{u}_p(\mathbf{x}_p,t) = \sum_{j=1}^{N_n} \mathbf{u}_j(t) N_j(\mathbf{x}_p,t) \tag{3.10}$$

The same expression can be adopted for the velocity and acceleration of a material point.

3.3.2.2 Discretised momentum balance equation

The Weighted Residuals method (Finlayson, 1972; Finlayson and Scriven, 1966) can be applied to obtain the weak form of the linear momentum equation over the domain Ω. This is given by

$$\int_{\Omega} \delta\mathbf{u} \cdot \rho\mathbf{a} d\Omega = \int_{\delta\Omega^{\mathbf{t}}} \delta\mathbf{u} \cdot \widehat{\mathbf{t}} d\partial\Omega^{\mathbf{t}} - \int_{\Omega} \nabla\delta\mathbf{u} : \boldsymbol{\sigma} d\Omega + \int_{\Omega} \delta\mathbf{u} \cdot \rho\mathbf{b} d\Omega \tag{3.11}$$

$\delta\mathbf{u}$ is a test function which is zero on the boundary where displacements are prescribed $\partial\Omega^{\mathbf{u}}$.

Using the spatial discretisations (Eq.3.7, 3.9, and 3.10) and the constitutive equation (3.6), the weak form of the linear momentum equation (3.11) can be written as the following system of equations.

$$\sum_{j=1}^{N_n} \Big(\sum_{p=1}^{N_p} m_p N_i^p N_j^p \Big) \mathbf{a}_j = \int_{\partial\Omega^{\mathbf{t}}} N_i^p \widehat{\mathbf{t}} d\partial\Omega^{\mathbf{t}} - \sum_{p=1}^{N_p} \mathbf{B}_i^p \cdot \boldsymbol{\sigma}_p V_p + \sum_{p=1}^{N_p} m_p N_i^p \mathbf{b} \tag{3.12}$$

V_p is the volume associated with each material point and $N_i^p = N_i(\mathbf{x}_p, t)$. $\mathbf{B}_i^p$ is the nodal matrix $\mathbf{B}_i(\mathbf{x}, t)$ particularised for a material point, which includes the spatial derivatives of the nodal shape functions as follows.

$$\mathbf{B}_i(\mathbf{x}, t) = \begin{bmatrix} \frac{\partial N_i}{\partial x} & 0 & 0 \\ 0 & \frac{\partial N_i}{\partial y} & 0 \\ 0 & 0 & \frac{\partial N_i}{\partial z} \\ \frac{\partial N_i}{\partial y} & \frac{\partial N_i}{\partial x} & 0 \\ \frac{\partial N_i}{\partial z} & 0 & \frac{\partial N_i}{\partial x} \\ 0 & \frac{\partial N_i}{\partial z} & \frac{\partial N_i}{\partial y} \end{bmatrix} \tag{3.13}$$

Then, the final discretised system of equations results as

$$\mathbf{M} \cdot \mathbf{a} = \mathbf{F}^{ext} - \mathbf{F}^{int} \tag{3.14}$$

where $\mathbf{a}$ is the nodal acceleration vector, $\mathbf{M}$ is the mass matrix, $\mathbf{F}^{int}$ is the internal force vector and $\mathbf{F}^{ext}$ is the external force vector. These are given by

$$\mathbf{M} = \sum_{p=1}^{N_p} m_p \mathbf{N}^{pT} \cdot \mathbf{N}^p \tag{3.15}$$

$$\mathbf{F}^{int} = \sum_{p=1}^{N_p} \mathbf{B}^p \cdot \boldsymbol{\sigma}_p V_p \tag{3.16}$$

$$\mathbf{F}^{ext} = \int_{\partial\Omega^{\mathbf{t}}} \mathbf{N}^p \cdot \widehat{\mathbf{t}} d\partial\Omega^{\mathbf{t}} + \sum_{p=1}^{N_p} m_p \mathbf{N}^p \cdot \mathbf{b} \tag{3.17}$$

3.3.2.3 Mass matrix

To solve the system of equations (3.14), the mass matrix has to be inverted. In practise, to simplify computations, a lumped mass matrix may be used instead of the consistent mass matrix given by equation (3.15). The lumped mass matrix is a diagonal matrix in which each entry m_i is obtained by summing over the corresponding row of the consistent mass matrix. Matrix inversions become trivial, although the result of using a lumped mass matrix is some dissipation of kinetic energy that has been quantified by Brackbill et al. (1988). Using the property $\sum_{j=1}^{N_n} N_j^p = 1$ it becomes

$$\mathbf{M}^L = \sum_{p=1}^{N_p} m_p \mathbf{N}^p \tag{3.18}$$

Hereinafter, the subscript L is removed from the lumped mass matrix $\mathbf{M}^L$ to simplify the notation, and mass matrix always will refer to a lumped matrix.

In each time step, nodal velocity gradients are needed in order to calculate the strain increment at the material points. Therefore, it is necessary to determine the nodal velocities $\mathbf{v}_i$ from the velocities at the material points $\mathbf{v}_p$. The following equation must be solved.

$$m_i \mathbf{v}_i = \sum_{p=1}^{N_p} m_p N_i^p \mathbf{v}_p \tag{3.19}$$

Then, taking advantage that the lumped mass matrix is diagonal, the nodal velocities are calculated as

$$\mathbf{v}_i = \frac{1}{m_i} \sum_{p=1}^{N_p} m_p N_i^p \mathbf{v}_p \tag{3.20}$$

3.3.2.4 Time discretisation

The time has been discretised into different instants (k). Considering Δt the time step size, the time discretisation approach is $t^{k+1} = t^k + \Delta t$.

If the general system of equations (3.14) is posed at time t^k, it can be rewritten as equation (3.21), where the acceleration $\mathbf{a}^k$ is the unknown.

$$\mathbf{M}^k \cdot \mathbf{a}^k = \mathbf{F}^{int\,k} + \mathbf{F}^{ext\,k} \tag{3.21}$$

An explicit Euler time integration scheme is used to update the velocity (Eq.3.22). This is a first-order numerical procedure for solving ordinary differential equations (ODEs) with a given initial value. Being $\mathbf{v}^k$ the velocity at time t^k, the velocity at the next time step t^{k+1} is calculated using the acceleration at time t^k as follows.

$$\mathbf{v}^{k+1} = \mathbf{v}^k + \triangle t \mathbf{a}^k \tag{3.22}$$

On the other hand, the displacements at time t^{k+1} are calculated using the updated velocity $\mathbf{v}^{k+1}$ as indicated in equation (3.23).

$$\mathbf{u}^{k+1} = \mathbf{u}^k + \triangle t \mathbf{v}^{k+1} \tag{3.23}$$

3.3.3 Computational cycle

The algorithm presented here is based on the work presented by Sulsky et al. (1995), which was improved respected the original one Sulsky et al. (1994). The key point is to work with momentum instead of velocity as much as possible, thus avoiding divisions by nodal masses. In each time step, the MPM computational cycle can be listed as follows.

1. The nodal mass is calculated using the shape functions and the lumped mass matrix at time t^k is formed (Eq.3.18). The internal and external forces are evaluated in the nodes (Eq.3.16 and Eq.3.17).

2. The momentum balance equation (3.21) is solved and the nodal accelerations $\mathbf{a}_i^k$ are determined.

3. The velocity at the material points is updated considering equation (3.22) as

$$\mathbf{v}_p^{k+1} = \mathbf{v}_p^k + \Delta t \sum_{j=1}^{N_n} N_j^{p^k} \mathbf{a}_j^k \tag{3.24}$$

4. Updated nodal velocities are calculated taking into account equation (3.20) as

$$\mathbf{v}_j^{k+1} = \frac{1}{m_j^k} \sum_{p=1}^{N_p} m_p N_j^{p^k} \mathbf{v}_p^{k+1} \tag{3.25}$$

5. Particle positions are updated considering equation (3.23) as

$$\mathbf{x}_p^{k+1} = \mathbf{x}_p^k + \Delta t \sum_{j=1}^{N_n} N_j^{p^k} \mathbf{v}_j^{k+1} \tag{3.26}$$

6. The strain increment of a material points can be expressed in function of the nodal velocity as

$$\Delta \boldsymbol{\varepsilon}_p^{k+1} = \big(\sum_{j=1}^{N_n} \mathbf{B}_j^{p^k} \cdot \mathbf{v}_j^{k+1} \big) \Delta t \tag{3.27}$$

7. The constitutive stresses are updated using a material constitutive model (Eq.3.6).

8. The material properties are updated in the material points, such as volume and density, which are updated considering the increment of volumetric strain.

9. The computational grid is initialised for the next step, nodal values are discarded and the material points carry all the updated information.

3.3.4 Minimum time step criterion

A numerical algorithm is stable and well posed when the numerical solution is maintained close to the exact one throughout the calculation, which means that the errors stay bounded. The stability of a numerical algorithm depends on the integration scheme. Explicit time integration schemes, such as the one presented above, are conditionally stable. In order to determine the stability condition, an stability analysis based on the matrix method has been carried out. In this case, the stability criterion will provide the maximum time step value required to ensure the stability of the solution.

Being $\widehat{\mathbf{x}}^{k+1}$ the solution of a general scheme at time t^{k+1}, this can be expressed as

$$\widehat{\mathbf{x}}^{k+1} = |\mathbf{A}|\widehat{\mathbf{x}}^{k} \tag{3.28}$$

with $|\mathbf{A}|$ the determinant of the amplification matrix of the scheme.

The stability of the scheme is obtained if the spectral radius of the matrix $\mathbf{A}$ verifies

$$\varrho(\mathbf{A}) \leq 1 \tag{3.29}$$

where $\varrho(\mathbf{A}) = \max_i(\lambda_e)$ and λ_e are the eigenvalues of $\mathbf{A}$. Taking the previous condition equal to 1, the critical time step criterion can be established assuming that the characteristic polynomial of the amplification matrix is zero for $|\lambda_e| = 1$.

$$P_c[\mathbf{A} - \lambda_e \mathbf{I}]\Big|_{|\lambda_e|=1} = 0 \tag{3.30}$$

In order to study the solution stability of the 1-phase formulation presented in this Chapter, the above criteria has to be imposed to the explicit scheme described in Section 3.3.2.4.

The main governing equation solved at the nodes of the computational mesh is the dynamic momentum equation (Eq.3.21). Taking into account an elastic material, and considering the homogeneous form, equation (3.21) can be rewritten for a single node i per unit volume at time t^k as follows,

$$\rho \mathbf{a}_i^k + \kappa \mathbf{u}_i^k = 0 \tag{3.31}$$

where κ is the stiffness of the node per unit volume.

$$\kappa = \frac{E_c}{(L_i)^2} \tag{3.32}$$

Here, L_i is a characteristic length of the node i. E_c is the constrained elastic modulus which is function of the bulk modulus of the material K, and the shear modulus G as $E_c = K + \frac{4}{3}G$.

Taking into account the time discretisation scheme proposed in (3.22) and (3.23), the second-order ordinary differential equation (ODE) (Eq.3.31) is rewritten as a system of two first-order ODEs.

$$\begin{cases} \mathbf{u}_i^{k+1} = (1 - \frac{\kappa}{\rho})\mathbf{u}_i^k \Delta t^2 + \mathbf{v}_i^k \Delta t \\ \mathbf{v}_i^{k+1} = -\frac{\kappa}{\rho}\mathbf{u}_i^k \Delta t + \mathbf{v}_i^k \end{cases} \tag{3.33}$$

Therefore, the amplification matrix is given by

$$\mathbf{A} = \begin{bmatrix} 1 - \frac{\kappa}{\rho}\Delta t^2 & \Delta t \\ -\frac{\kappa}{\rho}\Delta t & 1 \end{bmatrix} \tag{3.34}$$

Finally, applying equation (3.30), the following critical time step criterion comes out,

$$\Delta t_{crit} = \frac{2}{\omega} \tag{3.35}$$

where ω is the natural frequency of the system which can be written as

$$\omega = \frac{1}{L_i}\sqrt{\frac{E_c}{\rho}} \tag{3.36}$$

In this Thesis, the well-known Courant-Friedrichs-Levy condition (CFL) (Courant et al. (1967)) is taken into account. It considers that the maximum time step in discrete systems is based on the fastest material wave speed and it must be below a critical value Δt_{crit}^{CFL}.

$$\Delta t_{crit}^{CFL} = \frac{L_e}{c_p} \tag{3.37}$$

L_e is the element length and c_p is the speed of the compression wave through the continuum. Considering an elastic material c_p is given by

$$c_p = \sqrt{\frac{E_c}{\rho}} \tag{3.38}$$

Comparing the critical step criterion (Eq.3.35) and the CFL condition (Eq.3.37), it is clear that both equations are equivalent when $L_i = \frac{L_e}{2}$. This is exactly true when considering the stability of a two-nodded linear finite element.

The characteristic element length L_i depends on the shape of the elements. Usually, to be conservative, the shortest distance of the element is considered. In this work the elements of the computational mesh are tetrahedrons, and it is assumed that L_e can be approximated as the minimum altitude of the tetrahedra h_{min}.

The time step criterion Δt used in the calculations, sometimes, is a bit a more conservative to ensure computational stability. It is considered a factor α_C smaller than one multiplying the Courant limit as

$$\Delta t = \alpha_C \Delta t_{crit} \tag{3.39}$$

3.3.5 Cell-crossing instability

The classical MPM approach suffers from a "cell-crossing instability" for problems involving large displacements. Whenever material points cross boundaries of any element in the computational background grid, an unphysical unbalance force appears at the nodes that are shared between previous and new elements of that crossing points. The explanation for that is the lack of smoothness of the nodal shape functions used in the interpolation of information between grid and material points. The shape functions are linear C^0, which means that the gradients of the shape functions within the element are constant but they are discontinuous at the element borders (they change the sign). These gradients are used in the calculation of the nodal internal forces according to (3.16). Therefore, when one material point crosses a border, the internal forces of those involved nodes suffer an unphysical instability due to a jump discontinuity in the gradient of linear shape functions.

This numerical difficulty was initially described by Zhou et al. (1999), and since then, several authors attempted to reduce this error. Bardenhagen and Kober (2004) proposed a particle characteristic function instead of a Dirac delta function (Eq.3.9), in this way the mass of the material point is distributed along a delimited domain instead of being concentrated in a point. This results in a family of methods known as Generalised Interpolation Material Point (GIMP) methods, such as uniform GIMP (uGIMP) and the contiguous-particle GIMP (cpGIMP), in which the particle characteristic function associated with each material points is constant or time-dependent respectively (Steffen et al., 2008b).

Other extensions of the MPM are the convected particle domain interpolation methods (CPDI1 and CPDI2) which are capable of tracking material point domains more accurately, especially for problems involving massive deformations (Kamojjala et al., 2013; Sadeghirad et al., 2011, 2013). These techniques typically increase the computational cost compared with the standard MPM. Although these approaches reduce the instability associated with the cell-crossing problem, higher computational time is needed since each material point involves its neighbouring cells due to the spread of the interpolation functions. Moreover, the application of boundary conditions is not trivial.

In this Thesis another procedure has been considered to mitigate the cell-crossing instability. This is a simple technique that was used previously by Zabala (2010) and Al-Kafaji (2013). It arises from calculating the stress of each element as a constant value that corresponds to the average of the stresses of the material points that at time t^k are located within the element. Based on that, Gauss integration is adopted to determine the internal forces (as in FEM), in which a single point with an averaged stress $\boldsymbol{\sigma}_{av}$ is considered in each element. The stress averaging is calculated according to the following expression (3.40), where N_p is the number of material points within the element, and $\boldsymbol{\sigma}_p$ and V_p are the stress and the volume of a material point, respectively.

$$\boldsymbol{\sigma}_{av} = \frac{\sum_{p=1}^{N_p} \boldsymbol{\sigma}_p V_p}{\sum_{p=1}^{N_p} V_p} \tag{3.40}$$

The calculation of the internal forces by means of the Gauss point integration is only considered in the elements located in the interior of the continuum. On the contrary, elements located on a boundary of a body are integrated with the classic MPM procedure.

3.3.6 Volumetric locking

The formulation of the MPM is very close to the FEM in many aspects. At some point, this similarity is beneficial because most of the existing knowledge can be transferred to the MPM. However, several shortcomings associated with the FEM have been inherited by the MPM. Probably one of the most important limitation is the kinematic locking that can occur due to the linearity of the traditional shape functions constructed on the computational mesh. Difficulties arise when determining the displacement field for a nearly incompressible solid.

As a simple example of this phenomenon, consider Figure 3.3. Element e_1, in Figure 3.3a, is defined by nodes 1 and 2 on the x axis, and node 3 on the y axis. The area of the triangular element must remain constant if it is incompressible. If nodes 1 and 2 are fixed, y_3 must remain constant and $u_y^3 = 0$. Therefore, the remaining degree of freedom is the horizontal displacement u_x^3. Similarly, the only remaining degree of freedom in the element e_2 (Fig. 3.3b) defined by nodes 4, 5, and 6, is the vertical displacement u_y^5. Two triangles may be assembled, see Figure 3.3c. Since incompressibility for element e_1 requires $u_y^3 = 0$ and incompressibility for element e_2 requires $u_x^3 = 0$, node 3 cannot move, and both elements are completely locked up. With nodes 1 through 4 locked up, the nodes for elements 3, 4, 5, 6, 7 and 8 will also be locked (Fig. 3.3c). Such locking usually propagates throughout the entire mesh yielding an unrealistic stiff response and an erroneous velocity field.

Several anti-locking approaches have been presented by different authors to mitigate this numerical problem associated with the linear shape functions (Detournay and Dzik, 2006; Mast et al., 2012). In this work, the Nodal Mixed Discretisation (NMD) technique for linear tetrahedra elements presented by Detournay and Dzik (2006) has been used to mitigate the over-stiff behaviour. This procedure has showed effectiveness in mitigating the locking associated with (near) incompressible deformations Al-Kafaji (2013). In this technique, the element volumetric behaviour is averaged over the elements sharing its nodes via a least squares smoothing process. The effect of applying the NMD scheme is to increase the number of degrees of freedom per element. Being $\dot{\boldsymbol{\varepsilon}}$ the strain rate of an element calculated from nodal velocities, it can be divided into deviatoric $\dot{\mathbf{e}}$ and

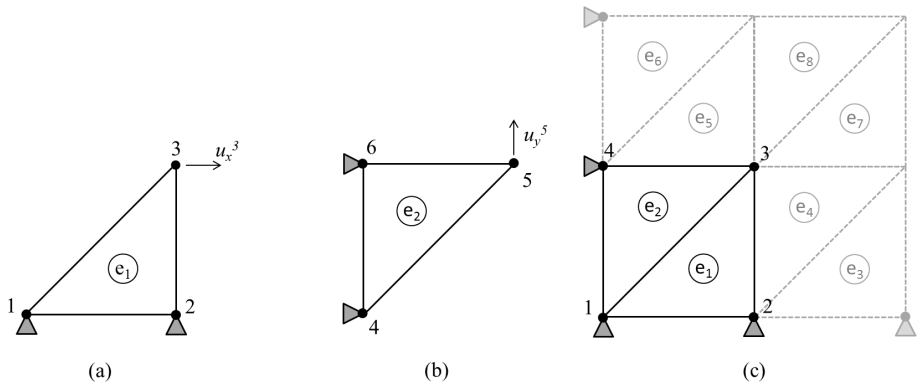

Figure 3.3: A pathological case of volumetric locking in triangular elements. Degrees of freedom are indicated.

volumetric $\dot{\varepsilon}_{vol}$ components as

$$\dot{\boldsymbol{\varepsilon}} = \dot{\mathbf{e}} + \dot{\varepsilon}_{vol}\mathbf{m} \tag{3.41}$$

where $\mathbf{m} = (1, 1, 1, 0, 0, 0)^T$.

The volumetric strain rate for a node i, can be defined as weighted average of the surrounding element values $\dot{\varepsilon}_{vol,e}$ with the following equation:

$$\dot{\varepsilon}_{vol,i} = \frac{\sum_{e=1}^{N_e} \dot{\varepsilon}_{vol,e} V_e}{\sum_{e=1}^{N_e} V_e} \tag{3.42}$$

where N_e are the elements surrounding the node n, and V_e is the volume of the element e.

Then, a mean value for the element, $\bar{\dot{\varepsilon}}_{vol}$ is calculated by taking the average of nodal quantities as

$$\bar{\dot{\varepsilon}}_{vol} = \frac{1}{N_{en}} \sum_{i=1}^{N_{en}} \dot{\varepsilon}_{vol,i} \tag{3.43}$$

where N_{en} is the number of nodes in an element.

Finally, the element strain rates is redefined by superposition of the deviatoric part and the volumetric average as

$$\dot{\boldsymbol{\varepsilon}} = \dot{\mathbf{e}} + \bar{\dot{\varepsilon}}_{vol}\mathbf{I} \tag{3.44}$$

3.3.7 Artificial damping

Having a dynamic formulation is very useful to study those engineering problems where the inertia plays an important role in its development. However, some problems in the geotechnical field involve very slow processes in which the steady state solution is of interest rather than the dynamic analysis of wave propagation. It can not be forgotten that the algorithm presented in this Section is explicit and the calculation progress is limited to small time increments. Then, the modelling of long periods of time has a high computational cost.

In order to converge to the quasi-static equilibrium as fast as possible, an artificial damping should be included in the formulation in order to introduce energy dissipation in the dynamic momentum conservation. In this work, a so-called local non-viscous damping Cundall (1987) has been considered. It assumes that the damping force on a node is proportional to the magnitude of the unbalanced force. The direction of the damping force is taken in such a way that energy is always dissipating (opposite to the velocity). Then, equation (3.14) is replaced with the following equation.

$$\mathbf{M} \cdot \mathbf{a}_j = \mathbf{F} + \mathbf{F}^{damp} \tag{3.45}$$

$\mathbf{F}$ corresponds to the unbalanced force ($\mathbf{F} = \mathbf{F}^{ext} - \mathbf{F}^{int}$).

Because the damping force can be understood as a frictional force, it is written as follows.

$$\mathbf{F}^{damp} = -sign(\mathbf{v})|\mathbf{F}|\alpha \tag{3.46}$$

in which $sign(\mathbf{v}) = \frac{\mathbf{v}}{|\mathbf{v}|}$ and α is a dimensionless parameter that ranges between 0 and 1.

3.3.8 Mass scaling

Another numerical technique to deal with calculation of large periods of time, is the mass-scaling procedure. It consists of applying an artificial uniform increase of the density considered in the mass matrix $\mathbf{M}$ as it is shown in equation (3.47).

$$(1 + \alpha_{ms})\mathbf{M} \cdot \mathbf{a} = \mathbf{F} \tag{3.47}$$

Such increase is represented by α_{ms}, which is a dimensionless parameter higher than 1 (smaller values would lead to a mass decrease).

This consideration reduces the speed of compression stress waves (see Eq.(3.38)) travelling through the continuum according to the following expression,

$$c_p^{ms} = c_p\sqrt{1 + \alpha_{ms}} \tag{3.48}$$

in which c_p^{ms} is the wave speed if the mass scaling is taken into account and c_p is the same without mass scaling.

Therefore, the critical time step with mass scaling results as

$$\Delta t_{crit}^{ms} = \frac{L_e}{c_p}\sqrt{1+\alpha_{ms}} = \Delta t_{crit}\sqrt{1+\alpha_{ms}} \tag{3.49}$$

3.3.9 Virtual material points

In a calculation, the continuum can experience large displacements and large deformations. During this process, material points move through the computational mesh and eventually, one element may remain empty during a few time steps until the next material point goes into it. This fact creates unrealistic small holes within the continuum and produces discontinuities of the strain and stress fields. The frequency of the problem depends on the spatial discretisation and gets worse when the initial number of material points per element is small or the computational mesh is very fine.

This numerical difficulty can be easily overcome by adding virtual materials points which are used as integration points in those empty elements. Despite increasing the number of material points, the total mass of the system must remain constant, thus the mass of virtual points should be negligible. The remaining properties, such as current stresses, can be obtained by averaging those values of the surrounding "true" material points. Each virtual material point is deleted from the calculation as soon as a material point moves into the element.

It is important to take into account that the continuum can deform, expand, fold on itself but also it can split or even real holes may appear in it. A simple criterion is considered in order to determine whether an empty element is part of a real opening or not. If the number of elements forming a hole is less than a threshold, it is considered that the opening is unrealistic and virtual particles should be created in it. On the contrary, the hole remains empty.

3.3.10 Boundary conditions

The application of boundary conditions is a subject rarely discussed in the literature of the Material Point Method. In this Section the different types of boundary conditions that can be found in a mechanical problem are presented.

From a numerical point of view, two kinds of boundary conditions can be distinguished: natural and essential. On the one hand, essential boundary conditions are imposed directly on the solution. In this way, degrees of freedom are directly eliminated from the system of equations. Dirichlet conditions are an example. On the other hand, natural boundary conditions are imposed on a secondary variable, such as in Newman or Newton (Robin) conditions.

The boundary conditions required in a mechanical problem are summarised in Table 3.1. Those are prescribed traction (Eq.3.2) and prescribed velocity (Eq.3.3), which correspond to natural and essential conditions respectively. In the numerical implementation, prescribed traction is included in the weak form of the governing equations, while calculated velocities are directly overwritten by the prescribed values.

Table 3.1: Types of boundary conditions in a mechanical problem.

Essential	Natural
Prescribed solid velocity (Eq.3.3)	Prescribed traction (Eq.3.2)

It is commonly accepted that boundary conditions are specified at the nodes of the mesh (Love and Sulsky, 2006b; Zabala, 2010). This idea makes sense considering that the governing equations are solved in the computational grid, and consequently the MPM formulation persists almost identical to that used in the FEM.

The problem of applying the boundary conditions at the nodes appears when a moving boundary is considered. In these cases, the boundary condition has to move attached to the body. However, in the standard MPM formulation, the computational mesh remains constant. Therefore, in such cases, the boundary condition should be carried by the material points.

This way of handling the boundary conditions to solve the issue of movement leads to some inaccuracies, specially in natural conditions. If the boundary condition is applied on a material point, this condition has to be distributed all over the nodes of the element to solve the system (3.14). If a material point is affected by a moving boundary condition, the element containing the point becomes part of the contour. Then, the contour has an equivalent thickness of the size of the element and the boundary condition is spread affecting all material points within the cell, even those which are not at the boundary. To minimise numerical errors, it is recommended to use a fine mesh.

Another difficulty of moving boundaries appears when external traction has not a prescribed direction. This means that if the shape of the contour changes, the direction of the applied condition has to be updated during the calculation. This is an expensive procedure, in which the normal vector must be calculated at every time step.

In Figure 3.4 a very simple problem is presented. It shows the movement of a beam that is fixed at one end and subjected to a vertical force F at the opposite end. In this example the fixity can be understood as an essential boundary condition in which the prescribed velocity is zero. Because it remain motionless, it can be applied at the nodes. On the other hand, the vertical force is a natural boundary condition which moves attached to the beam, therefore it should be carried by the material points.

In many problems, the computational domain can not be determined by a physical boundary. For instance, in a footing problem, while the ground surface or the contact between the footing and the ground are well-known realistic boundaries, the domain is unlimited downwards and a half space can be assumed (Fig.3.5a). Therefore, when such problem is

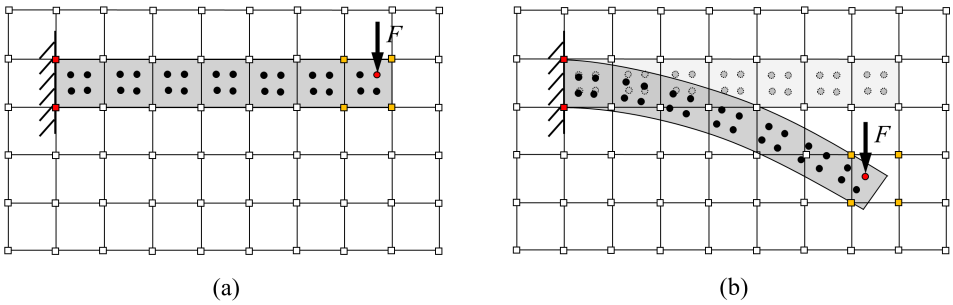

Figure 3.4: Problem of a beam subjected to a vertical force at one end and embedded at the other one. (a) Initial discretisation; (b) final discretisation. The boundary conditions are carried in those nodes and material points coloured in red. Yellow nodes are affected by the moving boundary condition although it is not stored in them.

discretised unphysical boundaries have to be defined in order to delimit the computational domain. Those numerical boundaries are indicated in Figure 3.5b (nodes in yellow). Because the MPM formulation is dynamic, when a load is applied, it propagates through the material domain. In the field, the wave spreads out. However, in the numerical simulation it reaches the numerical boundary and automatically it is reflected. This dynamic effect can modify the solution and unrealistic oscillations are originated.

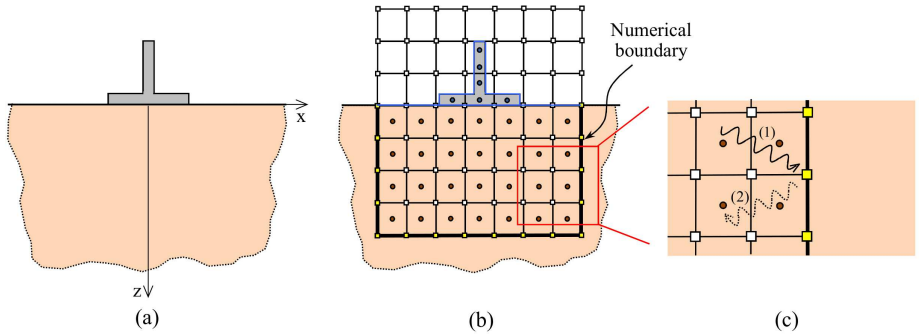

Figure 3.5: (a) Scheme of a shallow footing. (b) Distribution of material points and computational mesh. (c) Wave propagation: (1) incident wave, (2) reflected wave.

This effect is reduced by placing the mesh contours far enough from the origin of the loading. Hence the wave can be dissipated before reaching the boundary. The limitation here is the required computational time.

In order to attenuate the reflection of waves in artificial boundaries, Lysmer and Kuhlmeyer (1969) proposed to support such contours on dampers, including an external viscous force acting to such boundary nodes. Regarding the MPM, Al-Kafaji (2013) extended this concept by using Kelvin-Voigt elements, which considers the combination in parallel of one spring and one dashpot as shown in Figure 3.6. The spring and dashpot are connected to

the boundary nodes and its characteristics are chosen to provide a virtual layer beyond the real boundary of the numerical mesh capable of absorbing unphysical wave reflections. An additional external force has to be included in the dynamic momentum balance (Eq.3.21). Mechanically, this kind of boundary can be considered as in between a free boundary and a fixed one.

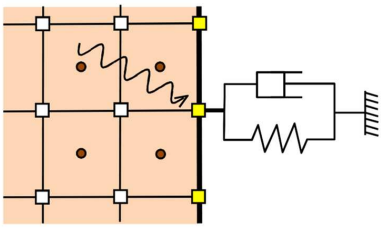

Figure 3.6: Detail of the Kelvin-Voigt element. In yellow those nodes affected by the viscous boundary.

3.3.11 Contact algorithm

The basic MPM formulation is capable to detect contact between different bodies. When two bodies approach enough to share one or more nodes of the computational mesh, a contact area is automatically created because a unique velocity field is calculated. In this way, special predefined element interfaces are not required and interpenetration of different bodies is naturally avoided (Sulsky et al., 1994). However, this is a non-slip contact which means that relative motion at the contact interfaces is not allowed.

In order to simulate more realistic contacts, several algorithms have been proposed (see Sec.3.2.2). They are straight to implement because they only effect the computational grid. The most accepted one was presented by Bardenhagen et al. (2000, 2001), and later on it was extended in Al-Kafaji (2013). It is capable of modelling sliding controlled by a frictional Mohr-Coulomb strength criterion, and separation controlled by an adhesive law. Assuming a system formed by several bodies (see Figure 3.7), the proposed algorithm consists on evaluating different velocity fields: one for each body and another one for the system. Comparing these nodal velocities, the contact nodes can be determined. Moreover, evaluating the normal vector to the contact surface, it can be distinguished if bodies are approaching or separating. Finally, material points surrounding contact nodes are updated with a corrected velocity field depending on the frictional and adhesive laws.

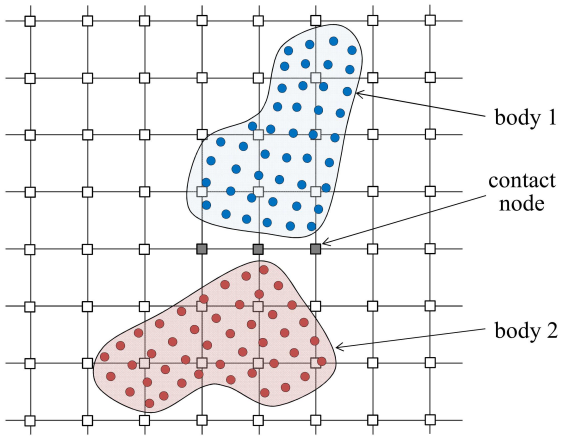

Figure 3.7: Scheme of two bodies. Contact nodes are indicated.

3.4 Validation

In this Section, two examples are presented in order to show the capability of the MPM formulation to reproduce dynamic problems. First the propagation of a compressive wave in a pile is validated with analytical solution. Afterwards, a blasting problem is presented.

3.4.1 Wave propagation

The propagation of a compressive wave through a one-dimensional sample is presented in order to analyse the dynamic effects of the mechanical formulation implemented here. This is one of the simplest problems of wave propagation in a mathematical sense.

Consider a one-dimensional problem simulating a pile 1 m deep. The bottom is completely fixed and an external compression of 1 kPa is suddenly applied at the upper boundary and it is maintained constant during the calculation. The material of the pile is linear elastic, with a Young's modulus E of 10 MPa. The density of the media ρ is 2300 kg/m^3 and 101 material points are uniformly distributed along the pile. Because nor artificial damping neither viscous boundaries are accounted in this simulation, the classical wave equation (Eq.3.50) fully describes the motion of the problem.

$$E\frac{\partial^2 \mathbf{u}}{\partial z^2} = \rho\frac{\partial^2 \mathbf{u}}{\partial t^2} \tag{3.50}$$

The speed of a compression wave c_p through that sample can be analytically calculated with the equation (3.38) and it results c_p=65.9 m/s. Therefore, the time required for a wave to travel through the entire length of the domain h is t_h=0.0152 s, being t_h=h/c_p.

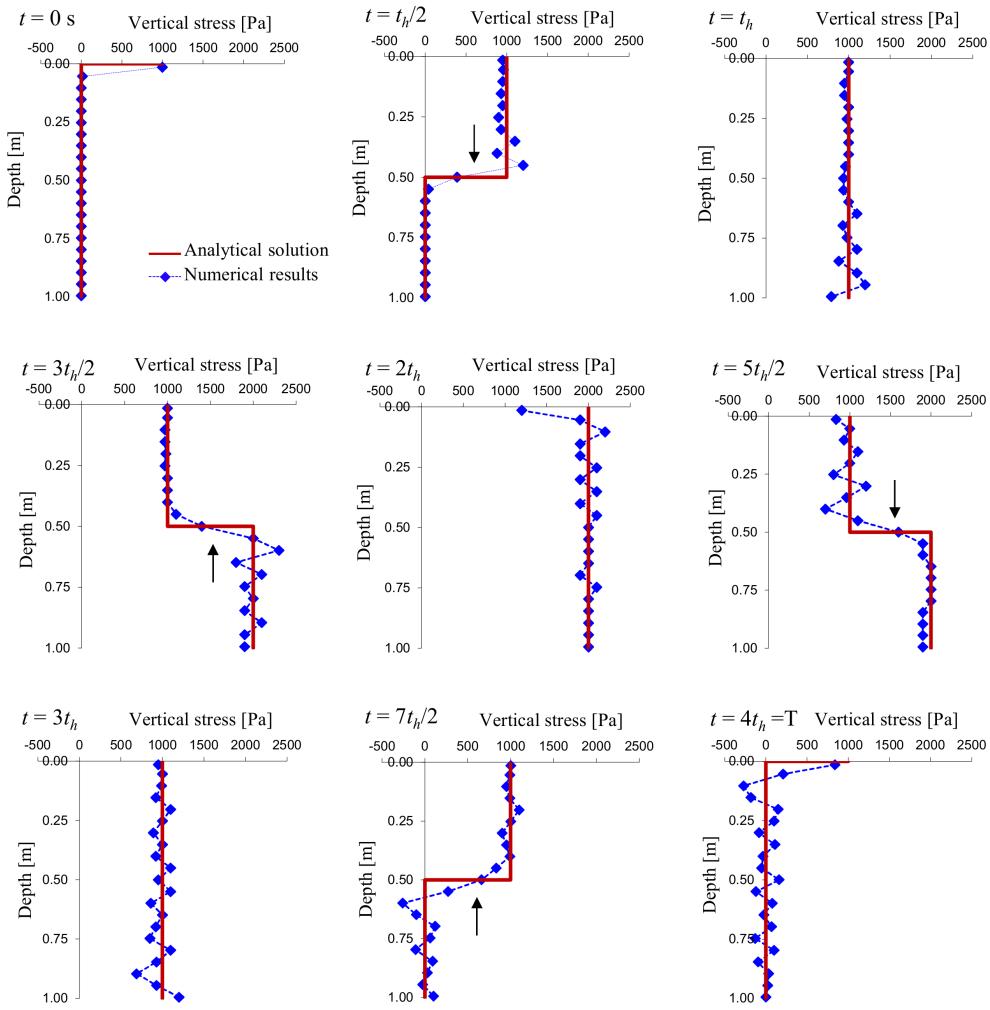

Figure 3.8: Wave propagation through a vertical sample. Comparison between analytical solution and numerical resutls.

The vertical stress distribution along the sample is represented in Figure 3.8 in which a comparison between analytical and numerical results is carried out. The entire sequence illustrates the wave propagation during one period T_p, which is the duration of one cycle in a repeating event. Initially, the compression wave moves downwards. When it reaches the fixed boundary at the bottom of the sample at $t{=}t_h$, the wave is totally reflected upwards and the stress value doubles. Note that the stress is maintained at the upper boundary as a result of the prescribed traction, meanwhile the stress at the bottom oscillates due to the reflection. The total time required to complete one cycle is $T_p{=}4t_h$.

Figures 3.9 and 3.10 shows the evolution of 3 material points located at the top, middle

and bottom of the sample. Vertical stresses and displacements obtained with the MPM code are compared with analytical expressions. Despite some numerical oscillations in the stresses, numerical results fit well the analytical values, especially the displacements.

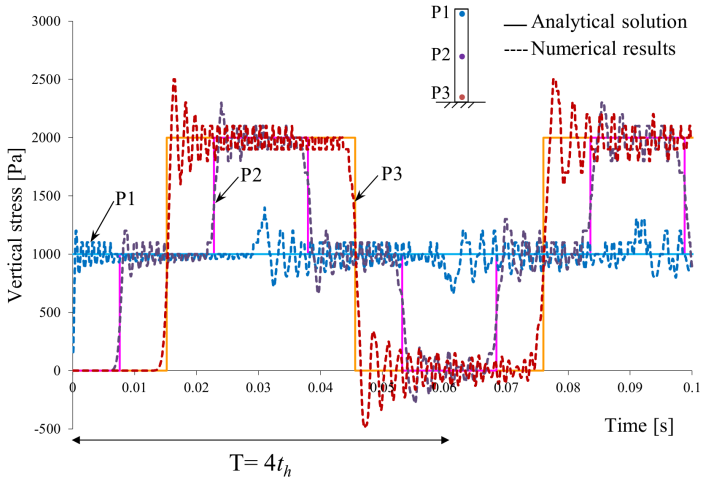

Figure 3.9: Vertical stress of three material points (P1, P2 and P3) located along the sample as a result of the wave propagation.

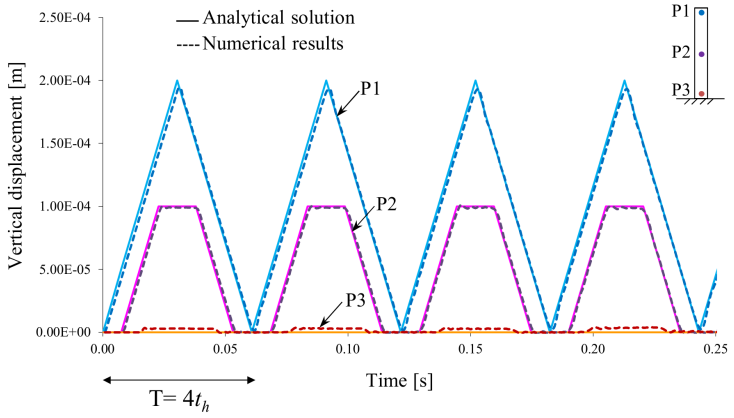

Figure 3.10: Displacements of three material points (P1, P2 and P3) located along the sample as a result of the wave propagation.

3.4.2 Blasting problem

The dynamic formulation of the MPM is useful to study some geotechnical problems such as the determination of stress and deformation in the vicinity of a blasting.

In the case analysed here, a detonation is applied in a fractured granite rock mass, which is covered by a more superficial layer of sand 5 m thick. Both materials have been modelled using an elastoplastic Mohr-Coulomb constitutive law (see parameters in Table 3.2). No additional damping has been considered neither in the material nor along the boundaries.

Table 3.2: General characteristics of the granite rock and the sand.

Material parameter	Granite	Sand
Density [kg/m^3]	2500	2300
Young's modulus [MPa]	10000	100
Poisson ratio	0.33	0.33
Cohesion [kPa]	600	50
Friction angle [^{o}]	42	35

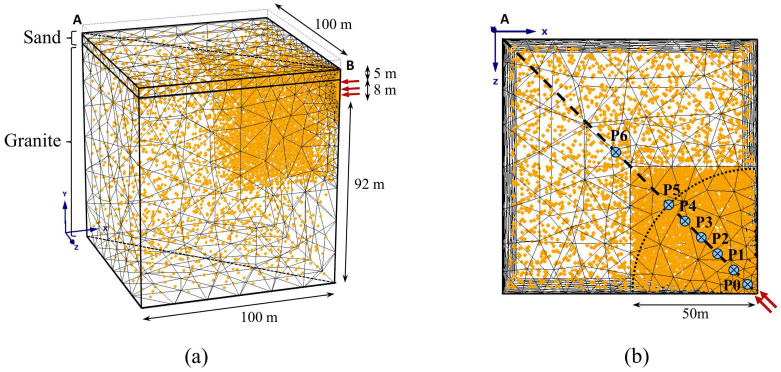

Figure 3.11: Simulation scheme; (a) dimensions and initial discretisation of the blasting problem; (b) top view in which points P0, P1, P2, P3, P4, P5 and P6 are indicated.

The problem is 3D and, taking into account two planes of symmetry, a cubic geometry is modelled (see Figure 3.11). The blasting is simulated by means of a horizontal pressure acting on a borehole length of 8 m along one of the edges as shown in Figure 3.11. This pressure is applied as a triangular ramp loading during 0.034 s, with a maximum of 2.5 GPa at 0.017 s. The mesh was made denser in the vicinity of the borehole in order to get more accurate results.

The rapid application of the load generates a compressive wave which extends in all directions throughout the domain. The speed of the wave propagation depends on the Young's modulus E and the density ρ of each material. According to 3.38, it is 250 m/s in the sand and 2500 m/s in the granitic rock. Taking into account these velocities and the distance to the boundaries of the computational domain, it has been determined that 0.06 s after the blasting, the compressive wave caused by the explosion may reach a point located at a distance of 50 m without being affected by artificial reflections.

The evolution of the calculated displacement field in section A-B is presented in Figure 3.12. The maximum displacements are concentrated in the area of the blasting and

propagates horizontally and downwards. As the wave propagates, it spreads on the ground and the displacement measured in the wave front decreases with time.

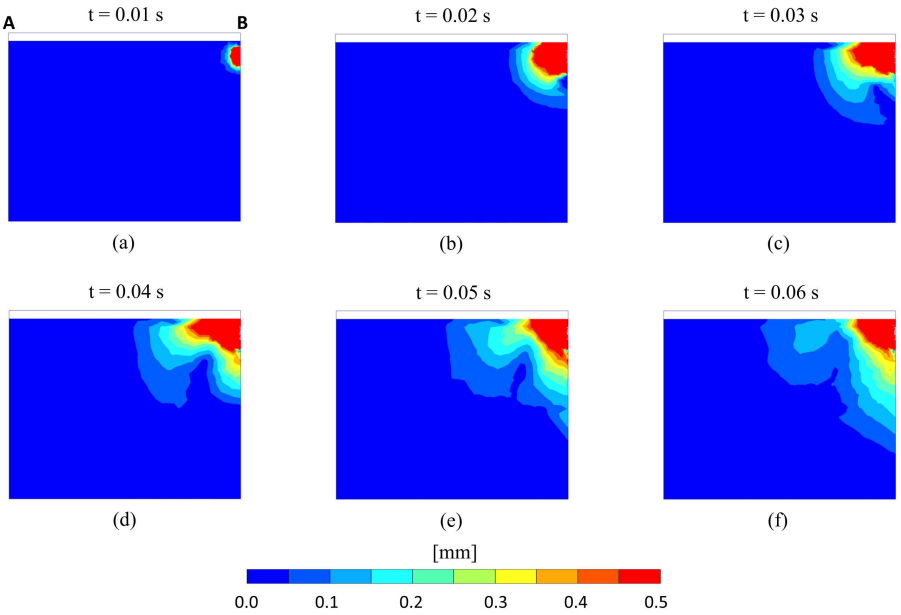

Figure 3.12: Displacements measured in section A-B at different times after the blasting: (a) 0.01 s; (b) 0.02 s; (c) 0.03 s;(d) 0.04 s; (e) 0.05 s; (f) 0.06 s.

The maximum amplitude measured 20 m deep at points P0, P1, P2, P3, P4, P5 and P6 (located and 4, 10, 20, 30, 40, 50 and 80 m far from the blasting) is illustrated in Figure 3.13. It is clear that the larger the affected area, the lower the amplitude of the wave front.

Because the Mohr-Coulomb constitutive model is an elastoplastic model, permanent (irreversible) plastic strain can be accumulated at some points if the stresses are sufficiently high to reach the failure criterion. Figure 3.14 shows in red colour those damaged material points that experience plastic deformation due to the compressive wave propagation. Areas located over 10 m from the blast remain in elastic conditions.

Finally, Figure 3.15 presents the stress paths of 3 material points P0, P1 and P5 the 0.06 s after the blasting. Only P0, which is the closest to the blasting, reaches the failure criterion.

With this simple analysis it can be concluded that the dynamic formulation of MPM is able to predict the propagation of a pressure wave caused by a blasting, and if a proper constitutive model is considered, those areas with further damage can also be delimited. Such studies are very useful in the engineering field and may have several applications in real geotechnical problems. For example, the determination of whether a blasting could

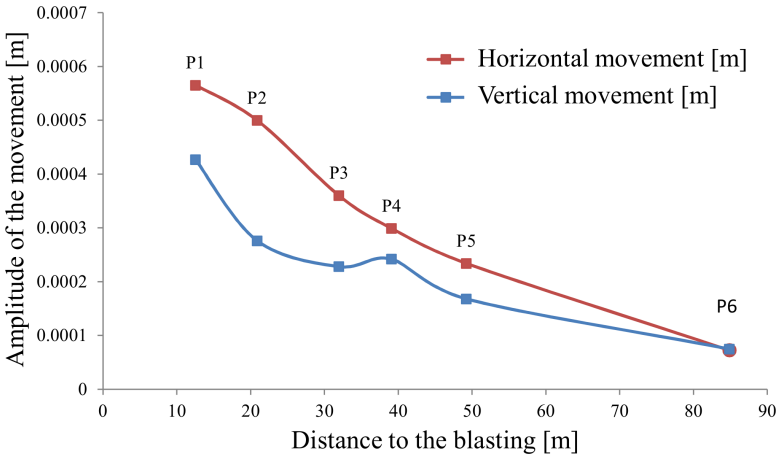

Figure 3.13: Maximum amplitudes measured at points P1, P2, P3, P4, P5 and P6.

affect adjacent infrastructures, such as a tunnel.

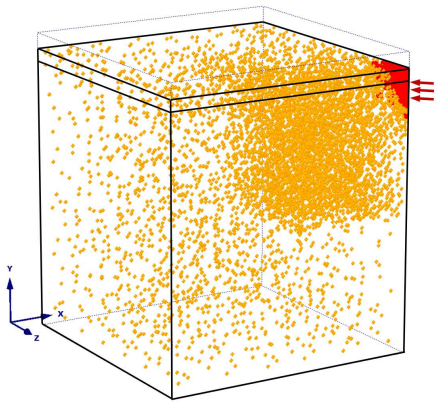

Figure 3.14: Distribution of the material points at the end of the calculation. Plastic points are indicated in red and elastic points are indicated in orange.

3.5 Concluding remarks

In this Chapter 3, an extensive literature review of the MPM history was performed. Recent applications in many different engineering fields indicate that MPM is becoming a powerful tool also in the geotechnical field.

The basis of the method were presented taking into account 1-phase material. A dynamic

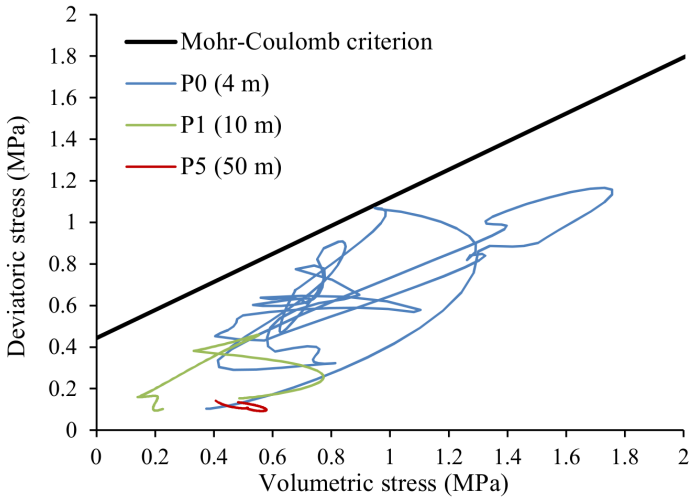

Figure 3.15: Stress paths in the stress plane (p-q) for points P0, P1 and P5. These are located at a depth of 20 m and at distances of 4, 10 and 50 m respectively from the origin of the blasting.

mechanical formulation is integrated by means an explicit time step algorithm. Some numerical difficulties related to the method itself (cell-crossing instability and virtual mass points), to the mesh discretisation (volumetric locking), and to the integration scheme (critical time step criterion) were discussed. Solutions presented by different authors to overcome such difficulties have been adopted in this work.

Finally, after validating the formulation by means a wave propagation problem, it can be concluded that MPM is capable of simulating dynamic problems such as blasting.

4

Chapter 4

Two-phase Formulation with MPM. Saturated Soils

In this Chapter 4, a 2-phase MPM formulation capable of modelling fully coupled hydromechanical problems is presented in order to simulate the behaviour of porous media under saturated conditions in large deformation problems.

The framework of saturated porous medium is defined in Section 4.1, and subsequently several MPM approaches capable of modelling solid-fluid interaction problems are introduced in Section 4.2. In Sections 4.3, 4.4 and 4.5, the 2-phase 1-point MPM formulation is presented in detail: governing equations, numerical implementation and the explicit computational cycle. Afterwards, several numerical issues are discussed. A stability analysis of the hydromechanical scheme has been carried out and a criterion to determine the critical time step is proposed in Section 4.6. The damping of the solution and boundary conditions are also outlined (Sec.4.7 and 4.8). Finally, the validation of the 2-phase MPM approach is presented by means of the simulation of the one-dimensional consolidation problem.

4.1 Saturated porous media

In a saturated porous media, it is assumed that pores are completely filled with liquid (e.g. water). Taking into account that the porosity n is the volume fraction of voids over the total volume, the continuum approximation of a saturated porous media as well as the volumetric relationship between its phases can be schematised as it is shown in Figure 4.1. In this way, the density of the mixture ρ_m is defined in function of the solid and liquid densities (ρ_s and ρ_l respectively) by considering the volume fractions of each phase (Eq.4.1).

$$\rho_m = (1-n)\rho_s + n\rho_l \tag{4.1}$$

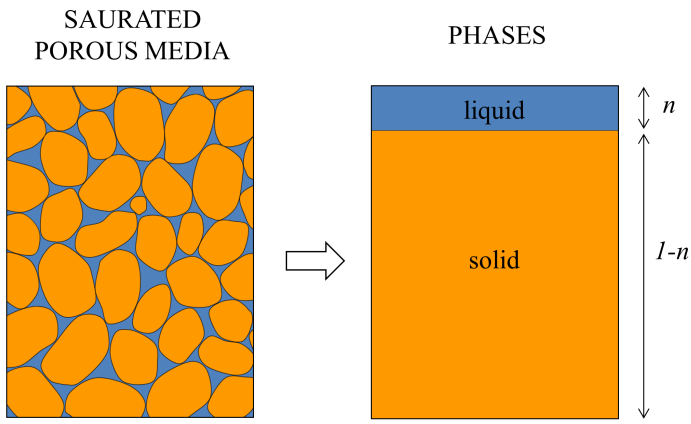

Figure 4.1: Continuum approximation of saturated porous media.

Taking into account the continuum mechanics theory, two important research lines of the porous media theory are commonly accepted. The first one is based on Biot's theory (Biot, 1941). This is a purely macroscale theory where the behaviour of porous media is described based on the kinematics of the solid skeleton. The second one proceeds from the mixture theory (Truesdell and Toupin, 1960), extended by the concept of volume fractions. It postulates that each point in space of a body is simultaneously occupied by a finite number of particles, one for each component of the mixture. In this way, the saturated media can be represented as a superposition of two continuous media (solid skeleton and liquid in the pores), following their own movement with the restriction imposed by the interaction between phases. These approaches have been generalised by different authors and many subsequent derivations are relevant today.

4.2 Two-phase problems in MPM

Within the context of the MPM, two different numerical approaches have been developed to model the behaviour of saturated soil (2-phases). Firstly, there is the so-called 1-point

formulation and it has been presented by different authors (Al-Kafaji, 2013; Jassim et al., 2013; Zabala and Alonso, 2011). It assumes that each material point represents a portion of saturated soil, carrying the information of both phases. In this case, while the material points are attached to the solid skeleton giving a lagrangian description of its movement, an eulerian approach with respect to the solid is considered to represent the motion of the liquid phase. In this approach, convective terms that appear in the liquid phase mass balance are commonly neglected. With this formulation, neither the simulation of a free water level nor the modelling of fluid-structure interaction with seepage are possible.

A second discretisation has been presented more recently in Abe et al. (2014) and Bandara (2013). It is referred as a 2-point formulation because the solid skeleton and the liquid phase are represented separately by two sets of lagrangian material points. The fluid phase is modelled as an independent material; therefore the solid-fluid medium can be viewed as a superposition of two continuous media. Thus, the material points that represent the fluid phase, e.g. water, can simulate both, water within the pores (in a saturated porous media) and free water. In this way, erosion problems and free water interactions can be naturally solved with this formulation. This MPM approach allows modelling liquid convective terms properly and it conserves both the mass of solid and liquid automatically. However, the computational cost of this approach is higher because the number of material points needed in a calculation is twice the number of a single-point formulation.

Figure 4.2 gives an schematic overview of the existing MPM approaches for 1-phase and 2-phase formulations.

In this Chapter 4, the 2-phase 1-point MPM approach has been considered in terms of the generalised Biot's formulation (Zienkiewicz and Shiomi, 1984) in order to model geotechnical problems under saturated conditions, in which the liquid phase is always considered as seeping fluid (water) within the pores and never it refers to free water.

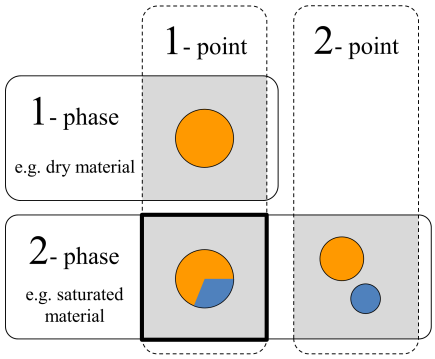

Figure 4.2: Scheme of the different MPM numerical existing approaches depending on the number of phases and the number of material point sets.

4.3 Governing equations

The dynamic behaviour of saturated porous media can be formulated by specifying a set of physical laws: the momentum balances and the mass balances. Considering these basic equations, Zienkiewicz and Shiomi (1984) presented different numerical solutions of the generalised Biot's formulation.

The most common form used in finite element procedures is the $\mathbf{u}_s - p_l$ approximation and it was adapted to the MPM by Zabala (2010). The equations are solved considering solid displacement ($\mathbf{u}_s$) and liquid pressure (p_l) as primary unknowns. It is known that mixed displacement-pressure approaches suffer from pressure instability problems if the number of degrees of freedom used to interpolate the pressure is lower than that used to interpolate the displacements (Babuska-Brezzi condition). Here the relative acceleration of the liquid phase and the convective terms are neglected. Because of that, Esch et al. (2011) shown that such formulation cannot accurately reproduce certain 2-phase dynamic processes.

In order to capture the physical response of the porous media under dynamic conditions, the numerical approach considered in this work includes all acceleration terms. It is the $\mathbf{v}_s - \mathbf{v}_l$ formulation, where the velocities of each phase become fundamental unknowns of the system. This approach was extended to the MPM by Jassim et al. (2013).

In addition to the balance equations, other constitutive relationships, that depend on the characteristics of the saturated porous media and the phases themselves, are needed to define the coupled hydromechanical problem.

In order to have a clear and precise notation, from this point to the end of this document the subscript s denotes that a variable is referred to the solid and the subscript l refers to the liquid phase.

4.3.1 Momentum balance equations

In a 2-phase problem, three different momentum balances can be posed: for the liquid phase, for the solid phase and for the mixture. Since one of the equations can always be written as a linear combination of the others, it is only strictly necessary to solve two of the three balances, for instance, the liquid momentum and the mixture momentum.

The momentum balance equation of the liquid phase (per unit of liquid volume) can be written as follows,

$$\rho_l \mathbf{a}_l = \nabla p_l - \frac{n\mu_l}{k_l}(\mathbf{v}_l - \mathbf{v}_s) + \rho_l \mathbf{b} \tag{4.2}$$

where $\mathbf{a}_l$ is the acceleration of the liquid phase, $\mathbf{v}_l$ and $\mathbf{v}_s$ are the total liquid and solid velocities, p_l is the liquid pressure, μ_l is the dynamic viscosity of the liquid, k_l is the

intrinsic permeability of the liquid, and **b** is the body force vector. This expression describes the so-called generalised Darcy's law.

The boundary conditions of the liquid momentum balance are defined in the following expressions: equation (4.3) is the prescribed liquid pressure and equation (4.4) is the prescribed displacements of the liquid phase. Those are applied on $\partial\Omega^{p_l}$ and $\partial\Omega^{\mathbf{u}_l}$ respectively.

$$p_l(\mathbf{x}, t) \cdot \mathbf{n} = \widehat{\mathbf{p}}_l(t) \tag{4.3}$$

$$\mathbf{u}_l(\mathbf{x}, t) = \widehat{\mathbf{u}}_l(t) \tag{4.4}$$

where $\mathbf{x}$ is the position vector, $\mathbf{u}_l$ is the total displacement vector of the liquid and t is time.

The momentum balance of the mixture (per unit of volume of mixture) can be written as

$$(1-n)\rho_s \mathbf{a}_s + n\rho_l \mathbf{a}_l = \nabla \cdot \boldsymbol{\sigma} + \rho_m \mathbf{b} \tag{4.5}$$

where $\boldsymbol{\sigma}$ is the total stress of the mixture. Here, the inertial term is split in two parts, one for each phase.

Two boundary conditions are required to determine the boundary value problem: prescribed traction (Eq.4.6) and prescribed displacements of the solid skeleton (Eq.4.7). These are applied on the domains $\partial\Omega^{\mathbf{t}}$ and $\partial\Omega^{u_s}$ respectively.

$$\boldsymbol{\sigma}(\mathbf{x}, t) \cdot \mathbf{n} = \widehat{\mathbf{t}}(t) \tag{4.6}$$

$$\mathbf{u}_s(\mathbf{x}, t) = \widehat{\mathbf{u}}_s(t) \tag{4.7}$$

Comparing equation (4.2) with (4.5), an additional term appears in the liquid momentum balance (second term on the right hand side). This is due to the interaction between the two phases within the pores. In the mixture balance it does not appear because it is cancelled with the same coming from the solid momentum.

4.3.2 Mass balance equations

Considering a reference volume of the porous media, the mass of each phase has to be conserved during all the calculation.

The solid mass balance can be written as follows in equation (4.8). This equation indicates that the temporal variation of solid mass (first term) should be compensated with the solid mass entering and/or leaving the reference volume (second term). No external sources nor sinks of mass have been taken into account.

$$\frac{\partial}{\partial t}((1-n)\rho_s) + \nabla \cdot ((1-n)\rho_s \mathbf{v}_s) = 0 \tag{4.8}$$

Developing such expression (Eq.4.8) and considering that the solid is incompressible ($\frac{D^s\rho_s}{Dt} \approx 0$), the mass balance equation for the solid skeleton becomes the following expression which describes the material derivative of the porosity.

$$\frac{D_s n}{Dt} = (1-n)\nabla \cdot \mathbf{v}_s \tag{4.9}$$

The material derivative with respect to the solid has been used in the previous development and it is defined as

$$\frac{D_s(\bullet)}{Dt} = \frac{\partial(\bullet)}{\partial t} + \mathbf{v}_s \cdot \nabla(\bullet) \tag{4.10}$$

where, $\frac{\partial(\bullet)}{\partial t}$ is the spatial derivative and the term depending on the gradient is the convective term.

In the 2-phase-1-point MPM formulation, the solid mass of a material point is constant. Therefore, the solid mass conservation is automatically satisfied, even though there are changes in volume or solid density. However, the total mass of a material point can vary with time, since the liquid can move apart.

The mass balance of the liquid phase can be written very similar to equation (4.8) as

$$\frac{\partial(n\rho_l)}{\partial t} + \nabla \cdot (n\rho_l \mathbf{v}_l) = 0 \tag{4.11}$$

Deriving the previous expression and considering the material derivative with respect the solid motion (4.10), it results the following equation.

$$\rho_l \frac{D_s n}{Dt} + n\frac{D_s \rho_l}{Dt} + (\mathbf{v}_l - \mathbf{v}_s)\cdot\nabla(n\rho_l) + n\rho_l \nabla \cdot \mathbf{v}_l = 0 \tag{4.12}$$

Assuming that liquid is barotropic (in the absence of changes due to temperature), its density is supposed to be a function of the liquid pressure depending on the liquid bulk modulus K_l as follows.

$$\frac{1}{\rho_l}\frac{\partial \rho_l}{\partial p_l} = -\frac{1}{K_l} \tag{4.13}$$

Liquid density can be first approximated with the following expression, where β is liquid compressibility ($\beta = -\frac{1}{K_l}$). ρ_{l0} and p_{l0} are liquid density and liquid pressure reference values.

$$\rho_l = \rho_{l0} e^{\beta(p_l - p_{l0})} \tag{4.14}$$

Therefore, considering the liquid pressure p_l as state variable and including the solid mass balance (Eq.4.9) in equation (4.12), the liquid mass balance becomes the expression (4.15) which describes the liquid pressure variations ($\dot{p}_l = \frac{\partial p_l}{\partial t}$).

$$\dot{p}_l = \frac{K_l}{n}\left[(1-n)\nabla\cdot\mathbf{v}_s + n\nabla\cdot\mathbf{v}_l\right] + \frac{K_l}{n\rho_l}(\mathbf{v}_l - \mathbf{v}_s)\cdot\nabla(n\rho_l) \tag{4.15}$$

Finally, the previous equation can be simplified as follows (4.16) in those problems where the liquid velocity with respect to the skeleton one is negligible ($\mathbf{v}_l - \mathbf{v}_s \approx 0$) or when spatial variations of liquid mass are sufficiently small ($\nabla(n\rho_l) \approx 0$).

$$\dot{p}_l = \frac{K_l}{n}\left[(1-n)\nabla\cdot\mathbf{v}_s + n\nabla\cdot\mathbf{v}_l\right] \tag{4.16}$$

4.3.3 Constitutive equations

In saturated soils, the Terzaghi's effective stress concept (Terzaghi, 1925) is assumed to be valid. The effective stress $\boldsymbol{\sigma}'$ is defined as that part of the total stress $\boldsymbol{\sigma}$ that governs the deformation of the soil, and both are related with the liquid pore pressure p_l as follows.

$$\boldsymbol{\sigma} = \boldsymbol{\sigma}' + \alpha_B p_l \mathbf{m} \tag{4.17}$$

α_B is Biot's coefficient, $\alpha = 1 + K_{sk}/K_s$ where K_{sk} is the bulk modulus of the solid skeleton and K_s is the bulk modulus of the solid grains. For soils, α is close to 1 because the compressibility of solid particles is very small compared to the compressibility of porous material. Therefore, the effective stress principle reduces to

$$\boldsymbol{\sigma} = \boldsymbol{\sigma}' + p_l \mathbf{m} \tag{4.18}$$

Taking into account the equation (4.18), the saturated porous media behaviour is modelled using a constitutive model that relates the strains with the effective stresses. The general form of a suitable stress-strain relationship can be written incrementally as

$$\dot{\boldsymbol{\sigma}}' = \mathbf{D} \cdot \dot{\boldsymbol{\varepsilon}} \tag{4.19}$$

in which $\mathbf{D}$ is the tangent matrix.

4.4 Numerical implementation. Two-phase One-point MPM formulation

In this section, considering the solid and liquid velocities as principal unknowns of the problem, the momentum balances for the liquid (Eq.4.2) and for the mixture (Eq.4.5) are integrated and discretised according to the 2-phase 1-point MPM approach. As a result, a system of equations is posed. Finally, an explicit time discretisation scheme is presented.

4.4.1 Spatial discretisation

The 2-phase-1-point MPM formulation also requires a computational mesh and a set of material points to describe the continuum (see Figure 4.3).

The mesh discretisation is performed as in the case for 1-phase. Because the $\mathbf{v}_s - \mathbf{v}_l$ formulation is used in this work, the same set of standard linear shape functions N_j can be used to discretise all the principal unknowns to the nodes of the mesh. For instance, solid and liquid displacements can be approximated as

$$\mathbf{u}_s(\mathbf{x}, t) = \sum_{j=1}^{N_n} \mathbf{u}_{s_j}(t) N_j(\mathbf{x}, t) \tag{4.20}$$

$$\mathbf{u}_l(\mathbf{x},t) = \sum_{j=1}^{N_n} \mathbf{u}_{l_j}(t) N_j(\mathbf{x},t) \tag{4.21}$$

where $\mathbf{u}_{s_j}(t)$ and $\mathbf{u}_{l_j}(t)$ are the solid and liquid displacements of node j.

The discretisation to the material points is done considering that each material point represents a portion of the saturated porous media, and the mass of such mixture (solid and liquid) is concentrated at the corresponding material point position. Then, the density of the mixture ρ_m can be expressed as

$$\rho_m(\mathbf{x},t) = \sum_{p=1}^{N_p} m_p \delta(\mathbf{x} - \mathbf{x}_p) \tag{4.22}$$

in which m_p and $\mathbf{x}_p$ are the total mass and the position of the material point p, is the Dirac delta function, and N_p is the total number of material points.

Moreover, in the 2-phase 1-point MPM formulation, it is also necessary to consider the liquid density ρ_l and the solid density ρ_s as

$$\rho_l(\mathbf{x},t) = \sum_{p=1}^{N_p} \widetilde{m}_{l_p} \delta(\mathbf{x} - \mathbf{x}_p) \tag{4.23}$$

$$\rho_s(\mathbf{x},t) = \sum_{p=1}^{N_p} \widetilde{m}_{s_p} \delta(\mathbf{x} - \mathbf{x}_p) \tag{4.24}$$

$\widetilde{m}_{l_p}$ and $\widetilde{m}_{s_p}$ are equivalent to the mass that would have a material point made up entirely of liquid or solid respectively, according to the following expressions.

$$\widetilde{m}_{l_p} = \rho_l V_p \tag{4.25}$$

$$\widetilde{m}_{s_p} = \rho_s V_p \tag{4.26}$$

Then, the real mass of liquid and solid in a material point can be written as

$$m_{l_p} = n\widetilde{m}_{l_p} \tag{4.27}$$

$$m_{s_p} = (1-n)\widetilde{m}_{s_p} \tag{4.28}$$

4.4.2 Discretisation of the momentum balance equations

The Galerkin method of Weighted Residuals has been applied to obtain the weak form of the momentum balance equations (Eq.(4.2) and Eq.(4.5)). Taking into account the

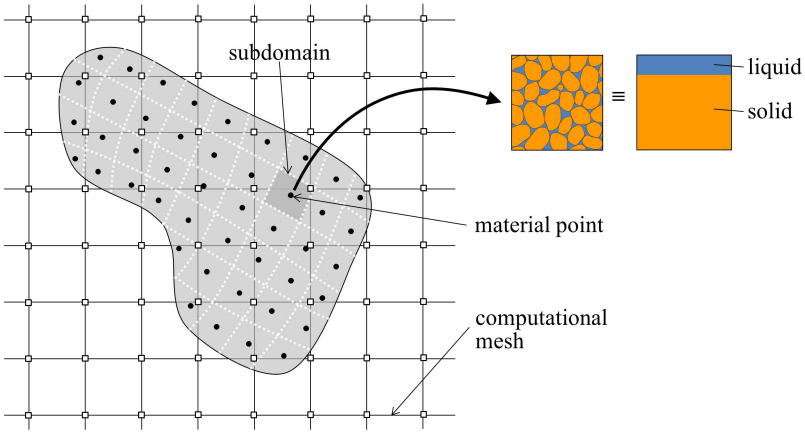

Figure 4.3: Scheme of the spatial discretisations of a saturated porous media.

discretisation to the nodes (Eq.4.20 and Eq.4.21), the momentum balances for the liquid and for the mixture can be written as

$$\sum_{j=1}^{N_n} \int_{\Omega} \rho_l N_i^p N_j^p d\Omega \mathbf{a}_{l_j} = \int_{\partial\Omega^{p_l}} N_i^p \widehat{\mathbf{p}}_l d\partial\Omega^{p_l} - \int_{\Omega} \mathbf{B}_i^p p_{l_p} \mathbf{m} d\Omega - \sum_{j=1}^{N_n} \int_{\Omega} \frac{n\mu_l}{k_l} N_i^p N_j^p d\Omega (\mathbf{v}_{l_j} - \mathbf{v}_{s_j}) + \int_{\Omega} \rho_l N_i^p \mathbf{b} d\Omega \tag{4.29}$$

$$\sum_{j=1}^{N_n} \int_{\Omega} (1-n)\rho_s N_i^p N_j^p d\Omega \mathbf{a}_{s_j} + \sum_{j=1}^{N_n} \int_{\Omega} n\rho_l N_i^p N_j^p d\Omega \mathbf{a}_{l_j} = \int_{\partial\Omega^{\mathbf{t}}} N_i^p \widehat{\mathbf{t}} d\partial\Omega^{\mathbf{t}} - \int_{\Omega} \mathbf{B}_i^p \cdot \boldsymbol{\sigma}_p d\Omega + \int_{\Omega} \rho_m N_i^p \mathbf{b} d\Omega \tag{4.30}$$

Using expressions (4.22) and (4.23) to approximate the integrals over the domain as a quadrature on the material points, the final system of equations can be written in a compact form as follows.

$$\widetilde{\mathbf{M}}_l \cdot \mathbf{a}_l = \mathbf{F}_l^{ext} - \mathbf{F}_l^{int} - \mathbf{Q}_l \cdot (\mathbf{v}_l - \mathbf{v}_s) \tag{4.31}$$

$$\mathbf{M}_s \cdot \mathbf{a}_s + \mathbf{M}_l \cdot \mathbf{a}_l = \mathbf{F}^{ext} - \mathbf{F}^{int} \tag{4.32}$$

where $\mathbf{a}_s$, $\mathbf{a}_l$, $\mathbf{v}_s$ and $\mathbf{v}_l$ are the nodal acceleration and velocity vectors for each phase. $\mathbf{F}_l^{ext}$ is the vector of the liquid external forces and $\mathbf{F}^{ext}$ is the vector of the external forces of the mixture. Internal forces are indicated by means the superscript int. $\mathbf{Q}_l$ is the liquid dragging matrix. $\widetilde{\mathbf{M}}$ and $\mathbf{M}$ are the corresponding lumped mass matrixes per unit of volume. All of them are defined below.

$$\widetilde{\mathbf{M}}_l = \sum_{p=1}^{N_p} \widetilde{m}_{l_p} \mathbf{N}^p \tag{4.33}$$

$$\mathbf{M}_s = \sum_{p=1}^{N_p} m_{s_p} \mathbf{N}^p \tag{4.34}$$

$$\mathbf{M}_l = \sum_{p=1}^{N_p} m_{l_p} \mathbf{N}^p \tag{4.35}$$

$$\mathbf{Q}_l = \sum_{p=1}^{N_p} \frac{n\mu_l}{k_l} \mathbf{N}^{pT} \cdot \mathbf{N}^p V_p \tag{4.36}$$

$$\mathbf{F}_l^{ext} = \int_{\partial\Omega^{p_l}} \mathbf{N}^p \cdot \widehat{\mathbf{p}}_l d\partial\Omega^{p_l}\Big|_p + \sum_{p=1}^{N_p} \widetilde{m}_{l_p} \mathbf{N}^p \cdot \mathbf{b} \tag{4.37}$$

$$\mathbf{F}^{ext} = \int_{\partial\Omega^{\mathbf{t}}} \mathbf{N}^p \cdot \widehat{\mathbf{t}} d\partial\Omega^{\mathbf{t}}\Big|_p + \sum_{p=1}^{N_p} m_p \mathbf{N}^p \cdot \mathbf{b} \tag{4.38}$$

$$\mathbf{F}_l^{int} = \sum_{p=1}^{N_p} \mathbf{B}^p \cdot p_{l_p} \mathbf{m} V_p \tag{4.39}$$

$$\mathbf{F}^{int} = \sum_{p=1}^{N_p} \mathbf{B}^p \cdot \boldsymbol{\sigma}_p V_p \tag{4.40}$$

4.4.3 Time discretisation

To integrate the equations in time, an explicit Euler scheme based on Section 3.3.2.4 is used. Meanwhile liquid and solid velocities are updated with accelerations at time t^k(see Eq.4.41 and Eq.4.42), liquid and solid displacements are updated with velocities calculated at time t^{k+1} (see Eq.4.43 and Eq.4.44).

$$\mathbf{v}_l^{k+1} = \mathbf{v}_l^k + \triangle t \mathbf{a}_l^k \tag{4.41}$$

$$\mathbf{v}_s^{k+1} = \mathbf{v}_s^k + \triangle t \mathbf{a}_s^k \tag{4.42}$$

$$\mathbf{u}_l^{k+1} = \mathbf{u}_l^k + \triangle t \mathbf{v}_l^{k+1} \tag{4.43}$$

$$\mathbf{u}_s^{k+1} = \mathbf{u}_s^k + \triangle t \mathbf{v}_s^{k+1} \tag{4.44}$$

4.5 Computational cycle

Considering the 2-phase 1-point MPM approach and the $\mathbf{v}_s - \mathbf{v}_l$ formulation, the computational cycle in each time step can be extended from the one presented in Section 3.3.3. Initially all the properties related with the saturated porous media are stored in the material points.

1. The lumped mass matrixes are evaluated at the nodes at time t^k with equations (4.33), (4.34) and (4.35). The internal and external forces for the liquid and for the mixture are calculated with expressions (4.39), (4.40), (4.37) and (4.38) as well as the dragging force term (Eq.4.36).

2. The momentum balance equation of the liquid phase (Eq.4.31) is solved and the nodal liquid accelerations $\mathbf{a}_l^k$ are determined.

3. The momentum balance equation of the mixture (Eq.4.32) is solved taking into account the liquid accelerations $\mathbf{a}_l^k$, thus the nodal solid accelerations $\mathbf{a}_s^k$ are obtained.

4. Liquid and solid velocities are updated at the material points considering equations (4.41 and 4.42).

5. Nodal liquid and solid velocities are calculated as follows.

$$\mathbf{v}_{l_j}^{k+1} = \frac{1}{m_{l_j}^k} \sum_{p=1}^{N_p} m_{l_p}^k N_j^{p^k} \mathbf{v}_{l_p}^{k+1} \tag{4.45}$$

$$\mathbf{v}_{s_j}^{k+1} = \frac{1}{m_{s_j}^k} \sum_{p=1}^{N_p} m_{s_p}^k N_j^{p^k} \mathbf{v}_{s_p}^{k+1} \tag{4.46}$$

6. Particle positions are updated considering equation (4.44).

7. Solid and liquid strain increments are calculated for each material point in function of the nodal velocities following equation (3.27).

8. The liquid pressure increment is calculated at the material points according to the mass balance of liquid (Eq.4.15). With this, the liquid pressure is updated according to

$$p_{l_p}^{k+1} = p_{l_p}^k + \dot{p}_{l_p}^{k+1} \Delta t \tag{4.47}$$

9. The constitutive effective stresses are updated using the solid skeleton strains and the stress-strain relationship (Eq.4.19).

10. The material properties are updated in the material points, such as the particle volume which is updated considering the increment of volumetric strain. The porosity of each material point can also be updated considering the mass balance of solid equation (4.9).

11. The computational grid is initialised for the next step, nodal values are discarded and the material points carry all the updated information.

4.6 Minimum time step criterion

The explicit scheme proposed in this Chapter 4 to solve hydromechanical problems is conditionally stable. In order to achieve the stability of the solution and optimise the computational time, it is important to determine an appropriate critical time step criterion.

First, the critical time step for a set of numerical tests has been determined through a trial-error procedure. Then, the stability of the governing equations describing problems in saturated porous media has been studied and 4 different analytical criterions have been identified by using the same procedure presented in Section 3.3.4. Finally, after a comparison between numerical results and analytical expressions and some discussion, a critical time step criterion is proposed.

4.6.1 Numerical results

The quasi-static one-dimensional consolidation is a well-known problem in geotechnics and it was analytically described by Terzaghi (1943) (Sec.4.9). The critical time step value for a certain simulation is the maximum time step value that allows a stable numerical solution converging to the analytical one (Terzaghi's solution). Therefore, the critical time step Δt_{crit} of a set of oedometric consolidation tests can be easily determined by a trial-error procedure.

Two different geometries have been modelled. The first one is a 1 m column 0.05 m thick and the second one is a 10 m column 1 m thick (see Figure 4.4). Both are meshed with tetrahedra of an average side of L_e=0.05 m and 0.5 m respectively. The minimum element altitude h_{min} in the fine mesh is 0.02886 m, and in the coarse one h_{min} is 0.13347 m. 4 material points are considered within each element. The bottom is fixed and only vertical movement is allowed along lateral boundaries. All contours are impervious excluding the upper surface.

The material is linear elastic according to Table 4.1. A total of 64 simulations have been performed (38 with the fine mesh and 26 with the coarse one) by changing porosity and permeability of the material. 4 different porosities are considered (0.1, 0.2, 0.3 and 0.5) and the intrinsic permeability ranges between 10^{-13} and 10^{-9} m^2. Other properties summarised in Table 4.1 are assumed constant.

All simulations are initially saturated, and a vertical loading of 10 kPa is applied suddenly on top of each sample. The gravity has been neglected. The calculation finishes when liquid pressure is completely dissipated.

Figure 4.5 shows Δt_{crit} obtained for both geometries and different porosities n depending on intrinsic permeability k_l. It is clear that the smaller the permeability, the smaller the

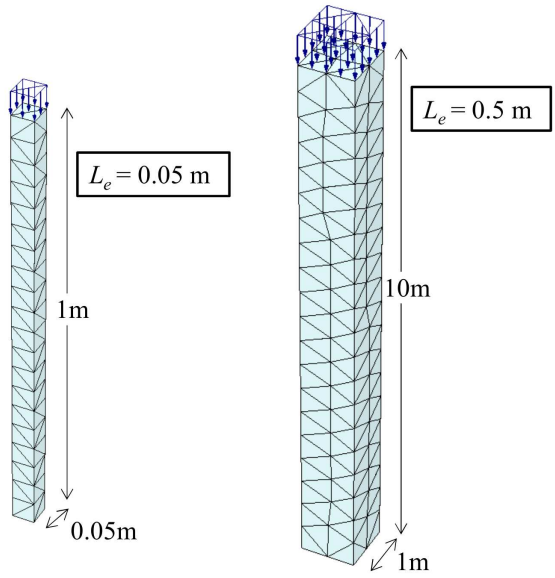

Figure 4.4: Scheme of the two oedometric tests.

Table 4.1: Material properties.

Material property	Value
Solid density ρ_s [kg/m^3]	2700
Liquid density ρ_l [kg//m^3]	1000
Liquid bulk modulus K_l [kPa]	80000
Young's modulus E [kPa]	10000
Poisson ratio ν [-]	0.33
Liquid viscosity μ_l [kg/s·m]	0.001

critical time step. It is also observed that for each porosity a S-shape curve is defined. For $k_l < 10^{-12}m^2$, the critical time step is very small ($\Delta t_{crit} < 10^{-5}s$). For higher permeabilities, Δt_{crit} increases up to a constant value. As the porosity increases, the S-shape curve shifts to the right (to higher values of permeability) and tends to a higher critical time step threshold. Note that when $n = 0.1$ and 0.2 the S-shape curve changes sharply from vertical to horizontal, while for the rest it is smoother and more rounded. Finally, comparing results from both meshes, it is confirmed that larger mesh size allows larger time steps.

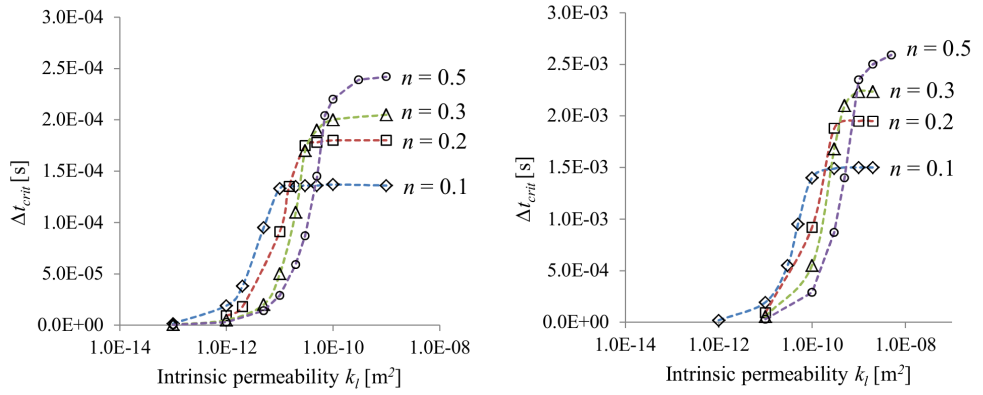

Figure 4.5: Critical time step depending on intrinsic permeability obtained for both geometries; (a) $L_e = 0.05m$ and (b) $L_e = 0.5m$

4.6.2 Stability of undrained problem

According to the work published by Verruijt (2010), for dynamic effects, the saturated porous media can be considered as a soil in undrained conditions. Both phases are supposed to move attacked one to each other, hence $\mathbf{u}_s = \mathbf{u}_l$, $\mathbf{v}_s = \mathbf{v}_l$ and $\mathbf{a}_s = \mathbf{a}_l$.

If a single node i is considered, the momentum balance per unit volume at time t^k can be written as a second-order ODE. The homogeneous form is the following expression,

$$\rho_m \mathbf{a}_s^k + \kappa_m \mathbf{u}_s^k = 0 \tag{4.48}$$

being $\mathbf{a}_s$ and $\mathbf{u}_s$ nodal acceleration and nodal displacement, and ρ_m is the density of the mixture (saturated density). Because the constitutive relationship is already included in equation (4.48), κ_m refers to the stiffness of the node per unit volume, which can be written as

$$\kappa_m = \frac{E_{c,u}}{(L_i)^2} \tag{4.49}$$

L_i is a characteristic length of the node i and $E_{c,u}$ is the undrained constrained elastic modulus

$$E_{c,u} = K_{sk} + \frac{{\alpha_B}^2}{nC_l + (\alpha_B - n)C_s} + \frac{4}{3}G \tag{4.50}$$

The first term K_{sk} is the bulk modulus of the skeleton, α_B is the Biot's coefficient, and C_s and C_l are solid grains and liquid compressibilities respectively. Considering that solid grains are incompressible and Biot's coefficient equals to 1 for soils, the undrained constrained elastic modulus can be rewritten as

$$E_{c,u} = K_{sk} + \frac{K_l}{n} + \frac{4}{3}G \tag{4.51}$$

where $K_l = \frac{1}{C_l}$ is the bulk modulus of the liquid phase.

Taking into account the time discretisation scheme stated in Section 4.4.3, the two-order ODE (4.48) becomes the following system of first-order ODEs.

$$\begin{cases} \mathbf{u}_s^{k+1} = (1 - \frac{\kappa_m}{\rho_m})\mathbf{u}_s^k \Delta t^2 + \mathbf{v}_s^k \Delta t \\ \mathbf{v}_s^{k+1} = -\frac{\kappa_m}{\rho_m}\mathbf{u}_s^k \Delta t + \mathbf{v}_i^k \end{cases} \tag{4.52}$$

Then, the amplification matrix from the previous scheme is given by

$$\mathbf{A}_u = \begin{bmatrix} 1 - \frac{\kappa_m}{\rho_m}\Delta t^2 & \Delta t \\ -\frac{\kappa_m}{\rho_m}\Delta t & 1 \end{bmatrix} \tag{4.53}$$

Then, the characteristic polynomial of the amplification matrix $\mathbf{A}_u$ can be calculated. Assuming the stability criterion (Eq.3.30), the critical time step results in

$$\Delta t_{crit,u} = \frac{2}{\omega_u} \tag{4.54}$$

where

$$\omega_u = \frac{1}{L_i}\sqrt{\frac{E_{c,u}}{\rho_m}} = \frac{1}{L_i}\sqrt{\frac{E_c + \frac{K_l}{n}}{(1-n)\rho_s + n\rho_l}} \tag{4.55}$$

Note that when the stability of a two-nodded linear finite element is posed, and $L_i = \frac{L_e}{2}$ the critical time step criterion $\Delta t_{crit,u}$ is identical to the Courant-Friedrichs-Levy (CFL) condition (Eq.3.37) for saturated porous media. In this case, the speed of the undrained wave c_p is

$$c_p = \sqrt{\frac{E_{c,u}}{\rho_m}} \tag{4.56}$$

The criterion $\Delta t_{crit,u}$ (Eq.4.54) depends on the density and the compressibility of the mixture and it is also proportional with L_i. However, it does not include any dependence with hydraulic permeability.

Although it is a generalised criterion, in practise, it has been observed that in some cases it is not sufficient to ensure the stability of the solution (Ceccato, 2014; Mieremet, 2015).

4.6.3 Stability of the coupled system

In order to determine a more accurate critical time step criterion, an specific stability analysis based on the conditionally-stable integration algorithm presented in this Chapter 4 has been carried out.

According to the computational cycle presented in Section 4.5, a system of two momentum balances is solved. First, the dynamic equilibrium of the liquid phase (Eq.4.31) is solved

in order to calculate liquid accelerations $\mathbf{a}_l^k$ at time t^k. Afterwards, $\mathbf{a}_l^k$ are included in the dynamic equilibrium of the mixture (Eq.4.32) and the accelerations of the solid phase $\mathbf{a}_s^k$ are obtained.

In here, the principal variables are both liquid and solid displacements, $\mathbf{u}_l$ and $\mathbf{u}_s$. Then, including the liquid mass balance and the constitutive relationship in the dynamic equilibrium, the following system of two-order ODEs (equilibrium of liquid and mixture respectively) can be posed at t_k.

$$\begin{cases} \rho_l \mathbf{a}_l^k + q_l \mathbf{v}_l^k - q_l \mathbf{v}_s^k + \kappa_l \mathbf{u}_l^k + \frac{(1-n)}{n} \kappa_l \mathbf{u}_s^k = 0 \\ (1-n)\rho_s \mathbf{a}_s^k + n\rho_l \mathbf{a}_l^k + \kappa_s \mathbf{u}_s^k + \frac{(1-n)}{n} \kappa_l \mathbf{u}_s^k + \kappa_l \mathbf{u}_l^k = 0 \end{cases} \tag{4.57}$$

This is the homogeneous form written per unit volume at a single node i.

The terms are the following

$$q_l = \frac{n\mu_l}{k_l} \tag{4.58}$$

$$\kappa_l = \frac{K_l}{(L_i)^2} \tag{4.59}$$

$$\kappa_s = \frac{E_c}{(L_i)^2} \tag{4.60}$$

being μ_l the liquid viscosity, k_l the intrinsic permeability, E_c the confined elastic modulus of the solid skeleton and K_l the liquid bulk modulus. Note that q_l is a viscous coefficient.

The stability analysis of the system (4.57) can be solved in different manners, for instance, considering the stability of the coupled system, or studying separately the stability of each balance equation (liquid and mixture balances).

The stability of the coupled system of equations (4.57) is analysed here. Note that it is a system of 2 second-order ODEs. Considering the time integration scheme indicated in Section 4.4.3, each second-order ODE can be decomposed into 2 first-order ODEs. Therefore, 4 first-order ODEs form the system of the coupled numerical scheme, hence the dimension of the amplification matrix is 4. The amplification matrix is determined with the following expression.

$$\mathbf{A}_c = \begin{bmatrix} 1 - \frac{\kappa_l}{\rho_l}\Delta t^2 & \Delta t - \frac{q_l}{\rho_l}\Delta t^2 & -\frac{(1-n)}{n}\frac{\kappa_l}{\rho_l}\Delta t^2 & \frac{q_l}{\rho_l}\Delta t^2 \\ -\frac{\kappa_l}{\rho_l}\Delta t & 1 - \frac{q_l}{\rho_l}\Delta t & -\frac{(1-n)}{n}\frac{\kappa_l}{\rho_l}\Delta t & \frac{q_l}{\rho_l}\Delta t \\ -\frac{\kappa_l}{\rho_s}\Delta t^2 & n\frac{q_l}{\rho_l}\Delta t^2 & 1 - \frac{\kappa_s}{(1-n)\rho_s}\Delta t^2 - \frac{\kappa_l}{n\rho_s}\Delta t^2 & \Delta t - n\frac{q_l}{(1-n)\rho_s}\Delta t^2 \\ -\frac{\kappa_l}{\rho_s}\Delta t & n\frac{q_l}{\rho_l}\Delta t & \frac{\kappa_s}{(1-n)\rho_s}\Delta t - \frac{\kappa_l}{n\rho_s}\Delta t & 1 - n\frac{q_l}{(1-n)\rho_s}\Delta t \end{bmatrix} \tag{4.61}$$

Calculating the characteristic polynomial of A_c according to the stability condition (Eq.3.30), and assuming $\Delta t^3 << \Delta t$, the critical time step for the coupled system of momentum equations results as

$$\Delta t_{crit,c} = \frac{2}{\omega_c}\left[-\xi_c + \sqrt{{\xi_c}^2 + 1}\right] \tag{4.62}$$

where

$$\omega_c = \frac{1}{L_i}\sqrt{\frac{K_l}{\rho_l} + \frac{E_c}{(1-n)\rho_s} + \frac{(1-n)}{n}\frac{K_l}{\rho_s}} \tag{4.63}$$

$$\xi_c = \frac{n\mu_l}{2k_l\omega_c}\left(\frac{1}{\rho_l} + \frac{n}{(1-n)\rho_s}\right) \tag{4.64}$$

This criterion depends on permeability and porosity of the porous media. It is limited between 0 (for small permeability) and a maximum threshold $\frac{2}{\omega_c}$ (for high permeability).

4.6.4 Stability of the momentum balance of the liquid

The stability of the dynamic equilibrium of the liquid (see first equation in (4.57)) is analysed here.

Considering that the principal unknowns are the liquid variables ($\mathbf{u}_l$, $\mathbf{v}_l$, and $\mathbf{a}_l$) the liquid momentum balance can be written as

$$\rho_l \mathbf{a}_l^k + q_l \mathbf{v}_l^k + \kappa_l \mathbf{u}_l^k = q_l \mathbf{v}_s^k - \frac{(1-n)}{n}\kappa_l \mathbf{u}_s^k \tag{4.65}$$

For the stability analysis, the homogeneous form of equation (4.65) is taken into account.

$$\rho_l \mathbf{a}_l^k + q_l \mathbf{v}_l^k + \kappa_l \mathbf{u}_l^k = 0 \tag{4.66}$$

Considering the explicit time integration scheme presented in 4.4.3 for liquid velocity and liquid displacement, the following system of first-order ODEs is obtained.

$$\begin{cases} \mathbf{u}_l^{k+1} = \mathbf{u}_l^k - \frac{\kappa_l}{\rho_l}\mathbf{u}_l^k\Delta t^2 + \mathbf{v}_l^k\Delta t - \frac{q_l}{\rho_l}\mathbf{v}_l^k\Delta t^2 \\ \mathbf{v}_l^{k+1} = -\frac{\kappa_l}{\rho_l}\mathbf{u}_l^k\Delta t + \mathbf{v}_l^k - \frac{q_l}{\rho_l}\mathbf{v}_l^k\Delta t \end{cases} \tag{4.67}$$

The amplification matrix is written as

$$\mathbf{A}_l = \begin{bmatrix} 1 - \frac{\kappa_l}{\rho_l}\Delta t^2 & \Delta t - \frac{q_l}{\rho_l}\Delta t^2 \\ -\frac{\kappa_l}{\rho_l}\Delta t & 1 - \frac{q_l}{\rho_l}\Delta t \end{bmatrix} \tag{4.68}$$

Finally, the critical time step criterion results from imposing equation (3.30) for $\mathbf{A}_l$. It gives the following expression

$$\Delta t_{crit,l} = \frac{2}{\omega_l}\left[-\xi_l + \sqrt{{\xi_l}^2 + 1}\right] \tag{4.69}$$

where

$$\omega_l = \frac{1}{L_i}\sqrt{\frac{K_l}{\rho_l}} \tag{4.70}$$

$$\xi_l = \frac{n\mu_l}{2k_l\omega_l}\frac{1}{\rho_l} \tag{4.71}$$

Note that $\Delta t_{crit,l}$ has a factor depending on permeability which takes values from 0 to 1, which means that $\Delta t_{crit,l} \in (0, \frac{2}{\omega_l})$. In this case, ω_l does not depend on porosity, which means that the threshold of this criterion is controlled by the liquid characteristics (K_l and ρ_l) and the characteristic mesh size L_i, but not by the porous medium properties (n,k_l,μ_l,E_c).

4.6.5 Stability of the momentum balance of the mixture

The stability of the dynamic equilibrium of the mixture (second equation of (4.57)) is analysed here. All variables related to solid ($\mathbf{u}_s$, $\mathbf{v}_s$, and $\mathbf{a}_s$) are considered as principal unknowns. Including $\mathbf{a}_l^k$ from the liquid momentum balance (4.72), the mixture equilibrium equation per unit volume can be written as (4.73).

$$\mathbf{a}_l^k = -\frac{q_l}{\rho_l}\mathbf{v}_l^k + \frac{q_l}{\rho_l}\mathbf{v}_s^k - \frac{\kappa_l}{\rho_l}\mathbf{u}_l^k - \frac{(1-n)}{n}\frac{\kappa_l}{\rho_l}\mathbf{u}_s^k \tag{4.72}$$

$$(1-n)\rho_s\mathbf{a}_s^k + nq_l\mathbf{v}_s^k + \kappa_s\mathbf{u}_s^k + \frac{(1-n)^2}{n}\kappa_l\mathbf{u}_s^k = nq_l\mathbf{v}_l - (1-n)\kappa_l\mathbf{u}_l \tag{4.73}$$

For the stability analysis, the homogeneous form of (4.73) is taken into account.

$$(1-n)\rho_s\mathbf{a}_s^k + nq_l\mathbf{v}_s^k + \kappa_s\mathbf{u}_s^k + \frac{(1-n)^2}{n}\kappa_l\mathbf{u}_s^k = 0 \tag{4.74}$$

Considering the explicit time integration scheme presented in 4.4.3 for solid velocity and solid displacement, the following 2 first-order ODEs comes out.

$$\begin{cases} \mathbf{u}_s^{k+1} = \mathbf{u}_s^k - (\frac{1}{1-n}\frac{\kappa_s}{\rho_s} + \frac{1-n}{n}\frac{\kappa_l}{\rho_s})\mathbf{u}_s^k\Delta t^2 + \mathbf{v}_s^k\Delta t - \frac{n}{1-n}\frac{q_l}{\rho_s}\mathbf{v}_s^k\Delta t^2 \\ \mathbf{v}_s^{k+1} = -(\frac{1}{1-n}\frac{\kappa_s}{\rho_s} + \frac{1-n}{n}\frac{\kappa_l}{\rho_s})\mathbf{u}_s^k\Delta t + \mathbf{v}_s^k\frac{n}{1-n}\frac{q_l}{\rho_s}\mathbf{v}_s^k\Delta t^2 \end{cases} \tag{4.75}$$

The amplification matrix of such a system is the following.

$$\mathbf{A}_m = \begin{bmatrix} 1 - \frac{(\kappa_s + \frac{(1-n)^2}{n}\kappa_l)}{(1-n)\rho_s}\Delta t^2 & \Delta t - n\frac{q_l}{(1-n)\rho_s}\Delta t^2 \\ -\frac{(\kappa_s + \frac{(1-n)^2}{n}\kappa_l)}{(1-n)\rho_s}\Delta t & 1 - n\frac{q_l}{(1-n)\rho_s}\Delta t \end{bmatrix} \tag{4.76}$$

Finally, the critical time step results in

$$\Delta t_{crit,m} = \frac{2}{\omega_m}\left[-\xi_m + \sqrt{{\xi_m}^2 + 1}\right] \tag{4.77}$$

where

$$\omega_m = \frac{1}{L_i}\sqrt{\frac{E_c}{(1-n)\rho_s} + \frac{(1-n)}{n}\frac{K_l}{\rho_s}} \tag{4.78}$$

$$\xi_m = \frac{n\mu_l}{2k_l\omega_m}\frac{n}{(1-n)\rho_s} \tag{4.79}$$

In this case, $\Delta t_{crit,m} \in (0, \frac{2}{\omega_m})$. Note that $\Delta t_{crit,m}$ depends on permeability and porosity.

4.6.6 Discussion

A total of 4 critical time step criteria have been determined for the 2-phase formulation presented in this Chapter 4. Each criterion corresponds to a different stability analysis:

- $\Delta t_{crit,u}$ for undrained conditions (equivalent to the CFL condition) (4.54),

$$\Delta t_{crit,u} = \frac{2}{\omega_u} \tag{4.80}$$

- $\Delta t_{crit,c}$ for the coupled system of momentum balances (4.62)

$$\Delta t_{crit,c} = \frac{2}{\omega_c}\left[-\xi_c + \sqrt{{\xi_c}^2 + 1}\right] \tag{4.81}$$

- $\Delta t_{crit,l}$ for the liquid momentum balance (4.69),

$$\Delta t_{crit,l} = \frac{2}{\omega_l}\left[-\xi_l + \sqrt{{\xi_l}^2 + 1}\right] \tag{4.82}$$

- $\Delta t_{crit,m}$ for the mixture momentum balance (4.77),

$$\Delta t_{crit,m} = \frac{2}{\omega_m}\left[-\xi_m + \sqrt{{\xi_m}^2 + 1}\right] \tag{4.83}$$

Note that all criteria have a similar structure. Each one is inversely proportional to an angular frequency that depends on the system (w_u, w_c; w_l and w_m). Note that damped schemes ($\Delta t_{crit,c}$, $\Delta t_{crit,l}$ and $\Delta t_{crit,m}$) have a factor depending on permeability that takes values from 0 (for low permeabilities) to 1 (for high permeabilities). Then, the critical time step decreases with permeability, from a maximum value ($\frac{2}{\omega_c}$,$\frac{2}{\omega_l}$ and $\frac{2}{\omega_m}$ respectively) down to 0. On the contrary, $\Delta t_{crit,u}$ is an undamped system and it is independent of permeability.

In order to determine what is the prevailing critical time step criterion, it has proceed to adjust each criterion to the MPM numerical results obtained with the oedometric simulations (Figure 4.5) by varying the L_i input value. The characteristic length L_i is the unique parameter appearing in the critical time step expressions which is not prefixed by the material properties. It should depend on the mesh size, but in tetrahedral meshes this is not a well-known value, but it should be $L_i \leq L_e$.

In Figures 4.6 and 4.7, the value L_i is adjusted so that MPM results (Figure 4.5) tend $\Delta t_{crit,u}$ for high permeability. In Figures 4.8 and 4.9 the MPM results tend $\Delta t_{crit,c}$; in Figures 4.10 and 4.11 the MPM results adjust $\Delta t_{crit,l}$; and finally in Figures 4.12 and

4.13 L_i is adjusted with the aim that numerical results tend $\Delta t_{crit,m}$. Note that the results illustrated in the first figure of each pair corresponds to that obtained with the fine mesh (L_e=0.05 m), and the results presented in the second one are calculated with the coarse mesh (L_e=0.5 m). Moreover, the value of porosity as well as the L_i required in the adjustment are both indicated in each single graphic. In this way, all simulations can be easily compared.

Taking into account all adjustments, it is clear that none of the analytical criteria fits perfectly the S-shaped curves described by the numerical results. But instead, it seems to be the combination of several criteria what determines the stability of the scheme.

The combination that best fits the numerical results is that bounded by $\Delta t_{crit,m}$ (presented in Figures 4.12 and 4.13). For high permeabilities, the numerical results obtained with the MPM simulations fit especially well the criterion that ensures the stability of the mass balance of the mixture $\Delta t_{crit,m}$. However, a change in behaviour is observed from a certain k_l, and for smaller permeabilities the numerical results approach more the stability criteria of the liquid momentum $\Delta t_{crit,l}$. This can be explained considering that the liquid phase and the solid phase play different roles, in terms of bearing capacity of the media, depending on the permeability. Any perturbation on a very permeable material is supported fundamentally by the solid skeleton because the liquid can flow rapidly and the liquid pressure remains essentially unchanged. On the contrary, when the permeability is low, the dissipation of the liquid pressure occurs slowly. The limit between both behaviours is not well defined. For the studied cases, it lies between $10^{-11}\mathrm{m}^2$ and $10^{-10}\mathrm{m}^2$ (Fig.4.12 and 4.13).

The combination that follows $\Delta t_{crit,l}$ for small permeability but for high permeability tends the undrained criterion $\Delta t_{crit,u}$ is also suitable (see Fig.4.6 and 4.7). However, it is more restrictive than $\Delta t_{crit,m}$, especially in high porosities and permeabilities. Finally, the analytical criterion that ensures the stability of the coupled system $\Delta t_{crit,c}$ is too restrictive in all cases.

There is another important issue in this analysis which has to take into account. This is the L_i value required in the adjustments. As explained in Chapter 3, the characteristic length L_i is a mesh dependent parameter but it should not depend on the material characteristics, for instance, the porosity.

Figure 4.14 shows the obtained L_i values for the two meshes (L_e=0.05m and L_e=0.5m) for all simulations. When, for high permeabilities the critical time step approaches $\Delta t_{crit,l}$ or $\Delta t_{crit,m}$, L_i changes with porosity, whereas if it tend $\Delta t_{crit,l}$ or $\Delta t_{crit,m}$ the characteristic length is independent of porosity. The same pattern is observed in both meshes. In addition, note that $h_{min} < L_i < L_e$.

Given these latest remarks, the most reasonable expression which ensures the stability of the explicit hydromechanical scheme is the one that considers the minimum value of $\Delta t_{crit,u}$ and $\Delta t_{crit,l}$. It can be written as follows.

$$\Delta t_{crit} = \min \{\Delta t_{crit,u}, \Delta t_{crit,l}\} \tag{4.84}$$

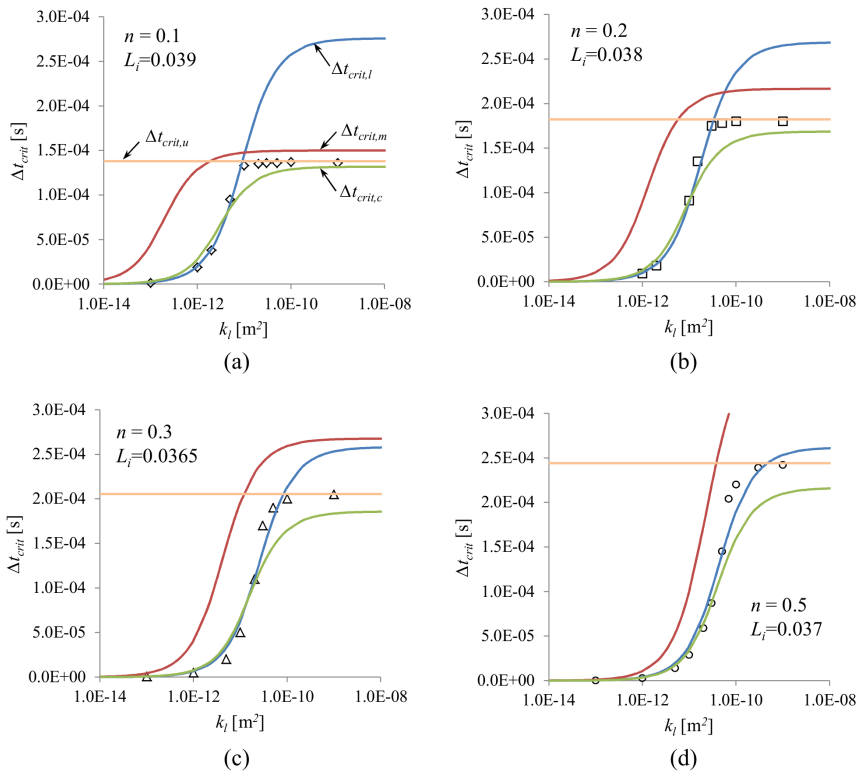

Figure 4.6: Adjustment of L_i to fit $\Delta t_{crit,u}$. Results of model $L_e = 0.05$ m. Porosity changes: (a) $n = 0.1$, (b) $n = 0.2$, (c) $n = 0.3$ and (d) $n = 0.5$.

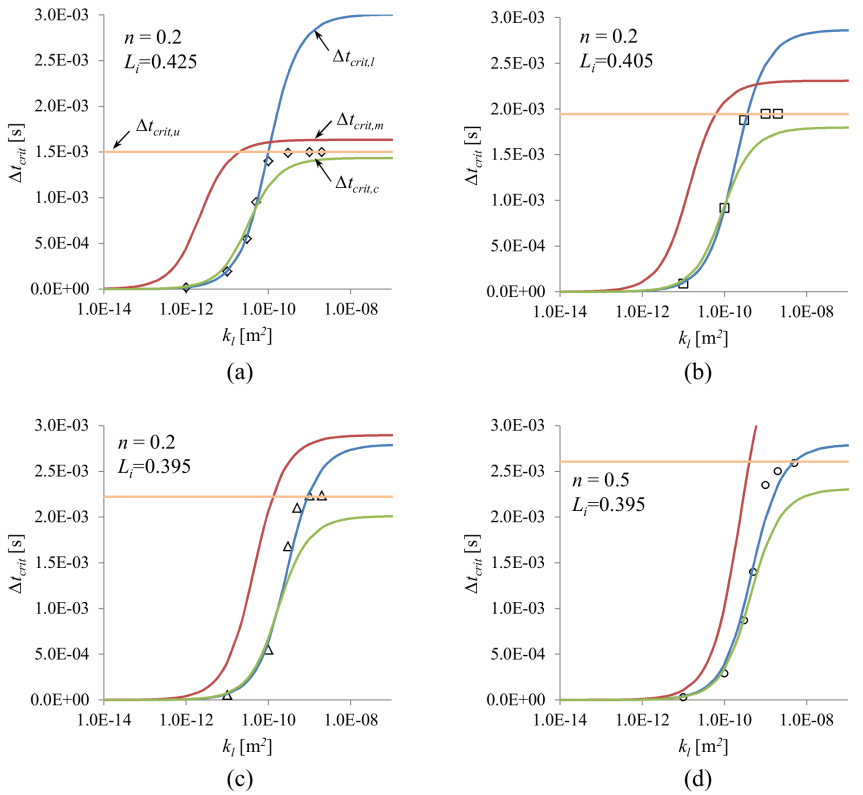

Figure 4.7: Adjustment of L_i to fit $\Delta t_{crit,u}$. Results of model $L_e = 0.5$ m. Porosity changes: (a) $n = 0.1$, (b) $n = 0.2$, (c) $n = 0.3$ and (d) $n = 0.5$.

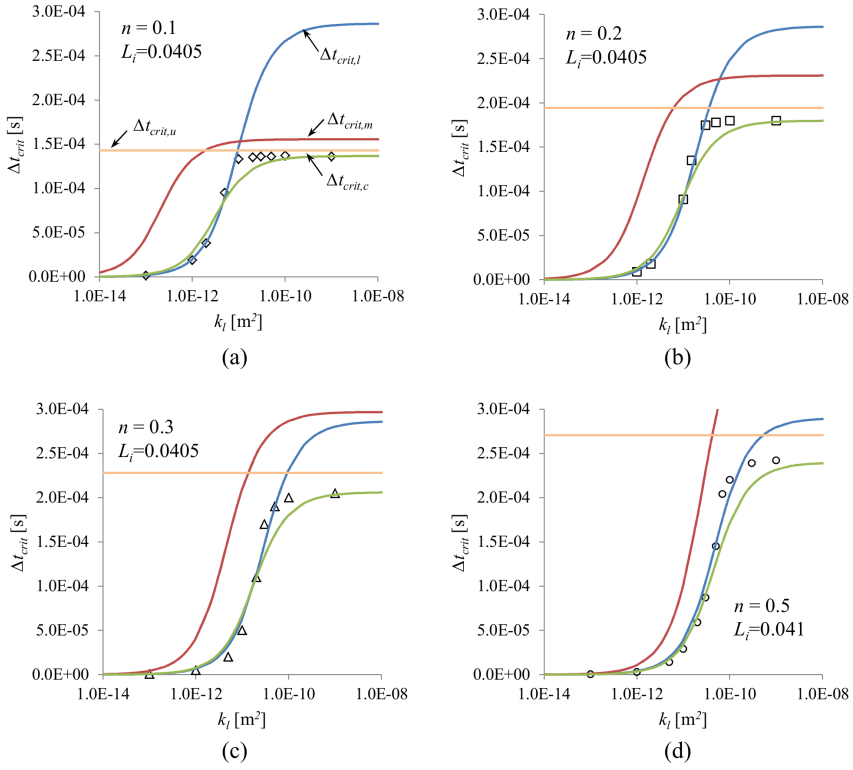

Figure 4.8: Adjustment of L_i to fit $\Delta t_{crit,c}$. Results of model $L_e = 0.05$ m. Porosity changes: (a) $n = 0.1$, (b) $n = 0.2$, (c) $n = 0.3$ and (d) $n = 0.5$.

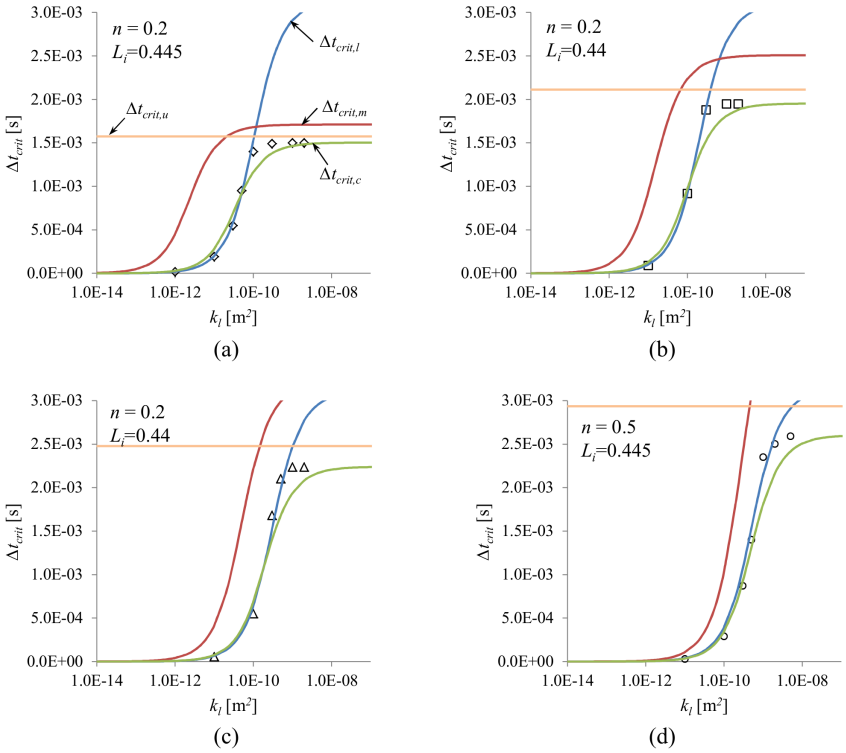

Figure 4.9: Adjustment of L_i to fit $\Delta t_{crit,c}$. Results of model $L_e = 0.5$ m. Porosity changes: (a) $n = 0.1$, (b) $n = 0.2$, (c) $n = 0.3$ and (d) $n = 0.5$.

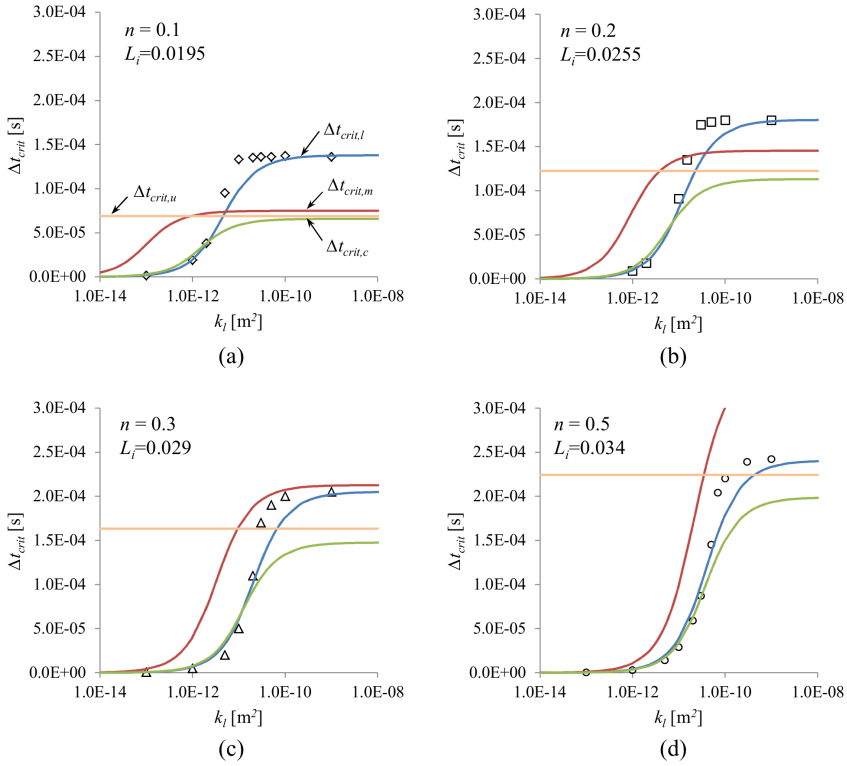

Figure 4.10: Adjustment of L_i to fit $\Delta t_{crit,l}$. Results of model $L_e = 0.05$ m. Porosity changes: (a) $n = 0.1$, (b) $n = 0.2$, (c) $n = 0.3$ and (d) $n = 0.5$.

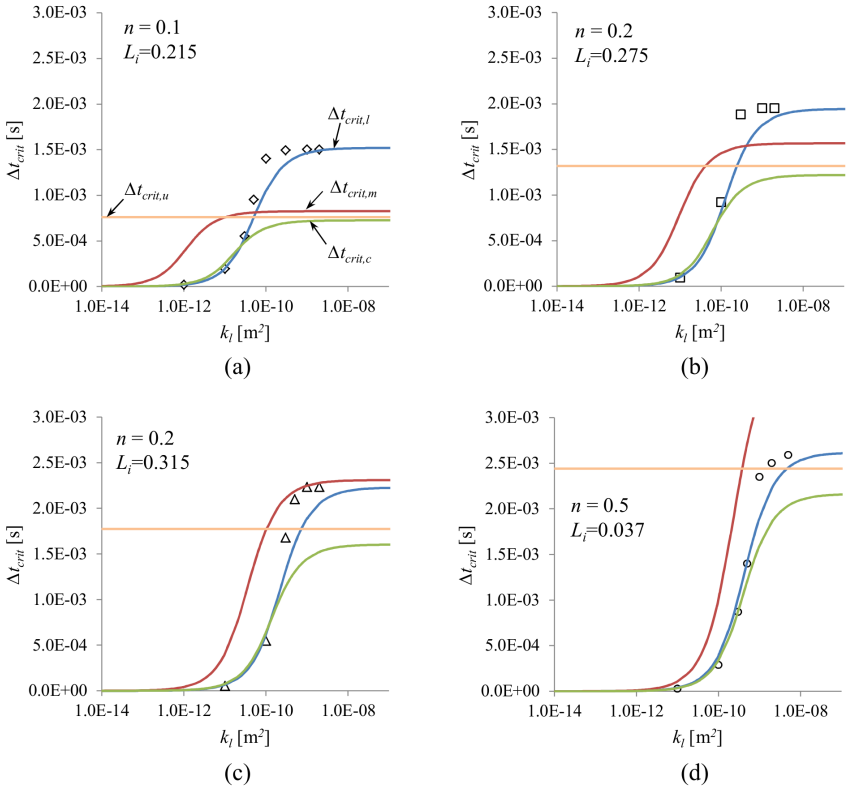

Figure 4.11: Adjustment of L_i to fit $\Delta t_{crit,l}$. Results of model $L_e = 0.5$ m. Porosity changes: (a) $n = 0.1$, (b) $n = 0.2$, (c) $n = 0.3$ and (d) $n = 0.5$.

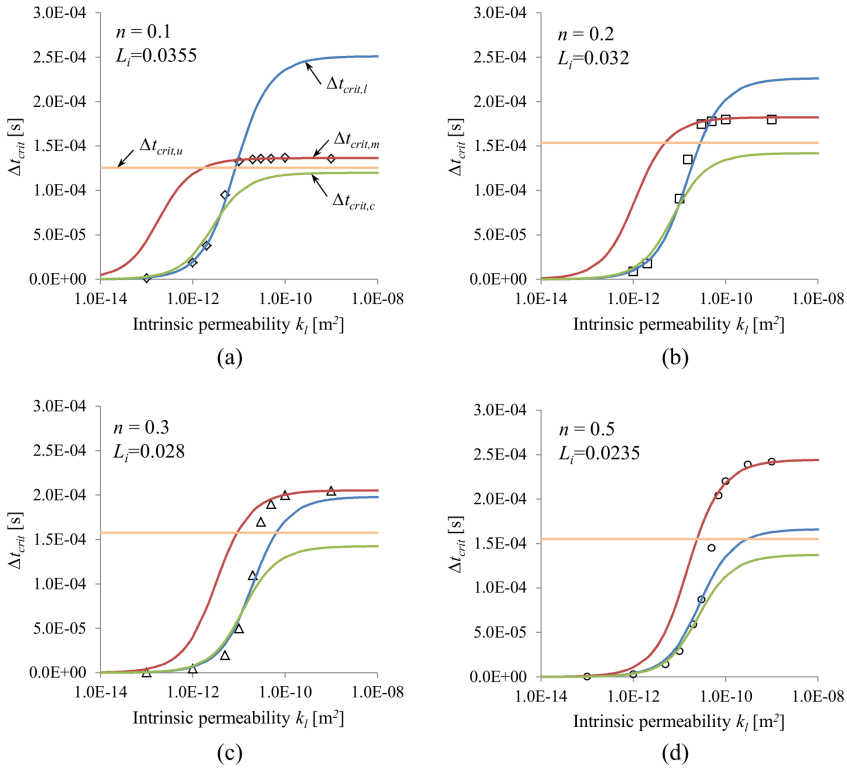

Figure 4.12: Adjustment of L_i to fit $\Delta t_{crit,m}$. Results of model $L_e = 0.05$ m. Porosity changes: (a) $n = 0.1$, (b) $n = 0.2$, (c) $n = 0.3$ and (d) $n = 0.5$.

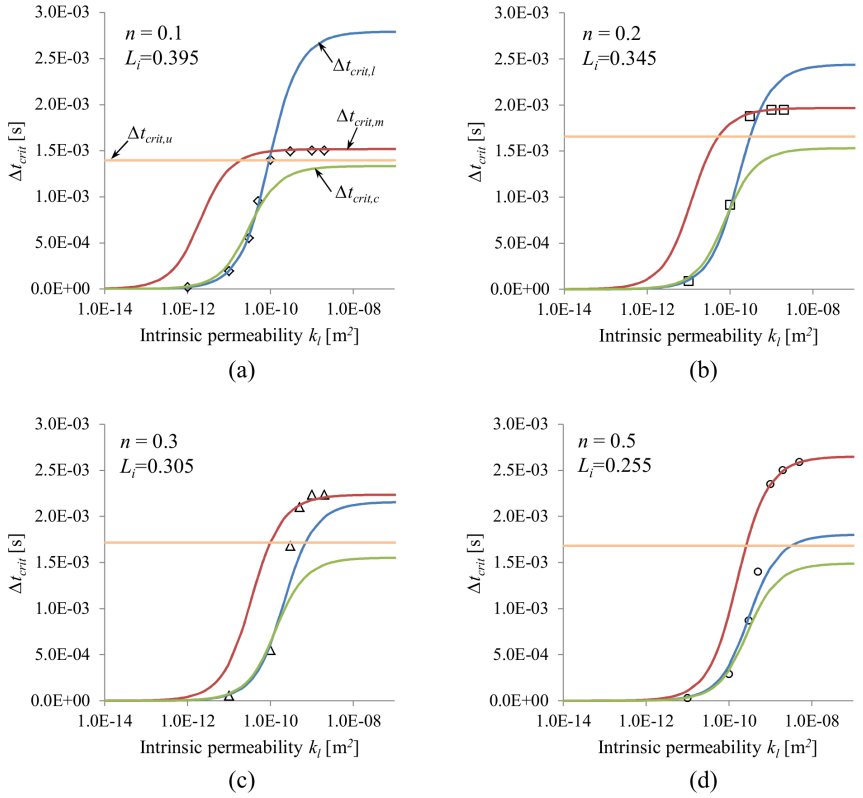

Figure 4.13: Adjustment of L_i to fit $\Delta t_{crit,m}$. Results of model $L_e = 0i5$ m. Porosity changes: (a) $n = 0.1$, (b) $n = 0.2$, (c) $n = 0.3$ and (d) $n = 0.5$.

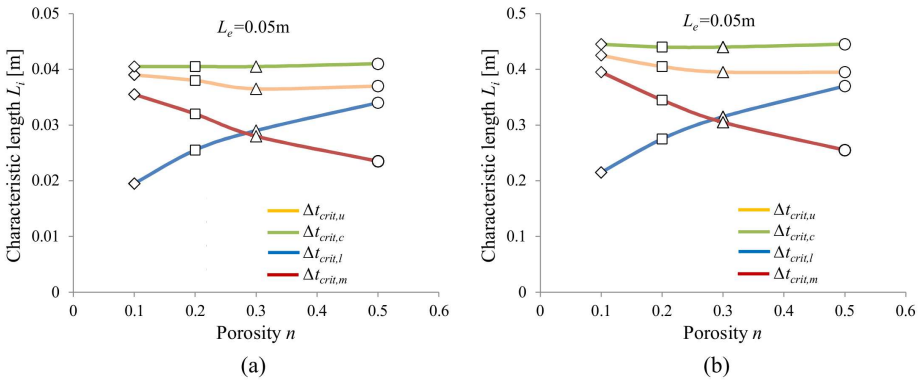

Figure 4.14: Obtained values of the characteristic length L_i depending on the critical time step criterion and the porosity of the material. (a) $L_e = 0.05$ m, (b) $L_e = 0.5$ m.

4.7 Damping of the solution

The hydromechanical formulation is provided with a natural damping. Because of the solid-liquid interaction within the pores, the momentum balance equation of the liquid have a coupling term that is proportional to the difference between the velocities of the two phases. This is the so-called dragging term which generates a viscous force that damps the solution and eliminates part of the unphysical and numerical oscillations.

However, in some problems such as in homogenous linear elastic materials it is necessary to include an artificial energy dissipation term in order to reduce numerical instabilities or to converge to the quasi-static solution as quick as possible. Here, the local non-viscous damping (Cundall, 1987) presented in Section 3.3.7 is extended to the 2-phase formulation. Two additional forces should be considered: a damping force for the liquid phase $\mathbf{F}_l^{damp}$ and another one for the mixture $\mathbf{F}^{damp}$. Those are included in the momentum balances as follows.

$$\widetilde{\mathbf{M}}_l \cdot \mathbf{a}_l = \mathbf{F}_l^{ext} - \mathbf{F}_l^{int} - \mathbf{Q}_l \cdot (\mathbf{v}_l - \mathbf{v}_s) + \mathbf{F}_l^{damp} \tag{4.85}$$

$$\mathbf{M}_s \cdot \mathbf{a}_s + \mathbf{M}_l \cdot \mathbf{a}_l = \mathbf{F}^{ext} - \mathbf{F}^{int} + \mathbf{F}^{damp} \tag{4.86}$$

Considering the liquid unbalanced force as $\mathbf{F}_l = \mathbf{F}_l^{ext} - \mathbf{F}_l^{int}$, the damping force for the liquid phase is proportional to its absolute value according to 4.87. It is important to note that $\mathbf{F}_l^{damp}$ takes the opposite direction of the liquid velocity $\mathbf{v}_l$.

$$\mathbf{F}_l^{damp} = -sign(\mathbf{v}_l)|\mathbf{F}_l|\alpha_l \tag{4.87}$$

The damping force of the mixture is not calculated directly from the mixture unbalance force $\mathbf{F} = \mathbf{F}^{ext} - \mathbf{F}^{int}$. To be consistent with the definition of the momentum balance of the mixture, $\mathbf{F}^{damp}$ must be divided considering the volumetric fractions associated to each phase as it is shown in equation (4.88).

$$\mathbf{F}^{damp} = (1-n)\mathbf{F}_s^{damp} + n\mathbf{F}_l^{damp} \tag{4.88}$$

In this way, the damping of liquid and solid can be treated separately. The damping force of the solid $\mathbf{F}_s^{damp}$ can be calculated considering the solid velocity $\mathbf{v}_s$ according to the following expression.

$$\mathbf{F}_s^{damp} = -sign(\mathbf{v}_s)|\mathbf{F}_s|\alpha_s \tag{4.89}$$

The unbalanced force of the solid phase can be obtained as

$$\mathbf{F}_s = \frac{1}{1-n}(\mathbf{F} - \mathbf{F}_l) \tag{4.90}$$

The parameters α_l and α_s range between 0 and 1 and control the amount of damping for each phase. In this work, the same value α has been considered for both of them.

In dynamic problems, where the accelerations have an important role in the course of the calculation, the damping factor should be very small (0 to 0.05) in order to approximate the correct solution.

Table 4.2: Types of boundary conditions in a hydromechanical problem.

Condition	Essential	Natural
Mechanical	Prescribed solid velocity (Eq.4.7)	Prescribed traction (Eq.4.6)
Hydraulic	Prescribed liquid velocity (Eq.4.4)	Prescribed liquid pressure (Eq.4.3)

4.8 Boundary conditions

The boundary conditions for the hydromechanical problem have been presented in Section 4.3.1 and they are summarised in Table 4.2. These can be classified into essential or natural (whether the condition is applied directly on the solution or on a secondary variable); and mechanical or hydraulic (whether they affect directly the solid skeleton or the liquid phase).

It is important to note that a boundary without any restriction means that

- solid skeleton can moves freely,
- total stress is zero,
- liquid phase can moves freely (permeable boundary), and
- liquid pressure is zero (no excess pore pressure).

This is specially useful in slope problems, in which the water table will be automatically kept on the ground surface, even during the instability. However, if $p_l \neq 0$ or external traction are applied along a moving boundary but have not a prescribed direction, the normal vector along the contour must be calculated at every time step.

4.9 Validation. Oedometric consolidation

The aim of this Section is to validate the 2-phase 1-point MPM formulation by means of the simulation of a one-dimensional consolidation problem. An oedometric consolidation test with small deformation has been simulated. The results of pressure dissipation are compared with the analytical solution given by Terzaghi (1943). Here, the effects of damping on dynamic numerical solutions are analysed.

A saturated sample of 1 m high is considered, in which traction of 10 kPa is suddenly applied at the upper boundary and maintained throughout the calculation. The material is considered elastic and all properties are summarised in Table 4.3. Because the bottom is impervious, the drainage length h is 1 m. Gravity is neglected and the bottom is fixed.

Table 4.3: Material properties of oedometric tests.

Material property	Value
Porosity [-]	0.3
Solid density [kg/m^3]	2700
Liquid density [kg/m^3]	1000
Liquid bulk modulus [kPa]	80000
Young's modulus [kPa]	10000
Poisson ratio [-]	0.0
Liquid viscosity [kg/sům]	0.001
Intrinsic permeability [m^2]	$5 \cdot 10^{-5}$

The consolidation process can be mathematically described with the diffusion equation as follows,

$$\frac{\partial p_l}{\partial t} = c_v \frac{\partial^2 p_l}{\partial z^2} \tag{4.91}$$

where c_v is the consolidation coefficient and z represents the flow direction. Assuming that the load is entirely carried by the water and total stresses are constant, the initial excess pore pressure within the sample p_0 is 10 kPa. As times goes on, the water flows out and pressure dissipates.

Because all process depends on c_v, a dimensionless time T can be defined as equation (4.92). The analytical solution in the case of the oedometer test was presented by Terzaghi (Terzaghi, 1943). Taking the properties presented in Table 4.3, the analytical results of the pore pressure dissipation along depth z are shown in Figure 4.15. It is important to highlight that this is a quasi-static solution, in which the accelerations are not taken into account.

$$T = \frac{c_v t}{h^2} \tag{4.92}$$

Three numerical simulations are presented considering different values of the damping factor α. The first one is a purely dynamic calculation (α=0), meanwhile the two others are subjected to additional non-viscous damping (α=0.05 and α=0.75).

Figures 4.16a, 4.16b and 4.16c show the comparison between Terzaghi's analytical expression and numerical results considering α=0, α=0.05 and α=0.75 respectively. Figure 4.17 provides the evolution of pore pressure of a material point located at 0.45 m depth.

Considering the simulation with no additional damping, Figure 4.16b shows that for small T there are some oscillations the pore pressure evolution. This is because the dynamic nature of the formulation and due to the wave reflection on the boundaries (see Figure 4.17b). However, these fluctuations are clearly damped and at $T \approx 0.5$ the numerical solution fits the quasi-static one. This fact is explained by the viscous therm which appears in the momentum balance equation of the liquid (Eq.4.29) as a dragging therm. In this work, this has been called as natural damping (Sec.4.7).

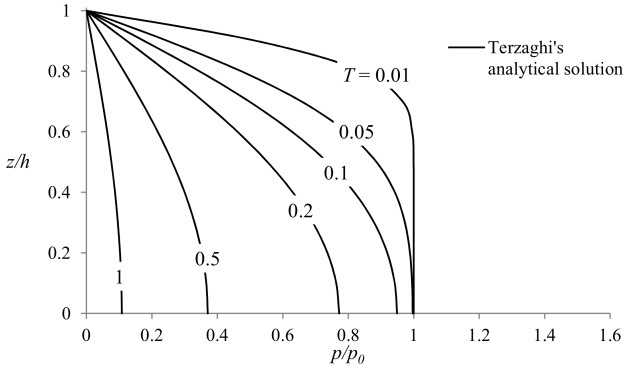

Figure 4.15: Pore pressure evolution along depth z at different times. Terzaghi's analytical solution

In order to reduce the oscillations and to capture the quasi-static solution equilibrium as quick as possible, artificial non-viscous damping can be added. With α=0.05, MPM results and quasi-static solution are nearly identical except for a very small T (Fig.4.17c). However, if α is too high (i.e. α=0.75 in Figure 4.17d) the system becomes overdamped. In this case, pore pressure tends to quasi-static solution without oscillating but in a much more slowly manner. Numerical results differ from analytical ones and higher excess pore pressures are longer maintained. Dissipation is finally completed at T=8 (Fig.4.17).

From this analysis, it can be concluded that a damping factor of 0.05 is suitable to simulate the quasi-static solution.

4.10 Concluding remarks

A 2-phase 1-point MPM formulation capable of modelling fully coupled hydromechanical problems is presented in this Chapter. This is a dynamic formulation in which a portion of saturated porous media is considered in each material point. A validation of the coupled formulation is presented by means of the simulation of the one-dimensional consolidation problem.

The main contribution of this Chapter is determining an analytical expression for the critical time step. The analysis has been carried out studying the stability of the explicit algorithm and comparing it with numerical results. Several analytical expressions were determined, and finally a compound solution was determined as a critical criterion. A part from the mesh element size, the material permeability is also essential to determine the stability time step value. Small values of permeability leads to very restrictive time steps. Other parameters, such as density and porosity, also have some influence in the time step values. However, the changes of permeability in the field are much more relevant than the variability of porosity and density. This fact complicates those simulations with

low pervious materials such as clays because small time steps lead to excessively high computation time.

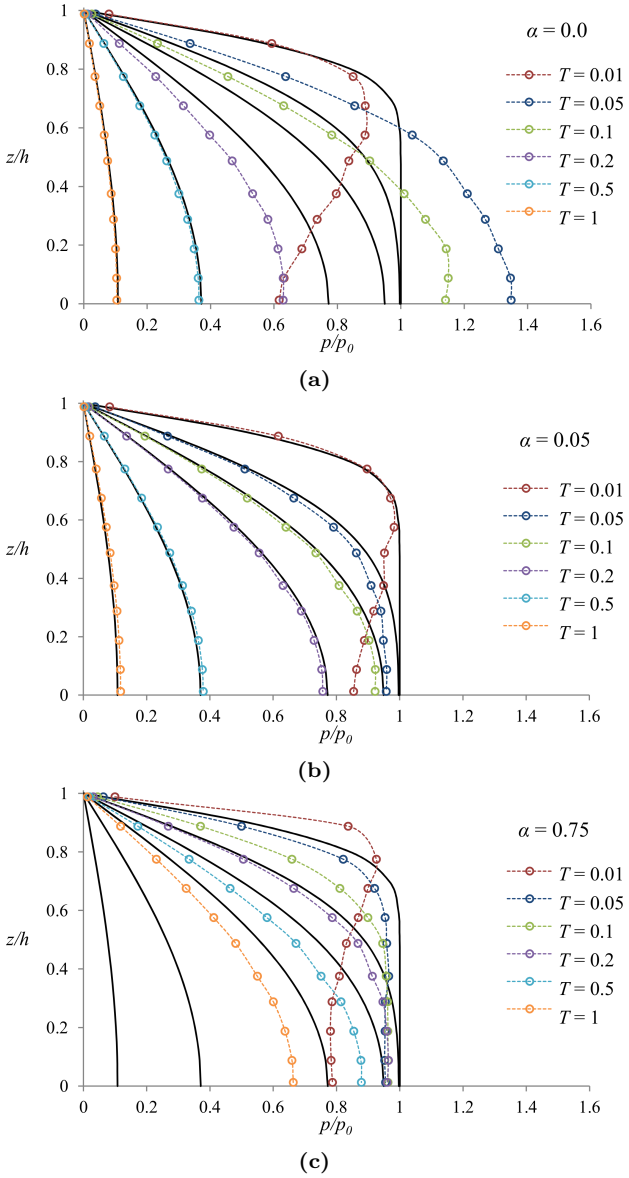

Figure 4.16: Pore pressure evolution along depth z at different times. Comparison between Terzaghi's analytical solution and numerical solutions: (a) α=0.0, (b) α=0.05 and (c) α=0.75.

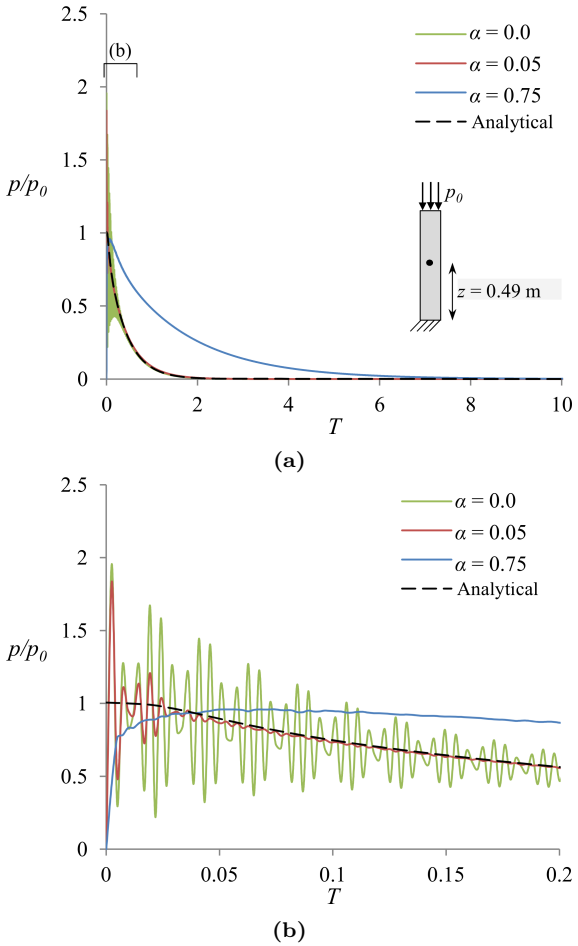

Figure 4.17: Evolution of pore pressure of a material point located at z=0.45 m. (a) Comparison between Terzaghi's analytical expression and numerical solutions considering different damping factors. (b) Detail/zoom in for small T.

5

Chapter 5
Slope Failures in Brittle Materials

Slope instability problems are very common in the geotechnical field. The capabilities of MPM to model large deformations makes it an ideal tool to study the entire instability process: the static stability, the failure triggering and the subsequent run-out.

The current Chapter 5 focuses on the study of landslide initiation and post-failure evolution in brittle materials, such as cemented soils and overconsolidated plastic clays. These materials are characterised by the reduction of the available strength with increasing strain. This strain-softening behaviour leads to progressive failure mechanisms.

In the first Section 5.1, the progressive failure phenomenon is described. Then, the constitutive elastoplastic model implemented for this study is presented (Sec.5.2). The non-associated Mohr-Coulomb is extended by introducing strain softening plasticity, hence the strength loss typically from brittle materials can be simulated. Afterwards, three slope instabilities triggered by the increase of pore water pressure will be analysed. First, the Selborne failure experiment is presented (Sec.5.3) and numerical results are compared with real field data. In a second analysis (Sec.5.4), the effect of internal shearing in a deep seated compound slide is discussed. This case is inspired by one of the representative cross sections of Vajont landslide. Finally, in Section 5.5, a parametric study is presented, in which, for a given slope geometry, the influence of the brittleness of the material is evaluated on the triggering of instability and run-out.

5.1 Progressive failure phenomenon

One of the factors that may lead to the acceleration of a slide is the loss of resistant forces associated with the drop of available soil strength. This behaviour is typically observed in first time failure developed in "intact" sites in materials exhibiting a brittle behaviour, for instance hard soils and weak rocks. Overconsolidated and cemented clayey soils are particularly relevant for high plasticity soils. These materials exhibit a softening behaviour from a peak value, associated with a low value of shearing displacements, to a low residual strength when bonds are destroyed and clay particles orient in the direction of shearing. This reduction of strength leads to the propagation of the failure following a process of progressive failure.

The progressive failure phenomenon is a common problem in the geotechnical engineering field. This was first recognised by Terzaghi and Peck (1948) and Taylor (1948). It was further discussed in the context of overconsolidated clays and clay shales by Skempton (1964), Bjerrum (1967) and Bishop (1967). Further contribution are made by Palmer and Rice (1973), Stark and Eid (1994), and Puzrin and Germanovich (2005).

The results of a direct shear test on overconsolidated high-plasticity clay are shown in Figure 5.1. This material was located in the foundation of Aznalcóllar dam (Alonso and Gens, 2006), which failed catastrophically in 1998 causing one of the worst-ever environmental disasters in Spain. The construction of the embankment and the brittle nature of the clay led to a progressive failure mechanism which played a significant role on the stability of the dam.

Because in this kind of materials the rate of softening is linked with the magnitude of shear strain, the strength loss does not occur simultaneously along a potential rupture surface. If for any reason some particular point within the mass is forced to pass the maximum available strength, a degradation process initiates and the strength at that point will decrease according to the constitutive law. Then, the unbalanced stresses are transferred and redistributed to surrounding areas which in turn may overstress neighbouring points in the process. This stress transfer phenomenon generally develops along a zone of limited thickness (shear zone). As the strain increases within this zone, the slip surface propagates leading to a progressive failure mechanism.

Under this conditions, the maximum total mobilised resistance along the failure surface must be less than the peak shear stress multiplied by the contact area along the sheared zone. This is because once a progressive failure has started, the available strength will decrease inexorably. In the limit, the strength along the entire length of the slip surface will fall to the residual value.

According to Potts and Zdravković (2001), the type of failure triggering, for instance the way of loading a slope, affects the amount of progressive failure, and consequently the maximum resistance. Moreover, they state that for progressive failure to occur: (i) the material must be brittle, (ii) a stress concentration must exist, and (iii) the loading must

be non-uniform. In addition, the progression of failure is influenced by; (i) the relative stiffness of the materials involved (this is controlled by the stress strain behaviour of both, the localised shearing surface(s) and the continuum medium itself), (ii) the nature of the loading, and (iii) the scale of the shearing surface.

Under this complex circumstances, conventional methods of stability analysis such as Limit Equilibrium methods (LEM) can be useful for a preliminary analysis. However, these are incapable of dealing with a complete understanding of such a mechanism. Elastoplastic constitutive models with strain-softening are required. Therefore, numerical methods are essential to reproduce the progressive mechanism.

Several real cases involving progressive failure are collected and analysed in the literature, most of them by using Finite Element methods (Gens and Alonso, 2006; Potts et al., 1990, 1997; Yamaguchi et al., 1976; Zabala and Alonso, 2011). Troncone (2005) presents a 2D numerical analysis of well documented Senise large landslides in Southern Italy and an extension 3D in Troncone et al. (2014). These analysis are focussed on the failure propagation but they provide limited information on the post-failure behaviour.

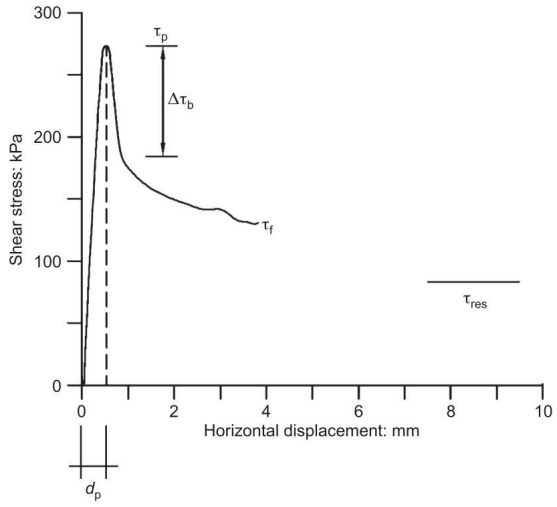

Figure 5.1: Direct shear test on specimen of foundation clay in Aznalcóllar dam foundation. Normal effective stress 400 kPa. (Alonso and Gens, 2006)

5.2 Constitutive modelling: Mohr-Coulomb with strain-softening

Because the classical elastic constitutive models cannot simulate many of the characteristics of the real soil behaviour, the theory of plasticity and the elastoplastic concept is essential to reproduce the progressive failure phenomenon. With the aim of modelling a

strength loss after peak strength conditions typical from brittle materials, the basic non-associated Mohr-Coulomb is extended introducing strain softening plasticity. Moreover, with the aim of reducing the singularities of the classical Mohr-Coulomb yield surface, the modifications proposed by Abbo and Sloan (1995) have been implemented.

The Mohr-Coulomb yield surface can be written as follows.

$$q = c' cos\varphi' + p' sin\varphi' \tag{5.1}$$

In which p' and q are the effective volumetric and deviatoric stresses,

$$q = \frac{{\sigma_1}' - {\sigma_3}'}{2} \tag{5.2}$$

$$p' = \frac{{\sigma_1}' + {\sigma_3}'}{2} \tag{5.3}$$

being σ'_1 and σ'_3 the maximum and minimum effective principal stresses.

The softening behaviour is accounted for by reducing the effective strength parameters (effective friction angle φ' and effective cohesion c') with the accumulated equivalent plastic strain ε^p_{eq} according to the following exponential softening rules:

$$c' = c'_r + (c'_p - c'_r)e^{-\eta\varepsilon^p_{eq}} \tag{5.4}$$

$$\varphi' = {\varphi'}_r + ({\varphi'}_p - {\varphi'}_r)e^{-\eta\varepsilon^p_{eq}} \tag{5.5}$$

The deviatoric plastic strain invariant is defined as:

$$\varepsilon^p_{eq} = \sqrt{\frac{2}{3}\mathbf{e}^p : \mathbf{e}^p} \tag{5.6}$$

where $\mathbf{e}^p$ is the deviatoric part of the plastic strain tensor.

The model requires the specification of peak (${c'}_p$,${\varphi'}_p$) and residual (${c'}_r$,${\varphi'}_r$) strengths. An additional parameter η is also necessary in order to control the rate of strength decrease.

Figure 5.2 shows the effect of η in a simple shear test simulation (see Figure 5.2a), in which the brittle soil is modelled by a row of elements. A vertical stress is applied (50 kPa) to a rigid layer sitting on the soil layer, and a horizontal stress (25 kPa) is also applied to confine the sample. The lower boundary is fixed and a horizontal prescribed velocity is imposed to the rigid cap layer at the top of the sample. The calculated results for a material point centred within the sample show that high values of η lead to faster degradation of the soil. This relationship is unique for a given material and it is element size independent.

In order to implement a constitutive realtionship in the MPM framework explicit and implicit methods can be used. Implicit techniques are generally accurate but are difficult to implement and, in some cases, they require special pocedures to converge. On the

contrary, explicit methods are generally robust but can be very inaccurate if the errors are not properly controlled.

In this case, it has been integrated by means an explicit integration scheme based on Sloan et al. (2001). This is a sub-stepping algorithm, in which the yield surface (Eq.5.1) and the softening laws (Eq.5.4 and Eq.5.5) are all evaluated at known stress states an no iteration is strictly necessary to predict the final stresses. However, in order to improve the accuracy in the results, an iterative correction with error control has been implemented. It reduces automatically the time step to satisfy the yield criterion. Moreover, at the end of each step, a projecting back method has also been implemented to correct the effects of violating the yield condition as these are cumulative (Potts and Gens, 1985). This correction is specially recommended for critical state constitutive models such as the Mohr-Coulomb law.

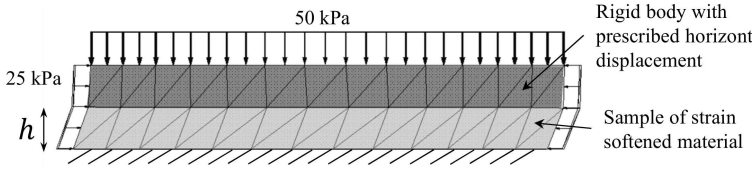

(a)

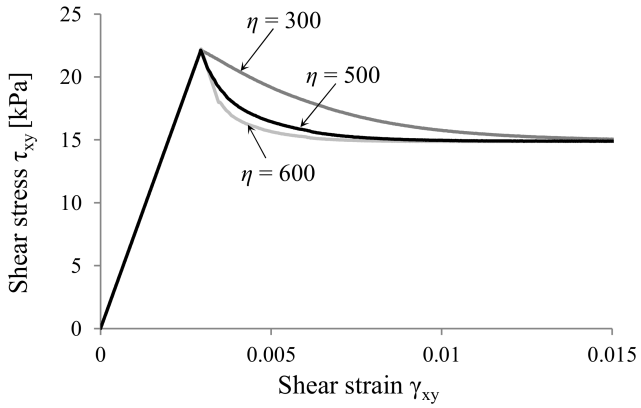

(b)

Figure 5.2: (a) Scheme of the numerical shear test. (b) Evolution of shear stress with shear strain of a material point centred within the sample considering several values of the shape factor η.

5.2.1 Calibration of shape factor for mesh dependence

It is well known that the inclusion of strain-softening features in standard continuum numerical methods leads to mesh dependent strain-localisation problems (Oliver and Huespe, 2004). A smeared crack approach (Rots et al., 1985) has been used as a regularisation

technique. It postulates that the total work dissipated by a shear band of thickness h (W_h) is equivalent to the fracture energy dissipated in a theoretical discrete crack (W_c), hence W_c=W_h.

In MPM the thickness of a shear band h can be approximated by the mesh element size. Then, in order to avoid the mesh size dependence and according to the smeared crack approach concept, the work dissipated by a shear band formed by elements of thickness h_1 (W_{h_1}) should be equal to the work dissipated by another shear band of thickness h_2 (W_{h_2}). It means that W_c=W_{h_1}=W_{h_2}. Then, to be consistent, the constitutive modulus of the material should depend on the mesh element size.

One way to include this dependence is to carry out a set of numerical shear tests with different element mesh sizes. The work dissipated within a certain shear test (per unit length) can be written as

$$W_h = \int_0^{U_x} \tau du_x \tag{5.7}$$

Maintaining the bottom of the sample fixed, a horizontal prescribed velocity is applied at the top of it ensuring that the final relative displacement between both sides of the band (U_x) is enough to degrade the material down to residual state (Fig.5.3). Then, a calibration of the shape factor η can be performed in order to ensure that the dissipated work is the same for all cases. Taking into account equation (5.7), the dissipated work is the area defined under the curve τ-u_x, hence two different shear bands dissipate the same energy when areas A1 and A2 are equal (see Figure 5.3).

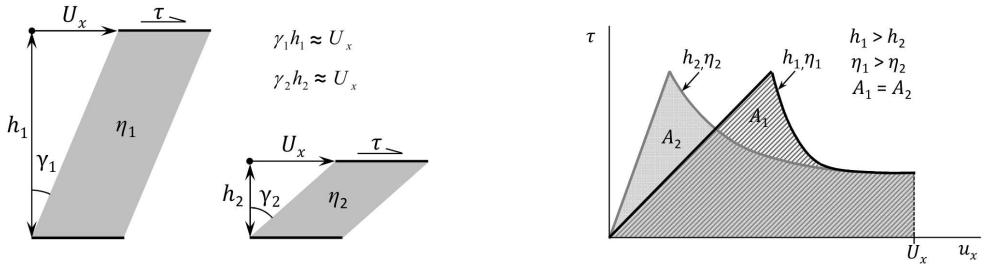

Figure 5.3: Scheme of two bands after being deformed with the same relative displacement U_x. These are equivalent when A_1=A_2 in the relationship τ-u_x.

5.3 The Selborne failure experiment. Modelling of a real first failure

The Selborne landslide was a field experiment in which a slope was brought to failure by pore pressure recharge (Cooper, 1996; Cooper et al., 1998). It was conducted with

the purpose of investigating the nature of progressive failure in overconsolidated clays. In fact, this was the first time that the development of a progressive mechanism was observed in a cut slope (Leroueil, 2001).

Some of the relevant field observations, namely:

- the simultaneous development of failure conditions starting at the slope toe and at the slope crest,
- the recorded time history of pore pressures in the vicinity of the failure surface,
- the geometry of the slip surface, described as a compound sub-circular surface and
- the measured displacements of some points of the slope surface after the failure will be the benchmark data to compare model response and field data.

An MPM modelling of the Selborne failure experiment is presented here, in which both the failure mechanism as well as the post-failure behaviour are analysed. Model parameters and the process leading to the instability are directly based on published data (Cooper et al., 1998) and the strain softening Mohr-Coulomb constitutive model simulates the clay brittleness. The rate of strength decrease is calibrated against an accepted shear stress-displacement relationship, with the purpose of avoiding mesh-dependency of computed results. Finally, a sensitivity analysis, analysing different parameters such as the effect of the residual strength and the clay permeability are also presented.

In this way, the Selborne experiment is an interesting case because will contribute to the validation of the dynamic MPM model and to check its capability to capture the slide run-out, a piece of information that is generally absent in Limit Equilibrium and Finite Element analysis.

5.3.1 Summary of the case and available data

The Selborne experiment was carried out in 1989 (Cooper, 1996) and it was designed to induce failure in a 9 m high, cut slope (Fig.5.4). The triggering mechanism was the increase of pore pressures within the slope by injecting water in vertical wells.

A geological cross-section of the slope in a west-east direction is given in Figure 5.5. The substratum is early Cretaceous unconsolidated sandstone (Lower Greensand). It is covered by a Gault clay deposit (GC) which is overconsolidated, brittle, high plasticity clay. Two layers can be distinguished within the clay deposit according to the degree of weathering. The upper weathered clay level is subdivided into Lower Gault clay and Upper Gault clay. A layer of soliflucted material covers the clay.

(a) (b)

Figure 5.4: Pictures of the slope (a) before and (b) after failure. (Bromhead et al., 1998)

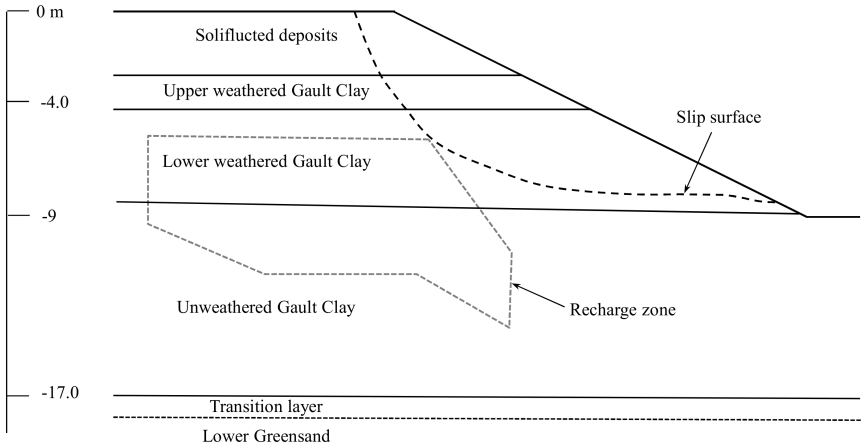

Figure 5.5: General scheme of the centerline soil profile, recharge zone and estimated slip surface (based on Grant (1996))

A laboratory testing program (Cooper et al., 1998) provided several geotechnical properties that are summarised in Table 5.1. The liquid limit ranges from 70-75% near the surface to 60-65% at a depth of 16 m whereas the plastic limit is fairly constant, about 22%. Water content is close to the plastic limit, but it increases up to 35% close to the surface. Peak and residual effective shear strength parameters were also estimated for all materials by means of laboratory tests (Table 5.1).

The ground surface was initially excavated to create a 2:1 slope. Its lateral boundaries were isolated from the remaining clay formation by means of trenches and low friction panels with the purpose of inducing a 2D failure mechanism. Pore pressures were raised for about 6 months by increasing the pressure heads (up to 7 m of water column) in a system of 20 wells. The recharge zone is indicated in Figure 5.5.

The slope was instrumented by means of extensometers, piezometers and inclinometers in

Table 5.1: Geotechnical properties (based on Cooper et al. (1998)).

	Soliflucted clay	Weathered GC		Unweathered GC
		Upper	Lower	
Liquid limit [%]	70-75	70-75	60-65	60-65
Plastic limit [%]	22	22	22	22
Water content [%]	35	30-35	20-30	18
Deformation modulus [MPa]	-	20-35	20-35	15-40
Effective peak cohesion [kPa]	5	10	15	25
Effective residual cohesion [kPa]	0	0	0	0
Effective peak friction angle [°]	21	24	25	26
Effective residual friction angle [°]	13	13	14	15

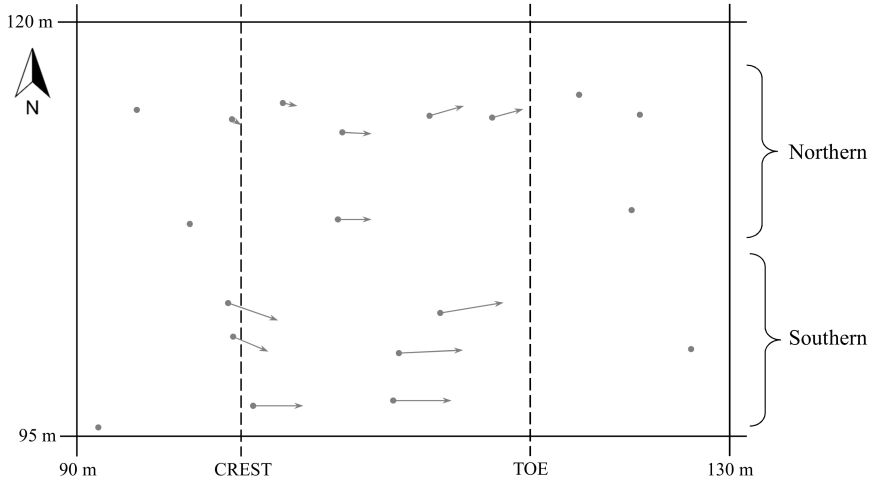

Figure 5.6: Plan view of the measured final displacements.

order to monitor the development of failure in the brittle clay. A detail of their position is given in plain view in Figure 5.7. The slip surface was fixed by precise surveying of two post mortem-trenches and also by interpreting the information given by the inclinometers. Inclinometers provided indications on the development of a progressive failure mechanism (Cooper, 1996). Displacements after failure, which reached maximum values of 4 m, were also measured at some points of the slope surface (see Figure 5.6; Grant (1996)).

Some piezometers recorded negative pore pressures despite the water recharge, especially those located near the toe of the slope (Figure 5.7b). This behaviour can be explained by the stress reduction caused by the excavations made and possibly by the atmospheric action.

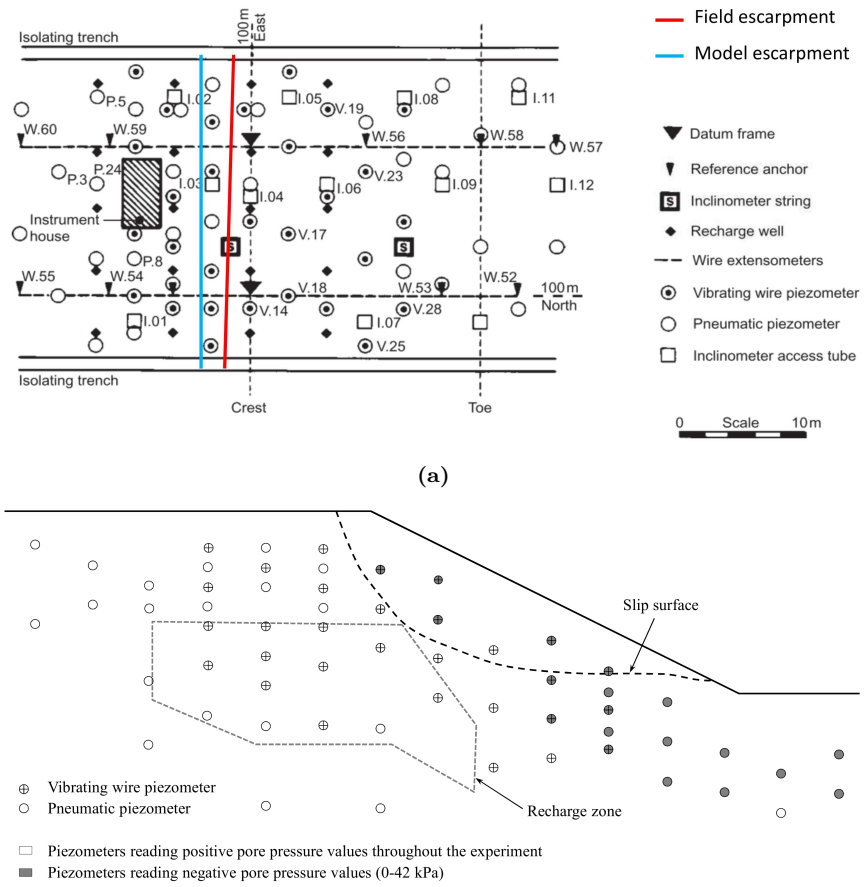

Figure 5.7: (a) Plan view of position of monitoring instruments. (b) Cross section with the location of piezometers (based on Cooper (1998))

5.3.2 Description of the model

The soil is saturated throughout the calculation and a thin 3D mesh of tetrahedral elements is used. The reference mesh (Figure 5.8) having an edge element size of 0.7 m is refined in the domain where failure is expected in order to get more accurate results and to optimise the computational cost.

The initial stress state in the model was due to gravity effects. The excavation process and the subsequent period of time until the initiation of the water recharge (about 5 months) were not simulated in the set of results described below. This is admittedly a limitation because of the relatively high K_0 value expected in these overconsolidated clays ($K_0 \simeq 1.5$ to 2). Therefore some differences between the actual initial stress state in the

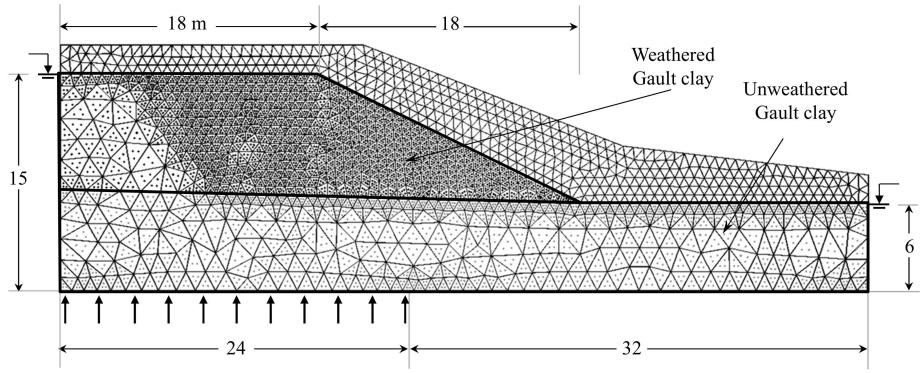

Figure 5.8: Initial geometry and material point's distribution within the computational mesh (refined element size of 0.7 m). The location of the pressure boundary condition is also indicated.

Table 5.2: Material parameters of the modelling.

	Weathered GC	Unweathered GC
Porosity [-]	0.3	0.3
Permeability [m/s]	0.001	0.001
Solid density [kg/m^3]	2700	2700
Young's modulus [kPa]	20000	20000
Poisson's coefficient	0.33	0.33
Effective peak cohesion [kPa]	13	25
Effective residual cohesion [kPa]	4.7	0.5
Effective peak friction angle [°]	13.5	15
Effective residual friction angle [°]	13.5	15

slope and the assumed gravity-related distribution are expected.

This is a plane strain simulation, where the horizontal displacements along the vertical contours are prevented and the lower boundary is fixed. The water pressure is kept to zero along the ground surface and the remaining boundaries are impervious. A damping factor α of 0.05 has been considered in all the calculations.

Two clay layers, an upper weathered Gault clay and a lower unweathered Gault clay, define the soil profile (Fig.5.8). Given the small differences found in the peak and residual strength parameters of the two upper weathered clay levels a simple layer is adopted in the model for the weathered material. Both materials are characterised by a brittle behaviour. The strength parameters of the strain softening Mohr-Coulomb constitutive model of the clays are based on laboratory results (Table 5.1) and are summarised in Table 5.2.

Under unsaturated conditions, strength increases due to suction effect, specially the cohesive component. When soil is close to saturated conditions, the additional cohesion due

to suction c_s can be estimated, if effective stress holds, as

$$c_s = s \tan \varphi' \tag{5.8}$$

where s is suction and φ' is effective friction angle. The residual cohesion of the weathered clay was given a positive albeit small value (4.7 kPa). This value is justified as follows. Negative pore water pressures were consistently measured in many points in the vicinity of the final failure surface, as shown in Figure 5.7b. The recorded values ranged between 0 and 42 kPa and an average suction of 20 kPa can be estimated. Certainly the clay is essentially saturated for this small suction value. Equation (5.8) for a residual friction angle of 13.5° provides the residual cohesion adopted for the weathered clay. This is considered to be a rough indication of an existing small residual strength but its effect will be further analysed in a sensitivity analysis reported below.

Because the numerical scheme is explicit, the calculation is conditionally stable and the time step increments are very small. For this reason, the permeability used in the simulation is several orders higher than the real one. While the Selborne failure took place on day 196 after the beginning of the water recharge, in the MPM calculation the instability occurs 39 seconds after starting the water loading. In order to compare measured data with numerical results, time (t) has been normalised by the failure time (T_f):

$$t^* = \frac{t}{T_f} \tag{5.9}$$

In order to simulate the artificial recharge, an excess of pore water pressure is applied on the lower boundary (Figure 5.8). The pressure rises linearly during 10 s, up to 110 kPa. After this time, the pressure on the boundary is maintained constant during all the calculation.

Pore pressures were recorded in a high number of sensors. Figure 5.9 shows the evolution of the excess pore water pressure at three different points within the slope ($t^* = 1$). Numerical results are compared with field data (Bromhead et al., 1998). The agreement is quite reasonable especially in piezometers B and C. Note that increments in pore pressure above the initial values are plotted. The initial pore pressures in the model were positive and resulted from an initial saturation of the slope. However, the actual piezometer records show negative pore pressures in several locations. By plotting the increase in pore pressure induced by the water surcharge, model results and measurements could be compared. Field data as well as calculations show a decrease in pore pressure in the vicinity of failure time. Cooper et al. (1998) attributed this decrease to dilatancy. However, model calculations were run for zero dilatancy. The decrease in calculated pore pressure is attributed to a volumetric extension state in locations shown in Figure 5.7b. If some dilatancy is included in the model, a more intense decrease in pore pressure is predicted.

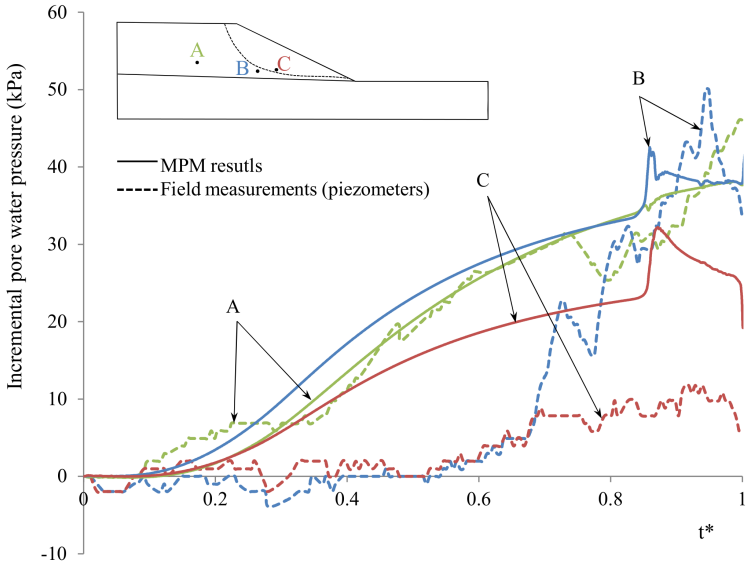

Figure 5.9: Piezometer records and model calculations.

5.3.3 Model performance and numerical results

5.3.3.1 Mesh effects

In addition to mesh dependent strain-localisation problems, separation and splitting in an MPM discretisation also depends on the mesh size because the material points remain numerically "in contact" whenever they have a node in common. This fact may lead to non-physical increase of material stiffness when two points tend to separate (Huang et al., 2011).

Three different refined meshes were analysed to evaluate the effect of the mesh size on the results (h): 1 m, 0.7 m and 0.5 m. Figure 5.10 shows that, at the same shape factor η, the smaller the element size, the higher the final displacements after the failure.

In order to minimise the mesh dependency, the shape factor η is calibrated according to Section 5.2.1. Simple shear tests are simulated for a varying thickness h of the shearing layer. Figure 5.11 shows the calibrated relationship $\tau - ux$ for three mesh sizes. The η parameter is adjusted to get equivalent shear stress-relative displacement response of the layer. When these η values are adopted, the slope response in terms of the displacement of the crest point of the slope becomes independent on the mesh size after the calibration (see Figure 5.10). Note, also, that finer meshes require smaller rates of strength decrease.

Figure 5.12 illustrates the final geometry and the displacement field once the slope stops

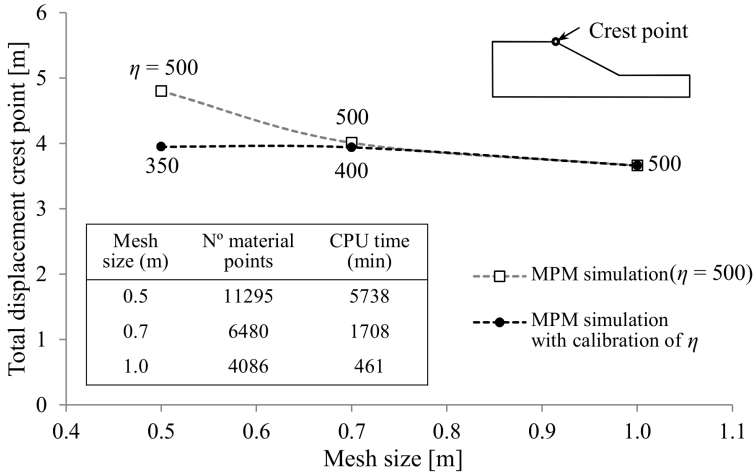

Figure 5.10: Total displacement of the crest point depending on the mesh size win shich the effect of the shape factor calibration is shown. Number of material points and CPU time are included.

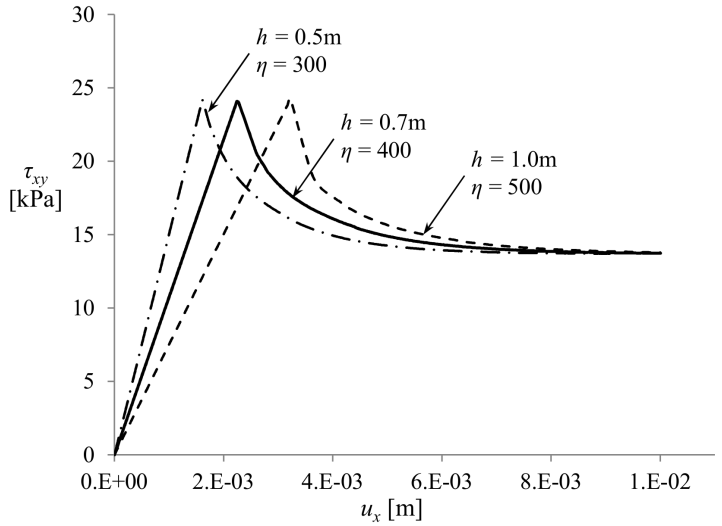

Figure 5.11: Calibrated relationship τ-u_x for three different mesh sizes. Areas under the curves are the same.

for the three MPM calculations, showing that the slope response is essentially mesh independent. The sliding surface measured in situ is also represented in the Figure.

The initial failure mechanisms obtained with the three meshes are compared with the measured slip surface in more detail in Figure 5.13. It is clear that the geological discon-

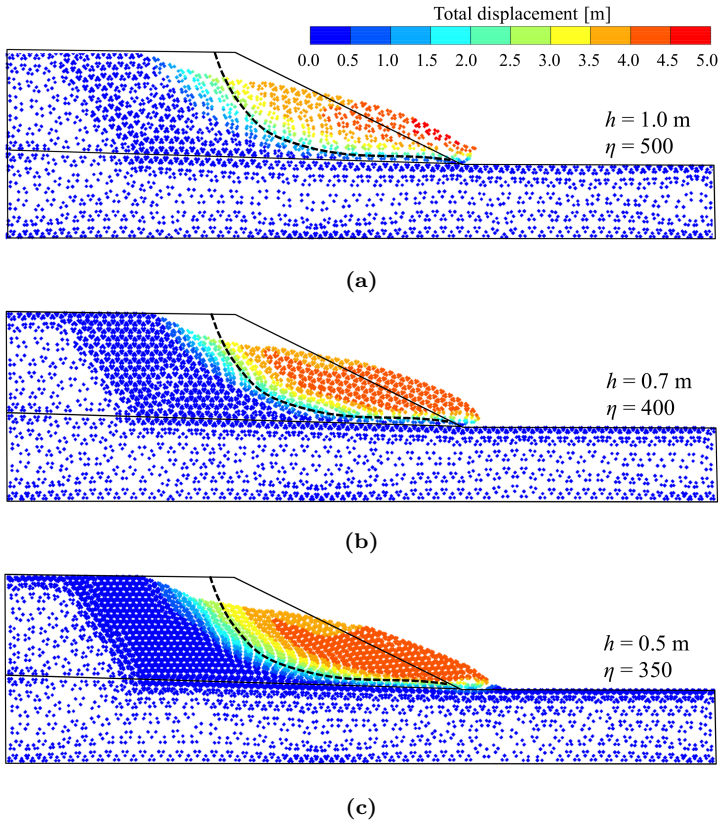

Figure 5.12: Effect of mesh size and the shape factor parameter on final displacement pattern. Refined mesh sizes are (a) h=1.0 m, (b) h=0.7 m, and (c) h=0.5 m. The slip surface measured in the field is indicated.

tinuity between weathered and unweathered clay plays an important role on the failure geometry. The lower part of the slip surface is almost horizontal following the contact, although it is included completely in the weathered layer. Numerical results indicate that the failure mechanism is located slightly deeper into the slope than the measurements. This could be an effect of the orientation of element faces in the MPM mesh discretisation. Moreover, the initial failure mechanism depends on the stress field. Therefore, some differences can be expected between numerical results and measurements because the initial excavation is not performed in this analysis.

MPM-predicted surface displacements are compared with measurements (Figure 5.6) in Figure 5.14. Because the purely two-dimensional failure regime was not achieved in the Selborne failure, data has been grouped into two zones (Northern and Southern). The order of magnitude as well as the distribution of the calculated horizontal displacements fit very well with field data on the Southern side. The Northern side appears to provide some restrain to the motion.

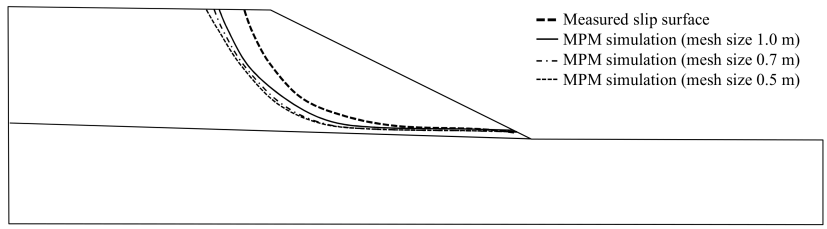

Figure 5.13: Comparison between measured and predicted shape of failure surface.

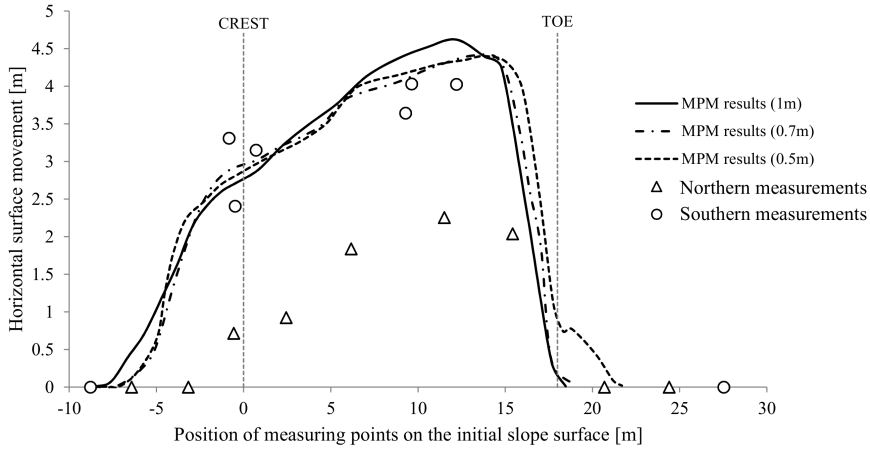

Figure 5.14: Measured and calculated displacements after failure.

According to the comparison carried out with three different meshes (Figures 5.10, 5.12, 5.13, and 5.14) it has been considered that the one with refined elements of 0.7 m is appropriate to analyse the Selborne experiment. In addition, the CPU time consumed for this mesh is acceptable (see CPU times consumed for different meshes in Figure 5.10).

5.3.3.2 The process of instability

The whole instability process is illustrated in Figure 5.15. The evolution of equivalent plastic strain, excess pore pressure and vertical effective stress is shown at 5 different dimensionless times (t^*). Note that some scales varies in order to capture the results properly.

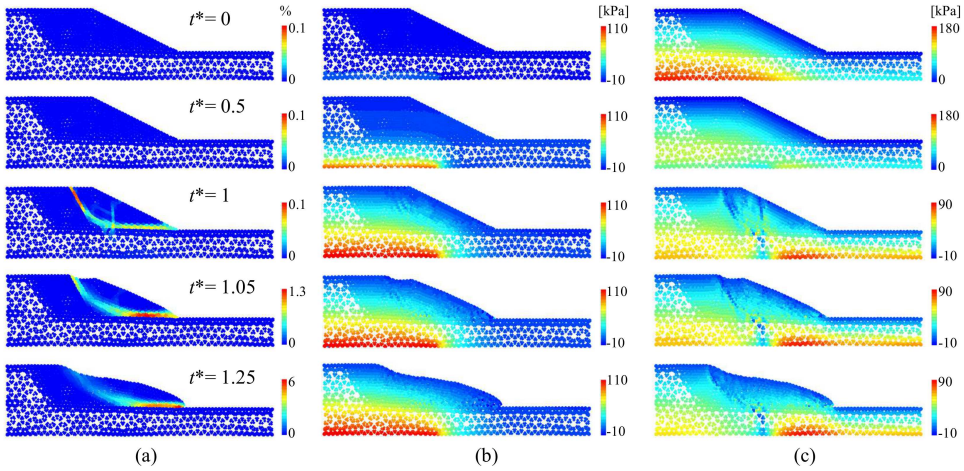

Figure 5.15: Evolution of (a) equivalent plastic shear strain, (b) excess pore pressure (kPa), and (c) vertical effective stress (kPa). Time is normalised (t^*).

5.3.3.3 Inclinometer readings

Inclinometer readings allow also a further set of data to check the validity of the model. Readings for inclinometers located on the excavated slope (I04, I06, I07 and I09; see Figure 5.7a) are compared with model calculations in Figure 5.16. Predicted displacements for two times close to the failure time are given. They approximate the time of inclinometer readings before the final run-out time. Note the scale of the horizontal displacements, which belong to the quasi-static, pre-failure stage of the slide. The calculation's results bound the actual measurements. The patterns of displacements are also reasonably well captured by the model and show the position of the failure surface.

5.3.3.4 Progressive Failure

The interpretation of several inclinometer profiles (Cooper, 1996) indicated that the failure surface developed progressively in the manner proposed by Bishop (1971). This qualitative data is shown conceptually in Figure 5.18. Accepting that the toe of the slope was in residual conditions at the beginning of the experiment, the shearing localisation progressed simultaneously from the higher and lower parts of the final slip surface. It propagated from both sides towards the centre part.

Following the idea of Skempton (1964) a mobilised friction angle $\widehat{\varphi}'$ is defined as

$$\sin \widehat{\varphi}' = \frac{q}{p^*} \tag{5.10}$$

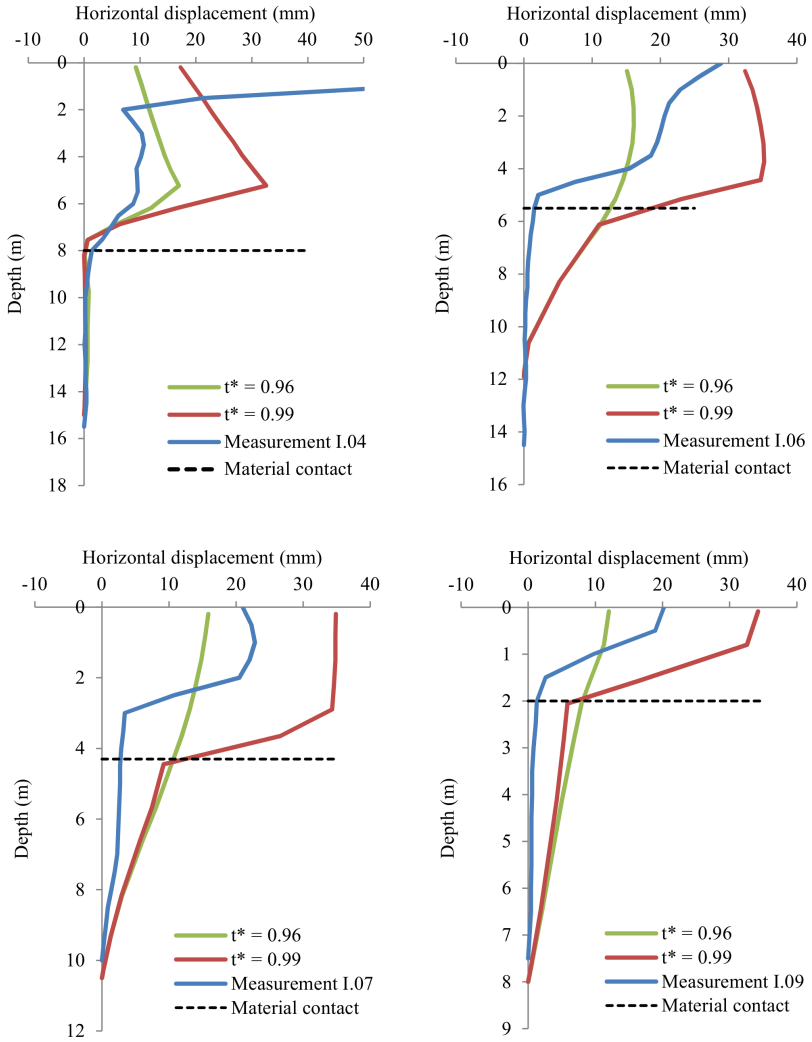

Figure 5.16: Measured and predicted inclinometer readings.

where

$$p^* = p' + (c' / \tan \varphi') \tag{5.11}$$

This measure of the mobilised strength allows us to compare the evolution of stresses of points belonging to failure surface. Under peak and residual conditions the mobilised friction angle coincides with the peak and residual friction angles respectively.

Taking as a reference the results calculated via the 0.7 m mesh, the mobilised friction angle (Eq.5.10) of 7 material points distributed along the initial failure mechanism (see Fig.5.18a) has been determined for different times. The resulting distributions are shown in Figure 5.18. These plots provide a clear view of the progressive failure phenomenon.

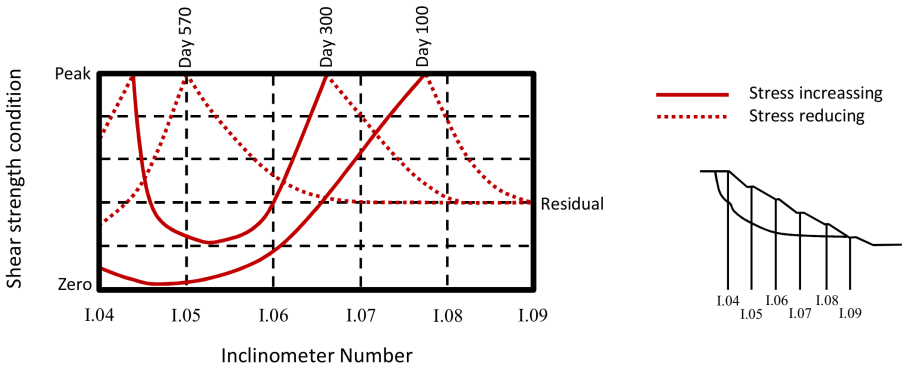

Figure 5.17: Qualitative shear stress states around slip surface (Cooper, 1996).

The strength loss does not occur simultaneously, but according to the stress state and the accumulated plastic shear strain. Initially all material points are in elastic regime and the mobilised friction angle distribution corresponds to the gravity effect (Fig.5.18b). As water pressure increases, $\sin\widehat{\varphi'}$ approaches the peak value. P2 is the first point to reach the peak yield surface at t^*=0.81 (Figure 5.18c). The failure propagates and at t^*=0.85 the upper part of the shear band (P1, P2) is at residual conditions. At this time, the toe of the slope (P7) reaches also the peak conditions (Figure 5.18c). Afterwards, the progressive failure stops whereas the shear stressing increases within the elastic range in the central part of the slide surface. Progressive failure is resumed at t^*=0.953 and it progresses from the toe to the centre part of the slope (plastifying points P6, P5 and P4) (Figure 5.18d). Finally, the failure mechanism is completed and the entire failure surface approaches residual conditions. Immediately after, the sliding motion starts (t^*=1).

Even if the numerical simulation performed does not consider the effects of the initial excavation, it is clear that a comparison of Figure 5.18 with the progressive mechanisms described in Cooper (1996) (Figure 5.17) reveals that both failures develop in a similar way: the higher and the lower part of the slope plastify first and finally the central part reaches residual conditions.

The evolution of progressive failure in terms of an average friction angle can be followed in Figure 5.19a. The mean friction angle increases continuously until peak strength conditions are reached for the first time at a point around P2 for t^*=0.83. Immediately afterwards there is a drop of available mobilised strength. Then the process of progressive failure progresses at essentially constant average mobilised strength. This process ends abruptly when the final point in the failure surface to reach peak conditions evolves towards a residual state. This sudden final drop of mobilised strength marks the beginning of an accelerated motion. The average (p', q) points at the three critical instants mentioned are plotted in Figure 5.19b in a triaxial stress space.

5.3.3.5 Kinematics of the motion

A significant improvement over static formulations is that the dynamic behaviour of the slide instability can be analysed in conjunction with the pre-rupture phenomenon. The calculated motion paths, total displacement, velocity and acceleration of points C1, C2, C3 and C4 (Figure 5.20a) are shown in Figure 5.20. When analysing these plots it can be observed that the embankment remains stable until t^*=1. When the failure mechanism develops those material points located above the shear band (C1, C2 and C3) accelerate quickly and a peak velocity is attained at t^*=1.1. Afterwards, the acceleration becomes negative and the velocity decreases towards a new state of equilibrium. At t^*=1.2 the slope tends to stabilise. Note that the dynamic variables depend on the position of the point within the slope: C4 remains motionless during all the calculation and C3 initially at the slope toe moves a small distance. In fact, soil located above the toe level rolls over the toe. The model indicates that the maximum sliding velocity was around 0.83 m/s in the middle and upper parts of the slope.

5.3.3.6 Stress paths

The stress path $p' - q$ of the material points P2, P5 and C4 are represented in Figure 5.21, in which peak and residual Mohr-Coulomb yield surfaces have also been included. The evolution of p', q and effective cohesion c' of these points are also represented in Figure 5.21. Note that P2 and P5 are located in the weathered clay layer whereas C4 is in the unweathered material. Starting at an initial gravity-induced elastic stress state, the effective volumetric stress p' reduces in P2 and P5 due to the rise of pore pressure along part of the lower boundary. Afterwards, the shear stress q slightly increases until the peak yield surface is reached at t^*=0.83. At this point the softening process drifts the strength down to residual conditions whilst pore pressures continue to increase. During the motion ($1.0 < t^* < 1.2$), the stresses vary but remain in residual conditions. Finally, when the slope is stabilised ($t^* > 1.2$), the stresses relax slightly and both P2 and P5 come again into elastic conditions. Point C4 behaves in a different manner. Because it is located under the toe of the slide, far from the water recharge, p' does not decrease and it remains in elastic conditions throughout all the calculation. On the contrary, p' increases due to stacked material lying on top of it at the end of the instability.

5.3.3.7 Overall view of the slope instability

In order to provide an overall view of the slope instability, Figure 5.22 shows in a unified way the progressive failure process, the stress evolution and the kinematic behaviour of the slide. The evolution of mobilised friction angle and total displacement of three selected material points initially located at the shear band (P1, P5 and P7) are presented. In addition, reference times of Figure 5.18 are also indicated by vertical arrows. Some time is needed until the water pressure is high enough to bring some points to a failed state.

Between t^*=0.83 and t^*=0.85 progressive failure starts at the higher part (P1) and the toe (P7) of the slope. The progressive shear localisation reactivates along the base and the central part of the failure mechanism (P5). Residual strength conditions along the entire failure surface are necessary to initialise the motion of the slope at t^*=1.0. Immediately afterwards, total displacements increase fast with the motion and all points of the sliding surface remain at residual conditions. Finally a new stable geometry is achieved at t^*=1.2 and the slope stops. Some points experience a small unloading and enter into elastic state.

Figure 5.23 shows the available effective cohesion in each material point at different times of the instability process. In Figure 5.23a different peak values can be distinguished for the two materials. The initiation of the progressive failure appears with the reduction of the effective cohesion down to the residual value at these points located along a primary shear band, the thickness of which is 1 or 2 elements (Figures 5.23b and 5.23c). Furthermore, a secondary vertical band under residual conditions c'_r appears at the centre of the primary one and progresses upward to the surface of the slope. During the instability (Figures 5.23d and 5.23e) the vertical shearing plane splits the mobilised mass into two blocks while the material degradation area becomes wider. Figure 5.23f shows the final distribution of available c'.

5.3.4 Sensitivity analysis

Several sensitive analysis have been carried out in order to study the effect of several parameters in run-out and slope stability.

5.3.4.1 Effect of effective residual cohesion

Different values of c'_r for the weathered clay material have been considered. It is observed that the final motion of the slope is highly dependent on the effective residual cohesion (Figure 5.24a). The lower the strength, the higher the run-out. Still, failure mechanism is very similar in all cases.

5.3.4.2 Effect of time increment in calculations

Figure 5.24b shows the final displacement of the crest point for different time increments. It is concluded that results converge to a stable displacement value when time increments are reduced. The point marked with an arrow is the value adopted in the presented simulations.

5.3.4.3 Effect of permeability

The time step increment depends on permeability. The smaller the permeability, the smaller the time step and the longer the computational time. For this reason the permeability considered in the calculation is 0.001 m/s which is several orders of magnitude higher than the real one. In order to analyse the effect of permeability, the original model is compared with another one with a smaller permeability of 0.0001 m/s.

The initiation of failure in the analysis with lower permeability is delayed (T_f=382s) with respect the higher permeability one (T_f=39s) due to the slower pressure dissipation. However, Figure 5.25 shows that if the results are presented considering the normalised time (t^*), both cases are very similar. The evolution of point P is presented. The final displacement observed in both analysis are identical, 0.65 m, and the evolution of pore pressures is also very similar (see Figure 5.25).

5.3.5 Specific conclusions

The Selborne failure experiment remains as one of the most informative field experiences to illustrate the nature of progressive failure in overconsolidated brittle, high plasticity clays. The interest of the case increases because of the available information on post-failure behaviour. Therefore, an opportunity exists to perform an integrated analysis of pre and post-failure slope behaviour. Validating such an experiment, which was preceded by a good identification of laboratory-based soil properties, provides an interesting support to the analysis performed.

The analysis provided remarkable consistent and accurate results. The "static" part of the analysis described is in itself a valuable addition to the interpretation of field measurements.

Some relevant points of the review of the pre-failure part of the experiment are:

- The identification of the progressive failure mechanism, which progresses from the two extremes of the failure surface towards the central part of the sliding surface.

- The quantitative evolution of the mobilised average shear strength that shows two distinct critical moments: the first arrival to peak strength and the last one. In between, the average mobilised strength is essentially constant. The final sudden drop in average mobilised strength triggers the accelerated slide motion.

The "availability" of field displacements after failure allowed a further check of the MPM model. The calculated displacement pattern agreed well with actual measurements. However, the result is highly dependent on the adopted residual effective cohesion. Small changes of this strength parameter (justified in the Selborne case by the occurrence of "in

situ" suctions) result in significant changes of run-out results.

One limitation of the analysis refers to the effect of the initial excavation, which was not considered. This is expected to modify to some degree the initial stress state. A second difficulty is the very long computational time for the explicit code in cases of low permeability. However, results plotted in terms of relative time with respect to the failure time seem to be consistent with field data.

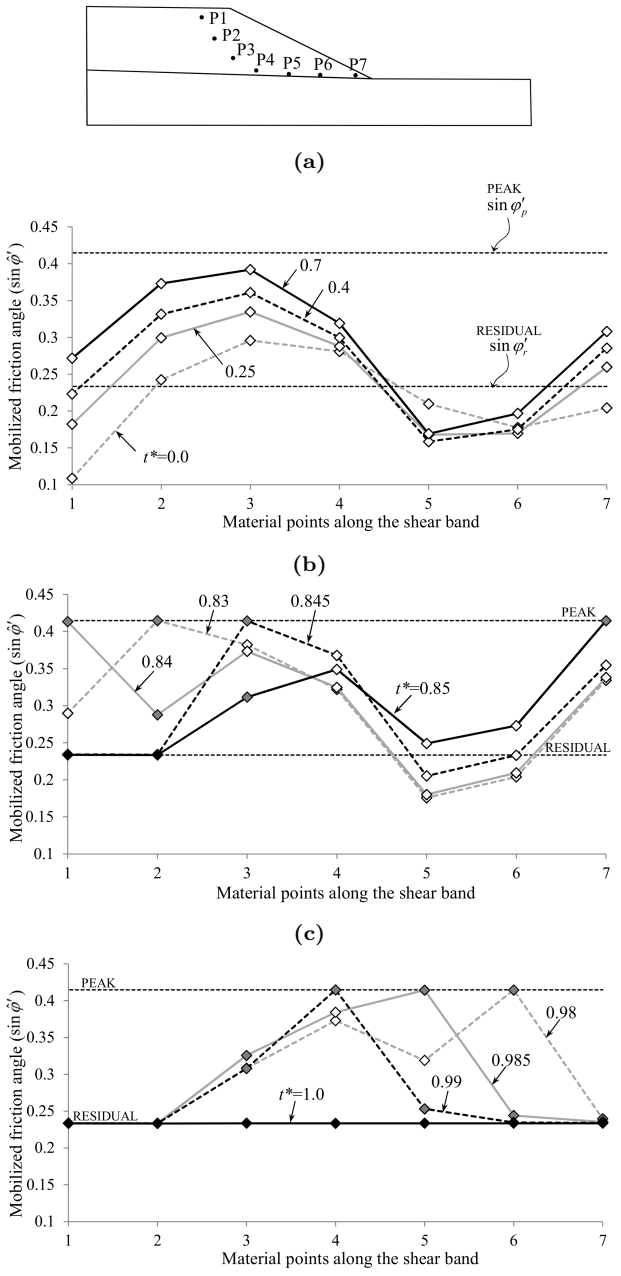

Figure 5.18: (a) Distribution of 7 material points located at the shear band. Evolution of the mobilised friction angle along the failure surface during (b) the elastic loading, (c) the progressive failure initiation, and (d) the final part of the progressive failure.

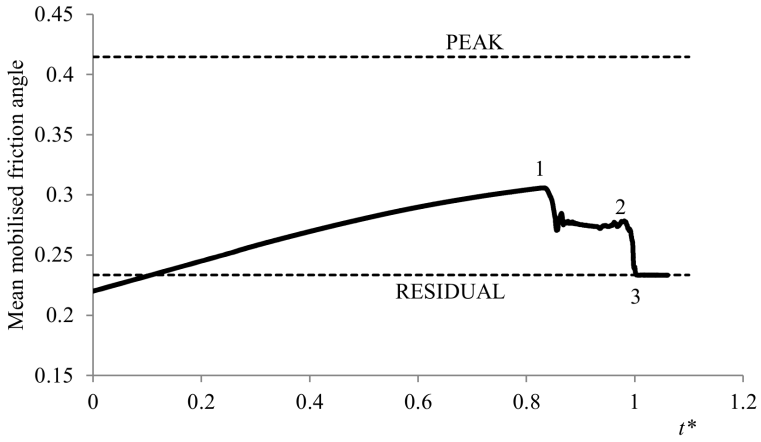

(a)

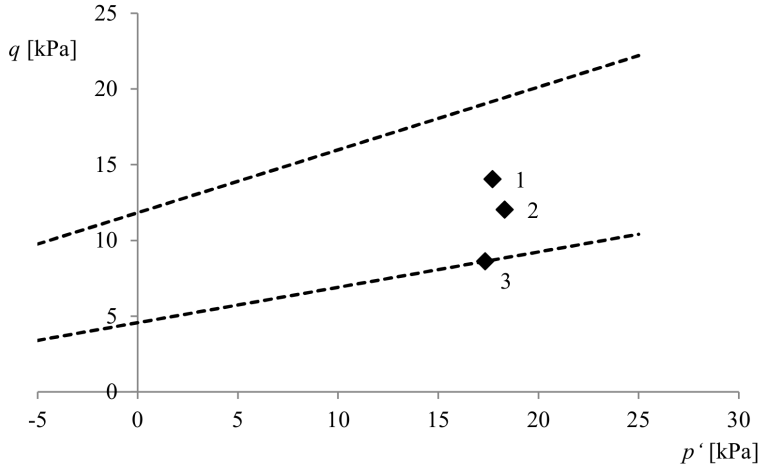

(b)

Figure 5.19: (a) Evolution mean mobilised friction angle and (b) averaged stress points.

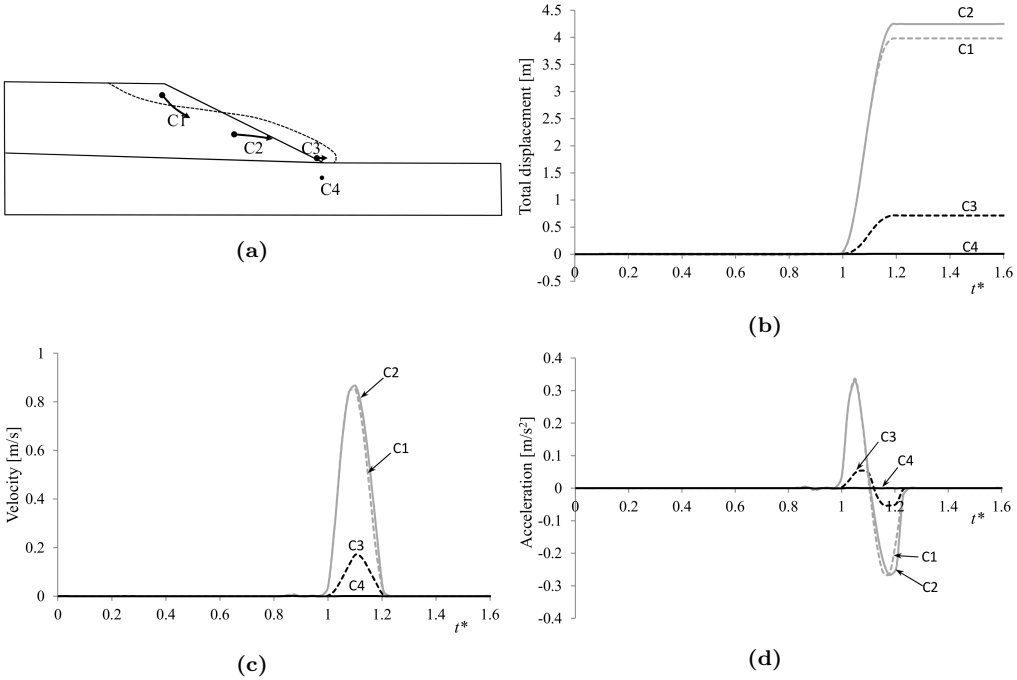

Figure 5.20: Kinematics of the motion. (a) Displacement vectors of points C1, C2, C3 and C4. Evolution of (b) total displacement, (c) velocity, and (d) acceleration of four points of the slide.

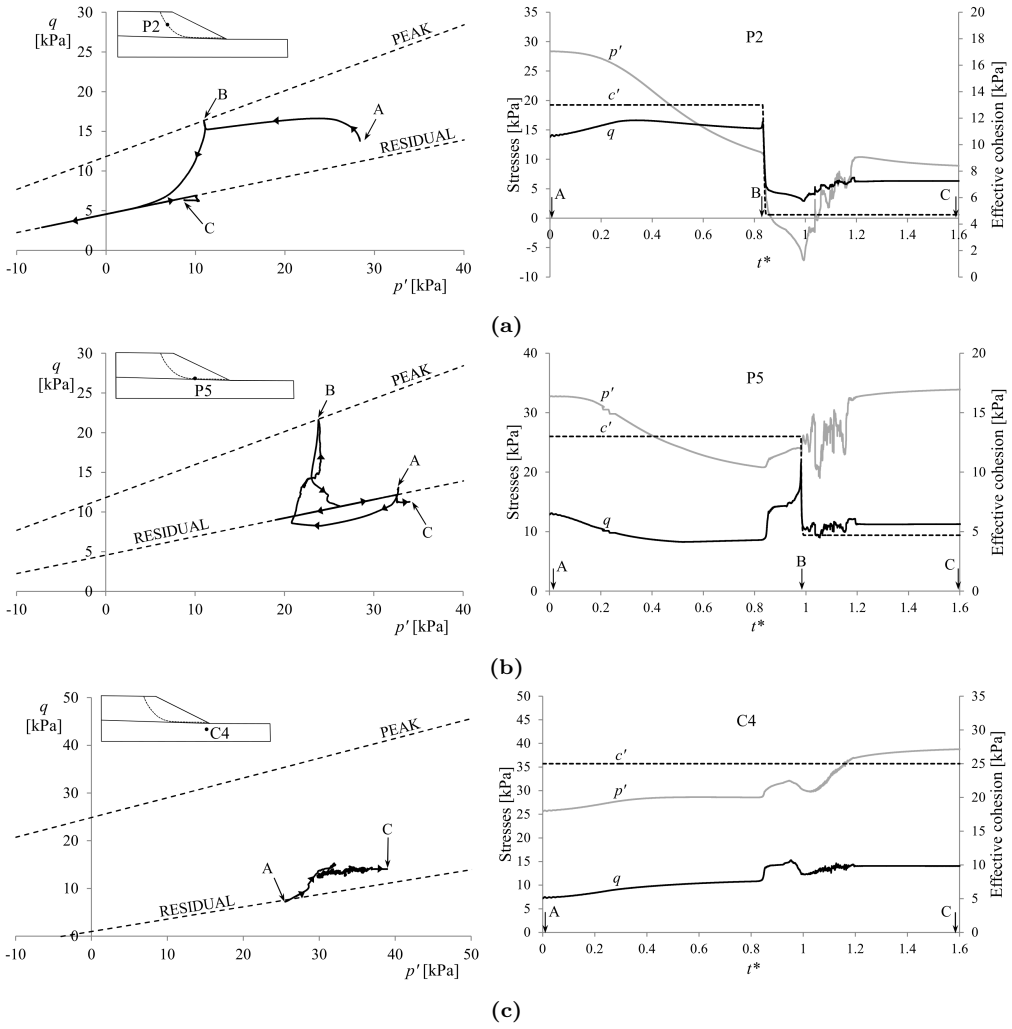

Figure 5.21: Stress paths p'-q of points P2, P5 and C4.

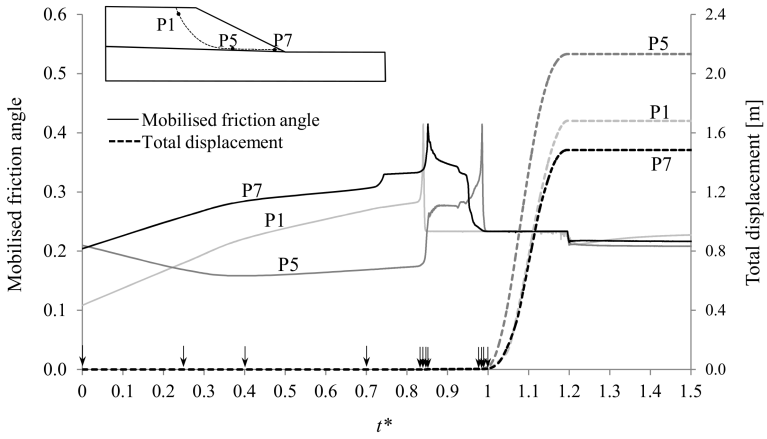

Figure 5.22: Evolution in time of mobilised friction angle and slope displacements before and after failure for points P1, P5 and P7.

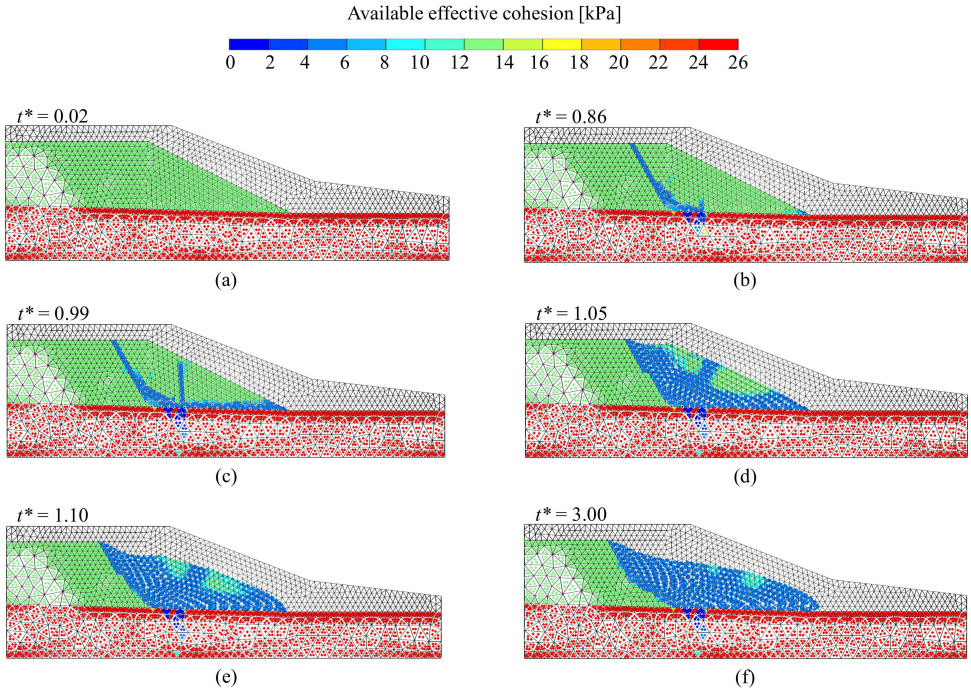

Figure 5.23: Available effective cohesion during the overall instability.

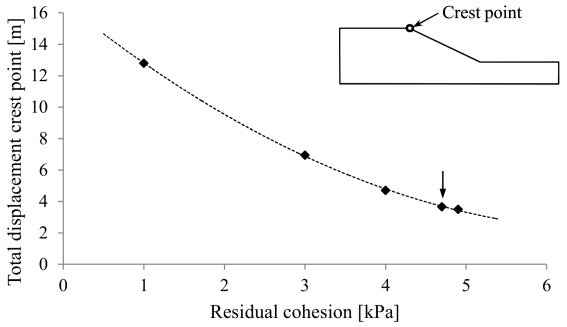

(a)

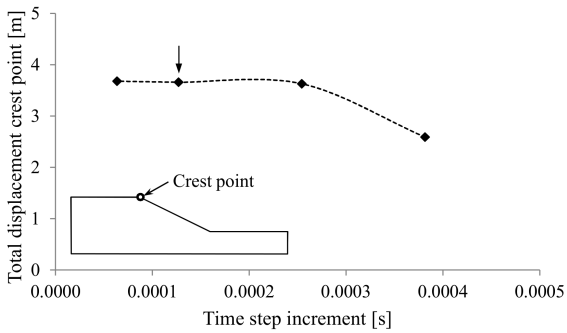

(b)

Figure 5.24: Total displacement of the crest point depending on: (a) the residual cohesion of the weathered Gault Clay layer; and (b) the time step increment of the explicit calculation.

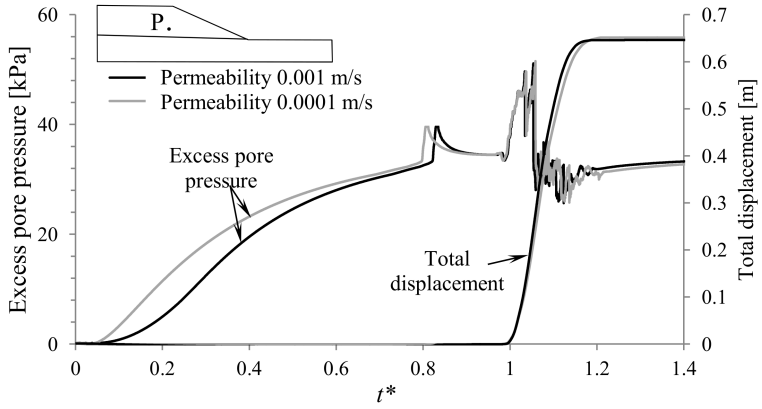

Figure 5.25: Effect of permeability on excess pore pressure and displacement of point P.

5.4 Internal progressive failure in deep seated landslides

5.4.1 Introduction

The kinematics of a landslide motion is fundamental information to approach the mechanisms of deformation and their implication. The expected geometry of the sliding surface and the terrain topography provide useful initial information. However, the complexity of internal interactions within the rock mass, because of the imposed strain field during sliding, is better addressed through appropriate models. This Section focuses on internally sheared compound landslides (see the updated Varnes classification of landslides, Hungr et al. (2014)). Different failure mechanisms (Glastonbury and Fell, 2008a) may be identified in compound slides (Figure 5.26). In these cases the slope response is determined by the generation of internal shears that make it possible to convert the landslide into a kinematically admissible mechanism. In an internally sheared compound slide, the pre-failure stage, defined as the initial motion leading to the development of a continuous rupture surface, requires the continuous shearing not only along the basal failure surface but also along internal planes.

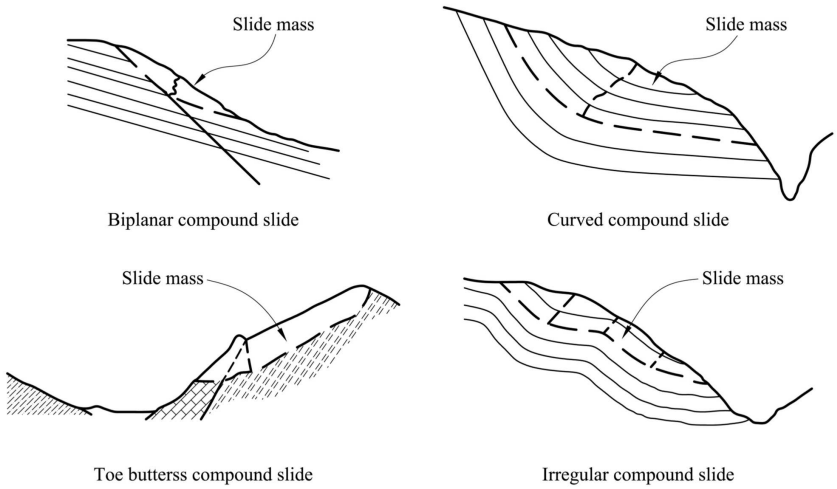

Figure 5.26: Schematic illustrations of the mechanisms of internally sheared compound slides. (Glastonbury and Fell, 2008a)

The onset of failure will be determined by the available strength along the basal and internal shearing surfaces. It is common to find in nature landslides whose basal rupture surface is defined by bedding planes. Others follow low strength strata that have been pre-sheared under tectonic deformation events or previous sliding (some examples are collected and discussed in Glastonbury and Fell (2008b)). This is the case, for instance, of slides associated with synclines or complex rupture surfaces with undulations. These

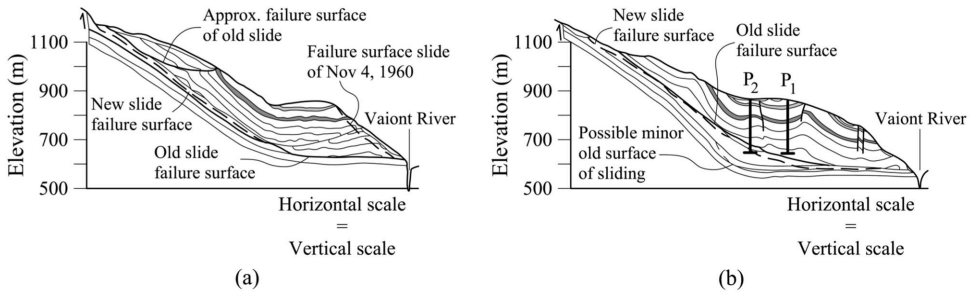

Figure 5.27: Two representative cross-sections of Vajont landslide: (a) Section 2; (b) Section 5. (After Hendron and Patton (1985)). P1 and P2 indicates the position of and length of piezometers.

slopes can remain stable even if the safety factor with respect to the basal slip surface is below unity. This fact can be explained because internal shearing planes require the fracture of intact rock in orientations normal to the major direction of anisotropy (see Figure 5.26). This mechanism implies that the available strength associated with internal shearing is relatively high compared with the resistance offered by basal surfaces. Hence the strength along both the basal surface and the internal shearing bands determine the stability of the slope. The effect of the contribution of the available strength of internal shearing planes is analysed in Alonso et al. (2010b) for the case of a biplanar compound slide.

A strain weakening behaviour is expected when shearing rock masses. A progressive failure mechanism is then expected. It will explain the acceleration of the landslide once the kinematically admissible mechanism is generated and a set of failure surfaces are completely formed. This aspect was also analysed, in a simple manner, by Alonso et al. (2010b).

The relevant effect of internal shearing and internal brittleness was invoked by Hutchinson (1987) to interpret the response of Vajont slide (Hendron and Patton, 1985). Vajont slide is described as an ancient landslide reactivated due to the combined effect of a reservoir impoundment which submerged part of the slope toe and rainfall infiltration. Two representative cross-sections of Vajont slope are plotted in Figure 5.27.

The valley slope follows the shape of a syncline structure which folded Jurassic and Cretaceous strata. The basal failure surface was located in clayey layers subjected to intense shearing in past geological times because of previous instability. Above the sliding surface, finely stratified layers of marl and limestone from the Mälm period were identified. Given the shape of the basal failure surface the slide movement requires the shearing along internal planes crossing the marl and limestone strata as a result of the sharp transition between the upper and steeper failure surface and the lower and practically horizontal part.

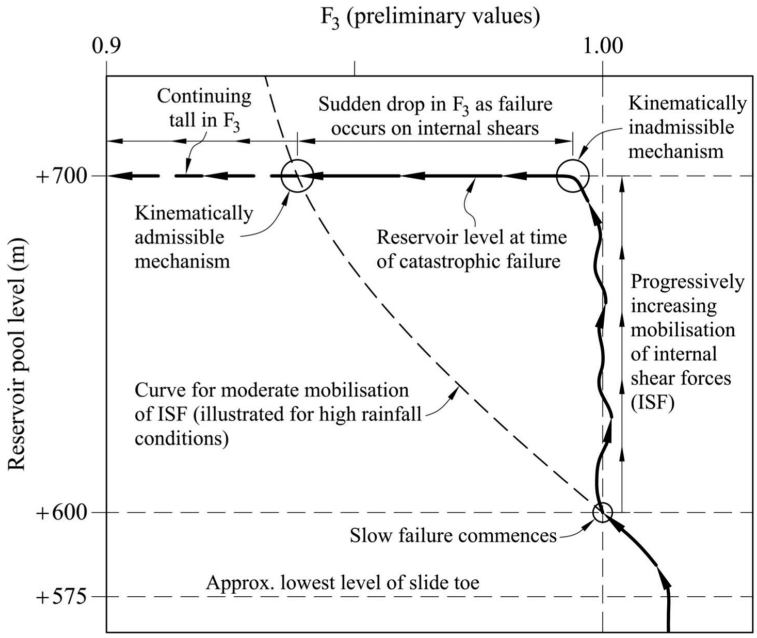

Figure 5.28: Approximate variation of the safety factor with rising reservoir level showing the internal breaking effect and the sudden acceleration resulting from brittle failure on internal shears (from Hutchinson (1987)).

Vajont slide movements were correlated with the impounding of the reservoir. During three years, from 1960 to 1963, the reservoir level rose from 580 m a.s.l to 700 m a.s.l. During this period of time about 4 m of surface displacement were accumulated (Nonveiller, 1987). The increase of the reservoir level up to 700 m led to a violent and accelerated failure. The Vajont slide behaviour was interpreted by Hutchinson (1987, 1994) who included the effect of internal shearing planes. Consider in Figure 5.28, the critical stability condition of Vajont slope when the reservoir water level rose to an elevation of about 600 m a.s.l. Under this condition a safety factor equal to 1 can be formally assigned within the context of overall limit equilibrium. The increase of the reservoir level (from 600 m a.s.l. to 700 m a.s.l.) resulted in a pore pressure build-up and a reduction of the effective shearing strength along the basal plane surface. As a result a progressive increment of the mobilised shearing strength along the internal shearing planes crossing the rock mass is expected in order to maintain equilibrium. Taking into account the brittleness of the Cretaceous limestones and marly limestones, the internal shearing strength will be progressively mobilised. But this process has a limit. Continuous internal shearing planes will eventually develop and a kinematically admissible mechanism will be formed. According to Figure 5.28, at this moment the safety factor drops suddenly. This time instant marks the sudden acceleration of the sliding mass.

The post-failure behaviour in the case of internally sheared compound landslides, in general, and in the case of Vajont, in particular, should be analysed as a new stage of dynamic deformation. Once the residual strength is reached along the most stressed internal shearing planes and the slide accelerates and moves forward, "new" material from the upper wedge having an available strength higher than the residual one, because it has not been mobilised yet, should be sheared in order to fulfil the kinematic conditions of the motion. This stage will be included in the analysis, as well as the new sliding geometry which is continuously evolving with the motion.

The objective of this Section is to analyse the relevance of internal kinematics and the internal degradation of the sliding mass through an appropriate computational tool capable of describing the landslide motion including the onset of the failure and the run-out in the case of a brittle (strain-softening) rock.

The analysis presented here refers to a particular case which is inspired in Vajont landslide. The landslide is triggered by increasing the pore water pressure inside the slope. Before discussing the results obtained, the computational model, details of the analysis and limitations are described. The evolution of the slope deformation during the pre-failure stage and the post-failure response up to the stabilisation of the landslide is described.

Vajont landslide was characterised by the high velocity reached, which was estimated to be about 20-30 m/s after 400 m of displacement approximately. These values were estimated according to the height of the generated wave, which reached 235 m above the reservoir level (Hendron and Patton, 1985). Such acceleration can be explained assuming a drop of the basal shear strength to values near zero. The favourite explanation in a number of published contributions on the subject is associated with the development of frictional heat at the sliding surface which induces the increase in water pressure due to the dilation of pore water as temperature increases (Cecinato and Zervos, 2012; Cecinato et al., 2011; Goren and Aharonov, 2009; Hendron and Patton, 1985; Pinyol and Alonso, 2010a,b; Vardoulakis, 2002; Veveakis et al., 2007). In some contributions heat induced soil plastic collapse of the shearing band is also included in the formulation.

The loss of strength available on the basal failure surface will also be introduced in the analysis presented here. The objective is to calculate the slide run-out and maximum velocity and to compare it with field behaviour. Unlike previous contributions the analysis performed include a massive internal shearing in a brittle rock during the entire motion of the slide, which implies major changes in geometry. The initial and final geometry of Vajont landslide is plotted in Figure 5.29. The mass crossed the valley and climbed up the opposite slope. This stage of the slide resulted also in internal rock shearing which was incorporated into the analysis.

Analyses of Vajont were recently reported by Crosta et al. (2015) and Zhao et al. (2015). The first paper describes a FE modelling adopting an arbitrary Eulerian-Lagrangian method. They pay special attention to the generation of impulse waves in the reservoir. The second paper represents the sliding mass by a DEM model.

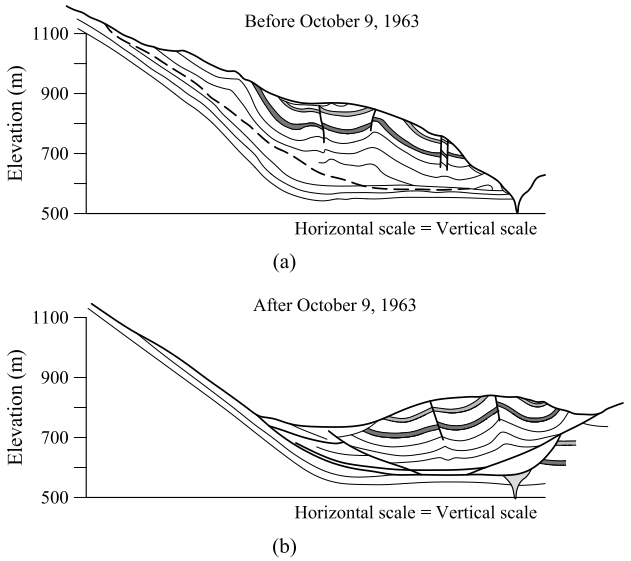

Figure 5.29: Cross sections (a) before and (b) after the landslide (from Del Ventisette et al. (2015))

5.4.2 Description of the model

5.4.2.1 Geometry and numerical parameters

A simplified initial geometry of the Vajont slope but close to the real one is analysed here (Figure 5.30). It is based on a representative cross-section of the valley located 600 m upstream of the dam's position, presented by Hendron and Patton (1987).

The geometry of the problem consists of a rock mass volume lying above a pre-existing

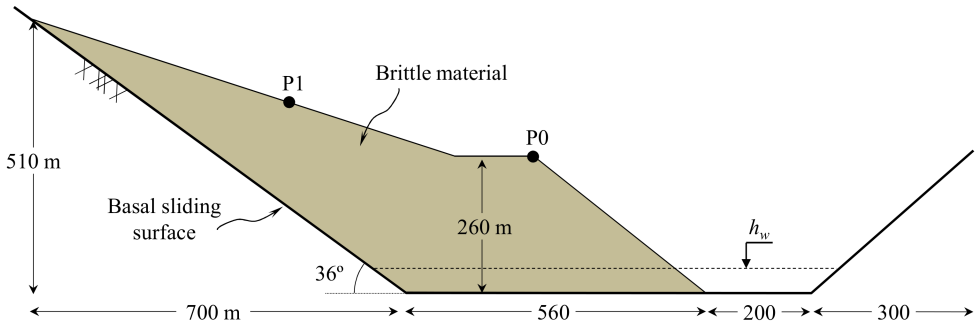

Figure 5.30: Cross-section of the MPM model. Initial geometry. Length in meters.

basal sliding surface (Figure 5.30). Below the sliding surface the material remained unaffected hence it is not studied in this analysis.

The model presented in this work is a thin slice, 20 m wide, made of 4609 tetrahedral elements. All nodes of the computational mesh are contained within the two slice faces. In this way, a plane strain modelling is carried out restraining to zero the perpendicular movement to the slice faces.

Figure 5.31 illustrates the initial distribution of the material points representing the rock mass above the sliding surface. The computational mesh defines the whole domain of the problem. Four material points are initially distributed within the fully filled elements. The mean edge element size where the failure is expected is 20 m. A small value of numerical damping has been considered (α=0.05) in this analysis.

Although the relationship between reservoir level and slide velocity was not entirely clear, it seemed evident that the reservoir filling was the determining triggering mechanism of the Vajont landslide. In fact, the groundwater conditions are poorly known. Only the measurements of a few piezometers distributed along the slide (Figure 5.27) were available (Hendron and Patton, 1987; Müller, 1964). Probably, the water pressures that really controlled the stability of the slope were those prevailing at the sliding surface, but none of the piezometers was deep enough to reach it.

In the MPM model presented here, the water level is maintained horizontal throughout the calculation. This hypothesis is, to some extent, supported by the piezometric measurements, which recorded levels very similar to the water table of the reservoir. This fact indicates that the toe of the sliding mass was permeable, which suggests that this area was intensely fractured.

A drained analysis has been carried out, by means of the MPM mechanical formulation combined with an effective stress analysis. At each time step, the water pressure is

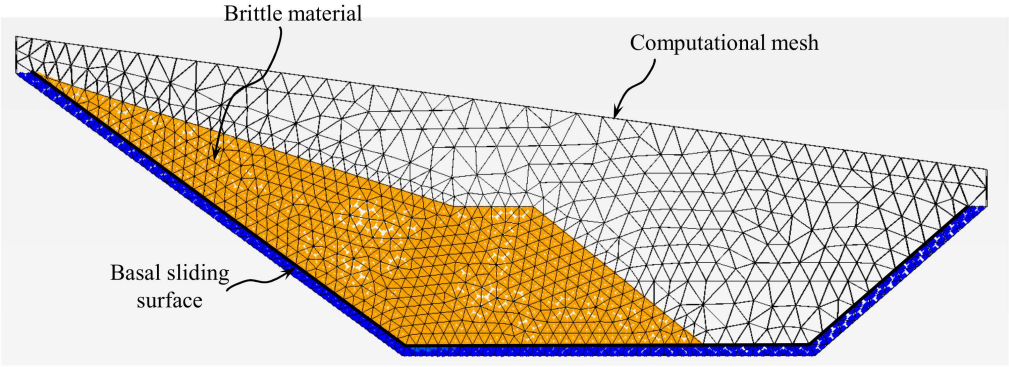

Figure 5.31: Computational mesh and initial distribution of the material points.

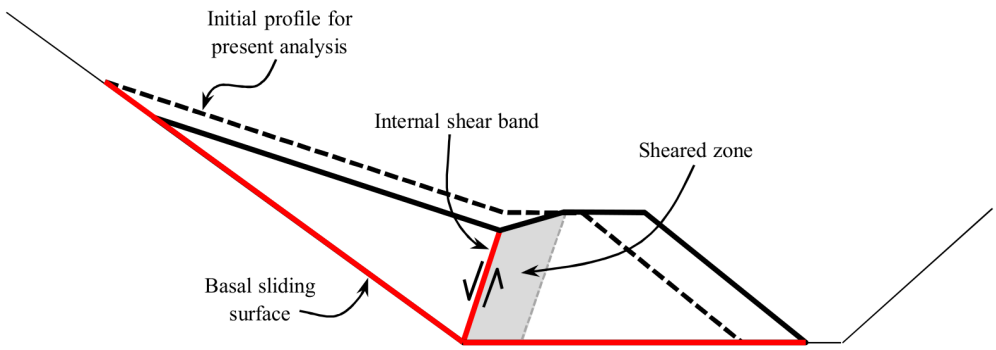

Figure 5.32: Kinematics of sliding. Two-block mechanism and internal rock degradation (a case of compound landslide in a brittle material).

imposed directly on the material points. For a certain level of the reservoir, points located above this level remain with no pressure; meanwhile the water pressure in points located below the water table (including those along the contact surface) corresponds to the hydrostatic profile for the given level at a corresponding time. In addition, free reservoir water is not modelled in this analysis; hence the hydrostatic pressure against the slope is not taken into account. This assumption implies that the model is closer to a limiting state than the actual field conditions. However, this effect is small in this case.

5.4.2.2 Kinematic constrains of the model

Alonso et al. (2010a) analysed the kinematics of Vajont slide. They assumed that all points slid parallel to the basal failure surface with the same absolute velocity. In advanced stages of the post-failure, the motion of the slide implies that mass from the upper wedge becomes part of the lower one (Figure 5.32). During this process, the lower sliding surface accumulates shearing strains. On the other hand, the rock mass arriving to the position of the internal shearing band becomes sheared to a certain extent and moves downhill leaving intact the rock upslope (as indicated in Figure 5.32). According to this scenario, the internal shearing band receives continuously new undisturbed rock as the slide moves downhill. Shearing along the internal shearing band will result in a process of progressive failure which, in an extreme case, will take the rock to residual conditions.

The model presented below will clarify if these assumptions are consistent with the brittle constitutive model of the rock material and the overall geometrical dynamic evolution of the motion.

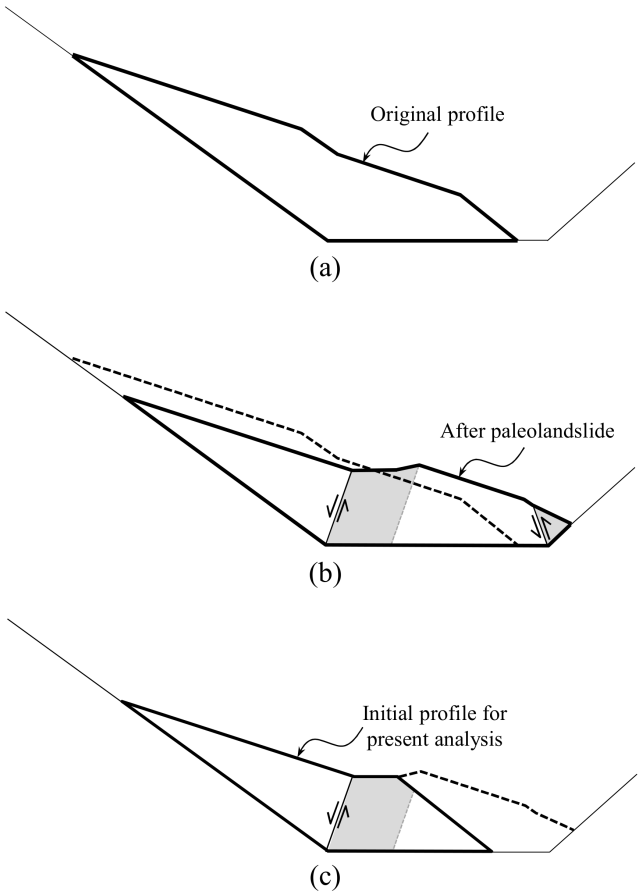

Figure 5.33: Simplified reconstruction of the paleolandslide: (a) original profile; (b) profile after paleolandslide; (c) initial profile for the present analysis after erosion of the toe.

5.4.2.3 Materials and initial state

Vajont rockslide was, in fact, the reactivation of a paleolandslide. Semenza (2001) attempted to reconstruct the past history of the slide and he came up with a set of cross-sections illustrating a possible sequence of events. He interpreted that erosion processes at the toe of the slope caused by the Vajont river could explain the initiation of the failure surface and the past motion of the slope. Figure 5.33 illustrates a simplified reconstruction of the paleolandslide. During the deformation process the slope was subjected to cumulative relative displacements and intense fracturing, because of the kinematic constraints imposed by the kink of the sliding surface. Because the rock strength depends on the deformation history, it could be expected that, at the time of the dam construction, some areas could already be damaged.

Table 5.3: Material parameters of rock mass.

Material parameter	Value
Porosity	0.2
Young's modulus [GPa]	5
Poisson's coefficient	0.33
Solid density [kg/m^3]	2700
Effective peak cohesion [kPa]	1900
Effective residual cohesion [kPa]	300
Effective peak friction angle [°]	42
Effective residual friction angle [°]	36
Shape factor η [-]	150

The nature of the Vajont sliding surface was discussed by Hendron and Patton (1985). They concluded that it was a layer of a few centimetres thick of high plasticity clay. Taking into account the scale of the whole problem (the final displacement of the slope was several hundred meters) the thickness of the shear band is neglected in this work. A contact algorithm proposed by Bardenhagen et al. (2001) and implemented by Al-Kafaji (2013) is used to model the basal sliding surface. This is a frictional contact in which the slip occurs when the tangential force exceeds the maximum allowable threshold determined by Coulomb friction.

Considering the past history of the landslide it is clear that the residual friction angle of the clay layers was the most relevant parameter controlling the strength of the basal sliding surface. Most of the early Vajont stability analyses concentrated on determining the basal sliding strength necessary to maintain the equilibrium of the slope (Kenney, 1967; Mencl, 1966; Skempton, 1966). Some of them are based on classic LEM in which the basal stability angle (φ'_b) was estimated in the range of 18-28^o. These values are not consistent with laboratory tests. Some authors (Hendron and Patton, 1985; Tika and Hutchinson, 1999) examined the shearing strength by direct and ring shear tests on clay samples from the basal sliding surface and estimated that the static residual friction angle was around φ'_b=10^o. Hendron and Patton (1985) suggested that the rugosity of the failure surface could amount to two additional degrees and proposed φ'_b=12^o as a suitable choice. In this analysis φ'_b=12^o has been used in the contact algorithm.

Above the basal sliding surface, marls layers were identified. Lying above marls, there were limestone strata (Semenza, 2001). In this model, a unique rock material has been used to simulate the whole rock volume. Following Hoek (2007), Alonso et al. (2010a) approximated the strength envelope of the material above the sliding surface. The effective Mohr-Coulomb strength parameters were determined for a range of normal stresses of 2 MPa (c'=787 kPa and φ'=38.5^o). They also analysed the static equilibrium of the slide by using a simple two-block model and suggested a range of effective strength values. These strength parameters are rough average approximations.

Rock material is typically characterised by brittle behaviour. In this work the Mohr-Coulomb peak envelope is defined by the strength parameters c'_p=1900 kPa and φ'=42^o;

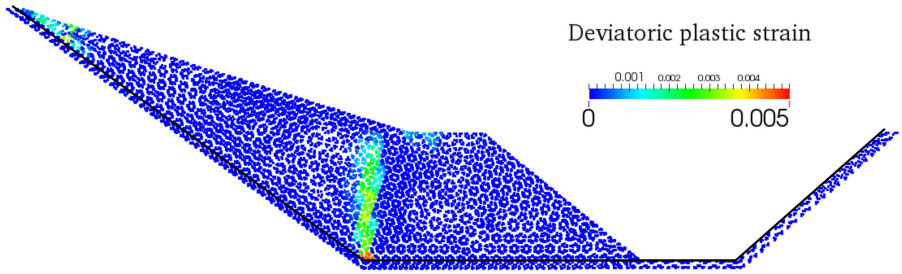

Figure 5.34: Scheme of deviatoric plastic strain field under gravity loading (initial state).

the residual strength of the rock is defined by c'_p=300 kPa and φ'=36^o. The shape factor adopted to control the rate of strength decrease is η=150. Other material parameters are summarised in Table 5.3. Even if there are uncertainties on an appropriate set of average "in situ" parameters (Superchi, 2012), the selected set offers a good approximation to discuss the effect of internal degradation of the material during the landslide motion.

Reproducing the initial stress state in the field is a difficult task in the absence of data. However, trying to exactly reproduce the processes that have affected the rock mass during its past geological history is out of the scope of this work. In this analysis, a gravity loading has been applied to the intact material in order to calculate an initial stress state. It seemed reasonable to consider the rock weight as the most relevant factor to determine the initial stress state in the slope.

In the model presented below, a gradual gravity loading is applied to the intact material. As a result, some points above the kink are sheared accumulating plastic and a two-block kinematically admissible mechanism is initiated. The strength is reduced locally along this "initial" internal shear band and its mean value becomes intermediate between peak and residual states (Figure 5.34). Finally, a stable geometry is obtained. During this process, the level of the reservoir is maintained at the position of the horizontal lower basal sliding surface (h_w=0 m). As a consequence, the rock located within the current internal shear band damages according to the brittleness of the material.

Because the paleolandslide was not simulated, the toe of the slope remains under peak conditions. The stability of a compound slide is essentially controlled by the strength of both the basal surface and the internal shearing band. Therefore, the strength of the rock mass that has already been sheared at the kink does not play a significant role in the stability of the slope.

Figure 5.34 shows the accumulated deviatoric plastic strain after gravity loading. It is localised along an almost vertical band that initiates at the existing kink of the basal surface and progresses a significant distance upwards.

5.4.3 Numerical results

5.4.3.1 Dynamic behaviour and internal degradation of rock mass

According to Hendron and Patton (1985); Hutchinson (1987) (Fig.5.28), Vajont slide reached critical stability conditions when the reservoir water level was about 20 m above the lowest level of the slide toe. However, surface measurements indicated an accelerated movement, for the first time, when the water level was around 70 m. Immediately afterwards, the reservoir was partially emptied in order to stabilise the slope. Later on, the reservoir level was increased and decreased again. Finally, the fast landslide occurred when the reservoir elevation was about 120 m.

In this work, only an initial increase (60 m) the water level has been simulated and no further decrease of reservoir elevation has been considered. For this reason, the reservoir level was maintained at 60 m. In the model presented here, the water level is increased in intervals of 10 m up to failure (Figure 5.35). Afterwards, it is maintained constant thereafter until stabilisation of the motion.

The movement of point P0 (Figure 5.30) is illustrated in Figure 5.36. Note that the displacement is in meters and the scale is logarithmic. As the water pressures increase within the slope, P0 is stable. When the water level reaches a value of 60 m, the displacement of P0 increases rapidly leading to a final movement of 8.5 m. In the same figure, the movement of point P1, located at the upper sliding wedge, is also represented. It is clear that both points (P0 and P1) displace the same amount, which supports the kinematic hypothesis suggested by Alonso et al. (2010a).

Water level rise causes a reduction of the mean effective stresses within the slope, leading more points to reach the yield function envelope. The strain softening behaviour reduces the available strength and the progressive internal degradation of the rock mass continues. This mechanism was identified as a progressive failure phenomenon by early contributions (Bishop, 1971; Cooper, 1996; Skempton, 1964). The displacement of the slope increases slowly during this process whereas a shearing plane, dividing the sliding rock mass in two well defined wedges, is being formed. When h_w=60 m, the admissible kinematic mechanism is completely developed and the slope accelerates immediately afterwards.

In Figure 5.37 the evolution of plastic strain is illustrated at five different times. As water pressure increases, the initial internal shear band is formed (Figures 5.37a, 5.37b). It can be distinguished in Figure 5.37c. In Figure 5.37d the reservoir level reaches 60 m and just afterwards the instability occurs. Figure 5.37e corresponds to the final stabilised geometry of the slope, in which a noticeably wider shear band can be observed. A moderate change in the direction of the shearing band is also noticed. The initial shearing band (Figure 5.34 and 5.37a) is subvertical. The shear band at the end of the progressive failure (Figure 5.37e) follows closely the bisector plane of the two basal sliding planes.

In order to analyse the progressive failure mechanism developed within the internal shear

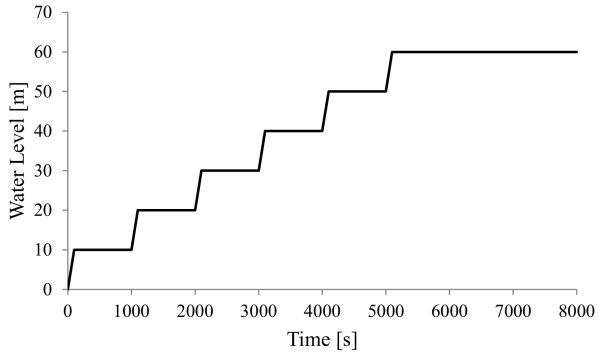

Figure 5.35: Water table evolution.

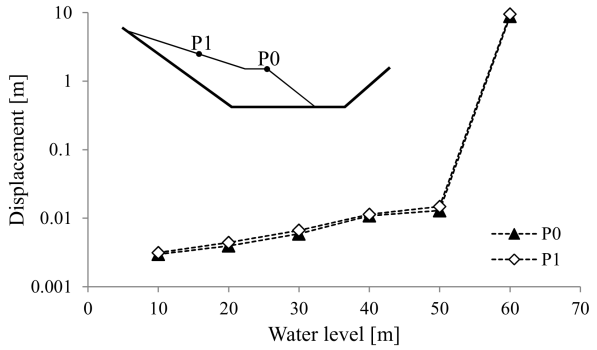

Figure 5.36: Run out of the slide. Variation of absolute displacements of points P0 and P1, in terms of reservoir water level.

band just before the instability, the mobilised friction angle $\widehat{\varphi}'$ (Eq.5.10) has been determined at 8 material points distributed along the internal failure surface (Fig.5.38). The curves indicate the evolution at different times of the calculation. It is important to highlight that the available strength at the initial state (t_0) depends on the material point because some points have previously plastified during the gravity loading. As h_w increases, the material degrades progressively upwards. Point 8 is the last one to reach the peak strength envelope just when h_w=60 m (t_4). Finally, when the motion begins the strength of the whole surface is reduced to residual conditions (t_5). Note that the mean available strength at the beginning of this process is smaller than the peak value due to previous accumulated shearing.

The relationship between run-out and velocity of the moving mass is presented in Figure 5.39. The slide reaches a maximum velocity of 0.5 m/s and stops after a displacement of 8.9 m. Following the classification system proposed by the International Union of Geological Sciences Working Group on Landslides (1995), this can be considered as "very rapid" landslide (velocity limits: 0.05-5 m/s). The calculated run-out-velocity relationship

is very similar to the relationship calculated by Alonso et al. (2010a) in which the dynamic motion equation for two interacting wedges was solved.

5.4.3.2 Reduction of basal surface friction angle

Vajont slide moved forward approximately 450 m in a few seconds, reaching an estimated velocity of 20-30 m/s (Hendron and Patton, 1985), which is an "extremely rapid" motion. The main relevant question is why the sliding mass accelerated so much. The maximum speed in the model discussed in the previous section is about two orders of magnitude lower, despite the effort to reproduce the real case.

Authors tried to explain the increase in speed in different ways. One of them is the effect of strain rate on clay friction. Tika and Hutchinson (1999) tested at different strain rates remoulded specimens from clay layers belonging to the sliding surface. They found that friction angle decreases with strain rate and they reported minimum residual values of φ'_b=5^o. Many authors have reported in recent years the results of high velocity shearing (limited to around 1.3 m/s in most cases) in a variety of soil types (Di Toro et al., 2006; Ferri et al., 2010; Han and Hirose, 2012; Liao et al., 2011; Mizoguchi et al., 2007; Yang et al., 2014) tested both saturated and unsaturated. The change in friction angle with shearing rates is however a controversial issue discussed in some detail in Alonso et al. (2015).

The most accepted explanation for the extremely high sliding velocity is associated with the development of frictional heat at the basal sliding surface (Nonveiller, 1987; Pinyol and Alonso, 2010a; Uriel Romero and Molinia, 1977; Vardoulakis, 2002; Voight and Faust, 1982). The initiation of the movement and the frictional work input on the sliding shearing band results in an increase in temperature. Then, water pressure within the clayey band increases and the available effective stress along the basal sliding surface is reduced to near-zero values and shearing strength vanishes (which is equivalent to the condition $\varphi'_b \approx 0^o$).

In order to analyse the effect of the basal strength on the sliding speed two additional calculations have been carried out. Starting at the stabilised geometry (described in the previous section), and maintaining the water level at h_w=60 m, the effective friction angle imposed along the basal contact surface was reduced from φ'_b=12^o to φ'_b=5^o in the first calculation, and to φ'_b=0^o in the second one.

Figure 5.40 shows the results for the two analyses. The evolution of the accumulated deviatoric plastic strain is presented. The two slides accelerate immediately after the reduction of the basal contact strength. Mass from the active wedge enters into the internal shearing zone. Strength in the band reduces due to the brittle behaviour of the rock and, this degraded mass becomes part of the passive wedge as the motion proceeds. When the mobilised mass reaches the opposite side of the valley another shearing zone is developed at the position of the kink of the basal surface. Now, the toe of the slope,

which until now has remained at peak strength, is sheared as it climbs the slope. The smaller the basal strength, the longer the upward displacement of the rock mass before getting a new stable geometry.

In order to illustrate the degradation of the rock material during the post-failure stage (when φ'_b=0^o), 13 material points located 130 m above the basal surface and distributed along the landslide have been analysed (see Figure 5.41). Figure 5.42 shows the evolution of the mobilised friction angle. Note that points 5 and 6 are initially plastified because they are located within the shear band developed during the increase of the water level in the reservoir. The upper wedge is sheared as it approaches the position of the kink (Figure 5.42a). When the slope reaches the opposite side, the material points from the lower wedge plastify as well (Figure 5.42b). Finally, points 7 and 8, located in the central zone, remain in elastic conditions.

Figure 5.43 shows the relationship between run-out and the velocity of the moving mass in the two calculations. For φ'_b=5^o, the slide reaches a maximum velocity of 14 m/s and it moves forward 344 m. If the basal friction vanishes (φ'_b=0^o), the mobilised mass moves faster, reaches a maximum velocity of 25 m/s and the calculated final run-out is 491 m. This data is consistent with the accepted behaviour of Vajont landslide.

5.4.4 Discussion and specific conclusions

This Section provides some insight into the role of internal shearing to explain the motion of compound landslides. The example analysed, directly based on Vajont geometry, is typical of an initial syncline folding of strata followed by river erosion. In cases of reactivation of previous instability, internal shearing plays a key role to stabilise the impending motion. The limit is the exhaustion of the strength in a shearing area. If the material involved is brittle, the internal failure results in a progressive failure mechanism.

In the example presented, the internal failure process is complex because the initial equilibrium state resulted in some post-peak strain softening at a few locations. Further loading (in our case controlled by a rise in water level) resulted in a progressive failure which essentially evolved from the "kink" defined by the geometry of the basal slip surface towards the surface of the slope. Once the last point resisting under peak conditions in the internal shear band advances into strain softening, the failure mechanism becomes kinematically admissible. Afterwards, the slide acceleration begins.

An interesting outcome of the analysis presented is that the resulting kinematic mechanism is essentially defined by a single localisation plane which, after some displacement, can be defined as the bisector of the two planes defining the basal sliding surface. This outcome was not obvious because many kinematic mechanisms may explain the motion of the geometry analysed. However, details of the precise continuity and irregularities of the sliding plane will most likely control the geometry of the kinematic mechanism and the position, orientation and number of internal shearing surfaces.

The calculated thickness of the internal shearing plane was significant (20-50m) but this result may be a consequence of the size of elements of the computational mesh. Note also that the rock was discretised as a homogeneous elastoplastic brittle material with no internal structure: bedding planes and fractures. They could play a significant role in the development of kinematic mechanisms. The computational method (MPM), inherently dynamic, provides interesting information on the post-failure motion of the slide. Velocity and run-out are calculated, as well as the evolving geometry during the motion.

There was a special interest in checking if the known velocity and run-out of Vajont landslide could be simulated by a combination of internal rock brittleness and a non-zero friction angle at the sliding surface. In fact, a number of previous analyses which rely on thermal pressurisation along the basal sliding surface indicated that a zero shear strength was required to reproduce the actual observation. The present contribution confirms that this is the case, even if a significant brittleness is assigned to the internal shearing and even if the kinematic sliding mechanism is simulated with a reasonable accuracy.

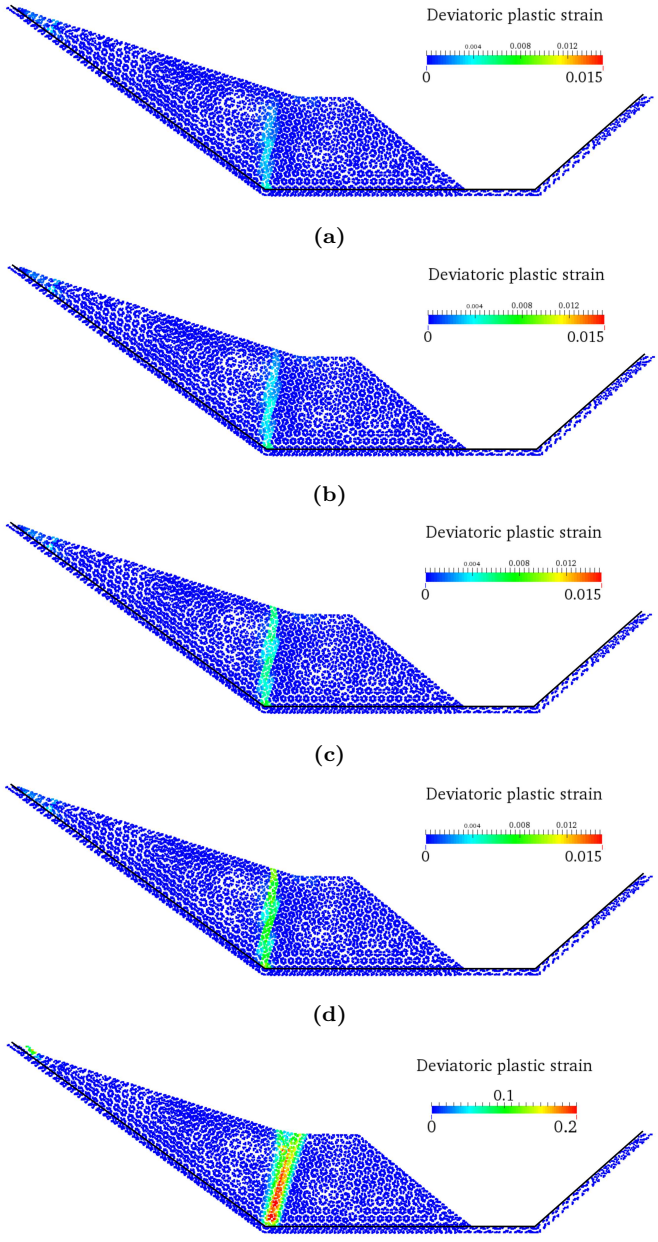

Figure 5.37: Contours of deviatoric plastic strain at different positions of the water level. (a) h_w=50 m; (b) h_w=54 m; (c) h_w=57 m; (d) h_w=60 m; (e) final stable geometry.

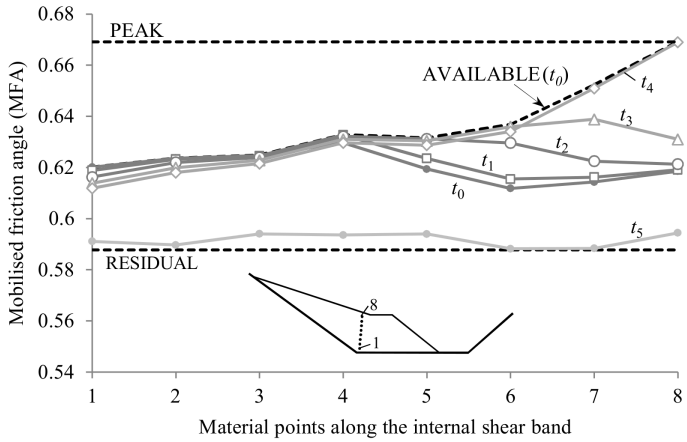

Figure 5.38: Progressive failure. Evolution of mobilised friction angle along the internal shear band at different times (in terms of water level): (t_0) initial state; (t_1) h_w=20 m; (t_2) h_w=40 m; (t_3) h_w=50 m; (t_4) h_w=57 m; (t_5) h_w=60 m.

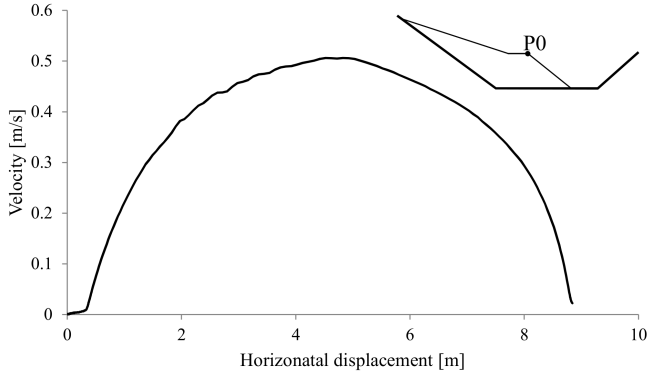

Figure 5.39: Calculated run-out and slide velocity of point P0.

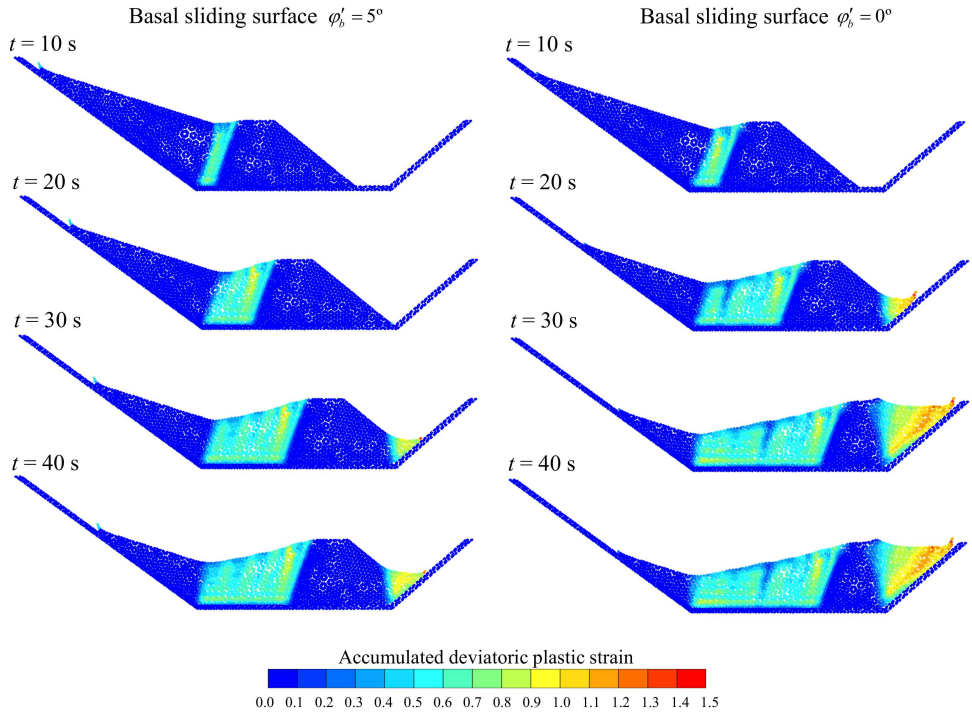

Figure 5.40: Accumulated deviatoric plastic strain at different times. Effect of effective friction angle at the basal sliding surface.

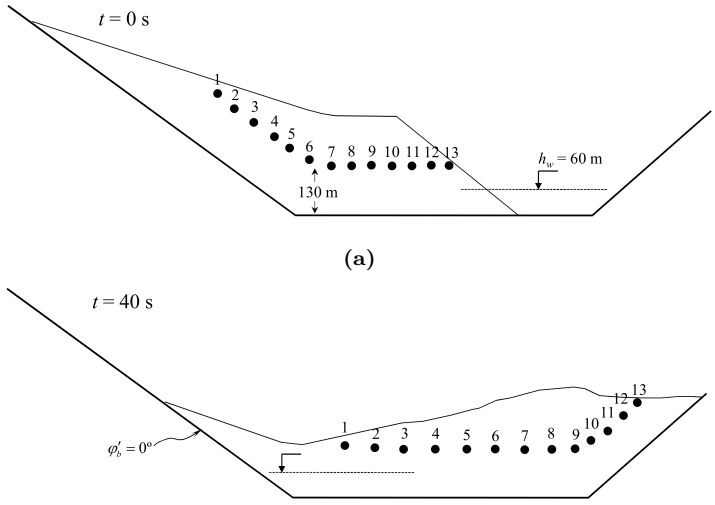

Figure 5.41: Location of thirteen material points (a) just before the vanishing (φ'_b=0^o) of the basal friction angle and (b) at the final stable geometry.

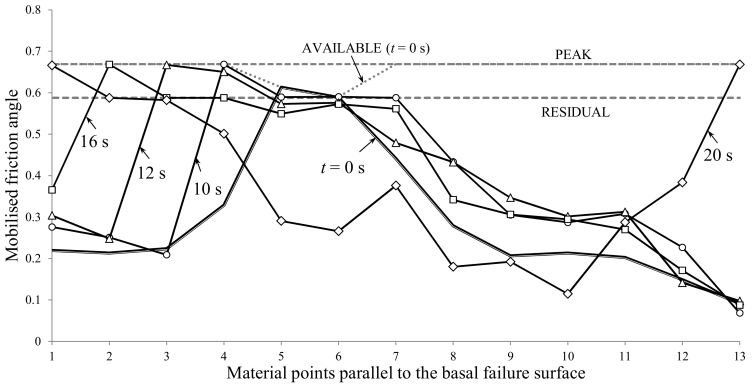

(a)

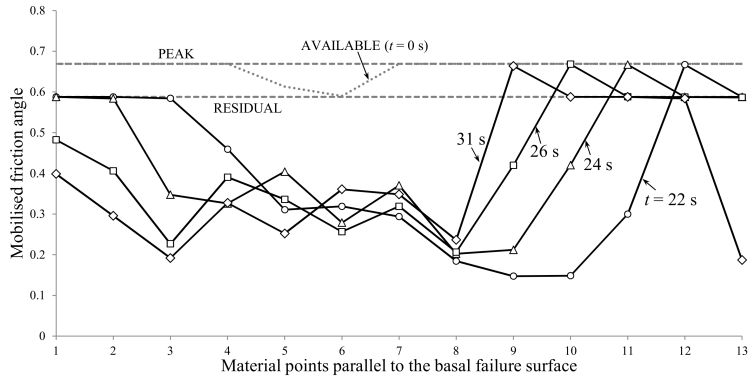

(b)

Figure 5.42: Rock degradation for φ'_b=0^o. Evolution of mobilised friction angle at thirteen material points distributed along the slope, parallel to the basal failure surface (indicated in Figure 5.41). (a) Initial degradation of the upper wedge; (b) toe degradation.

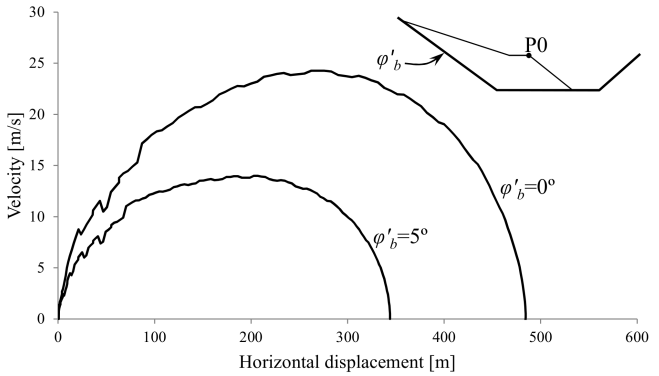

Figure 5.43: Calculated run-outs and sliding velocity. Effect of friction angle at the basal sliding surface.

5.5 Numerical slope instability problem. Effect of brittleness on run-out

In this Section a theoretical slope is analysed, in which he shear band propagation and shear stress distribution are discussed. However, the focus here is on exploring the material properties controlling the run-out distance and velocity of the unstable mass. The influence of the brittleness of the material on the triggering of instability and run-out is evaluated by means of a parametric study varying peak and residual strength. Correlations between run-outs and brittleness are presented. The results are discussed with the aim of deriving practical conclusions.

5.5.1 Description of the model

The instability of a slope, 6 m high and 37°steep, is analysed here. The slope failure was triggered by increasing the pore water pressure at the lower boundary simulating a phreatic level rise. This is a plane strain simulation; the lower boundary was fixed and horizontal displacements along vertical contours were prevented. The water pressure is zero along the slope surface, the lateral contours are impermeable and saturated conditions are considered during the calculation. The mesh was refined in the region where the failure is expected in order to get more accurate results and to optimise the computational cost.

Initially the slope remains in equilibrium. The calculation starts with the application of a 40 kPa increase in pore pressure along the lower boundary during 1 second. Afterwards, the water pressure on the boundary is maintained constant during the entire simulation.

The Mohr-Coulomb strain softening constitutive model described in the previous section was used to simulate the brittle behaviour of a soil. The properties of the material are presented in Table 5.4 and a shape factor of 500 is adopted. Since permeability is not a relevant parameter in the analysis presented here, a high value (0.001 m/s) has been

Table 5.4: Soil parameters of the slope.

Soil parameter	Value
Porosity [-]	0.2
Permeability [m/s]	0.001
Young's modulus [kPa]	20000
Poisson's coefficient [-]	0.33
Effective peak cohesion [kPa]	5
Effective residual cohesion [kPa]	0.5
Effective peak friction angle [°]	35
Effective residual friction angle [°]	20
Shape factor η [-]	500

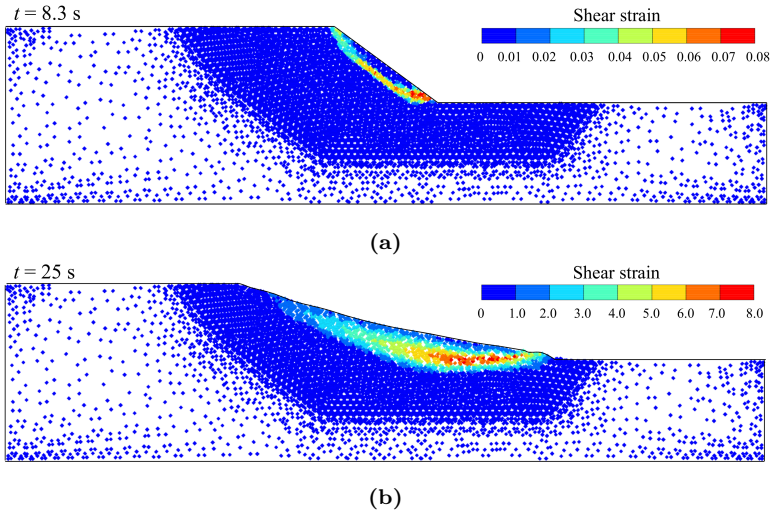

Figure 5.44: Distribution of the shear strain at different times. Note the different scales of the shear strain.

adopted to simulate the slope failure in a relatively short time.

In order to reduce numerical instabilities, a damping force has been included in the momentum balance equation. It is proportional to the corresponding unbalanced force by means a proportional factor α=0.05 (Table 5.4).

The increase of pore pressure reduces the effective stresses in the slope. This fact leads to some points to reach peak conditions. The strain softening effect decreases progressively the strength parameters of the plastic zones down to the residual yield surface. As a result, the gravitational stresses are sufficient to induce a progressive failure in the case analysed.

Failure development is illustrated in Figure 5.44 by representing the shear strain contours at two different times. At 8.3 s a shear band localises providing a failure mechanism and afterwards the instability initiates. During the movement, the shear band spreads. Finally, when the new geometry becomes stable, a wider shear zone is observed (Figure 5.44b). Figure 5.45 shows the final displacements field. In this case, the achieved maximum displacement is 9.1 m and the displacement between the toe of the initial and the final slope geometries is 9.5 m.

A similar analysis of the progressive failure mechanism presented in previous sections has been carried out here (see Figure 5.46). Figure 5.46a indicates that, in this case, the degradation of the material initiates at the foot of the slope and propagates upwards. It is clear that points along the failure surface reach the peak yield envelope at different moments depending on the evolution of the progressive failure mechanism. Because of that, the stability of the slope will not be strictly controlled by the material peak strength,

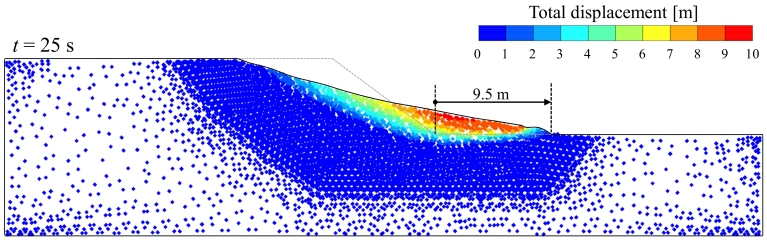

Figure 5.45: Distribution of the calculated total displacement at 25 s after the initiation of the failure. The maximum displacement of the toe is also indicated.

but, rather, by the maximum mean strength that can be mobilised along the slip surface, which is a value intermediate between peak and residual strengths.

In Figure 5.46b, the evolution of the progressive failure is represented in terms of the average mobilised friction angle. A very similar behaviour is observed in modelling of the Selborne experiment (Sec.5.3). Due to the increase of water pressure in the slope, the mean friction angle increases up to a maximum value. Afterwards, there is a drop of the available mobilised strength. Then, the progressive failure develops maintaining the mean mobilised friction angle approximately constant. This process ends abruptly at t=8.6 s, when the final point in the failure mechanism reaches peak conditions and is softens down to residual conditions. This leads to the onset of instability and the motion begins.

Figure 5.47a presents the time evolution of the effective cohesion and the displacement experienced by point P5. Figure 5.47b shows the stress path of P5. Initially, stress conditions are given by point A in Figure 5.47b. The slope remains stable. Due to the increase of pore pressure imposed at the bottom boundary, the effective mean stress decreases and, at 8.2 s (indicated by point B in the figure), the material point reaches the peak yield surface. The material point plastifies, triggering a sudden drop of the cohesion (controlled by η), from peak to residual value. At t=8.6 s (the time required to develop the global failure mechanism) the slope becomes unstable and the displacement increases significantly. At t=15 s, after 5 m of displacement, the material point stops when equilibrium has been established for the final geometry. Beyond t=15 s the stress state of point P5 unloads slightly and enters into the elastic domain.

5.5.2 Parametric study

A parametric study was carried out with the aim of studying the slope stability and the post-failure behaviour as a function of the soil brittleness.

The brittleness of the soil has been defined in terms of the brittleness index I_B (5.12) proposed by Bishop (1967). It is a measure of the decrease of the shear strength from a

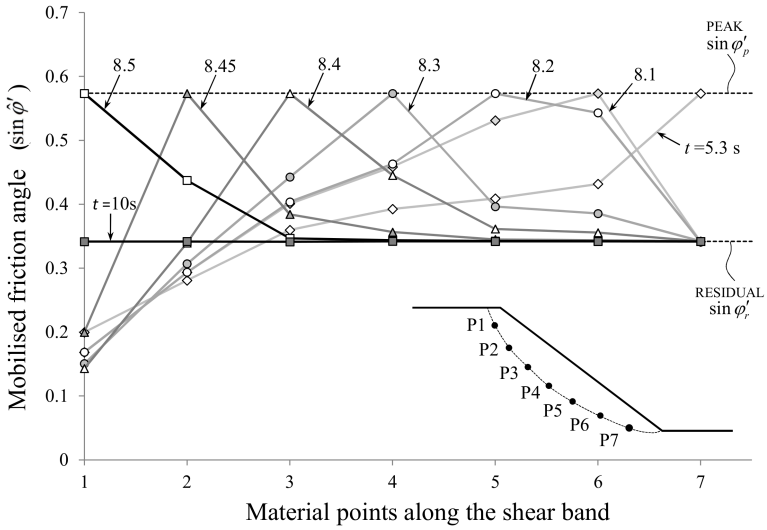

(a)

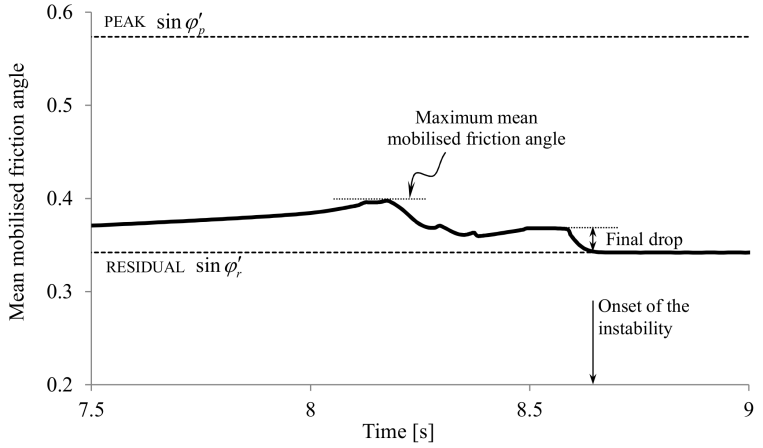

(b)

Figure 5.46: (a) Distribution of the mobilised friction angle along the initial shear band at different times. (b) Evolution of progressive failure in terms of mean mobilised friction angle.

peak value (Eq.5.13) to a residual one (Eq.5.14) and it ranges from 0 to 1.

$$I_B = \frac{\tau_p - \tau_r}{\tau_p} \tag{5.12}$$

Shear strengths cam be calculated as

$$\tau_p = c'_p + \sigma_n{}' \tan \varphi'_p \tag{5.13}$$

$$\tau_r = c'_r + \sigma_n{}' \tan \varphi'_r \tag{5.14}$$

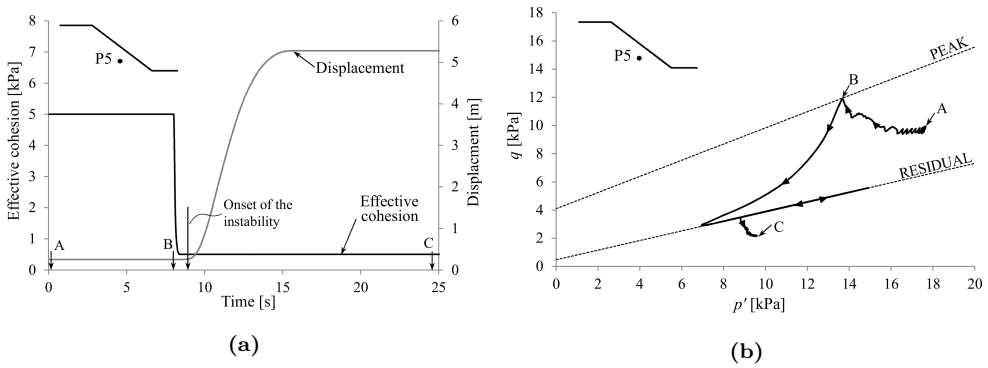

Figure 5.47: Variable evolution of a point located on the sliding surface. (a) Effective cohesion evolution and displacement calculated. (b) Stress path in terms of deviatoric stress q and mean effective stress p'.

where $\sigma_n{}'$ is the effective normal stress in a particular point on the sliding surface.

A total of 82 simulations for different values of peak and residual strength were run. The initial geometry is the same for all of them and it is identical to the case described previously. Two different excess pore pressures (ΔP) were introduced at the lower boundary, 40 and 70 kPa to examine the effect of the destabilising action on the slide run-out and velocity. Common material properties were given in Table 5.4. The strength parameters that vary for each particular case are indicated in Tables 5.5 and 5.6.

A representative value of I_B is calculated for each simulation that becomes unstable. When the slope remains stable, determining a particular I_B is not possible because no sliding surface can be defined. Note that I_B depends on $\sigma_n{}'$ (Eq.5.12, Eq.5.13 and Eq.5.14). Therefore, different values of effective normal stress may lead to different values of brittleness. In order to characterise each case with a unique value of I_B, $\sigma_n{}'$ has been calculated as the average of the normal stresses to the sliding surface of a set of material points distributed along the initial failure mechanism at the moment in which the global failure develops.

In order to evaluate the post-failure slope response, the run-out is an important parameter to determine. Published data on run-out, based on simple approaches, consider a landslide represented by the centre of mass of the total mobilised volume, hence the run-out calculated in those cases is considered as the movement of such a point (Hsü, 1975; Sassa, 1988; Scheidegger, 1973). However, these models do not consider the changes in geometry that may experience the moving mass during the instability.

In this Section, run-out is defined as the distance between the toe of the initial slope and the toe of the slope after failure once equilibrium has been re-established. This is a convenient parameter to evaluate the extent of the slide and it is directly related to the associated risk. It is important to highlight that this definition is not necessarily equivalent to the maximum displacement achieved by any point of the slope.

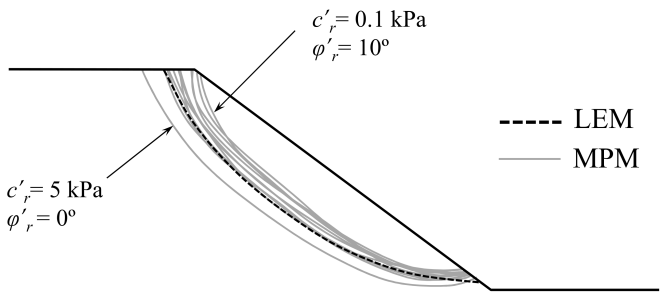

Figure 5.48: Comparison between the initial failure mechanisms obtained using MPM and LEM analysis.

5.5.3 Change in residual strength

Accepting a common peak strength of c'_p=5 kPa and φ'_p=35°, 61 simulations have been carried out in order to study the effect of residual strength on the onset of instability and post-failure behaviour. A list of these simulations is presented in Table 5.5, in which values of I_B and run-out are also indicated.

A comparison between initial failure mechanisms obtained with MPM and with a Limit Equilibrium Method LEM (Morgensten-Price) is shown in Figure 5.48. The shape of the failure surfaces is very similar to LEM's prediction. However, the depth of the failure surface slightly depends on the case simulated, ie.: the higher c'_r, the deeper the failure surface.

Figure 5.49a shows the correlation between run-out and I_B. The results converge in a unique curve which indicates that run-out increases with I_B. When I_B exceeds 0.83, the toe of the mobilised mass reach the right boundary of the domain, which is located at a distance of 26 m from the initial toe. Therefore, the maximum run-out calculated is limited to 26 m. Moreover, when $I_B > 0.75$, mobilised material points abandon the dense computational mesh and enter into a rougher mesh. In these cases the integration becomes less accurate and results may be slightly less reliable.

If the maximum displacement achieved by a point of the slope is considered instead of run-out, a similar trend but much more dispersion of the results is observed in Figure 5.49b. However the dispersion is significantly higher in this case.

Different values of ΔP barely affect the I_B-run-out relationship. However, the minimum brittleness required to induce instability ($\hat{I}_B$) varies with ΔP. If ΔP=40 kPa, $\hat{I}_B$ is around 0.5 ($\hat{I}_B^{40}$), whereas for ΔP=70 kPa it decreases to 0.22 ($\hat{I}_B^{70}$). The higher intensity of the triggering mechanism, the lower is the I_B to induce instability.

Figure 5.50 shows the final geometries of two simulations characterised by the same value

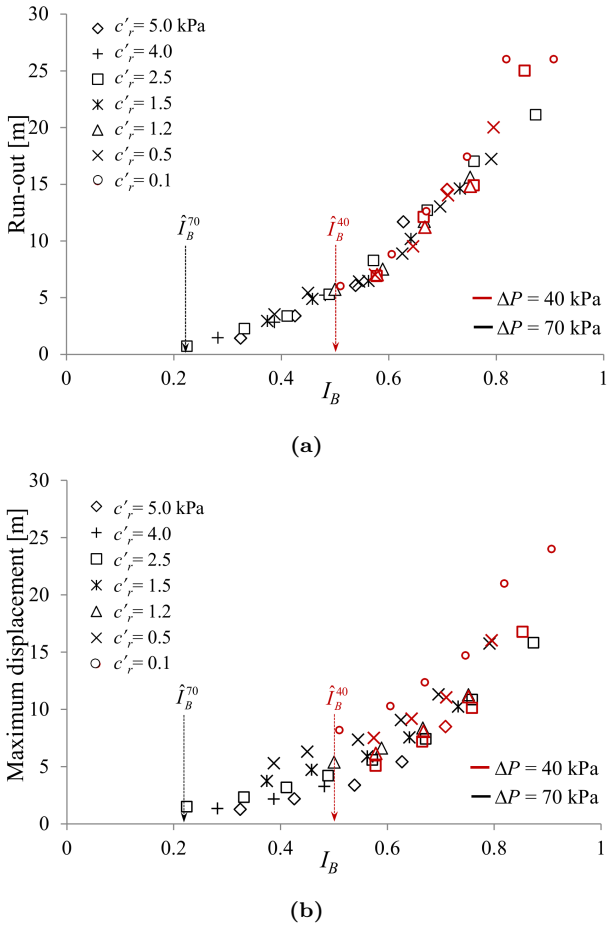

Figure 5.49: (a) Relationship between run-out and I_B. (b) Relationship between maximum displacement achieved by a point and I_B. All simulations have the same peak strength (c'_p=5 kPa and φ'_p=35°). P indicates the imposed pore water pressure which induced the failure.

of I_B. Despite having a similar value of the run-out, the distribution of final displacements is very different due to the different values of the residual cohesion. Materials having a low residual cohesion c'_r lead to shallow failures unlike the deep failures associated with higher residual cohesion.

Figure 5.51 illustrates the stable geometries after failure for 5 simulations with the same c'_r=0.5 kPa. The same pattern of displacements is observed in all the cases. However, the run-out increases and the slope becomes flatter with increasing values of brittleness.

In order to highlight the dynamics of the failure, Figure 5.52 show the evolution of the displacement (Figure 5.52a) and the velocity (Figure 5.52b) of a material point initially located just above the initial shear band. They correspond to the same unstable simu-

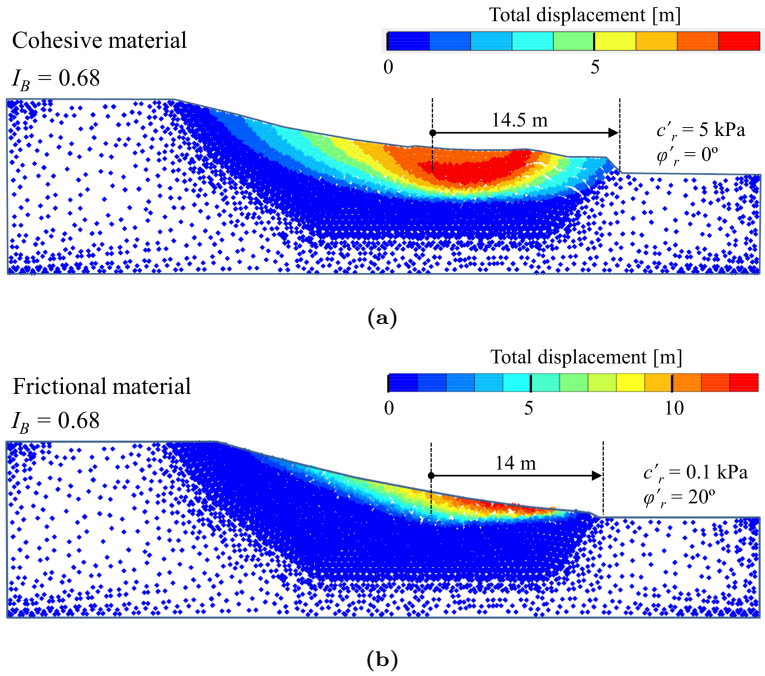

Figure 5.50: Final geometry for two simulations with same I_B. The displacements of the material points are indicated in the colour scales.

lations presented previously in Figure 5.51. These plots illustrate different phases of an instability process. Initially, and for a given period of time, the slope is stable and displacements and velocities are zero. At the end of this stage, the progressive failure takes place. When the initial failure mechanism develops, velocity increases rapidly and the mobilised mass moves forward. After a peak value of the velocity (in the cases analysed it varies from 1 to 2 m/s), velocity decreases until the slope reaches a new stable profile.

Additionally it can be observed that in slopes with larger values of I_B, for the same peak strength: (i) the instability occurs earlier; (ii) the velocity increases more suddenly; (iii) the peak velocities reach larger values; (iv) it is necessary more time to reach the stable geometry; and (v) the final run-out is longer.

5.5.3.1 Change in peak strength

The following combinations of c'_p and φ'_p have been adopted in order to study the effect of peak strength on the slope behaviour. The corresponding peak envelopes are illustrated in Figure 5.53.

- c'_p=5 kPa, φ'_p=35° (already analysed in the previous section)

- c'_p=5 kPa, φ'_p=45°
- c'_p=9 kPa, φ'_p=20°

For each case, several simulations have been carried out varying the residual strength parameters according to Table 5.6.

Following the same procedure described previously, the brittleness index I_B has been calculated for each unstable simulation. The effect of I_B on run-out is presented in Figure 5.54a. Although it is clear that for larger values of I_B the run-out increases, two different relationships can be distinguished. Whereas the combination of c'_p=5 kPa and φ'_p=45° matches with the correlation defined in Figure 5.54a, those simulations with c'_p=9 kPa and φ'_p=20° define a distinct correlation.

Figure 5.54b shows the variation of the maximum displacement achieved by a point depending on I_B, and, as occurs in Figure 5.54b, a scattered distribution of the results is shown.

In order to explain the distinct behaviour, three simulations with the same I_B and different peak strengths are analysed in Figures 5.55 and 5.56. While in the first two simulations the shear strain localises along a single band (Figures 5.55a and 5.55b), in the third simulation (Figure 5.55c) an additional shear band appears deeper and less intense. This leads to a generation of a completely different failure mechanism.

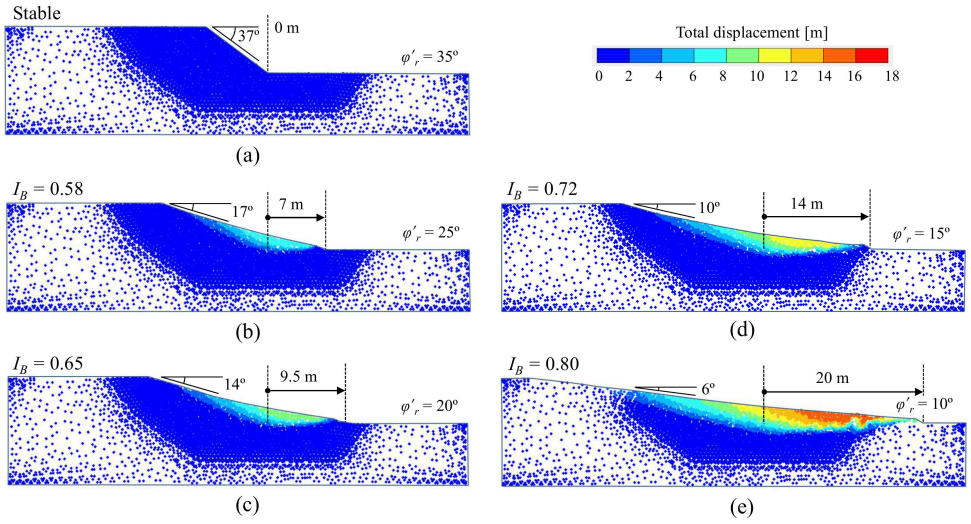

Figure 5.51: Final geometries of simulations with c'_r=0.5 kPa. The displacements of the material points are indicated in the indicated colour scale.

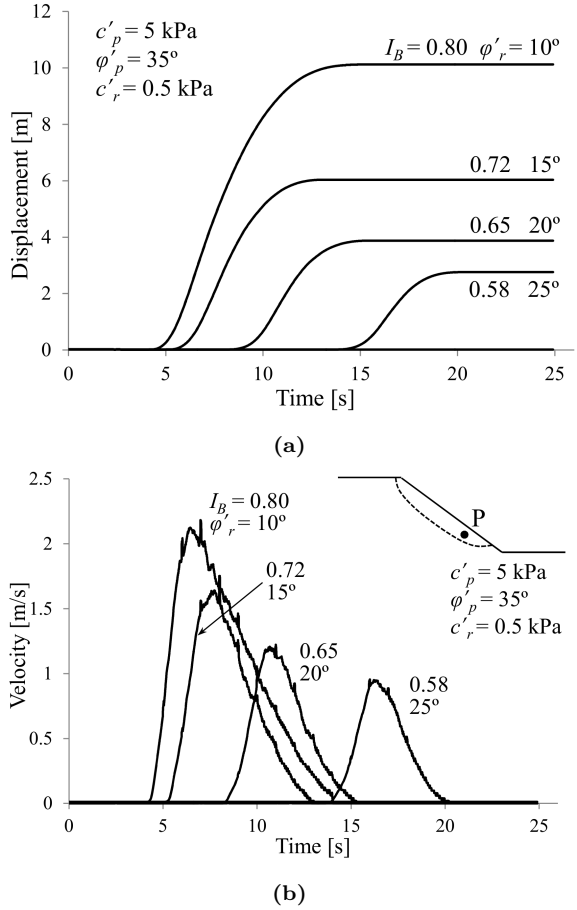

Figure 5.52: (a) Displacement and (b) velocity of the material point P for simulations with c'_r=0.5 kPa.

Finally, in Figure 5.56, the final displacements field are presented for the previous three simulations. It is clear that the mobilised mass is larger in the third simulation.

5.5.4 Discussion

It has been shown that run-out, defined as the distance between the toe of the initial slope and the toe once equilibrium has been re-established after the instability, is not equivalent to the maximum displacement achieved by any point of the slope (see Figures 5.49 and 5.54). While a clear relationship cannot be obtained between I_B and maximum displacement, I_B and run-out correlate well.

The difference between these two parameters (run-out and maximum displacement) is

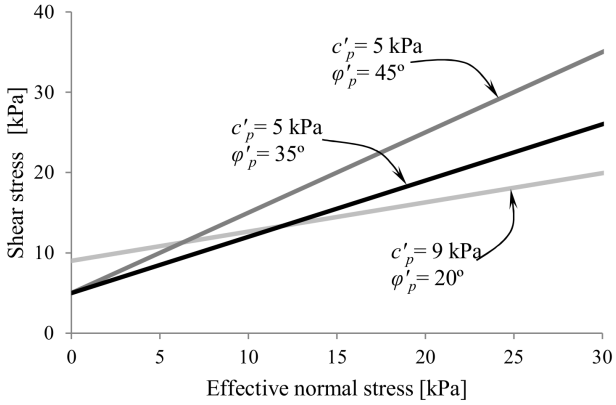

Figure 5.53: Peak Mohr-Coulomb envelopes.

evident especially when the failure mechanism is deep and the landslide is essentially a rotational movement. However, both measures are much more similar when the initial failure is shallow (see Figures 5.55 and 5.56). An explanation is that sliding displacements analysed here are similar to the initial height of the slope and, therefore, the displacement fields are dominated by the initial geometry of the failure mechanism.

In "large-scale" instabilities, in which the travelled distance is much larger than the initial size of the slope, the expected differences between run-out and maximum travelled distance will be lower, even irrelevant. However, the run-out will essentially depend on the topography rather than the brittleness of the source material.

It has been observed that when different peak strength envelopes are considered, the I_B-run-out relationship is not unique (see Figure 5.54a). In order to fully understand this behaviour it is important to note that I_B combines peak and residual values into a simple parameter. Hence it is essential to determine the role played by both peak and residual strengths in the stability of the slope, in the slip surface geometry and in the post-failure response.

In order to determine what parameters control the stability of the slope, the effect of cohesion drop (Eq.5.15) and friction decrease (Eq.5.16) has been examined as well as its relationship with the external triggering action (pore water pressure increase in the lower boundary).

$$\Delta c' = (c'_p - c'_r)/c'_p \tag{5.15}$$

$$\Delta\varphi' = (\tan\varphi'_p - \tan\varphi'_r)/\tan\varphi'_p \tag{5.16}$$

Figure 5.57 shows all the combinations of $\Delta c'$ and $\Delta\varphi'$ shown in Table 5.5 for ΔP=40 kPa and ΔP=70 kPa. Since in all cases the peak strength is the same, it is clear that the lower the increments of water pressure, the higher is the required strength reduction to make the slope unstable. Furthermore, these results suggest that the available strength that defines the stability of the slope results from an intermediate value between peak

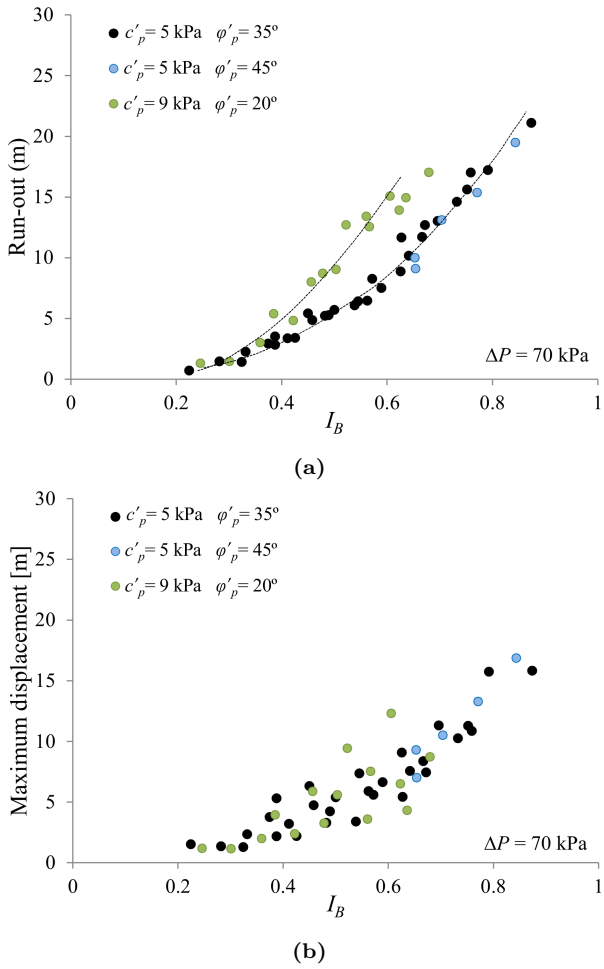

Figure 5.54: Relationships between I_B and (a) run-out and (b) maximum displacement achieved by a point.

and residual strength envelopes. Moreover, both cohesion and friction angle play a similar role in determining a threshold that define whether the slope will become unstable, or on the contrary, will remain stable.

These observations make sense with the results presented in Figure 5.46, where the evolution of the progressive failure mechanism is shown. The strength that controls the initiation of the progressive failure development depends on the maximum value of the averaged mobilised strength along the slip surface. This means that the maximum strength delivered by the failure mechanism depends on both peak and residual strengths.

Therefore, the geometry of the initial failure mechanism will be definitely influenced by both peak and residual strengths (see Figures 5.48 and 5.55). In particular, the depth

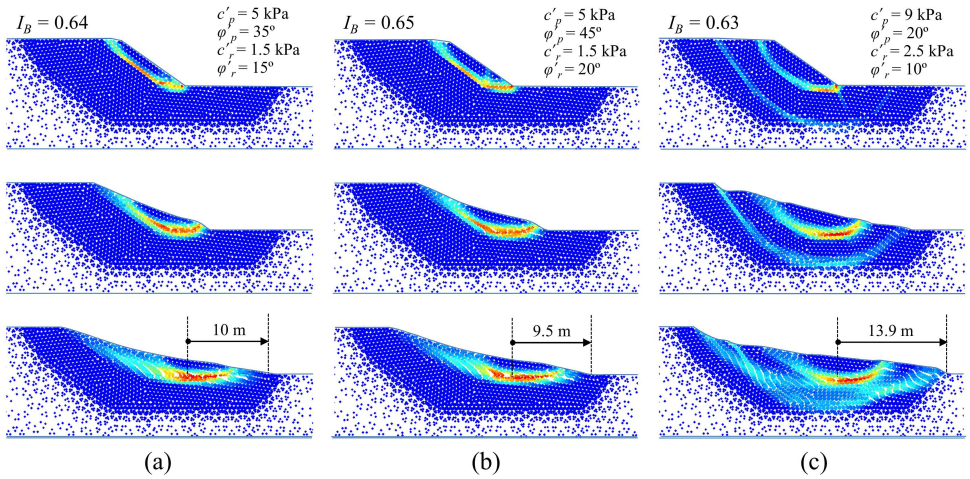

Figure 5.55: Distribution of the shear strain at different times for three simulations with similar I_B but different peak and residual strength envelopes.

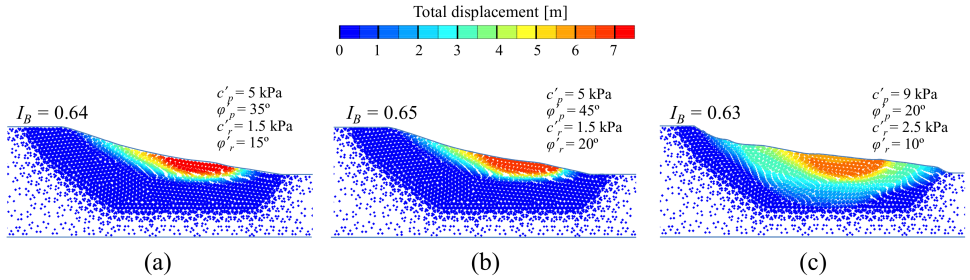

Figure 5.56: Final distribution of total displacements field for 3 cases with similar I_B but different peak strengths.

is controlled by the residual cohesion but mostly by the peak cohesion. Higher values of cohesion lead to deeper failure mechanisms.

In addition, the influence of peak and residual strengths on the value of run-out has been analysed. Figure 18 shows most of the cases presented in Table 5.6. It is clear that simulations having the same residual strength have quite similar values of run-out even if different peak yield surface envelopes define the material (see Figure 5.58). This means that the post-failure behaviour is strongly influenced by the residual state It makes sense because when the post-failure stage initiates, material located in shear bands has experienced enough plastic shear strain to be totally softened. This has also been shown in Figure 5.46b.

However, post-failure behaviour is also influenced by the initial acceleration of the motion, which is proportional to the strength drop just at the end of the progressive failure

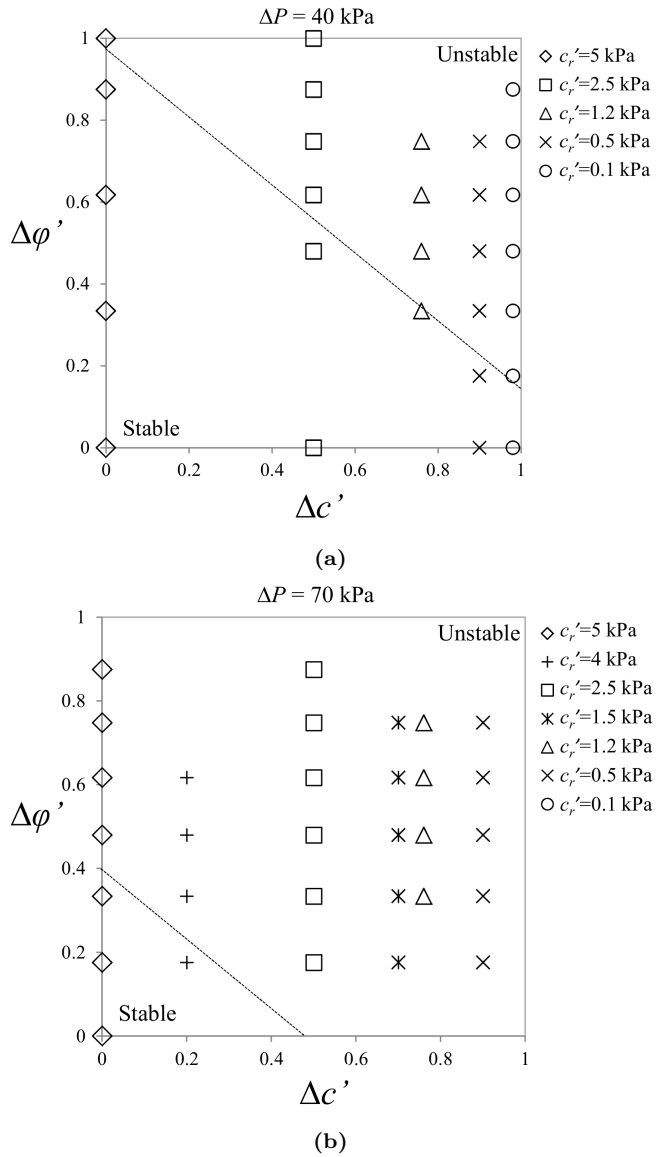

Figure 5.57: Stability of the slope depending on the combination of cohesion drop ($\Delta c'$) and friction angle decrease ($\Delta\varphi'$). The increase of pore pressure at the lower boundary is (a) ΔP=40 kPa and (b) ΔP=70 kPa. The same peak strength is maintained in all these simulations (c'_p=5 kPa and φ'_p=35°).

development. Such a magnitude also depends on peak conditions.

Finally, Figures 5.50 and 5.56 show that the final displacements field is very dependent on the failure geometry for these "small-scale" instabilities, and lower residual frictional

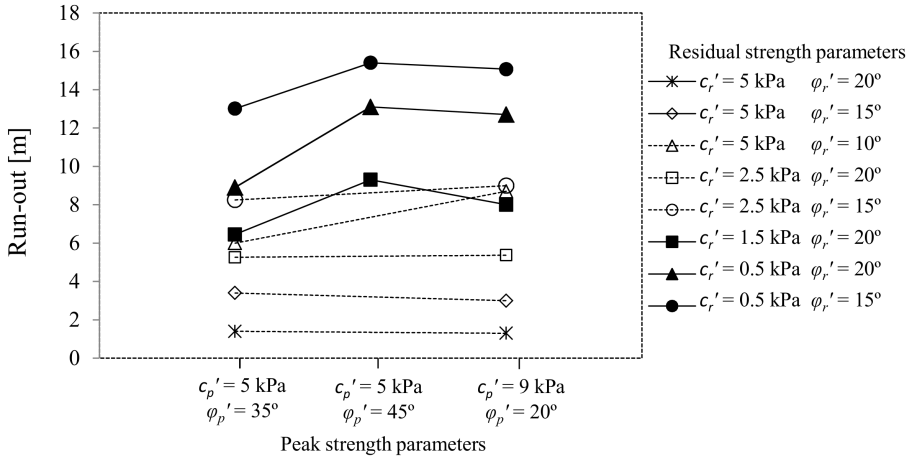

Figure 5.58: Influence of residual strength on run-out for three different peak Mohr-Coulomb envelopes.

angles lead to flatter final slopes. The kinematic behaviour has been analysed (Figure 5.52) and it was found that the maximum slide acceleration has been calculated at the early stages of the motion. Maximum velocities increase with increasing I_B.

5.5.5 Specific conclusions

An example involving a regular geometry and a homogeneous slope has been analysed. The triggering mechanism is an imposed increase in water pressure on the lower boundary of the domain.

The characterisation of the slope material by means of a strain softening elastoplastic constitutive law allows the simulation of the progressive failure phenomenon. Irreversible shear strain contours show the propagation of the failure surface from the foot of the slope towards the upper part.

Alternative combinations of peak and residual cohesion and friction have been selected and a degree of brittleness, I_B, proposed by Bishop (1967) has been assigned to the unstable cases. I_B is calculated for the average value of the normal effective stress acting on the initial failure surface.

Both run-out and maximum displacements have been represented in terms of the brittleness index. Run-out has been defined here as the distance between the toe of the initial slope and the toe of the slope after failure once equilibrium has been re-established. It was found that I_B and run-out correlate well when a common peak strength envelope is adopted. In all cases the run-out increases with I_B. It can be concluded that run-out is

a useful measure for landslide risk analysis which provides information of the downslope area invaded by the slide.

On the other hand, the stability of the slope and the failure mechanism process is heavily controlled by both peak and residual strengths; residual strength is more relevant during the post-failure behaviour and influences the run-out. Moreover, the geometry of the initial slip surface determines the final displacements field.

The onset of failure also depends on the magnitude of the triggering mechanism. It has been verified that the higher the magnitude of the triggering mechanism, the lower I_B is sufficient to induce instability. This fact allows defining a brittleness threshold $\hat{I}_B$ which determines the minimum brittleness required to induce instability for a certain excess pore pressure. However, the magnitude of the applied excess pressure (ΔP) does not change the general observations discussed above.

Table 5.5: Run-out and I_B for all simulations performed with a common peak strength envelope (c'_p=5 kPa and φ'_p=35°) for different residual strengths and two water pressure recharges (ΔP).

		ΔP=40 kPa		ΔP=70 kPa	
c'_r [kPa]	φ'_r [°]	I_B	Run-out	I_B	Run-out
5	35	stable	0.0	stable	0.0
5	25	stable	0.0	stable	0.0
5	20			0.32	1.4
5	15	stable	0.0	0.43	3.4
5	10			0.54	6.0
5	5	stable	0.0	0.63	11.6
5	0	0.68	14.5		
4	30			stable	0.0
4	25			0.28	1.4
4	20			0.39	2.8
4	15			0.48	5.2
2.5	35	stable	0.0	0.22	0.7
2.5	30			0.33	2.2
2.5	25			0.41	3.3
2.5	20	stable	0.0	0.49	5.2
2.5	15	0.57	6.9	0.57	8.2
2.5	10	0.66	12.1	0.67	12.7
2.5	5	0.74	14.9	0.75	17.0
2.5	0	0.83	25.0	0.87	21.1
1.5	30			0.37	2.9
1.5	25			0.46	4.9
1.5	20			0.56	6.4
1.5	15			0.64	10.1
1.5	10			0.73	14.6
1.2	25	stable	0.0	0.50	5.7
1.2	20	0.58	7.0	0.60	7.5
1.2	15	0.67	11.2	0.67	11.7
1.2	10	0.75	14.8	0.75	15.6
0.5	35	stable	0.0	0.39	3.5
0.5	30	stable	0.0	0.45	5.4
0.5	25	0.58	7.0	0.55	6.4
0.5	20	0.65	9.5	0.63	8.8
0.5	15	0.72	14.0	0.70	13.0
0.5	10	0.80	20.0	0.79	17.2
0.1	35	stable	0.0		
0.1	30	0.52	6.0		
0.1	25	0.62	8.8		
0.1	20	0.68	12.6		
0.1	15	0.76	17.4		
0.1	10	0.83	26.0		
0.1	5	0.91	26.0		

Table 5.6: Run-out and I_B for all simulations performed with three peak yield surface envelopes.

		ΔP=70 kPa					
c'_r [kPa]	φ'_r [°]	c'_p=5 kPa φ'_p=35°		c'_p=5 kPa φ'_p=45°		c'_p=9 kPa φ'_p=20°	
		I_B	Run-out	I_B	Run-out	I_B	Run-out
6	20					stable	0.0
6	15					0.3	1.4
6	10					0.42	4.8
6	5					0.56	13.4
5	35	stable	0.0				
5	25	stable	0.0				
5	20	0.32	1.4			0.25	1.3
5	15	0.43	3.4			0.36	3.0
5	10	0.54	6.0			0.48	8.7
5	5	0.63	11.6			0.64	15.0
4	30	stable	0.0				
4	25	0.28	1.4				
4	20	0.39	2.8				
4	15	0.48	5.2				
2.5	35	0.22	0.7				
2.5	30	0.33	2.2				
2.5	25	0.41	3.3				
2.5	20	0.49	5.3			0.38	5.4
2.5	15	0.57	8.2			0.5	9.0
2.5	10	0.67	12.7			0.62	13.9
2.5	5	0.75	17.0				
2.5	0	0.87	21.1				
1.5	30	0.37	2.9				
1.5	25	0.46	4.9				
1.5	20	0.56	6.4	0.65	9.5	0.46	8.0
1.5	15	0.64	10.0			0.57	12.5
1.5	10	0.73	14.6			0.68	17.0
1.2	25	0.50	5.7				
1.2	20	0.60	7.5				
1.2	15	0.67	11.7				
1.2	10	0.75	15.6				
0.5	35	0.39	3.5				
0.5	30	0.45	5.4				
0.5	25	0.55	6.4	0.65	10.0		
0.5	20	0.63	8.9	0.70	13.1	0.52	12.7
0.5	15	0.70	13.1	0.77	15.3	0.61	15.1
0.5	10	0.79	17.2	0.84	19.5		

5.6 Concluding remarks

Slope stability and post-failure behaviour were analysed by means of the coupled hydromechanical formulation (2-phase 1-point MPM formulation).

The study focusses in the modelling of brittle materials, such as cemented soils and overconsolidated plastic clays. A strain-softening Mohr-Coulomb constitutive model has been presented. It is able to reproduce the characteristic reduction of the available strength, from peak to residual state, with increasing plastic strain.

A regularisation technique is proposed in order to avoid mesh dependent strain-localisation problems associated to strain-softening features in standard continuum methods. It is based on the smeared crack approach and consists on calibrating a shape factor η included in the softening laws.

The progressive failure mechanism associated with brittle materials has been simulated with the MPM. A measure of the mobilised strength (mobilised friction angle) allows the identification of the failure propagation along the initial failure mechanism. The evolution of the mobilised average shear strength shows that, essentially, there are two distinct critical moments: the arrival to a maximum mobilised averaged strength (it can coincide with the first point reaching peak state) and the last point entering in the softening behaviour. In between, the average mobilised strength is essentially constant. The maximum strength is a value in between peak and residual conditions, and the final drop in average mobilised strength triggers the instability and the subsequent acceleration.

Three different slope instabilities were analysed in which the trigger factor is an increase of pore water pressures in the slope. In all cases, the establishment of initial stresses is the result of the gravity effect. The progressive failure mechanism has been analysed in all simulations. In each example, the failure propagation occurs in a different way.

First, the Selborne slope experiment has been simulated and numerical results have been compared with real data. The analysis provided remarkable consistent results: the failure progression and the final calculated displacement pattern (maximum displacements are about 4 m) fit well with the measurements. This case, well identified with laboratory data, has been an opportunity to perform a validation of the MPM formulation.

The second example analyses the relevance of internal degradation of the mobilised mass in a compound slide. A simplified geometry of the well-known Vajont landslide is presented. It has been confirmed that internal shearing is required to have a kinematically admissible failure mechanism. The location of such internal shear bands is controlled by the geometry of the basal sliding surface, which is essentially evolved from the kink and propagates as a progressive failure towards the ground surface. Finally, the post-failure velocity and the final run-out of the Vajont slide are simulated by an additional reduction of the basal friction angle, which coincides with the thermal pressurisation theories.

The effect of brittleness on failure and run-out was also studied by means a parametric study. Brittleness, defined in terms of brittleness index I_B, correlates well with final run-out. Run-out, understood as the distance between the toe of the initial slope and the toe after failure, increases with I_B. Meanwhile the stability of the slope and the failure mechanism depend on both peak and residual strengths, the post-failure behaviour is more influenced by the residual state.

One of the most important limitations of the presented dynamic MPM formulation is that the explicit algorithm is conditionally stable. Despite the existence of some numerical techniques (presented in Chapter 3) to increase the critical time step, the explicit scheme is definitely not well-suited to simulate long term problems. In the current Chapter, this limitation has been overcome by increasing the intrinsic permeability of the soil several orders of magnitude.

Finally, it can be concluded that MPM is able to simulate both the initiation of failure, which involves small strains, and the post-failure stage, generally characterised by large displacements in a unified calculation.

6

Chapter 6

Three-phase formulation with MPM. Unsaturated Soils

Applications of unsaturated soil mechanics often involve large deformations and displacements. This is the case of collapse behaviour of low density soils or the unrestrained swelling of expansive clays. Rain induced instability of unsaturated slopes is a further example of large displacements.

In this Chapter 6, the MPM formulation is extended to model unsaturated soil problems, where the soil is understood as a unique medium integrated by three distinct phases (solid, liquid and gas). All phases are combined in each material point and Balance and Momentum equations are formulated and numerically solved within the framework of a general MPM code. This is the 3-phase 1-point MPM formulation.

First, the basis of the unsaturated porous media, as well as a short discussion of which are the possible MPM strategies capable of simulating 3-phase interaction problems are presented (Sec.6.1 and 6.2). Then, the governing equations of the 3-phase 1-point MPM formulation are posed in Section 6.3. Afterwards, the numerical implementation and the explicit computational cycle are detailed (Sec.6.4 and 6.5), and later, several numerical issues are analysed: the stability of the scheme and boundary conditions (Sec.6.6 and 6.7). Finally, in Section 6.8, the validation of the 3-phase MPM approach is presented by means of the modelling of a one-dimensional infiltration problem.

6.1 Unsaturated porous media

The unsaturated porous media is assumed to be a combination of three different phases (ph): solid (s), liquid (l) and gas (g) (Fig.6.1). The solid phase constitutes the solid skeleton of the media; meanwhile the liquid and the gas phases fill the voids. Moreover, the fluids have been considered as a mixture of two components (c): water (w) and dry air (a).

Considering a portion of the unsaturated domain, its total volume V can be written as

$$V = \sum_{ph} V_{ph} = V_s + V_l + V_g \tag{6.1}$$

where V_{ph} is the partial volume of a phase and V_s, V_l, and V_g are the partial volumes for the solid, liquid and gas phases. The partial volumes can be written as

$$V_{ph} = n_{ph} \cdot V \tag{6.2}$$

where n_{ph} are the volume fractions associated with each phase.

Taking into account the volumetric relations of the porosity n and the degree of saturation S_l as

$$n = \frac{V_l}{V_l + V_g} \tag{6.3}$$

$$S_l = \frac{V_l}{V_l + V_g} 100 \tag{6.4}$$

The volume fraction of each phase can be written as

$$n_s = 1 - n \tag{6.5}$$

$$n_l = nS_l \tag{6.6}$$

$$n_g = nS_g \tag{6.7}$$

where $S_g = 1 - S_l$ is the gas degree of saturation.

The total mass m of a volume V is calculated as the sum of the partial masses of each phase m_{ph}.

$$m = \sum_{ph} m_{ph} \tag{6.8}$$

Taking into account that each phase can be considered as a mixture of components, the total mass is the sum of the partial masses of the components in each phase m^c_{ph}.

$$m = \sum_{ph} \sum_{c} m^c_{ph} \tag{6.9}$$

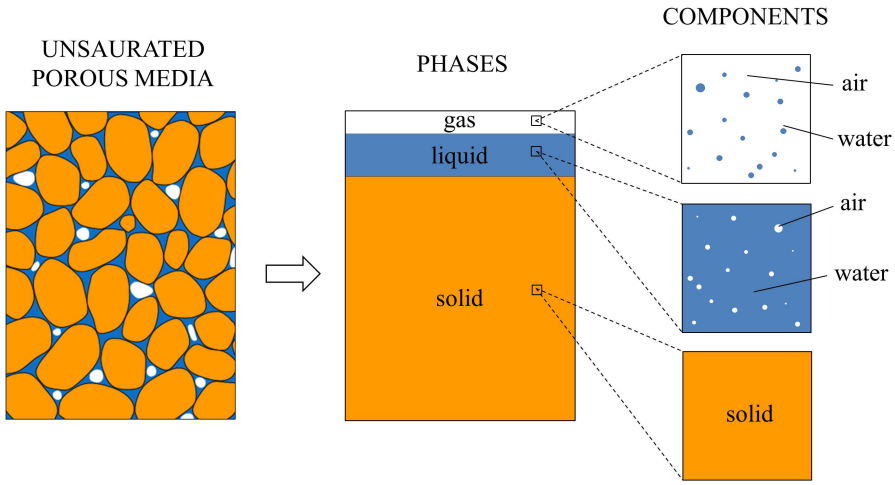

Figure 6.1: Continuum approximation of unsaturated porous media.

Defining the mass fraction of a component in a phase as

$$\omega_{ph}^{c} = \frac{m_{ph}^{c}}{m_{ph}} \tag{6.10}$$

and considering 6.2, the mass of a component in a phase is given by

$$m_{ph}^{c} = \omega_{ph}^{c} m_{ph} = \omega_{ph}^{c} \rho_{ph} V_{ph} = \omega_{ph} \rho_{ph} n_{ph} V \tag{6.11}$$

where ρ_{ph} is the density of a phase. Finally, the density of the mixture ρ_m is defined, by considering the volume fractions of each phase as

$$\rho_m = \sum_{ph} n_{ph} \rho_{ph} = (1-n)\rho_s + nS_l\rho_l + nS_g\rho_g \tag{6.12}$$

where ρ_s, ρ_l and ρ_g are the densities of solid, liquid and gas phases.

6.2 Three-phase problems in MPM

When the problem requires the simulation of 3 different phases, the MPM formulation can be stated in different ways (see Figure 6.2). The first approach corresponds to the 1-point discretisation extended from 2-phases to 3-phases. A second approach is the extension from 2-point to 3-point formulation, where each phase is represented by an independent set of material points. Moreover, a 3-phase 2-point formulation can also be defined as a third possible case where two phases (e.g. the fluids: liquid and gas) are represented by the same set of material points.

The purpose of this work is to simulate the unsaturated porous media as a unique continuous media formed by three phases. No independent motion of the water and air continua are expected in the applications envisaged. Therefore, it has been considered that the most appropriated modelling strategy in this case is the 3-phase-1-point formulation. The two other sketched multiple-point possibilities would require two or three layers of material points, which imply an excessive computational cost. Every material point represents a portion of the solid-liquid-gas mixture and it moves fixed to the solid skeleton carrying the water and the gas pressures as variables.

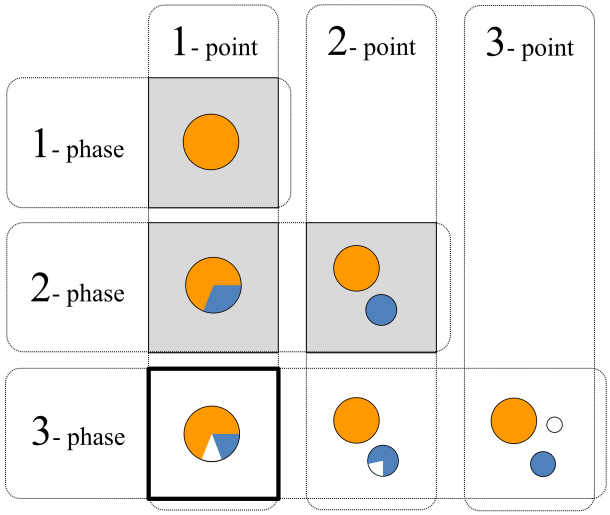

Figure 6.2: Scheme of the different MPM numerical approaches depending on the number of phases and the number of material point layers.

6.3 Governing equations

The dynamic behaviour of an unsaturated porous media can be formulated by specifying a set of physical laws: the momentum balances, the mass balances, the energy balance, and the first and second laws of thermodynamics. In the most common form of the finite element formulation, the relative accelerations of the liquid and gas phases are neglected and the equations are solved considering solid displacement, liquid pressure and gas pressure as the primary unknowns ($\mathbf{u}_s - p_l - p_g$ formulation) (Xikui and Zienkiewicz, 1992).

However, in order to capture the physical response of the porous media under dynamic conditions, the numerical approach presented in this work takes into account the relative accelerations and relative velocities of the pore fluids. Here, the velocities of each phase become the fundamental unknowns ($\mathbf{v}_s - \mathbf{v}_l - \mathbf{v}_g$ formulation).

6.3.1 General assumptions

The following assumptions have been adopted in the coupled MPM formulation described in the current Chapter:

1. Isothermal conditions
2. No mass exchange between solid and fluid phases
3. There is mass exchange of air and water between liquid and gas phases
4. Solid grains are incompressible
5. Diffusion of water in the liquid is neglected
6. Diffusion of air in the gas is neglected

6.3.2 Momentum balance equations

The momentum balance equation of the liquid phase (per unit of liquid volume) and the momentum balance of the gas phase (per unit of gas volume) can be written, respectively, as follows:

$$\rho_l \mathbf{a}_l = \nabla p_l - \frac{n S_l \mu_l}{k_l}(\mathbf{v}_l - \mathbf{v}_s) + \rho_l \mathbf{b} \tag{6.13}$$

$$\rho_g \mathbf{a}_g = \nabla p_g - \frac{n S_g \mu_g}{k_g}(\mathbf{v}_g - \mathbf{v}_s) + \rho_g \mathbf{b} \tag{6.14}$$

where $\mathbf{a}_l$ and $\mathbf{a}_g$ are the acceleration of the liquid and gas phase; $\mathbf{v}_l$, $\mathbf{v}_g$ and $\mathbf{v}_s$ are the total liquid, gas and solid velocities; p_l and p_g are the liquid and gas pressures, μ_l and μ_g are the dynamic viscosities of the liquid and the gas; k_l and k_g are the intrinsic permeabilities of the liquid and the gas; $\mathbf{b}$ is the body force vector. These expressions describe the so-called generalised Darcy's law.

In addition, the momentum balance equation of the mixture (per unit of volume of mixture) can be written as

$$\rho_s(1-n)\mathbf{a}_s + \rho_l n S_l \mathbf{a}_l + \rho_g n S_g \mathbf{a}_g = \nabla \cdot \boldsymbol{\sigma} + \rho_m \mathbf{b} \tag{6.15}$$

where $\boldsymbol{\sigma}$ is the total stress of the mixture. The momentum balance of the mixture has been selected instead of the momentum of the solid phase for convenience because, in practise, the total stress is usually known, unlike the stresses acting on the solid skeleton.

The boundary conditions of the liquid momentum balance and for the mixture are defined in Section 4.3.1 (Eq.4.3, Eq.4.4, Eq.4.6 and Eq.4.7), and for the gas momentum balance

are the following.

$$\mathbf{u}_g(\mathbf{x},t) = \widehat{\mathbf{u}}_g(t) \text{ on } \partial\Omega^{\mathbf{u}_g} \tag{6.16}$$

$$p_g(\mathbf{x},t)\mathbf{n} = \widehat{\mathbf{p}}_g(t) \text{ on } \partial\Omega^{p_g} \tag{6.17}$$

6.3.3 Mass balance equations

Because the exchange of mass between fluid phases is enabled, the mass balance equations have been formulated for each component (solid, water, air) instead of for each phase (solid, liquid, gas). In this manner, the flux terms become simpler because the evaporation and condensation of water and the dissolution and liberation of air are balanced within each component balance.

The mass balance equation of a component can be written as

$$\sum_{ph}\Big[\frac{\partial}{\partial t}\Big(\frac{m^c_{ph}}{V}\Big) + \nabla\cdot\mathbf{j}^c_{ph}\Big] = 0 \tag{6.18}$$

The first term in the sum is the time derivative of the partial mass m^c_{ph} per unit volume of porous media and the second one is the divergence of the flux. The external sources or sinks of mass might appear in the right side of the equation, but in this case they have not been considered. The flux referred to a particular component $\mathbf{j}^c_{ph}$ is written as the sum of diffusive flux ($\mathbf{i}^c_{ph}$) and advective flux,

$$\mathbf{j}^c_{ph} = \mathbf{i}^c_{ph} + \Big(\frac{m^c_{ph}}{V}\Big)\mathbf{v}_{ph} \tag{6.19}$$

The diffusive fluxes (i.e. diffusion of water in the gas and the diffusion of air in the water) can be modelled by means of the Fick's law (Fick, 1855), written as

$$\mathbf{i}^c_{ph} = -\rho_{ph}\mathbf{D}^c_{ph}\mathbf{I}\nabla\omega^c_{ph} \tag{6.20}$$

where $\mathbf{D}^c_{ph}$ is the dispersion tensor which includes non advective flux caused by molecular diffusion and hydromechanical dispersion.

Developing the expressions 6.18 and 6.19 (Appendix I), the mass balance equation for the solid skeleton becomes the following expression which describes the material derivative of the porosity.

$$\frac{Dn}{Dt} = (1-n)\nabla\cdot\mathbf{v}_s \tag{6.21}$$

Water and air mass balance equations have also been expanded (see Appendixes B) considering fluid pressures (P_l and P_g) as state variables, leading to the following expressions

$$\begin{aligned} n\frac{\partial(\omega^w_g\rho_g S_g + \rho_l S_l)}{\partial p_l}\dot{p}_l + n\frac{\partial(\omega^w_g\rho_g S_g + \rho_l S_l)}{\partial p_g}\dot{p}_g = \\ -\nabla\cdot(\omega^w_g n\rho_g S_g(\mathbf{v}_g - \mathbf{v}_s)) - \nabla\cdot(n\rho_l S_l(\mathbf{v}_l - \mathbf{v}_s)) \\ -(\omega^w_g\rho_g S_g + \rho_l S_l)\nabla\cdot\mathbf{v}_s - \nabla\cdot\mathbf{i}^w_g \end{aligned} \tag{6.22}$$

$$n\frac{\partial(\rho_g S_g + \omega_l^a \rho_l S_l)}{\partial p_l}\dot{p}_l + n\frac{\partial(\rho_g S_g + \omega_l^a \rho_l S_l)}{\partial p_g}\dot{p}_g = \\ -\nabla\cdot(n\rho_g S_g(\mathbf{v}_g - \mathbf{v}_s)) - \nabla\cdot(\omega_l^a n\rho_l S_l(\mathbf{v}_l - \mathbf{v}_s)) \\ -(\rho_g S_g + \omega_l^a \rho_l S_l)\nabla\cdot\mathbf{v}_s - \nabla\cdot\mathbf{i}_l^a \tag{6.23}$$

6.3.4 Constitutive equations

An important element in a coupled hydromechanical problems is the mechanical constitutive model for the soil. Since 25 years ago, a great number of elastoplastic models for unsaturated soils have been presented. Alonso et al. (1990) proposed to use net stress and suction as stress state variables. The net stress $\bar{\boldsymbol{\sigma}}$ is equal to the excess of total stress over gas pressure, and the suction is the difference between gas pressure and liquid pressure:

$$\bar{\boldsymbol{\sigma}} = \boldsymbol{\sigma} - p_g\mathbf{m} \tag{6.24}$$

$$s = p_g - p_l \tag{6.25}$$

where $\mathbf{m} = (\ 1 \quad 1 \quad 1 \quad 0 \quad 0 \quad 0\ )^T$
The net stress can be defined more generally as:

$$\bar{\boldsymbol{\sigma}} = \boldsymbol{\sigma} - \max\{p_g, p_l\}\mathbf{m} \tag{6.26}$$

The general form of a suitable stress-strain relationship can be written incrementally as follows,

$$\dot{\bar{\boldsymbol{\sigma}}} = \mathbf{D}^{ep}\cdot\dot{\varepsilon} + \mathbf{h}'\dot{s} \tag{6.27}$$

in which $\mathbf{D}^{ep}$ is the tangent matrix, $\mathbf{h}'$ is a constitutive vector. Both are defined by means of the constitutive model. $d\varepsilon$ is the strain increment vector. In Appendix D, the general form of the constitutive equation for unsaturated soils is presented in detail.

This is not the unique framework to descrive the mechanical behaviour of unsaturated soils. Several authors proposed other formulations based on an effective stress concept.

6.3.5 Hydraulic constitutive equations

The degree of saturation S_l is strongly dependent on pore liquid and gas pressures. There are a number of empirical equations that describe this characteristic for soil in the literature. In this work the well-known van Genuchten retention curve (Van Genuchten, 1980) has been implemented, where p_0, λ, S_{max} and S_{min} are assumed constants:

$$S_l = S_{min} + \left[1 + \left(\frac{s}{p_0}\right)^{\frac{1}{1-\lambda}}\right]^{-\lambda}(S_{max} - S_{min}) \tag{6.28}$$

It is also necessary to specify the dependence of the liquid permeability on the degree of saturation. Hillel expression (Hillel, 1971) defines the following expression, where k_{sat} is the liquid permeability under saturated conditions.

$$k_l = k_{sat} {S_l}^r \tag{6.29}$$

The power r typically takes values in range 2-4 (a value of 3 is used in this work).

In addition, the variation of water mass fraction in the gas phase can be calculated according to the psychometric law (Edlefson and Anderson, 1943) and the variations of air mass fraction in the liquid can be obtained via the Henry's law (Mackay and Shiu, 1981). Finally, other properties can also be written to depend on the fluid pressures, see C.

6.4 Numerical implementation. Three-phase One-point formulation

6.4.1 Spatial discretisation

MPM discretises the media in two different frames. First, the continuum is divided into a finite number of subdomains represented by material points (p) (see Fig.6.3). Each material point moves attached to the solid skeleton, carrying all the information and providing a Lagrangian description. Assuming that the whole mass of a material point is concentrated at the corresponding material point, the density of the mixture ρ_m can be expressed as:

$$\rho_m(\mathbf{x}, t) = \sum_{p=1}^{N_p} m_p \delta(\mathbf{x} - \mathbf{x}_p) \tag{6.30}$$

in which m_p and $\mathbf{x}_p$ are the mass and the position of the material point p, is the Dirac delta function, and N_p is the total number of material points. Moreover, in the 3-phase-1-point MPM formulation, it is also necessary to consider the density of each phase $\rho_p h$ as

$$\rho_{ph}(\mathbf{x}, t) = \sum_{p=1}^{N_p} \widetilde{m}_{ph_p} \delta(\mathbf{x} - \mathbf{x}_p) \tag{6.31}$$

where $\widetilde{m}_{ph_p}$ is related with mp according to the following relationship.

$$m_p = \sum_{ph} m_{ph_p} = \sum_{ph} n_{ph} \widetilde{m}_{ph_p} \tag{6.32}$$

The second discretisation frame is an eulerian computational mesh (see Figure 6.3). The momentum equations are solved in the nodes (i). The standard linear shape functions N_i

provide the relationship between the nodes and any point of the domain as follows:

$$\mathbf{w}(\mathbf{x},t) = \sum_{i=1}^{N_n} \mathbf{w}_i(t) \cdot N_i(\mathbf{x},t) \tag{6.33}$$

N_n being the total number of nodes and $\mathbf{w}_i$ a specific field, such as the displacement field, evaluated in the node i.

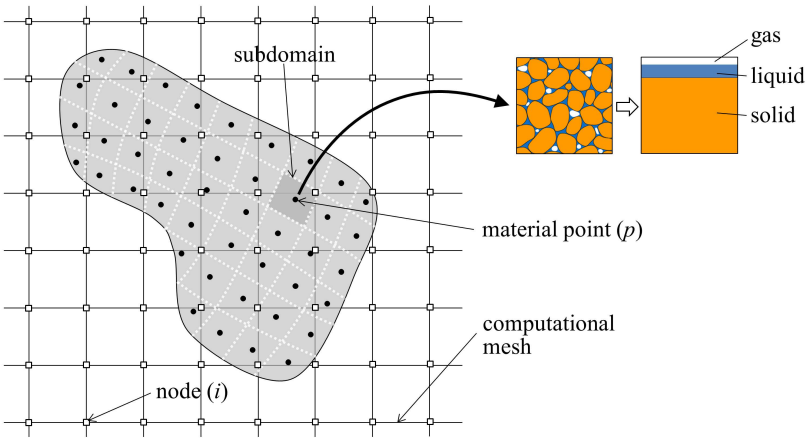

Figure 6.3: Scheme of the spatial discretisations of the domain.

6.4.2 Weak form of the momentum balance equations

The Galerkin method of weighted residuals (Galerkin, 1915) has been applied to obtain the weak form of the momentum balance equations (Eq.6.13, Eq.6.14, and Eq.6.15) (see the derivation in AppendixA). The expressions (6.30), (6.31) and (6.33) have been used to discretise the integrals over the domain into the nodes of the computational mesh considering the information carried by the material points. The final system of equations is written as

$$\widetilde{\mathbf{M}}_l \cdot \mathbf{a}_l = \mathbf{F}_l^{ext} - \mathbf{F}_l^{int} - \mathbf{Q}_l \cdot (\mathbf{v}_l - \mathbf{v}_s) \tag{6.34}$$

$$\widetilde{\mathbf{M}}_g \cdot \mathbf{a}_g = \mathbf{F}_g^{ext} - \mathbf{F}_g^{int} - \mathbf{Q}_g \cdot (\mathbf{v}_g - \mathbf{v}_s) \tag{6.35}$$

$$\mathbf{M}_s \cdot \mathbf{a}_s + \mathbf{M}_l \cdot \mathbf{a}_l + \mathbf{M}_g \cdot \mathbf{a}_g = \mathbf{F}^{ext} - \mathbf{F}^{int} \tag{6.36}$$

where $\mathbf{a}_s$, $\mathbf{a}_l$, and $\mathbf{a}_g$ and $\mathbf{v}_s$, $\mathbf{v}_l$, and $\mathbf{v}_g$ are the nodal acceleration and velocity vectors for each phase. $\mathbf{F}_l^{ext}$ and $\mathbf{F}_g^{ext}$ are the vector of the liquid and gas external forces, respectively and $\mathbf{F}^{ext}$ the vector of the external forces of the mixture. Internal forces are indicated by means the superscript int. $\mathbf{Q}_l$ and $\mathbf{Q}_g$ are the liquid and gas dragging matrixes. $\widetilde{\mathbf{M}}$ and $\mathbf{M}$ are mass matrix per unit of volume. The mathematical expression for each term is properly defined in the Appendix A.

6.4.3 Time discretisation

The solution of the momentum balance equations 6.34, 6.35 and 6.36 is obtained in a set of discrete times t_k by means of an explicit time integration scheme (see Section 3.3.2.4).

Since the acceleration terms are the unknowns of the system of equations, the explicit Euler scheme is used to update the velocities and displacements of each phase as follows.

$$\mathbf{v}_{ph}^{k+1} = \mathbf{v}_{ph}^{k} + \triangle t \mathbf{a}_{ph}^{k} \tag{6.37}$$

$$\mathbf{u}_{ph}^{k+1} = \mathbf{u}_{ph}^{k} + \triangle t \mathbf{v}_{ph}^{k+1} \tag{6.38}$$

6.4.4 Resolution of the mass balance equations

In order to determine the increments of liquid and gas pressure ($\dot{p}_l$ and $\dot{p}_g$) within the corresponding time step increment, water and air mass balance equations (6.22 and 6.23) are solved at the material points.

Mass balances can be written in a compact form with a linear system of equations (Eq.6.39), in which the first row corresponds to the water balance and the second row corresponds to the air equation.

$$\begin{pmatrix} W_1 & W_2 \\ A_1 & A_2 \end{pmatrix} \begin{pmatrix} \dot{p}_l \\ \dot{p}_g \end{pmatrix} = \begin{pmatrix} W \\ A \end{pmatrix} \tag{6.39}$$

Where

$$W_1 = n \frac{\partial \left(\omega_g^w \rho_g S_g + \rho_l S_l \right)}{\partial p_l} \tag{6.40}$$

$$W_2 = n \frac{\partial \left(\omega_g^w \rho_g S_g + \rho_l S_l \right)}{\partial p_g} \tag{6.41}$$

$$A_1 = n \frac{\partial \left(\rho_g S_g + \omega_l^a \rho_l S_l \right)}{\partial p_l} \tag{6.42}$$

$$A_2 = n \frac{\partial \left(\rho_g S_g + \omega_l^a \rho_l S_l \right)}{\partial p_g} \tag{6.43}$$

$$W = -\nabla \cdot \left(\omega_g^w \rho_g S_g n \left(\mathbf{v}_g - \mathbf{v}_s \right) \right) - \nabla \cdot \left(\rho_l S_l n \left(\mathbf{v}_l - \mathbf{v}_s \right) \right) - \left(\omega_g^w \rho_g S_g + \rho_l S_l \right) \nabla \cdot \mathbf{v}_s - \nabla \cdot \mathbf{i}_g^w \tag{6.44}$$

$$A = -\nabla \cdot \left(\rho_g S_g n \left(\mathbf{v}_g - \mathbf{v}_s \right) \right) - \nabla \cdot \left(\rho_l S_l n \left(\mathbf{v}_l - \mathbf{v}_s \right) \right) - \left(\rho_g S_g + \omega_l^a \rho_l S_l \right) \nabla \cdot \mathbf{v}_s - \nabla \cdot \mathbf{i}_l^a \tag{6.45}$$

Note that partial derivatives form terms W_1, W_2, A_1 and A_2 can be calculated taking into account expressions detailed in Appendix C.

It is important to higlight that A and B represent the gain or loss of water and air masses at the material point due to fluxes (advective and diffusive). In order to calculate such gradients at the material points, diffusive fluxes ($\mathbf{i}_g^w$ and $\mathbf{i}_l^a$), and masses of each component are additionally required at the nodes. Because this information is carried by the material points during the calculation, it can be temporary transferred to the nodes by a mass weighing. For instance, the following expression corresponds to the mass weighing of the water mass ($m^w = m_g^w + m_l^w = \omega_g^w \rho_g S_g + \rho_l S_l$).

$$m^{w\,k}_{\ j} = \frac{1}{m_j{}^k} \sum_{p=1}^{N_p} m_p^k N_j^{p^k} m^{w\,k}_{\ p} \tag{6.46}$$

Being $m^{w\,k}_{\ p}$ the water mass in a material point p and $m^{w\,k}_{\ j}$ the weighted mass of water at node j; m_p^k and m_j^k are the material point and nodal total masses respectively and $N_j^{p^k}$ is the shape function. All values are referred to the time t^k.

6.5 Computational cycle

The numerical procedure is described by the following steps, which are solved for each time step:

1. Nodal mass is calculated using the shape functions and mass matrices are formed. Internal forces of the gas phase, the liquid phase and the mixture are evaluated in the nodes (App.A).

2. Additional information is transferred form the material points to the nodes, such as non-advective fluxes of air in the liquid and water in the gas. In addition, water mass and air mass are also calculated from material point values according to equation (6.46).

3. Momentum balance of gas is solved and nodal accelerations of the gas phase are calculated (Eq.6.35).

4. Momentum balance of liquid is solved and nodal accelerations of the liquid phase are calculated (Eq.6.34).

5. Momentum balance of the mixture is solved using the liquid and gas accelerations previously obtained in steps 3 and 4. Nodal accelerations of solid skeleton are determined (Eq.6.36).

6. Particle velocities are updated using forward Euler scheme (Eq.6.37).

7. Nodal velocities are calculated form particle values (Eq.3.25).

8. Particle displacements are updated using updated velocities (Eq.6.38).

9. Strain increments for the solid phase and volumetric strain rates for the fluid phases are calculated on material point (Eq.3.27).

10. Mass balance of water and mass balance of air are solved as a linear system of equations (6.39). Increments of water and gas pressure are obtained in the material points.

11. Constitutive stresses are updated using a material constitutive model (Eq.6.27).

12. Material properties are updated in the material points. Particle volume is updated considering the increment of volumetric strain; porosity is updated with the mass balance equation of the solid; degree of saturation is updated considering the updated fluid pressures. Other properties can also be updated here, such as permeabilities, viscosities or mass fractions.

13. The computational grid is initialised for the next step and material points carry all the updated information.

6.6 Minimum time step criterion

As in Chapters 3 and 4, the 3-phase 1-point MPM formulation extended to solve problems in unsaturated soils has been integrated in time by means an explicit scheme. Hence the solution it is conditionally stable and a minimum time step criterion should be considered. In this case, an specific analysis was carried out and the same criterion obtained for the 2-phase 1-point formulation (Sec.4.6) is adopted as a reference value.

In fact, saturated conditions can be considered as a particular case of the 3-phase formulation, in which, no gas is accounted within the material points. Because the critical time step decreases with the bulk modulus of the material (see Section 4.6), it can be expected that the criterion for saturated conditions is the most restrictive one for the 3-phase formulation. This assumption is supported because of the stiffness of the gas is usually much lower than the stiffness of the liquid.

If solid grains are incompressible, the bulk modulus of a unsaturated soil K_m can be written as (Santamarina et al., 2001):

$$K_m = K_s + \frac{1}{\frac{nS_l}{K_l} + \frac{n(1-S_l)}{K_g}} \tag{6.47}$$

where K_s, K_l and K_g are the modulus of the solid skeleton, liquid and gas.

Figure 6.4 shows the variation of the unsaturated bulk modulus with the degree of sat-

Table 6.1: Types of boundary conditions in a hydromechanical problem.

Condition	Essential	Natural
Mechanical	Prescribed solid velocity (Eq.4.7)	Prescribed traction (Eq.4.6)
Hydraulic	Prescribed liquid velocity (Eq.4.4)	Prescribed liquid pressure (Eq.4.3)
Hydraulic	Prescribed gas velocity (Eq.6.16)	Prescribed gas pressure (Eq.6.17)

uration considering the water retention curve and the soil properties presented in Table 7.2 and 7.4. It is clear that when the soil is almost saturated and the degree of saturation is close to one, the stiffness of the soil increases abruptly towards the saturated bulk modulus. This effect can be explained because the stiffness of the gas is several orders of magnitude lower than the stiffness of water and soil skeleton.

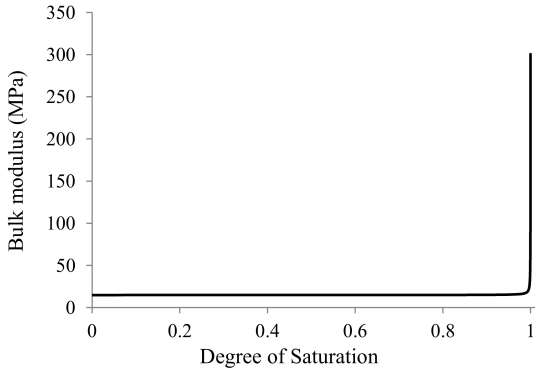

Figure 6.4: Variation of the unsaturated bulk modulus with the degree of saturation.

6.7 Boundary conditions

The boundary conditions considered in the boundary value problem defined by the momentum balances for the 3-phase hydromechanical formulation (App.A), are summarised in Table 6.1.

Note that a boundary without any restriction means that

- solid skeleton can moves freely,
- total stress is zero,
- liquid and gas phases can move freely (totally permeable boundary)
- liquid and gas pressures are zero (saturated boundary without excess pore pressure).

This means that in a slope problem, if no boundary conditions are applied on the ground surface, saturated conditions will be automatically fulfilled along such boundary because p_l and p_g are be zero. Even if the boundary moves and changes. This is an advantage when simple wetting problems are modelled.

Moreover, it gets complicated when fluid pressures have to be different than zero along a moving contour, for example, if a certain degree of saturation has to be maintained.

6.8 Validation. Infiltration problem

The equation that represents the movement of water in unsaturated soils is the Richards equation (Richards, 1931), which is derived from the water mass balance and the Darcy's equation (quasistatic liquid momentum balance). However, because the nonlinearities of soil hydraulic parameters (for instance, permeability depends on degree of saturation, and degree of saturation depends on fluid pressures), it is very difficult to obtain an analytical solution to describe the unsaturated flow.

In order to facilitate computations, only one component is considered within each phase (no air in liquid and no water in gas). Moreover, the following assumptions must be considered (Alonso and Lloret, 1983):

- vertical liquid flow,
- deformability of the solid skeleton is neglected,
- incompressible solid grains,
- constant permeability,
- constant liquid density, and
- constant total stress field

Finally, to get a simpler expression, the retention curve is linearised according to

$$S_l = 1 - a_s(p_g - p_l) \tag{6.48}$$

where a_s is a constant.

Then, the mathematical expression that describes the one-dimensional vertical water flow within an unsaturated soil can be written as

$$\frac{\partial p_l}{\partial t} = C_i \frac{\partial^2 p_l}{\partial z^2} \tag{6.49}$$

Table 6.2: Material properties of wetting test.

Material property	Value
Porosity [-]	0.3
Liquid density [kg/m^3]	1000
Liquid bulk modulus [kPa]	80000
Liquid viscosity [kg/sm]	0.001
Intrinsic permeability [m^2]	$5 \cdot 10^{-5}$
a_s [kPa^{-1}]	0.001

This expression is the diffusion equation, where z is the infiltration direction and C_s corresponds to

$$C_i = \frac{k_l}{n\gamma_l a_s} \tag{6.50}$$

A dimensionless time T can be defined depending on C_i as

$$T = \frac{C_i t}{h^2} \tag{6.51}$$

being h is the infiltration length.

A sample of 1 m high is considered. The material is linear elastic and all properties are summarised in Table 6.2. While contours are permeable for gas, liquid only can flow vertically. Initially, the sample is unsaturated with a constant suction value (s_0=0.5 MPa). Because the bottom is impervious for liquid ($\frac{\partial p_l}{\partial t}$=0), the infiltration length is 1 m. Gravity is neglected and the solid skeleton can not deform. The wetting process starts when s=0 kPa (saturation condition) is suddenly imposed at the upper boundary and maintained throughout the calculation.

Applying such conditions on equation (6.49), the analytical solution that comes out is equivalent to the one-dimensional consolidation problem in saturated media, the well-known Terzaghi's solution (Terzaghi, 1943). In Figure 6.5, the suction evolution along the depth of the sample is illustrated according to the analytical solution.

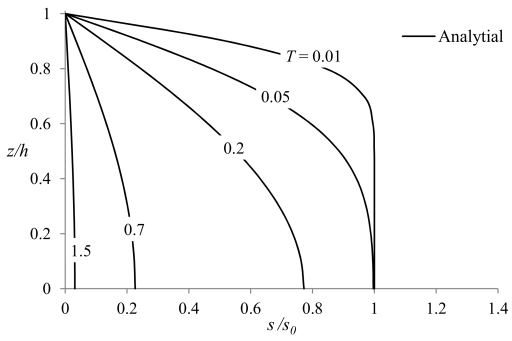

Figure 6.5: Analytical solution. Suction evolution along depth z

Different simulations have been carried out in order to study the effect of artificial damping and the number of material points placed within each element. Initially, 2 calculations without artificial damping (α=0) are performed considering 1 and 4 material points. In Figure 6.6 it can be seen that while the infiltration process calculated with 4 material points in each element fits perfectly the analytical solution (Fig.6.6b), some numerical oscillations are observed when only 1 material point is considered (Fig.6.6a).

Two more calculations are presented in Figure 6.7, considering 4 points in each element and different damping factors: α=0.05 (Fig.6.7a) and α=0.75 (Fig.6.7b). See also Figure 6.8, in which the suction evolution of a material point located at z= 0.49 m is presented for different damping factors.

It is clear that the infiltration is slower when larger damping factors are considered. Although inertial terms are considered in the momentum balances, no additional damping is required in this model to get the quasistatic solution. With damping factor α=0 solution is already "properly" damped.

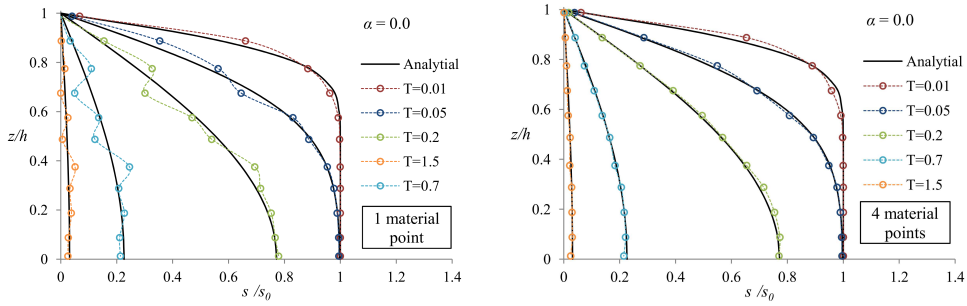

Figure 6.6: Numerical results of suction evolution along depth z. Damping factor $\alpha = 0$. (a) 1 material point in each element; (b) 4 material point in each element.

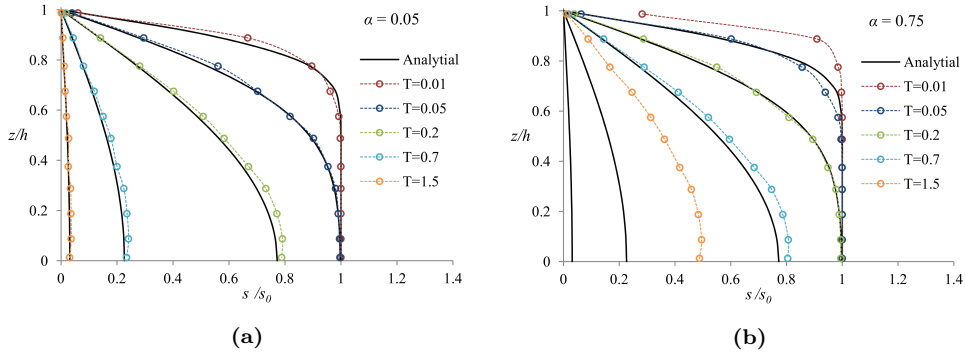

Figure 6.7: Numerical results of suction evolution along depth z. 4 material points are considered in each element. Comparison between different damping factors: (a) α=0.05; (b) α=0.75.

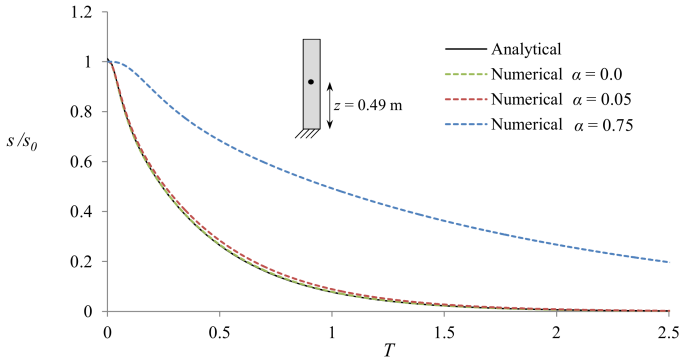

Figure 6.8: Suction evolution in a material point located at z=0.49 m. Comparison between analytical solution and numerical results obtained different damping factors and 4 material points per element.

Two additional calculations have been carried out in order to emphasise the importance of taking adequate assumptions in the mass balances calculation when unsaturated fluxes are modelled. The results presented in Figure 6.9 have been calculated assuming that the spatial variations of water and air masses are small ($\nabla(\omega_l^w \rho_l S_l n + \omega_g^w \rho_g S_g n) \approx 0$ and $\nabla(\omega_l^a \rho_l S_l n + \omega_g^a \rho_g S_g n) \approx 0$). This means that part of the advective fluxes are neglected, hence equations (B.17) and (B.23) have been used instead of the complete expressions (B.16) and (B.22) respectively.

One of the constitutive equation that plays a more significant role in the spatial distribution of the fluids masses is the relationship between the degree of saturation and suction (water retention curve). In this example, it is a linear variation that depends on a_s. According to equation (6.48), a small value of a_s implies that small change in suction correspond to small change of S_l. Figure 6.9 shows the obtained results when neglecting the advective fluxes due to spatial variations of water and air masses. All parameters taken in Figure 6.9a coincide with that presented in Table 6.2 (a_s=0.001 kPa^{-1}), meanwhile in Figure 6.9b a_s is a smaller value (a_s=0.0001 kPa^{-1}). Comparing these two images, it can be concluded that the larger the a_s, the larger the committed error. Therefore, the advective fluxes due to spatial variations of fluids masses can not be neglected in materials such as sand, meanwhile such terms will be less relevant in clay.

Another parameter that influences the spatial distribution of fluid mass is the porosity. If materials with very different porosities are in contact, the spatial gradients of fluid mass along the contact can not be neglected.

Despite assuming several restrictive hypothesis, the hydraulic part of the 3-phase 1-point MPM formulation has been validated. With damping factor α=0 the solution is already damped. Moreover, it has shown that 4 material points per element are better than only 1. A final discussion about assuming

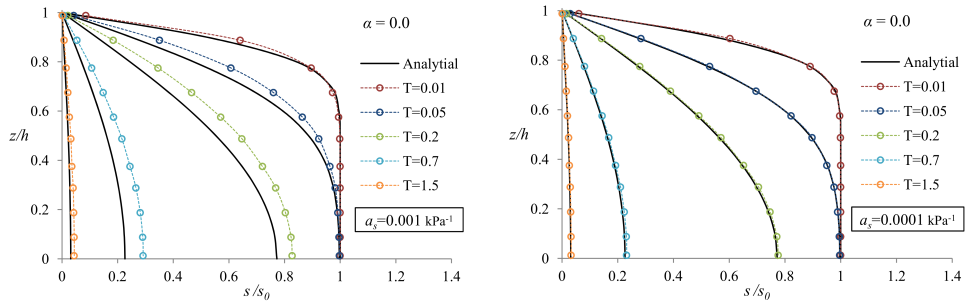

Figure 6.9: Infiltration process neglecting advective fluxes due to spatial variations of fluids masses. Comparison between different a_s values: (a) a_s=0.001 kPa^{-1}; (b) a_s=0.0001 kPa^{-1}.

6.9 Concluding remarks

This Chapter presents a step forward in the application of MPM to multiphase problems in porous media. Three phases are necessary in an analysis of unsaturated soils: gas, liquid and solid. Mass balance equations of the species (air, water, minerals) as well as all constitutive relationships are formulated at a material point level. Equilibrium is established in dynamic terms for the gas, the liquid and the mixture. Accelerations are calculated in the computational mesh. Velocities, displacements and strains are obtained into the material points. Soil properties are updated and mass balance equations provide the relationships to find liquid and gas pressures. The outlined computational cycle is an explicit marching scheme in time. This approach do not allow physical separation (different domains) between the granular skeleton and fluid phases.

A validation has been carried out by means the modelling of an infiltration problem. Numerical results have been compared with analytical expression.

7

Chapter 7

Rainfall Effects on an Embankment Slope

The main trigger of landslides is heavy or prolonged rainfall. A global survey of landslide occurrence in the 12 months to the end of September 2003 (Mandal and Maiti, 2015) revealed that there were 210 damaging landslide events worldwide. Of these, over 90% were triggered by heavy rainfall. Therefore, the importance of rainfall as a trigger for landslides can not be underestimated.

In this Chapter there is an interest in examining the behaviour of unsaturated slopes subjected to rain infiltration. In addition to determine the conditions leading to the onset of instability, another objective is to test the capability of the 3-phase 1-point MPM formulation to follow the run-out of the unstable mass and to determine the travelled distance, velocities and accelerations. All of these variables define the risk and the destructive power of landslides.

Initially, in Section 7.1, a suction dependent elastoplastic Mohr-Coulomb model, expressed in terms of net stress and suction variables is presented. Then, the instability of a slope subjected to rain infiltration, inspired from a real case, is solved and discussed (Sec.7.2). The model shows the development of the initial failure surface in a region of deviatoric strain localisation (Sec.7.3) and the evolution of stress and suction states in some characteristic locations (Sec.7.4); and the dynamics of the motion characterised by the history of displacement, velocity and acceleration of the unstable mass (Sec.7.5). The concluding remarks are given in Section 7.6.

7.1 Constitutive modelling: Mohr-Coulomb with suction dependence

The instability is essentially governed by the evolution of apparent soil cohesion and friction angle with the evolving suction. The shear strength of unsaturated soils has been examined by several authors (Delage and Graham, 1996; Escario and Juca, 1989; Fredlund et al., 1978; Gan et al., 1988). The most commonly used shear strength criterion was proposed by Fredlund et al. (1978), which considers a a linear increase of the apparent cohesion with suction. However, further investigations, showed that such increase is not constant (Escario and Juca, 1989; Gan et al., 1988). It is observed that the increase of apparent cohesion is not constant but decreases for high suction values. On the other hand, the friction angle can increase or decrease, but usually it does not vary much with suction.

Some experimental results from Escario and Juca (1989); Gan et al. (1988) are shown in Figures 7.1 and 7.2. The variation of shear strength with suction is illustrated. It is clear that cohesion increase nonlinearly with suction, while friction angle slightly increases.

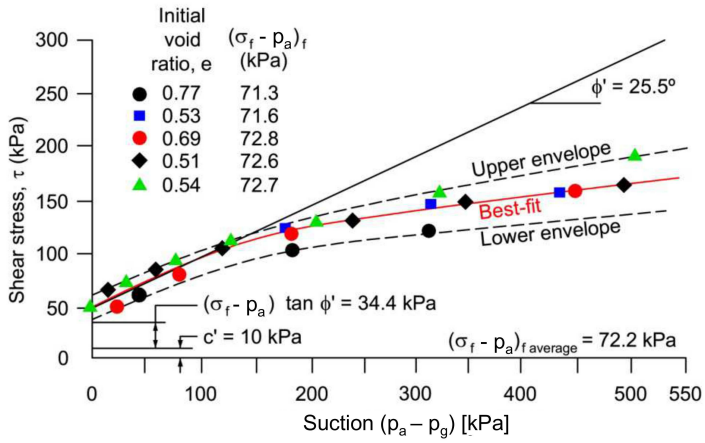

Figure 7.1: Failure envelope and variation of friction angle with suction from suction controlled direct shear tests on a glacial till (Gan et al., 1988)

In addition, it has been found also that it depends on the current degree of saturation (Han et al., 1995; Vaunat et al., 2002), but this dependence has not been included here for simplicity.

Here, the soil shear strength is defined by the Mohr-Coulomb yield function,

$$q = ccos\varphi + \bar{p}sin\varphi \tag{7.1}$$

where $\bar{p}$ is the volumetric net stress. The strength parameters, c and φ, are written as follows,

$$c = c' + c_s \tag{7.2}$$

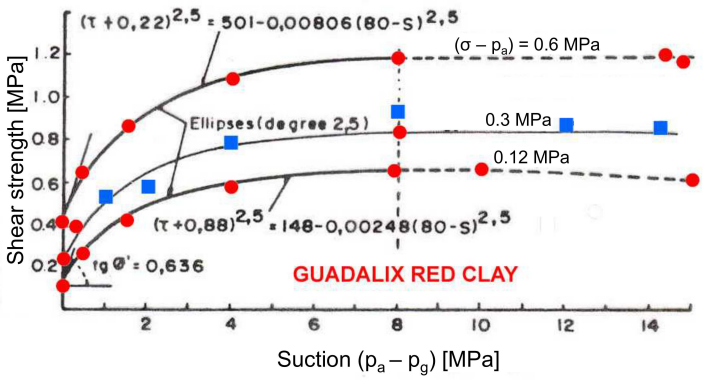

Figure 7.2: Variation of shear strength with suction and vertical stress. Guadalix red clay (Escario and Juca, 1989)

$$\varphi = \varphi' + \varphi_s \tag{7.3}$$

where c' and φ' correspond to the cohesion and friction angle for saturated conditions. The second terms of equations (7.2) and (7.3) includes the effect of suction in the material strength. It is accepted that cohesion increases with suction exponentially up to a maximum value $\triangle c_{max}$.

$$c_s = \triangle c_{max}(1 - e^{-Bs/p_{atm}}) \tag{7.4}$$

In which p_{atm} is the atmospheric pressure and B controls the rate of variation of apparent cohesion with suction. On the other hand, the friction angle is assumed to have a linear dependence with suction depending on parameter A.

$$\varphi_s = A(s/p_{atm}) \tag{7.5}$$

Obviously, other expressions could be introduced.

In order to reduce the singularities of the Mohr-Coulomb yield surface, an hyperbolic approximation is implemented (Abbo and Sloan, 1995). The same explicit sub-stepping algorithm with error control used in Section 5.2 has been applied, as well as a correction of the yield surface drift.

7.2 Case description

The problem solved was inspired in a real case described in Alonso et al. (2010b). Several road embankments of medium height (6-8 m) were subjected to heavy rainfall immediately after the end of construction. In some slopes, shallow failures, which damaged the road side shoulders, were observed. The slides moved downwards an estimated distance of 2-4 m. The embankments were built in summer time and the soil, a low to medium plasticity sandy clay, was compacted dry of optimum. Compaction conditions were investigated

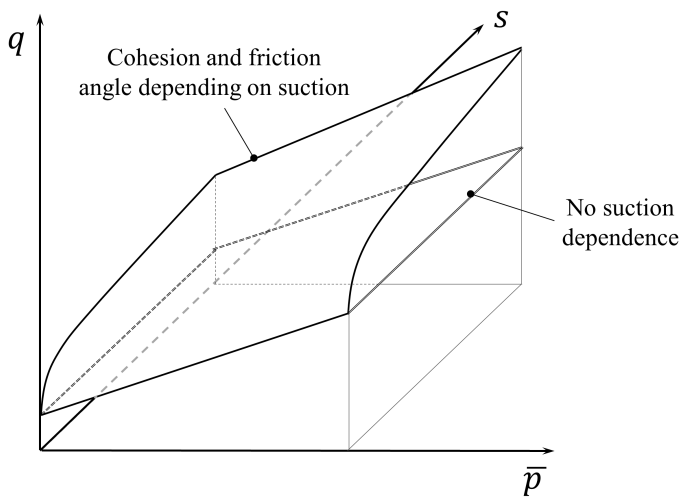

Figure 7.3: Scheme of the yield surface.

and some suction controlled direct shear tests were also carried out. The loss of strength upon soil saturation could be established.

The slope simulated has a height of 7 m and an angle of 32.5^o (Fig.7.4). The flat upper and lower surfaces reproduce the actual embankment geometry. The calculation was performed in three dimensions and plane strain conditions were assumed. The thickness of the model is 0.4 m.

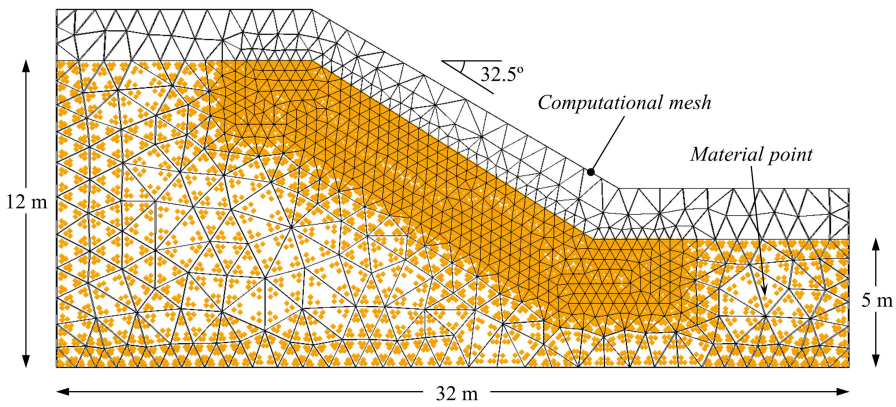

Figure 7.4: Geometry of the embankment slope, computational mesh and initial distribution of the material points.

Figure (7.4) also shows the computational mesh, formed by tetrahedrons, and the dis-

Table 7.1: Numerical parameters.

Numerical parameters	Value
Element type	Tetrahedron
Number of elements	3654
Number of material points	7593
Damping factor α	0.05
Time step $[s]$	$2 \cdot 10^{-4}$

tribution of material points. Those are initially distributed within each element and are initially located at the corresponding integration points of a 4-point Gaussian quadrature. The computational mesh covers a larger volume to allow for the expected large displacements associated with the slope instability.

MPM as well as FEM are mesh dependent. Some authors have discussed the influence of the number of material points and the mesh size on the accuracy of the solution (Abe et al., 2014; Buzzi et al., 2008).Buzzi et al. (2008) have shown that the mesh size is more determinant than the number of material points. Moreover, separation and splitting in an MPM discretisation also depends on the mesh size because the material points remain numerically "in contact" while they have a node in common. This fact is due to the no-slip contact, which is naturally included in the MPM formulation, and it may lead to non-physical increase of the stiffness of the material when it tends to separate (Huang et al., 2011). Although the degree of mesh dependency has not been established in this case, the mesh has been refined and made homogeneous in the region where the failure is expected in order to get accurate results.

Other numerical parameters are presented in Table 7.1. In this calculation a small value of damping (α=0.05) was adopted which may represent the friction that can occur between grains. A low value allows capturing the acceleration of the mass motion and reduces spurious numerical instabilities. A too high value of damping would slow down any movement of the soil.

Regarding boundary conditions, the lower boundary is fixed and horizontal displacements along vertical contours are prevented. Lateral and bottom contours are impervious for the liquid phase. A constant zero gas pressure in excess of atmospheric pressure is prescribed in all the boundaries (p_g=0 kPa).

The initial stresses and pore pressures of the slope are in equilibrium with the gravity force and the prescribed suction (s_0=800 kPa) distributed along the slope surface, which is in contact with the atmosphere. This initial suction was estimated from the known values of the compaction water content and the water retention curve determined experimentally.

The rainfall induced wetting is modelled by applying a decrease of suction on the ground surface from 800 to 0 kPa during 10 seconds. Afterwards, the saturated boundary condition (s=0 kPa) is maintained constant on the ground surface during the entire simulation period. An essentially downward flow is generated in the embankment due to suction

Table 7.2: General characteristics of the soil.

Material property	Value
Soil density [kg/m^3]	2700
Porosity	0.35
Poisson ratio	0.33
Young's modulus [MPa]	10
Liquid density [kg/m^3]	1000
Gas density [kg/m^3]	1
Liquid bulk modulus [MPa]	100
Gas bulk modulus [MPa]	0.01
Liquid viscosity [kg/ms]	0.001
Gas viscosity [kg/ms]	10^{-6}
Intrinsic permeability liquid [m^2]	10^{-10}
Intrinsic permeability gas [m^2]	10^{-11}

Table 7.3: Mohr-Coulomb parameters.

Parameter	Value
Cohesion $[kPa]$	1
Effective friction angle [°]	20
$\triangle c_{max}$ [kPa]	15
B	$7{\cdot}10^{-4}$
A	10^{-4}

Table 7.4: Retention curve parameters.

Parameter	Value
S_{min}	0
S_{max}	1
p_0 [kPa]	50
λ	0.09

gradients.

The embankment soil is assumed to be homogeneous and the properties of the different phases forming the soil (solid-liquid-gas) are presented in Table 7.2. Neither water vapour nor dissolved gas have been taken into account in this calculation. Therefore the liquid phase is pure water and the gas phase is considered to be dry air.

The water saturated permeability of the embankment was increased to accelerate wetting times and to reduce the computational time.

The elastoplastic suction-dependent Mohr-Coulomb model simulates the soil behaviour and the parameters of the constitutive model are summarised in Table 7.3. The elastoplastic suction-dependent Mohr-Coulomb model simulates the soil behaviour and the con-

stitutive parameters are summarised in Table 7.3. A small cohesion (1 kPa) is assumed under saturated conditions to avoid numerical difficulties in zones of very low effective confinement. The friction angle at saturated conditions was found to be close to 20^o in direct shear tests performed on recovered samples. These parameters lead to unstable conditions, in a limit equilibrium analysis, in a situation of full saturation of the slope and zero suction. The slope remains initially stable thanks to the additional strength induced by the suction which depends on parameters A, B and $\triangle c_{max}$ (Eq.7.4 and Eq.7.5). The estimated A value leads to a very small variation in friction with suction: less than 1° for the maximum range of change on suction (800 kPa). The selected B and $\triangle c_{max}$ values leads to a progressive reduction of cohesion with suction from a value c=67 kPa at the initial state (s=800 kPa) to c'=1 kPa for saturated conditions.

The parameters of the water retention curve (Eq.6.28) are listed in Table 7.4. The shape of the van Genuchten model is shown in Figure 7.5. The estimated field permeability of the embankment was increased to accelerate wetting times and to reduce the computational time.

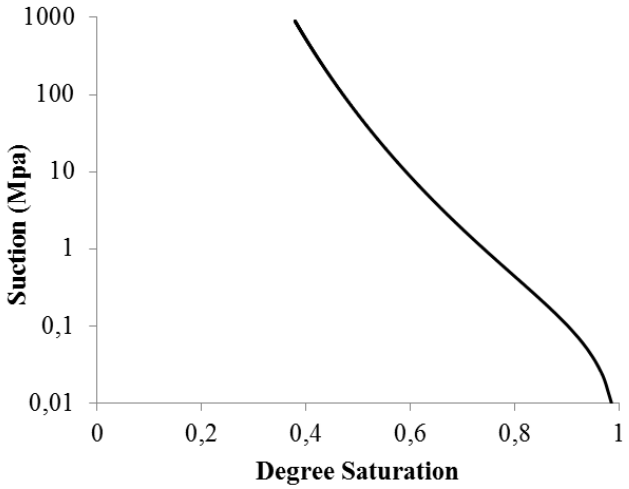

Figure 7.5: Water retention curve considered for the calculation.

7.3 Embankment response

In order to analyse the embankment behaviour, attention will focus on four material points located in the lower half of the embankment, close to the boundary slope, at depths of 0.5 m and 1.7 m. These shallow depths have been selected since a relatively shallow failure is expected in this case because the loss of suction is faster the closer to the boundary subjected to rainfall. The points (S1, S2, D1 and D2) are represented in Figure 7.6a. The evolution of suction may be followed in Figure 7.6. Contour plots of equal suction, at five different times, are selected: t_1=0 s, t_2=20 s, t_3=35 s, t_4=130 s and t_5=200 s.

The first 20 seconds result in a major change in suction if compared with the initial state characterised by an essentially constant value (s=700-800 kPa). The initial (t_1=0 s) vertical suction gradient reflects flow equilibrium conditions in view of the imposed boundary conditions.

Also shown in the figure are the contours of deviatoric plastic strain. High shear strains begin to develop at the slope toe soon after the beginning of wetting. A shear band defining a potential shallow failure surface at an average depth of 1.5 m is already defined at this early time. However the material points S1, S2, D1 and D2 remain essentially on their original positions. The slope is still stable. A few seconds later, t_3=35 s, the shear band is already well developed and a failure surface is defined. The slope becomes unstable and this is shown by the new positions of the control points (Figure 7.6e). The displacement vector of point S2 shows that the central part of the slope surface is having the maximum motion. The sliding mechanism is also appreciated by the successive shapes of the slope as wetting continues to increase. Soil masses located in the central and upper parts of the slope slide down and pass over the material points located in the slope toe (point S1) which experiences small displacements. The lowest point, D2, remains motionless because it is located below the shear band.

It is also interesting to check that small positive water pressure (negative values of suction in the figure) can be observed at some material points close to the bottom boundary on the right side of the embankment, at times t_4 and t_5 (sketched in Figures 7.6g and 7.6i).

The final run-out can be quantified to be 2.5 m, if it is defined as the distance between the initial toe of the slope and the toe of the final geometry. The wetting process is also illustrated in Figures 7.7 and 7.8. Figure 7.7 shows the evolution of "green field" suction for the left and right boundaries. We understand "green field" conditions, in the context of this example, as the conditions of the upper and lower horizontal "half spaces" in the absence of the presence of the slope. This condition is approximated by the left and right vertical boundaries of the example. The fast reduction of suction on the upper parts of the soil is well illustrated in the plots of Figure 7.7. Note that small positive pore water pressures are calculated in the lower part of the slope at t_5=200 s. Saturation is faster in this part of the slope. This is a consequence of the position of the impervious bottom boundary, which is closer to the ground surface (5 m below the surface) than on the left side (12 m below the surface). At the end of the calculation period the water still moves downwards in the left portion of the domain. However, on the left side the water begins to accumulate on the lower part ant the flow is directed towards the right, following pressure gradients.

Figure 7.8 shows the evolution of liquid pressure and the degree of saturation of points S1, S2, D1 and D2. Note that the plots of Figures 7.8a and 7.8b are directly related between them by the water retention relationship. According to the initial suction distribution, the degree of saturation at t_1=0 s is approximately 0.758. Points located at the same depth have similar wetting evolution. The reduction of suction is faster in shallow points (S1, S2) than in deeper points (D1, D2). As the calculation proceeds the degree of saturation increases and approaches almost fully saturated conditions at the end of the calculation

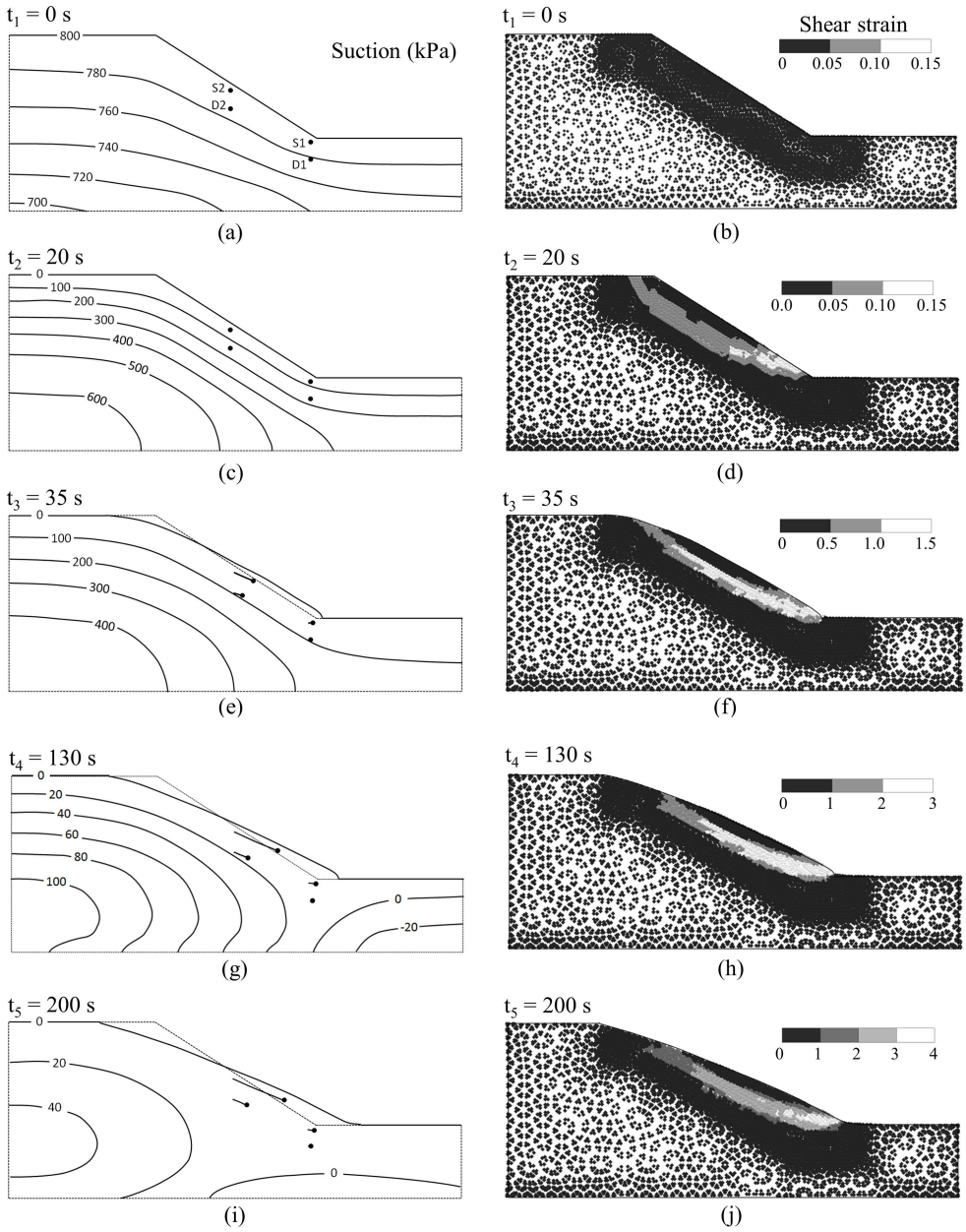

Figure 7.6: Calculated suction and equivalent shear strain contours at 5 different times (t_1, t_2, t_3, t_4 and t_5). The paths of 4 control material points (S1, S2, D1 and D2) are indicated.

period. However, significant suctions remain inside the embankment at this time (Figure 7.6i).

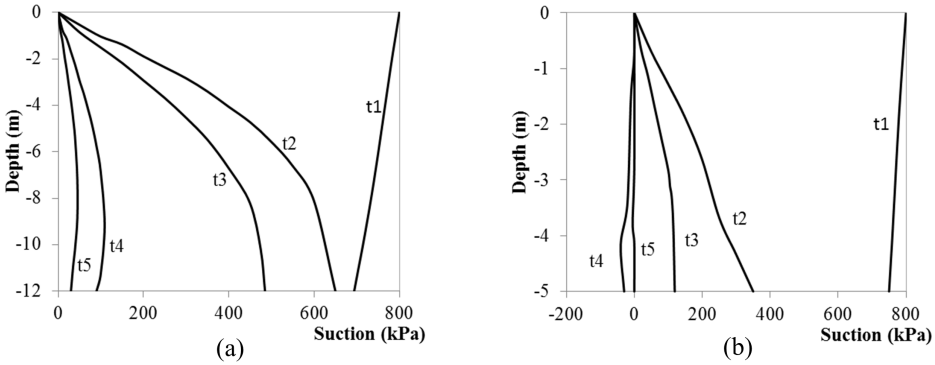

Figure 7.7: Suction evolution green field at 5 different times: (a) left boundary and (b) right boundary.

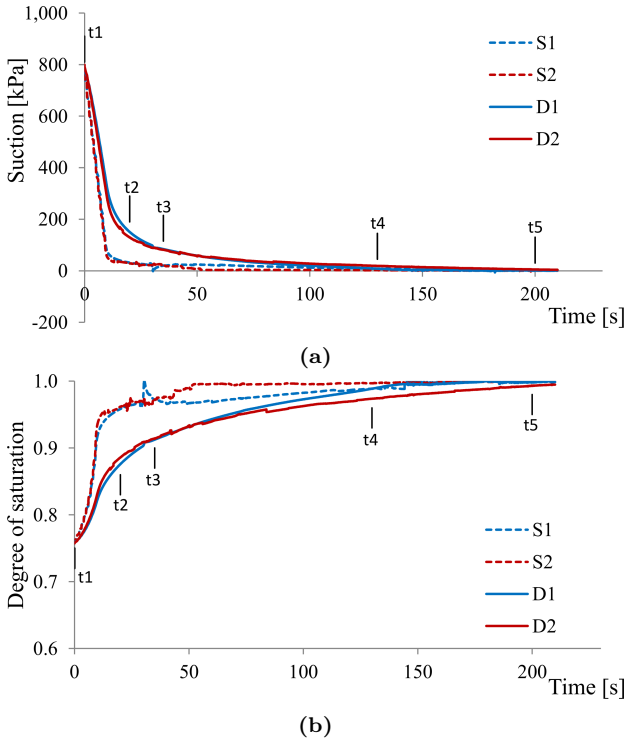

Figure 7.8: Evolution of (a) suction and (b) degree of saturation evolution of material points S1, S2, D1, D2.

7.4 Stress-suction-time

The stress evolutions have been analysed for the four control points (S1, S2, D1 and D2) and are presented in Figures 7.9, 7.10 and 7.11. Figure 7.9 shows the evolution of net mean stress and Figure 7.10 shows the evolutions of shear stress and the corresponding yield stress.

In these two figures some oscillations are observed. Because of the dynamic formulation, whenever there is an unbalanced force in a node, some elastic waves are generated and cross the domain reflecting at the boundaries (if the boundaries are not absorbing boundaries, as the case solved in the example). A sudden change of external or internal forces can be the reason of the excitation. For example, these could be related with some remaining cell crossing noise (Bardenhagen and Kober, 2004) during the motion of the slide. A sudden decrease of the stress level due to softening can also be a cause of the oscillations.

Another reason that can explain the onset of oscillations is a sudden change of the stiffness of the soil (Fig.6.4). Comparing Figures 7.9 and 7.10 with Figure 7.8b it can be noted that these oscillations are mainly originated when the degree of saturation of the material point is close to one (saturated material).

A smoothing of results has been introduced in Figures 7.9 and 7.10 to facilitate the plot of stress paths in Figure 7.11. The superimposed plot of the available Mohr-Coulomb strength provides an additional insight into the slope behaviour. The material point S1 at the slope toe is essentially yielding at the start of the simulation (Figure 7.10a) and it maintains plastic conditions throughout the sliding process. Point S2, the shallow point at mid slope plastifies about 12 s after the beginning of rainfall and it remains in a plastic state. D2, which is located within the shear band, behaves essentially as S2. Point D1 at the slope toe, at a certain depth, is apparently in an elastic state throughout the sliding process although it appears to be very close to plastification at the final stages of sliding (Fig.7.10b).

Stress paths in a $\bar{p} - q$ plane, plotted in Figure 7.11, offer a more precise information on the evolution of plastic states. Initially, when the wetting starts but the slope is still stable (from t_1 to t_2), the stress state for the deeper and more confined points (D1, D2) changes slightly. However, shallower points subjected to higher shear stresses such as the toe of the slope (S1) are subjected to a faster decrease of suction and a loss of strength is associated with suction softening. S1 is under plastic conditions from the beginning of the calculation. The material point remains on the yield surface as it shrinks, due to the rapid loss of suction. The point initially experiences a decrease in net mean stress, which is later recovered as the slide "flows" over this point.

The slide motion begins between times t_2 and t_3. Those points located mid-slope, in the "active" area of the failure (S2 and D2), suffer a small increase of mean and shear stresses but they remain in the current yield surface. Points located in the "passive"

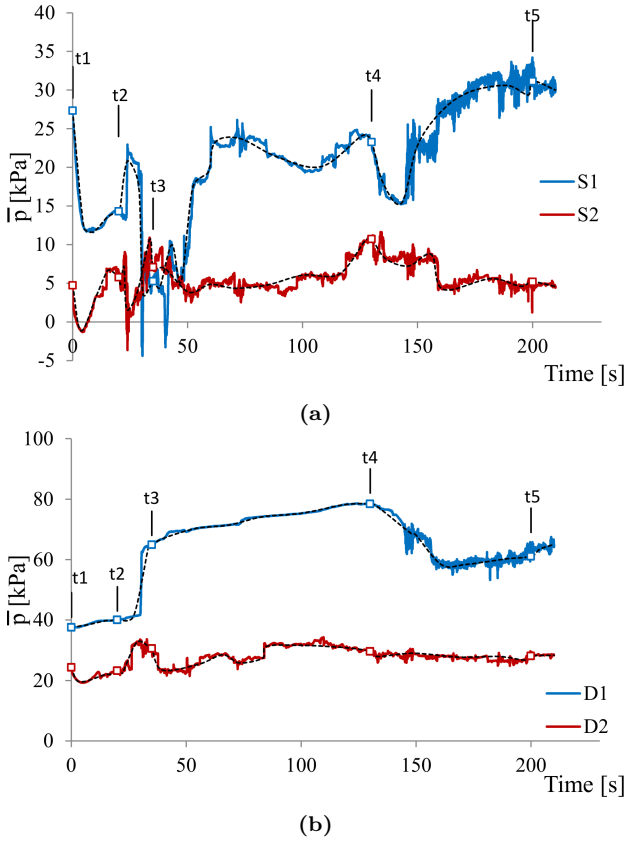

Figure 7.9: Calculated volumetric net stress evolution of (a) shallow points (S1, S2) and (b) deep points (D1, D2).

area experience large stress changes. The shallower S1 point softens because of the rapid reduction of suction. Beyond t_3, those points located at mid-slope (S2 and D2) maintain the stress state rather constant. Confinement increases on S1 and it is capable of offering more shear strength. The deeper D1 point is able to resist the stress changes associated with the change in slope geometry and the overall softening of the upper part of slope. D1 remains elastic but close to the failure envelope for saturated states at the advanced stages of wetting.

7.5 Dynamics of the motion

The model provides also information on the overall dynamic behaviour of the slide. This is a significant improvement over static formulations. The calculated total displacement, velocity and acceleration of S1, S2, D1 and D2 are shown in Figure 7.12. Velocities and accelerations represented in Figures 7.12b and 7.12c have been calculated by applying

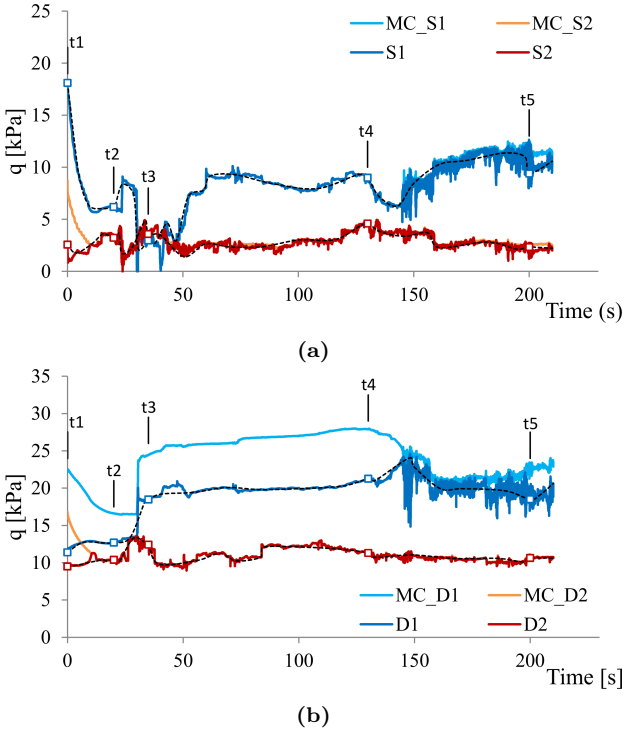

Figure 7.10: Calculated shear stress evolution of (a) shallow control points (S1, S2) and (b) deep control points (D1, D2). Evolution of Mohr-Coulomb (MC) yield shear stress is also indicated for each point.

a smoothing on the total displacements. Analysing these plots it can be seen that the embankment remains essentially stable during the first 20 seconds after the initiation of wetting. At time t_2, the failure mechanism develops and control points located in the mobilised volume (S1, S2 and D2) start moving. They accelerate fast during fifteen additional seconds. Peak velocity is attained at $t_3 = 35$ s. After a peak value, the velocity and the acceleration decrease ant the slope tends to stabilise. The resting period may be divided in two parts: a fast decrease of velocity and acceleration followed by a progressive reduction of velocity towards a new state of equilibrium. This reaction cannot be generalised and it will depend strongly on the slope geometry. The lower horizontal platform contributes, in the example solved, to arrest the motion after a relatively small displacement. The control point S2 moves 4 m, reaches a maximum velocity of 0.1 mm/s and achieves an acceleration of 9 mm/s^2. Note that the dynamic variables depend on the position of the point within the slope. Establishing a slope run-out requires some conventions. For instance, if it is defined as the distance between the slope toes before and after failure, a run-out of 2.5 m is calculated, as mentioned before. This is a smaller value than the distance travelled by the material points located at mid-slope, close to the surface, but larger than other material points examined in this analysis.

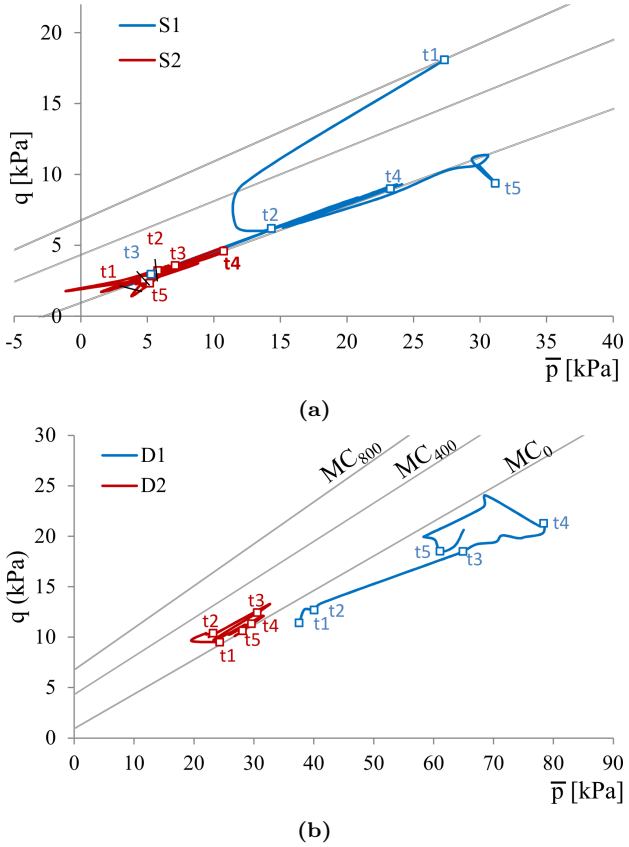

Figure 7.11: Stress paths of (a) shallow points (S1, S2) and (b) deep points (D1, D2). Mohr-Coulomb criterion is represented for three different suctions (800 kPa, 400 kPa and 0 kPa).

7.6 Concluding remarks

The general 3-phase 1-point MPM formulation has been applied to unsaturated soils described by an elastoplastic suction dependent Mohr-Coulomb model formulated in terms of two stress fields: net stress and suction.

The instability of unsaturated slopes induced by rainfall wetting is a relevant practical problem in virtually all climate and soil conditions. The method handles in a natural way the kinematics of sliding and it provides information on velocities, accelerations and run-outs, which help to estimate the expected damage in case of sliding.

A simple embankment slope, whose characteristics were taken from a real case, has been analysed. It involves surface instability induced by heavy rains. The model provides an insight into the coupled flow-stress-strain mechanisms developing in the slope. Suction

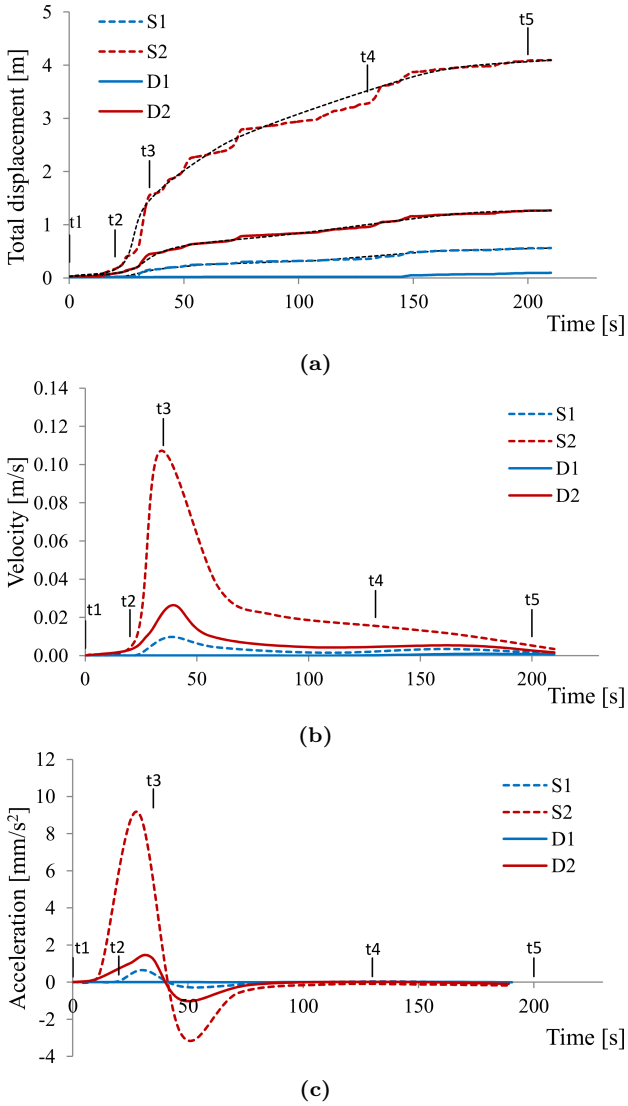

Figure 7.12: Evolution of (a) total displacement, (b) velocity and (c) acceleration of material points S1, S2, D1 and D2.

decrease results in a marked strength softening. Deviatoric strain localisation starts at the slope toe and eventually materialises into a full sliding zone. The slope motion starts when a shallow band of soil reaches a low (but non-zero) suction value and accelerates in a few seconds. The slide does not displace as a rigid body, however. Points close to the surface experience a faster and more intense suction reduction and their strength reaches soon the minimum value (saturated conditions). They are capable of "flowing" over the more resistant zones at depth. The end result is a complex motion which makes it difficult to define run-out, velocity and acceleration in a clear and simple way. In fact,

these variables depend on the material point position within the sliding volume. This is believed to be the case in practise when observing rain-induced instabilities.

The MPM, as formulated in Chapter 6, is an advanced prediction tool to investigate the stability of slopes in partially saturated soils.

Other large deformation problems, such as wetting induced collapse or swelling may be analysed by the same method but they will require the consideration of a different constitutive model. However, the general formulation of the three phase approach described will remain unchanged.

8

Chapter 8
Conclusions and Future Work

The aim of this Chapter 8 is to present the main conclusions of the research carried out. They respond to compliance with the general and specific objectives exposed in Chapter 1. Finally, some future research lines with which to continue the work of this Thesis are suggested.

8.1 Final conclusions and contributions

This Thesis deals with the modelling of large deformations in geotechnical problems by means the Material Point Method. It focusses on studying brittle failures and slope instabilities from static conditions to run-out in saturated and unsaturated materials.

Among the most common numerical techniques used in solid and fluid mechanics, MPM shows some attractive features against others when solving large displacements. The method handles in a natural way the kinematics of sliding and it provides information on velocities, accelerations and run-outs, which help to estimate the expected damage in the case of sliding. That makes it a powerful tool in geotechnics but also in many other engineering fields.

The dynamic MPM formulations for mechanic (1-phase material) and hydromechanic (2-

phase material) problems have been presented in detail. They are integrated explicitly in time. A numerical stability analysis has been carried out and an analytical expression for the critical time step has been determined. It depends not only on the mesh element size, but also on the material permeability. Small values of permeability lead to very restrictive time steps. Other parameters, such as density and porosity, also have some influence in the time step values. This fact leads to high computation time for low pervious materials.

The study focuses on the modelling of brittle materials, such as cemented soils and overconsolidated plastic clays. These materials are characterised by a strain softening behaviour. The available strength reduces from peak to residual state with increasing plastic strain. A strain-softening Mohr-Coulomb constitutive model has been presented in order to simulate this non-linear behaviour. In addition, in order to avoid mesh dependent strain-localisation problems associated with strain-softening features, a regularisation technique based on the smeared crack approach is proposed. It consists of calibrating a shape factor η included in the softening laws.

Different slope instabilities were presented. In all cases, the trigger factor is an increase of pore water pressures, and the establishment of initial stresses is the result of the effect of gravity.

First, the Selborne slope experiment is simulated. This case, well identified with laboratory data, has been an opportunity to perform a validation of the MPM formulation. Such analysis provides remarkably consistent results: the failure progression and the final calculated displacement pattern (maximum displacements are about 4 m) fit well with measured data.

The relevance of internal degradation of the mobilised mass in a compound slide, based on a simplified geometry of the Vajont landslide, is analysed in a second modelling. It has shown that a kinematically admissible failure mechanism in compound slides requires internal shearing of the mobilised mass. The location of such internal shear bands is controlled by the geometry of the basal sliding surface. Moreover, the post-failure velocity and the final run-out of the Vajont slide are simulated by an additional reduction of the basal friction angle, which coincides with thermal pressurisation theories.

The effect of brittleness on the onset of failure and run-out was also studied by means of a parametric study varying peak and residual strength. Run-out, understood as the distance between the toe of the initial slope and the toe after failure, is found to be directly related with brittleness index I_B. Meanwhile the onset of failure and the failure geometry are controlled by both peak and residual strengths, the post-failure behaviour is more influenced by the residual state.

Progressive failure mechanisms, typical of brittle materials, have been simulated in all examples. The mobilised strength is a good measure that allows the identification of the failure propagation along the initial failure surface. The failure propagation occurs in a different way depending on the simulation, but it follows a pattern. In all cases, the maximum achieved averaged mobilised strength (mobilised strength averaged along the

failure mechanism) is a value in between peak and residual conditions. The arrival at this maximum strength can coincide with the first point reaching peak state. Later on, the average mobilised strength is essentially constant until the last point entering in the softening behaviour. Immediately after, a final drop in average mobilised strength down to a residual value appears, triggering the instability and the subsequent acceleration.

Finally, a step forward in the application of MPM to multi-phase problems in porous media has been achieved. In order to simulate the behaviour of unsaturated materials, it is necessary to consider the interaction of three different phases: solid liquid and gas. Therefore, a coupled 3-phase 1-point MPM formulation capable of modelling partially saturated soils has been presented. Meanwhile dynamic equilibrium of phases are posed at the nodes of the mesh, mass balance equations of the species (air, water, minerals) as well as all constitutive relationships are formulated at a material point level. This approach considers a 3-phase mixture within each material point and has been validated by means the modelling of an infiltration problem.

An embankment slope instability, induced by heavy rains has been simulated. The model is based on a real case and it provides an insight into the coupled flow-stress-strain mechanisms developing in the slope. An elastoplastic suction dependent Mohr-Coulomb model formulated in terms of two stress fields (net stress and suction) has been implemented in order to model strength variations due to suction changes. Therefore, suction decrease in the slope results in a marked strength softening. The result is a complex motion which makes it difficult to define run-out, velocity and acceleration in a clear and simple way, as happens in practise when observing rain-induced instabilities.

Other large deformation problems, such as wetting induced collapse or swelling may be analysed by the same approach but they will require the consideration of a different constitutive model. However, the general 3-phase formulation described will remain unchanged.

It can be finally concluded that MPM is capable of simulating large displacements in complex materials and in multi-phase flows. This numerical tool has a good potential to examine in a unified calculation the conditions leading to slope failure but, also, it is capable of following the evolution of the unstable mass determining its final run-out, which is essential to evaluate the consequences of the instability and prevent severe damage.

8.2 Future work

One of the most important limitations of the presented dynamic MPM formulation is that the explicit algorithm is conditionally stable. Despite the existence of some numerical techniques to increase the critical time step, the explicit scheme is definitely not well-suited to simulate long term problems. Therefore, other integration schemes should be implemented in order to optimise the computational time.

Due to the difficulty to determine the initial stress field, in this Thesis it is assumed that initial stresses are the result of the gravitational effect. Improving the calculation of the initial stress distribution is an important issue that should be considered in future works, specially when non-linear materials are involved.

Other applications associated with unsaturated soils involving large deformations and history-dependent constitutive models can be modelled with the general 3-phase MPM formulation described in this study. However, the implementation of more realistic constitutive models is required. This is the case of swelling problems in expansive clays or collapse behaviour of low density materials.

The multi-phase MPM formulation proposed in this Thesis is capable to model solid-pore fluid couplings within the same domain. However, the interaction with free water is neglected in this analysis. Therefore, the implementation of multi-point formulations capable of modelling interactions between free fluid phases and pore fluids opens a wide range of applications in geotechnics and hydrodynamics.

The effects of temperature changes can also be considered. Especially in those cases where heat-induced excess pore pressures on the failure surface are capable of cancelling the normal stress. Then, the effective stress and the shearing resistance become negligible. As a result, the slide can accelerate very fast reaching high velocities in a few seconds.

A

Appendix A

Development of Momentum Balance Equations

In this Appendix, the strong forms (differential equation) of the momentum balance equations for liquid (Eq.6.13), gas (Eq.6.14) and mixture (Eq.6.15), are transformed to the weak forms (integral equation) using Weighted Residuals method. Then, the momentum balance equations are discretised considering the two MPM frames: nodes and material points.

A.1 Weak form of the momentum balance equation of fluid phases

Momentum balance equation is solved in a boundary value problem for the two fluid phases. To avoid the repetition of similar equations, in the following, the subscript f indicates the fluid phases corresponding to liquid and gas. Notice that s remains to indicate the solid phase.

Equation (A.1) is the strong form of momentum balance equations (A.2) and (A.3) the

corresponding displacement and pressure boundary conditions.

$$\rho_f \mathbf{a}_f = \nabla p_f - \frac{nS_f\mu_f}{k_f}(\mathbf{v}_f - \mathbf{v}_s) + \rho_f \mathbf{b} \tag{A.1}$$

$$\mathbf{u}_f(\mathbf{x},t) = \widehat{\mathbf{u}}_f(t) \text{ on } \partial\Omega^{\mathbf{u}_f} \tag{A.2}$$

$$p_f(\mathbf{x},t)\mathbf{n} = \widehat{\mathbf{p}}_f(t) \text{ on } \partial\Omega^{p_f} \tag{A.3}$$

The weak form is derived by multiplying equation (A.1) by a test function $\delta\mathbf{u}_f$ and integrating over the total domain Ω. In addition, the integration by parts and the divergence theorem are applied to the term with the liquid pressure gradient. Considering that any test function can be selected, in particular one that is zero on the boundary where displacements are prescribed $\partial\Omega^{\mathbf{u}_f}$, the above equation can be written as

$$\begin{aligned}\int_\Omega \rho_f \delta\mathbf{u}_f \cdot \mathbf{a}_f d\Omega = \int_{\partial\Omega^{p_f}} \delta\mathbf{u}_f \cdot \widehat{\mathbf{p}}_f d\partial\Omega^{p_f} - \int_\Omega (\nabla\cdot\delta\mathbf{u}_f) p_f d\Omega \\ - \int_\Omega \frac{nS_f\mu_f}{k_f}\delta\mathbf{u}_f\cdot(\mathbf{v}_f - \mathbf{v}_s)d\Omega + \int_\Omega \rho_f \delta\mathbf{u}_f\cdot\mathbf{b}d\Omega\end{aligned} \tag{A.4}$$

where $\partial\Omega^{p_f}$ is the boundary where the fluid pressure is prescribed.

Taking into account equation (6.33) particularised for the test function $\delta\mathbf{u}_f$, fluid velocity $\mathbf{v}_f$, solid velocity $\mathbf{v}_s$ and fluid acceleration $\mathbf{a}_f$, the integral form (Eq.A.4) is discretised on the nodes. Using the subscripts i and j to denote the nodal variables, the equation results in the following expression.

$$\begin{aligned}\sum_{i=1}^{N_n}\delta\mathbf{u}_{f_i}\cdot\sum_{j=1}^{N_n}\int_\Omega \rho_f N_i N_j \mathbf{a}_{f_j} d\Omega = \sum_{i=1}^{N_n}\delta\mathbf{u}_{f_i}\cdot\int_{\partial\Omega^{p_f}} N_i\widehat{\mathbf{p}}_f d\partial\Omega^{p_f} \\ - \sum_{i=1}^{N_n}\delta\mathbf{u}_{f_i}\cdot\int_\Omega(\nabla N_i)\cdot p_f\mathbf{m}d\Omega \\ - \sum_{i=1}^{N_n}\delta\mathbf{u}_{f_i}\cdot\sum_{j=1}^{N_n}\int_\Omega \frac{nS_f\mu_f}{k_f}N_iN_j(\mathbf{v}_{f_j}-\mathbf{v}_{s_j})d\Omega \\ + \sum_{i=1}^{N_n}\delta\mathbf{u}_{f_i}\cdot\int_\Omega \rho_f N_i\mathbf{b}d\Omega\end{aligned} \tag{A.5}$$

Because the components of the test function are arbitrary except at constrained boundary nodes where the components of displacement are prescribed, the previous scalar equation can be expanded into a system of equations. Rearranging terms, it can be shown that

$$\begin{aligned}\sum_{i=1}^{N_n}\int_\Omega \rho_f N_i N_j d\Omega \mathbf{a}_{f_j} = \int_{\partial\Omega^{p_f}} N_i\widehat{\mathbf{p}}_f d\partial\Omega^{p_f} - \int_\Omega(\nabla N_i)\cdot p_f\mathbf{m}d\Omega \\ - \sum_{j=1}^{N_n}\int_\Omega \frac{nS_f\mu_f}{k_f}N_iN_j d\Omega(\mathbf{v}_{f_j}-\mathbf{v}_{s_j}) + \int_\Omega \rho_f N_i\mathbf{b}d\Omega\end{aligned} \tag{A.6}$$

Finally, the spatial discretisation is further carried out with the introduction of equation (6.31). It is equivalent to consider a quadrature over the material points, in which the integrals are approximated by sums. The subscripts or superscript p is used to denote particle variable.

$$\sum_{j=1}^{N_n}\Big(\sum_{p=1}^{N_p}\widetilde{m}_{f_p}{N_i}^p{N_j}^p\Big)\mathbf{a}_{f\,j}=\int\limits_{\partial\Omega^{p_f}}N_i^p\widehat{\mathbf{p}}_f d\partial\Omega^{p_f}-\sum_{p=1}^{N_p}(\nabla N_i^p)\cdot p_f^p\mathbf{m}V_p \tag{A.7}$$
$$-\sum_{j=1}^{N_n}\Big(\sum_{p=1}^{N_p}\frac{nS_f\mu_f}{k_f}{N_i}^p{N_j}^pV_p\Big)(\mathbf{v}_{f\,j}-\mathbf{v}_{s\,j})+\sum_{p=1}^{N_p}\widetilde{m}_{f_p}{N_i}^p\mathbf{b}$$

In the previous equation V_p corresponds volume of the material point p, and N_i^p is the shape function of the node i evaluated on the corresponding material point location.

A.2 Weak form of the momentum balance equation of the mixture

The boundary value problem for the momentum balance of the mixture is the following, being equation (A.8) the strong form and expressions (A.9) and (A.10) the corresponding displacement and pressure boundary conditions.

$$\rho_s(1-n)\mathbf{a}_s+\rho_l nS_l a_l+\rho_g nS_g\mathbf{a}_g=\nabla\cdot\boldsymbol{\sigma}+\rho_m\mathbf{b} \tag{A.8}$$

$$\mathbf{u}_s(\mathbf{x},t)=\widehat{\mathbf{u}}_s(t)\text{ on }\partial\Omega^{\mathbf{u}_s} \tag{A.9}$$

$$\boldsymbol{\sigma}(\mathbf{x},t)\cdot\mathbf{n}=\mathbf{t}(t)\text{ on }\partial\Omega^{\mathbf{t}} \tag{A.10}$$

The weak form is derived by multiplying equation (A.8) by a test function $\delta\mathbf{u}$ and integrating over the total domain Ω. In addition, the integration by parts and the divergence theorem are applied to the term with the total stress gradient. Since test functions are arbitrary, in particular one that is zero on the boundary where displacements are prescribed, the above equation can be written as

$$\int\limits_\Omega\rho_s(1-n)\delta\mathbf{u}\cdot\mathbf{a}_s d\Omega+\int\limits_\Omega\rho_l nS_l\delta\mathbf{u}\cdot\mathbf{a}_l d\Omega+\int\limits_\Omega\rho_g nS_g\delta\mathbf{u}\cdot\mathbf{a}_g d\Omega= \tag{A.11}$$
$$\int\limits_{\partial\Omega^{\mathbf{t}}}\delta\mathbf{u}\cdot\mathbf{t}d\partial\Omega^{\mathbf{t}}-\int\limits_\Omega(\nabla\cdot\delta\mathbf{u})\cdot\boldsymbol{\sigma}d\Omega+\int\limits_\Omega\rho_m\delta\mathbf{u}\cdot\mathbf{b}d\Omega$$

where $\partial\Omega^{\mathbf{t}}$ is the boundary where the external traction is prescribed.

Taking into account equation (6.33) particularised for the test function $\delta\mathbf{u}$, solid acceleration $\mathbf{a}_s$, liquid acceleration $\mathbf{a}_l$ and gas acceleration $\mathbf{a}_g$, the integral form (Eq.A.11) is

discretised on the nodes. The equation results in the following expression.

$$\sum_{i=1}^{N_n}\delta\mathbf{u}_i\cdot\sum_{j=1}^{N_n}\int_\Omega\rho_s(1-n)N_iN_j\mathbf{a}_{s\,j}d\Omega+\sum_{i=1}^{N_n}\delta\mathbf{u}_i\cdot\sum_{j=1}^{N_n}\int_\Omega\rho_l nS_lN_iN_j\mathbf{a}_{l\,j}d\Omega \tag{A.12}$$
$$+\sum_{i=1}^{N_n}\delta\mathbf{u}_i\cdot\sum_{j=1}^{N_n}\int_\Omega\rho_g nS_gN_iN_j\mathbf{a}_{g\,j}d\Omega=$$
$$\sum_{i=1}^{N_n}\delta\mathbf{u}_i\cdot\int_{\partial\Omega^{\mathbf{t}}}N_i\mathbf{t}d\partial\Omega^{\mathbf{t}}-\sum_{i=1}^{N_n}\delta\mathbf{u}_i\cdot\int_\Omega(\nabla N_i)\cdot\boldsymbol{\sigma}d\Omega+\sum_{i=1}^{N_n}\delta\mathbf{u}_i\cdot\int_\Omega\rho_mN_i\mathbf{b}d\Omega$$

Because the components of the test function are arbitrary except at constrained boundary nodes where the components of displacement are prescribed, the previous scalar equation can be expanded into a system of equations. Rearranging terms, it can be shown that

$$\sum_{j=1}^{N_n}\Big(\int_\Omega\rho_s(1-n)N_iN_jd\Omega\Big)\mathbf{a}_{s\,j}+\sum_{j=1}^{N_n}\Big(\int_\Omega\rho_l nS_lN_iN_jd\Omega\Big)\mathbf{a}_{l\,j} \tag{A.13}$$
$$+\sum_{j=1}^{N_n}\Big(\int_\Omega\rho_g nS_gN_iN_jd\Omega\Big)\mathbf{a}_{g_j}=$$
$$\int_{\partial\Omega^{\mathbf{t}}}N_i\mathbf{t}d\partial\Omega^{\mathbf{t}}-\int_\Omega(\nabla N_i)\cdot\boldsymbol{\sigma}d\Omega+\int_\Omega\rho_mN_i\mathbf{b}d\Omega$$

Finally, the spatial discretisation is further carried out with the consideration of equation (6.31) in (A.14). It is equivalent to consider a quadrature over the material points, in which the integrals are approximated by sums.

$$\sum_{j=1}^{N_n}\Big(\sum_{p=1}^{N_p}m_{s_p}(1-n)N_i^pN_j^p\Big)\mathbf{a}_{s\,j}+\sum_{j=1}^{N_n}\Big(\sum_{p=1}^{N_p}m_{l_p}nS_lN_i^pN_j^p\Big)\mathbf{a}_{l\,j} \tag{A.14}$$
$$+\sum_{j=1}^{N_n}\Big(\sum_{p=1}^{N_p}m_g^pnS_gN_i^pN_j^p\Big)\mathbf{a}_{g\,j}=$$
$$\int_{\partial\Omega^{\mathbf{t}}}N_i^p\mathbf{t}d\partial\Omega^{\mathbf{t}}-\sum_{p=1}^{N_p}(\nabla N_i^p)\cdot\boldsymbol{\sigma}^pV_p+\sum_{p=1}^{N_p}m_pN_i^p\mathbf{b}d\Omega$$

A.3 Final system of momentum balance equations

The discrete momentum balance equations obtained in the previous developments for the fluid phases (Eq.A.7) and for the mixture (Eq.A.14), can be written in the same order, in a more compact form as follows

$$\widetilde{\mathbf{M}}_l\cdot\mathbf{a}_l=\mathbf{F}_l^{ext}-\mathbf{F}_l^{int}-\mathbf{Q}_l\cdot(\mathbf{v}_l-\mathbf{v}_s) \tag{A.15}$$

$$\widetilde{\mathbf{M}}_g \cdot \mathbf{a}_g = \mathbf{F}_g^{ext} - \mathbf{F}_g^{int} - \mathbf{Q}_g \cdot (\mathbf{v}_g - \mathbf{v}_s) \tag{A.16}$$

$$\mathbf{M}_s \cdot \mathbf{a}_s + \mathbf{M}_l \cdot \mathbf{a}_l + \mathbf{M}_g \cdot \mathbf{a}_g = \mathbf{F}^{ext} + \mathbf{F}^{int} \tag{A.17}$$

where $\mathbf{a}_s$, $\mathbf{a}_l$, and $\mathbf{a}_g$ are the nodal acceleration vectors for each phase, $\mathbf{v}_s$, $\mathbf{v}_l$, and $\mathbf{v}_g$ are the nodal velocity vectors, $\widetilde{\mathbf{M}}_l$ is liquid mass matrix per unit of liquid volume, $\widetilde{\mathbf{M}}_g$ is the gas mass matrix per unit of gas volume, $\mathbf{M}_s$ is the solid mass matrix per unit of total volume, $\mathbf{M}_l$ is the liquid mass matrix per unit of total volume, $\mathbf{M}_g$ is the gas mass matrix per unit of total volume, $\mathbf{F}_l^{ext}$ is the vector of the liquid external forces, $\mathbf{F}_g^{ext}$ is the vector of the gas external forces, $\mathbf{F}^{ext}$ is the vector of the external forces of the mixture, $\mathbf{F}_l^{int}$ is the vector of the liquid internal forces, $\mathbf{F}_g^{int}$ is the vector of the gas internal forces, $\mathbf{F}^{int}$ is the vector internal total forces of the mixture, $\mathbf{Q}_l$ and $\mathbf{Q}_g$ are the liquid and gas dragging matrixes. The mathematical expression for each term is the following:

$$\widetilde{\mathbf{M}}_l = \sum_{p=1}^{N_p} \mathbf{N}^T \cdot \widetilde{m}_{l_p} \mathbf{N} \tag{A.18}$$

$$\widetilde{\mathbf{M}}_g = \sum_{p=1}^{N_p} \mathbf{N}^T \cdot \widetilde{m}_{g_p} \mathbf{N} \tag{A.19}$$

$$\mathbf{M}_l = \sum_{p=1}^{N_p} \mathbf{N}^T \cdot m_{l_p} \mathbf{N} \tag{A.20}$$

$$\mathbf{M}_g = \sum_{p=1}^{N_p} \mathbf{N}^T \cdot m_{g_p} \mathbf{N} \tag{A.21}$$

$$\mathbf{M}_s = \sum_{p=1}^{N_p} \mathbf{N}^T \cdot m_{s_p} \mathbf{N} \tag{A.22}$$

$$\mathbf{Q}_l = \sum_{p=1}^{N_p} \mathbf{N}^T \cdot \frac{n S_l \mu_l}{k_l} \mathbf{N} V_p \tag{A.23}$$

$$\mathbf{Q}_g = \sum_{p=1}^{N_p} \mathbf{N}^T \cdot \frac{n S_g \mu_g}{k_g} \mathbf{N} V_p \tag{A.24}$$

$$\mathbf{F}_l{}^{ext} = \int_{\partial\Omega^{p_l}} \mathbf{N}^T \cdot \widehat{\mathbf{p}}_l d\partial\Omega^{p_l}\Big|_p + \sum_{p=1}^{N_p} \mathbf{N}^T \cdot \widetilde{m}_{l_p} \mathbf{b} \tag{A.25}$$

$$\mathbf{F}_g{}^{ext} = \int_{\partial\Omega^{p_g}} \mathbf{N}^T \cdot \widehat{\mathbf{p}}_g d\partial\Omega^{p_g}\Big|_p + \sum_{p=1}^{N_p} \mathbf{N}^T \cdot \widetilde{m}_{g_p} \mathbf{b} \tag{A.26}$$

$$\mathbf{F}^{ext} = \int_{\partial\Omega^{\mathbf{t}}} \mathbf{N}^T \cdot \mathbf{t} d\partial\Omega^{\mathbf{t}}\Big|_p + \sum_{p=1}^{N_p} \mathbf{N}^T \cdot m_p \mathbf{b} \tag{A.27}$$

$$\mathbf{F}_l{}^{int} = \sum_{p=1}^{N_p} \mathbf{B}^T \cdot p_{l_p} \mathbf{m} V_p \tag{A.28}$$

$$\mathbf{F}_g{}^{int} = \sum_{p=1}^{N_p} \mathbf{B}^T \cdot p_{g_p} \mathbf{m} V_p \tag{A.29}$$

$$\mathbf{F}^{int} = \sum_{p=1}^{N_p} \mathbf{B}^T \cdot \boldsymbol{\sigma}_p V_p \tag{A.30}$$

The mass matrices written above are consistent-mass matrices. For the numerical implementation the lumped-mass matrices, are used instead of the consistent ones.

B

Appendix B

Development of Mass Balance Equations

In this Appendix, the developments of the mass balance equations for the solid, water and air are presented in detail.

B.1 Mass balance equation of the solid component

Considering that there is no mass exchange between solid and fluid phases, the general mass balance equation (6.18) can be particularised for the solid component. It yields the differential equation (B.1), in which ρ_s is the solid density, n is the porosity and $\mathbf{j}_s^s$ are the solid fluxes. No external solid mass sources or sinks have been considered.

$$\frac{\partial}{\partial t}(\rho_s(1-n)) + \nabla \cdot \mathbf{j}_s = 0 \tag{B.1}$$

Taking into account the solid flux equal to the advective flux of the solid (Eq.B.2), equation (B.1) yields the expression (B.3).

$$\mathbf{j}_s = \rho_s(1-n)\mathbf{v}_s \tag{B.2}$$

$$\frac{\partial}{\partial t}(\rho_s(1-n)) + \nabla \cdot (\rho_s(1-n)\mathbf{v}_s) = 0 \tag{B.3}$$

Applying the chain rule for all the derivatives, the previous equation can be rewritten as:

$$(1-n)\frac{\partial \rho_s}{\partial t} + (1-n)(\mathbf{v}_s \cdot \nabla \rho_s) - \rho_s \frac{\partial n}{\partial t} - \rho_s(\mathbf{v}_s \cdot \nabla n) + \rho_s(1-n)\nabla \cdot \mathbf{v}_s = 0 \tag{B.4}$$

Regrouping terms considering the definition of the material derivative (Eq.B.5), the solid mass balance is simplified to equation (B.6).

$$\frac{D_s(\bullet)}{Dt} = \frac{\partial(\bullet)}{\partial t} + \mathbf{v}_s \cdot \nabla(\bullet) \tag{B.5}$$

$$(1-n)\frac{D_s \rho_s}{Dt} - \rho_s \frac{D_s n}{Dt} + \rho_s(1-n)\nabla \cdot \mathbf{v}_s = 0 \tag{B.6}$$

Rearranging, the following expression is obtained:

$$\frac{D_s n}{Dt} = \frac{(1-n)}{\rho_s}\frac{D_s \rho_s}{Dt} + (1-n)\nabla \cdot \mathbf{v}_s \tag{B.7}$$

Finally, considering that the solid grains are incompressible and the material derivative of the porosity is derived as:

$$\frac{D_s n}{Dt} = (1-n)\nabla \cdot \mathbf{v}_s \tag{B.8}$$

B.2 Mass balance equation of the water component

Taking into account that exchange of water mass is allowed between the fluid phases, the water mass balance equation should include the water content within both liquid and gas phases. Starting from equation (6.18), the mass balance equation for water, without considering external sources or sinks, can be written as

$$\frac{\partial}{\partial t}(\omega_g^w \rho_g S_g n + \omega_l^w \rho_l S_l n) + \nabla \cdot (\mathbf{j}_g^w + \mathbf{j}_l^w) = 0 \tag{B.9}$$

where ρ_g is the gas density, ρ_l is the liquid density, S_l is liquid degree of saturation, S_g is the gas degree of saturation ($S_g = 1 - S_l$), ω_g^w and ω_l^w are the mass fraction of the water in the gas and in the liquid respectively and $\mathbf{j}_g^w$ and $\mathbf{j}_l^w$ are the fluxes of water in the gas and liquid phases. Referring to fluxes the water flux in the gas phase (Eq.B.10) is equal to the sum of the diffusive term $\mathbf{i}_g^w$ and the advective term. On the other hand, the water flux in the liquid phase can be written as (B.11), in which the diffusive term can be neglected.

$$\mathbf{j}_g^w = \mathbf{i}_g^w + (\omega_g^w \rho_g S_g n)\mathbf{v}_g \tag{B.10}$$

$$\mathbf{j}_l^w = (\omega_l^w \rho_l S_l n)\mathbf{v}_l \tag{B.11}$$

Substituting equations (B.10) and (B.11) in the (B.9) and arranging terms, the water mass balance can be written with the following expression.

$$\frac{\partial}{\partial t}(\omega_g^w \rho_g S_g n + \omega_l^w \rho_l S_l n) + \nabla \cdot (\omega_g^w \rho_g S_g n \mathbf{v}_g) + \nabla \cdot (\omega_l^w \rho_l S_l n \mathbf{v}_l) + \nabla \cdot \mathbf{i}_g^w = 0 \tag{B.12}$$

Regrouping terms considering the definition of solid material derivative (B.5), the water mass balance is rewritten in equation (B.13).

$$n\frac{D_s(\omega_g^w\rho_g S_g+\omega_l^w\rho_l S_l)}{Dt}+(\omega_g^w\rho_g S_g+\omega_l^w\rho_l S_l)\frac{D_s n}{Dt}+\nabla\cdot(\omega_g^w n\rho_g S_g(\mathbf{v}_g-\mathbf{v}_s))+ \tag{B.13}$$
$$\nabla\cdot(\omega_l^w n\rho_l S_l(\mathbf{v}_l-\mathbf{v}_s))+(\omega_g^w n\rho_g S_g+\omega_l^w n\rho_l S_l)\nabla\cdot\mathbf{v}_s+\nabla\cdot\mathbf{i}_g^w=0$$

Including equation (B.8) in (B.13), the water mass balance equation can be rewritten as

$$n\frac{D_s(\omega_g^w\rho_g S_g+\omega_l^w\rho_l S_l)}{Dt}+\nabla\cdot(\omega_g^w n\rho_g S_g(\mathbf{v}_g-\mathbf{v}_s))+ \tag{B.14}$$
$$\nabla\cdot(\omega_l^w n\rho_l S_l(\mathbf{v}_l-\mathbf{v}_s))+(\omega_g^w\rho_g S_g+\omega_l^w\rho_l S_l)\nabla\cdot\mathbf{v}_s+\nabla\cdot\mathbf{i}_g^w=0$$

Taking into account the fluid pressures (p_l and p_g) as state variables, the material time derivative of equation (B.14) can be expanded as follows.

$$\frac{D_s(\omega_g^w\rho_g S_g+\omega_l^w\rho_l S_l)}{Dt}=\frac{\partial(\omega_g^w\rho_g S_g+\omega_l^w\rho_l S_l)}{\partial p_l}\dot{p}_l+\frac{\partial(\omega_g^w\rho_g S_g+\omega_l^w\rho_l S_l)}{\partial p_g}\dot{p}_g \tag{B.15}$$

Finally, the mass balance equation of water can be written as follows.

$$n\frac{\partial(\omega_g^w\rho_g S_g+\omega_l^w\rho_l S_l)}{\partial p_l}\dot{p}_l+n\frac{\partial(\omega_g^w\rho_g S_g+\omega_l^w\rho_l S_l)}{\partial p_g}\dot{p}_g= \tag{B.16}$$
$$-\nabla\cdot(\omega_g^w n\rho_g S_g(\mathbf{v}_g-\mathbf{v}_s))-\nabla\cdot(\omega_l^w n\rho_l S_l(\mathbf{v}_l-\mathbf{v}_s))$$
$$-(\omega_g^w\rho_g S_g+\omega_l^w\rho_l S_l)\nabla\cdot\mathbf{v}_s-\nabla\cdot\mathbf{i}_g^w$$

It can be noted that in those problems where the porosity distribution is sufficiently smooth and the spatial variations of water content in the liquid and in the gas are small, equation (B.16) can be simplified assuming that $\nabla(\omega_l^w\rho_l S_l n+\omega_g^w\rho_g S_g n)\approx 0$. This leads to the following expression.

$$n\frac{\partial(\omega_g^w\rho_g S_g+\omega_l^w\rho_l S_l)}{\partial p_l}\dot{p}_l+n\frac{\partial(\omega_g^w\rho_g S_g+\omega_l^w\rho_l S_l)}{\partial p_g}\dot{p}_g= \tag{B.17}$$
$$-(\omega_g^w n\rho_g S_g)\nabla\cdot\mathbf{v}_g-(\omega_l^w n\rho_l S_l)\nabla\cdot\mathbf{v}_l$$
$$-(1-n)(\omega_g^w\rho_g S_g+\omega_l^w\rho_l S_l)\nabla\cdot\mathbf{v}_s-\nabla\cdot\mathbf{i}_g^w$$

B.3 Mass balance equation of the air component

Similarly to what has been done with the water mass balance equation, the air mass balance equation has been developed considering air content in the two fluid phases. Starting from equation (6.18), the air mass balance, without considering external sources or sinks, can be written as:

$$\frac{\partial}{\partial t}(\omega_l^a\rho_l S_l n+\omega_g^a\rho_g S_g n)+\nabla\cdot(\mathbf{j}_l^a+\mathbf{j}_g^a)=0 \tag{B.18}$$

where $\mathbf{j}_g^a$ and $\mathbf{j}_l^a$ are the fluxes of air in the gas and liquid phases. The air flux in the liquid phase (Eq.B.19) is equal to the sum of the diffusive term $\mathbf{i}_l^a$ and the advective term. The air flux in the gas phase can be written as (B.20), in which the diffusive term is be neglected.

$$\mathbf{j}_l^a = \mathbf{i}_l^a + (\omega_l^a \rho_l S_l n)\mathbf{v}_l \tag{B.19}$$

$$\mathbf{j}_g^a = (\omega_g^a \rho_g S_g n)\mathbf{v}_g \tag{B.20}$$

Substituting equations (B.19) and (B.20) in (B.18), regrouping terms considering the definition of solid material derivative (Eq.B.5), and including the material derivative of the porosity (Eq.B.8), equation (B.18) is rewritten as

$$\begin{aligned} n\frac{D_s(\omega_g^a \rho_g S_g + \omega_l^a \rho_l S_l)}{Dt} + \nabla \cdot (\omega_g^a n \rho_g S_g(\mathbf{v}_g - \mathbf{v}_s)) + \\ \nabla \cdot (\omega_l^a n \rho_l S_l(\mathbf{v}_l - \mathbf{v}_s)) + (\omega_g^a \rho_g S_g + \omega_l^a \rho_l S_l)\nabla \cdot \mathbf{v}_s + \nabla \cdot \mathbf{i}_l^a = 0 \end{aligned} \tag{B.21}$$

Finally, taking into account the fluid pressures (p_l and p_g) as state variables, the mass balance equation of air can be written as follows.

$$\begin{aligned} n\frac{\partial(\omega_g^a \rho_g S_g + \omega_l^a \rho_l S_l)}{\partial p_l}\dot{p}_l + n\frac{\partial(\omega_g^a \rho_g S_g + \omega_l^a \rho_l S_l)}{\partial p_g}\dot{p}_g = \\ - \nabla \cdot (\omega_g^a n \rho_g S_g(\mathbf{v}_g - \mathbf{v}_s)) - \nabla \cdot (\omega_l^a n \rho_l S_l(\mathbf{v}_l - \mathbf{v}_s)) \\ - (\omega_g^a \rho_g S_g + \omega_l^a \rho_l S_l)\nabla \cdot \mathbf{v}_s - \nabla \cdot \mathbf{i}_l^a \end{aligned} \tag{B.22}$$

It can be noted that in those problems where the porosity distribution is sufficiently smooth and the spatial variations of air content in the liquid and in the gas are small, the previous equation can be simplified assuming that $\nabla(\omega_l^a \rho_l S_l n + \omega_g^a \rho_g S_g n) \approx 0$. This leads to the following expression.

$$\begin{aligned} n\frac{\partial(\omega_g^a \rho_g S_g + \omega_l^a \rho_l S_l)}{\partial p_l}\dot{p}_l + n\frac{\partial(\omega_g^a \rho_g S_g + \omega_l^a \rho_l S_l)}{\partial p_g}\dot{p}_g = \\ - (\omega_g^a n \rho_g S_g)\nabla \cdot \mathbf{v}_g - (\omega_l^a n \rho_l S_l)\nabla \cdot \mathbf{v}_l \\ - (1-n)(\omega_g^a \rho_g S_g + \omega_l^a \rho_l S_l)\nabla \cdot \mathbf{v}_s - \nabla \cdot \mathbf{i}_l^a \end{aligned} \tag{B.23}$$

Appendix C

Hydraulic Constitutive Laws

In this Appendix, several hydraulic constitutive equations are proposed in order to complete the hydromechanical formulation for unsaturated soils. Note that the following expressions depend essentially on liquid and gas pressures (p_g and p_l) which are the stat variables taken into account in the 3-phase 1-point MPM formulation outlined in Chapter 6.

C.1 Degree of saturation. Retention curve

The degree of saturation S_l is strongly dependent on pore liquid and gas pressures. There are a number of empirical equations that describe this characteristic for soil in the literature. Here, van Genuchten retention curve (Van Genuchten, 1980) has been proposed, where p_0, λ, S_{max} and S_{min} are assumed constants.

$$S_l = S_{min} + \left[1 + \left(\frac{p_g - p_l}{p_0}\right)^{\frac{1}{1-\lambda}}\right]^{-\lambda} (S_{max} - S_{min}) \tag{C.1}$$

C.2 Intrinsic permeability

The dependence of the liquid permeability on the degree of saturation is also very relevant in unsaturated soils. Hillel expression (Hillel, 1971) is one of the most accepted expressions to describe such relationship, and it is written as

$$k_l = k_{sat} {S_l}^m \tag{C.2}$$

where k_{sat} is the liquid permeability under saturated conditions, and the power m typically takes values in range 2-4.

C.3 Liquid density

If thermal effects are not taking into account, liquid density can be first approximated with the following expression, where C_l is liquid compressibility, and ρ_{l0} and p_{l0} are liquid density and liquid pressure reference values.

$$\rho_l = \rho_{l0} e^{C_l(p_l - p_{l0})} \tag{C.3}$$

C.4 Mass fraction of air in liquid. Henry's law

The mass fraction of air in liquid ω_l^a can be calculated applying the Henry's law (reviewed in Mackay and Shiu (1981)). It states that, at a constant temperature, the amount of a given gas that dissolves in a given type and volume of liquid is directly proportional to the partial pressure of that gas in equilibrium with that liquid. Considering that the liquid is a mixture of dry air and water, the following expression can be written,

$$\omega_l^a = \frac{p_g M_a}{H M_w} \tag{C.4}$$

where H is the Henry's constant, M_a is the molecular mass of air and M_w is the molecular mass of water.

Note that the mass fraction of air in liquid is essentially controlled by the gas pressure.

C.5 Mass fraction of water in gas. Psychrometric law

At a given temperature and gas pressure, air can only hold a certain maximum amount of water vapor. The higher the temperature and gas pressure, the higher the maximum

possible water content. This maximum water content for any given state of air is referred to as saturation (no suction). Gas pressure can be written as the sum of partial pressures (Dalton's law):

$$p_g = p_v + p_a \tag{C.5}$$

being air pressure p_a much smaller than water vapour pressure p_v.

The law that descrives the change in vapour pressure due to capillary effects is the psychrometric equation (Edlefson and Anderson, 1943), also known as Kelvin's equation (Thomson, 1871). It descrives p_v with respect the equilibrium vapour pressure with no capillary effects p_{v0} (p_v when suction is zero). It can be written as:

$$p_v = p_{v0} e^{-(p_g - p_l) M_w / R T_K \rho_w} \tag{C.6}$$

where R is the ideal gas constant (8.3144621 J/mol^{o}K), T_K is temperature (^{o}K), M_w is the molecular mass of water, and g is gravity. Note that vapour pressure is essentially controlled by the temperature.

Then, assuming that the mass fraction of water in gas ω_g^w is the ratio of the partial pressure of water vapor in the mixture to the equilibrium vapor pressure at a given temperature ($\frac{p_v}{p_{v0}} = \omega_g^w$), it can be calculated as follows.

$$\omega_g^w = e^{-(p_g - p_l) M_w / R T_K \rho_w} \tag{C.7}$$

C.6 Gas density

The gas phase is a mixture of two components (dry air and water vapour). Assuming that both components are distributed within the same volume, the gas density ρ_g can be written as follows, being ρ_v and ρ_a the density of vapour and air respectively.

$$\rho_g = \rho_v + \rho_a \tag{C.8}$$

Then, taking into account the ideal gas low and the Dalton's law ($p_g = p_v + p_a$), the previous equation can be rewritten, yielding

$$\rho_g = \frac{p_v (M_w - M_a) + p_g M_a}{R T_K} \tag{C.9}$$

in which T_K is the temperature (^{o}K), M_a is the molecular mass of air, M_w is the molecular mass of water, and R the ideal gas constant (8.3144621 J/mol^{o}K). Finally, p_v is the vapour pressure and can be calculated with the psychrometric expression.

D

Appendix D

Constitutive Modelling for Unsaturated Soils

A general form of the constitutive equation for unsaturated soils is presented here. Net stress $\bar{\boldsymbol{\sigma}}$ and suction s are considered as constitutive stresses. Note that it is also valid for saturated soils, if suction effects are neglected and effective stress $\boldsymbol{\sigma}'$ is used instead.

Yield function and plastic potential

Yield function F and plastic potential G are defined in terms of constitutive stresses and the hardening parameter ξ. ξ controls the position of F and P within the stress space.

$$F\left(\bar{\boldsymbol{\sigma}}, s, \xi\right) = 0 \tag{D.1}$$

$$P\left(\bar{\boldsymbol{\sigma}}, s, \xi\right) = 0 \tag{D.2}$$

Flow rule

The flow rule states that plastic strain increments are normal to the plastic potential surface (Eq.D.3). The magnitude of the plastic strain rate (plastic multiplier) is $d\Lambda$,

which is a non-negative scalar multiplier.

$$d\boldsymbol{\varepsilon}^p = d\Lambda \frac{\partial P}{\partial \bar{\boldsymbol{\sigma}}} \tag{D.3}$$

Hardening/softening law

The hardening/softening law describes the evolution of the hardening parameter ξ depending on plastic strain, hence $\xi(\boldsymbol{\varepsilon}^p) = 0$

Consistency condition

The consistency condition (Eq.D.4) states that the elastic limit is defined by the yield surface, enforcing a point in plastic conditions to remain on the yield surface.

$$dF = \left(\frac{\partial F}{\partial \bar{\boldsymbol{\sigma}}}\right)^T \cdot d\bar{\boldsymbol{\sigma}} + \frac{\partial F}{\partial s} ds + \frac{\partial F}{\partial \xi} d\xi = 0 \tag{D.4}$$

Stress-strain relationship

The incremental stress-strain relationship can be written as follows,

$$d\bar{\boldsymbol{\sigma}} = \mathbf{D}^{el} \cdot d\boldsymbol{\varepsilon}^{el} = \mathbf{D}^{el} \cdot \left(d\boldsymbol{\varepsilon} - d\boldsymbol{\varepsilon}^p - d\boldsymbol{\varepsilon}_s^{el}\right) \tag{D.5}$$

where $\mathbf{D}^{el}$ is the elastic stiffness matrix, $d\boldsymbol{\varepsilon}^{el}$ is the elastic strain increment, $d\boldsymbol{\varepsilon}$ is the total strain increment, $d\boldsymbol{\varepsilon}^p$ the plastic strain increment and $d\boldsymbol{\varepsilon}_s^{el}$ is the elastic strain increment corresponding to a change of suction.

Taking advantage of the flow rule (Eq.D.3) and being κ_s^{el} the elastic swell index corresponding to a change of suction, the previous equation can be written with the expression below.

$$d\bar{\boldsymbol{\sigma}} = \mathbf{D}^{el} \cdot d\boldsymbol{\varepsilon} - \mathbf{D}^{el} \cdot \frac{\partial P}{\partial \bar{\boldsymbol{\sigma}}} d\Lambda - \frac{1}{3}\mathbf{D}^{el} \cdot \mathbf{m} \frac{\kappa_s^{el}}{p_{atm} + s} ds \tag{D.6}$$

Plastic multiplier

The following relationship is used to describe the changes of F due to ξ,

$$\frac{\partial F}{\partial \xi} d\xi = \frac{\partial F}{\partial \xi}\left(\frac{\partial \xi}{\partial \boldsymbol{\varepsilon}^p}\right)^T \cdot d\boldsymbol{\varepsilon}^p = \frac{\partial F}{\partial \xi}\left(\frac{\partial \xi}{\partial \boldsymbol{\varepsilon}^p}\right)^T \cdot \frac{\partial G}{\partial \bar{\boldsymbol{\sigma}}} d\lambda = -H' d\Lambda \tag{D.7}$$

Substituting equations (D.7) and (D.6) in the consistency equation (Eq.D.4), and rearranging terms, the plastic multiplier $d\Lambda$ can be calculated with expression (D.8)

$$d\Lambda = \frac{\left(\frac{\partial F}{\partial \bar{\boldsymbol{\sigma}}}\right)^T \cdot \mathbf{D}^{el} \cdot d\boldsymbol{\varepsilon} + \left[\frac{\partial F}{\partial s} - \frac{1}{3}\left(\frac{\partial F}{\partial \bar{\boldsymbol{\sigma}}}\right)^T \cdot \mathbf{D}^{el} \cdot \mathbf{m}\frac{\kappa_s^{el}}{p_{atm}+s}\right] ds}{\left(\frac{\partial F}{\partial \bar{\boldsymbol{\sigma}}}\right)^T \cdot \mathbf{D}^{el} \cdot \frac{\partial P}{\partial \bar{\boldsymbol{\sigma}}} + H'} \tag{D.8}$$

Constitutive equation

Finally, including the previous expression of $d\Lambda$ into (Eq.D.6), the stress-strain relationship can be rearranged as

$$d\bar{\boldsymbol{\sigma}} = \mathbf{D}^{ep} \cdot d\boldsymbol{\varepsilon} + \mathbf{h}' ds \tag{D.9}$$

where $\mathbf{D}^{ep}$ is the elastoplastic tangent matrix (Eq.D.10) and $\mathbf{h}'$ is the constitutive vector controlling the influence of suction (Eq.D.11).

$$\mathbf{D}^{ep} = \left[\mathbf{D}^{el} - \frac{\mathbf{D}^{el} \cdot \frac{\partial P}{\partial \bar{\boldsymbol{\sigma}}}\left(\frac{\partial F}{\partial \bar{\boldsymbol{\sigma}}}\right)^T \cdot \mathbf{D}^{el}}{\left(\frac{\partial F}{\partial \bar{\boldsymbol{\sigma}}}\right)^T \cdot \mathbf{D}^{el} \cdot \frac{\partial P}{\partial \bar{\boldsymbol{\sigma}}} + H'}\right] \tag{D.10}$$

$$\mathbf{h}' = \left[\frac{\mathbf{D}^{el} \cdot \frac{\partial P}{\partial \bar{\boldsymbol{\sigma}}}\frac{1}{3}\left(\frac{\partial F}{\partial \bar{\boldsymbol{\sigma}}}\right)^T \cdot \mathbf{D}^{el} \cdot \mathbf{m}\frac{\kappa_s^{el}}{p_{atm}+s} - \mathbf{D}^{el} \cdot \frac{\partial P}{\partial \bar{\boldsymbol{\sigma}}}\frac{\partial F}{\partial s}}{\left(\frac{\partial F}{\partial \bar{\boldsymbol{\sigma}}}\right)^T \cdot \mathbf{D}^{el} \cdot \frac{\partial P}{\partial \bar{\boldsymbol{\sigma}}} + H'} - \frac{1}{3}\mathbf{D}^{el} \cdot \mathbf{m}\frac{\kappa_s^{el}}{p_{atm}+s}\right] \tag{D.11}$$

Acronyms

CFL Courant-Friedrichs-Levy condition

CPDI Convected Particle Domain Interpolation method

CRAMP CRAcks with Material Points method

cpGIMP contiguoug-particle Generalised Interpolation Material Point method

CPU Central Processing Unit

DEM Discretee Element Method

FDM Finite Difference Method

FEM Finite Element Method

FEMLIP Finite Element Method Lagrangian Interpolation Points

FVM Finite Volume Method

GIMP Generalised Interpolation Material Point method

LEM Limit Equilibrium Method

MPM Material Point Method

NMD Nodal Mixed Discretisation

ODE Ordinary Differential Equation Point method

PIC Particle-In-Cell method

PFEM Particle Finite Element Method

uGIMP uniform Generalised Interpolation Material Point method

SPH Smoothed Particle Hydrodynamics

UPC Universitat Politècnica de Catalunya

USF Updating Stress First

USL Updating Stress Last

Nomenclature

A	parameter that controls the rate of variation of friction angle	-
$\mathbf{A}$	amplification matrix	-
a_s	slope of a linear retention curve	-
$\mathbf{a}$	acceleration	m/s^2
$\mathbf{a}_f$	acceleration of a fluid phase f (liquid l, gas g)	m/s^2
$\mathbf{a}_{ph}$	acceleration of a phase ph (solid s, liquid l, gas g)	m/s^2
$\mathbf{b}$	body force vector	m/s^2
B	parameter that controls the rate of variation of cohesion	-
$\mathbf{B}$	matrix of nodal shape function gradients	-
C_i	infiltration coefficient	m^2/s
C_{ph}	liquid compressibility	Pa^{-1}
c	cohesion	Pa
c_p	speed of the compression wave	m/s
c_s	increase of cohesion due to suction	Pa
c_v	consolidation coefficient	m^2/s
c'	effective cohesion (in saturated conditions)	Pa
c'_p	peak effective cohesion	Pa
c'_r	residual effective cohesion	Pa
$\mathbf{D}$	constitutive tangent matrix	Pa
$\mathbf{D}^{el}$	elastic stiffness matrix	Pa
$\mathbf{D}^{ep}$	elastoplastic stiffness matrix	Pa
$\mathbf{D}^c_{ph}$	dispersion tensor of a component c (solid s, water w, air a) within a phase ph	m^2/s
$\frac{D(\bullet)}{Dt}$	material derivative	-
E	Young's modulus	Pa
E_c	constrained elastic modulus	Pa
$E_{c,u}$	undrained constrained elastic modulus	Pa
$\mathbf{e}$	deviatoric strain vector	-
F	yield function	-
$\mathbf{F}$	unbalanced force vector	N
$\mathbf{F}_{ph}$	unbalanced force vector of a phase ph	N

$\mathbf{F}^{damp}$	damping force vector	N
$\mathbf{F}^{ext}$	vector of external forces of a mixture	N
$\mathbf{F}^{int}$	vector of internal forces of a mixture	N
$\mathbf{F}^{damp}_{ph}$	damping force vector of a phase ph	N
$\mathbf{F}^{ext}_{ph}$	vector of external forces of a phase ph	N
$\mathbf{F}^{int}_{ph}$	vector of internal forces of a phase ph	N
G	shear modulus	Pa
H	Henry's constant	Pa^{-1}
h	depth/altitude	m
h_{min}	minimum altitude of the element	m
h_w	water level	m
$\mathbf{h}'$	constitutive vector	-
I_B	brittleness index	-
$\hat{I}_B$	brittleness index threshold	-
$\mathbf{I}$	identity matrix	-
$\mathbf{i}^c_{ph}$	diffusive flux of a component c within a phase ph	$\mathrm{kg/m^2s}$
$\mathbf{j}_{ph}$	total flux of a phase ph per unit volume	$\mathrm{kg/m^2s}$
$\mathbf{j}^c_{ph}$	flux of a component c within a phase ph per unit volume	$\mathrm{kg/m^2s}$
K	bulk modulus	Pa
K_m	bulk modulus of a mixture	Pa
K_{ph}	bulk modulus of a phase ph	Pa
K_{sk}	bulk modulus of the solid skeleton	Pa
K_0	coefficient of earth pressure at rest	-
k	time step iteration	-
k_{ph}	intrinsic permeability of a fluid phase	$\mathrm{m^2}$
k_{sat}	liquid intrinsic permeability under saturated conditions	$\mathrm{m^2}$
L_e	element length	m
L_i	characteristic element size	m
M_c	molecular mass of a component c	kg/mol
$\mathbf{M}$	mass matrix	kg
$\mathbf{M}^L$	lumped mass matrix	kg
$\mathbf{M}_{ph}$	mass matrix of a phase ph per unit of total volume	kg
$\widetilde{\mathbf{M}}_{ph}$	mass matrix of a phase ph per unit of phase volume	kg
m	mass	kg
m^c	mass of a component c	kg
m_p	material point mass	kg
m_i	nodal mass	kg
m_{ph}	mass of a phase ph	kg
m^c_{ph}	partial mass of a component c in a phase ph	kg
$\mathbf{m}$	$(1,1,1,0,0,0)^T$	-
N_e	number of elements surrounding a node	-

N_{en}	number of nodes in an element	-
N_j	nodal shape function	-
N_n	number of nodes	-
N_p	number of material points	-
$\mathbf{N}$	matrix of nodal shape functions	-
n	porosity	-
n_{ph}	volumetric fraction of a phase ph	-
$\mathbf{n}$	normal vector to a surface	-
P	plastic potential function	-
P_c	characteristic polynomial	-
p	volumetric stress	Pa
p_{atm}	atmospheric pressure	Pa
p_f	pressure of a fluid f (liquid l, gas g)	Pa
p_{l0}	liquid pressure reference value	Pa
p_v	vapour pressure	Pa
p_{v0}	equilibrium vapour pressure with no capillary effects	Pa
p_0	reference pressure in Van Genuchten retention curve	Pa
p'	volumetric effective stress	Pa
$\bar{p}$	volumetric net stress	Pa
$\widehat{\mathbf{p}}_f$	vector of prescribed fluid pressure (liquid l, gas g)	Pa
$\mathbf{Q}_g$	gas dragging matrix	kg/s
$\mathbf{Q}_l$	liquid dragging matrix	kg/s
q	deviatoric stress	Pa
q_l	viscous coefficient per unit volume	kg/m^{3}s
R	ideal gas constant	J/mol°K
r	exponent in the Hillel expression	-
S_f	degree of saturation of a fluid f	-
S_{max}	maximum degree of saturation of liquid	-
S_{min}	minimum degree of saturation of liquid	-
s	suction	Pa
s_0	initial prescribed suction	Pa
T	time dimensionless	-
T_f	failure time	s
T_K	temperature	°K
T_p	period	s
t	time	s
t_h	time required to reach the length h	s
t^*	normalised time	-
$\widehat{\mathbf{t}}$	vector of prescribed total traction	Pa
u_x	relative displacement between both sides of a shear band	m
$\mathbf{u}$	displacement vector	m

$\mathbf{u}_{ph}$	displacement vector of a phase ph	m
$\widehat{\mathbf{u}}$	prescribed displacement	m
$\widehat{\mathbf{u}}_{ph}$	prescribed displacement of a phase ph	m
V	reference volume of a mixture	m^3
V_e	element volume	m^3
V_p	material point volume	m^3
V_{ph}	partial volume of a phase ph	m^3
$\mathbf{v}$	velocity	m/s
$\mathbf{v}_{ph}$	velocity of a phase ph	m/s
$\mathbf{w}$	specific field vector	-
$\mathbf{w}_i$	specific field vector evaluated in a node i	-
W_c	fracture energy dissipated in a discrete crack	J
W_h	total work dissipated by a shear band of thickness h	J
x	Cartesian coordinate	m
$\mathbf{x}$	position vector	m
$\mathbf{x}_p$	material point position vector	m
$\widehat{\mathbf{x}}$	solution of a general scheme	-
y	Cartesian coordinate	m
z	Cartesian coordinate	m
α	damping factor	-
α_B	Biot's coefficient	-
α_C	Courant's factor	-
α_{ms}	mass scaling factor	-
α_{ph}	damping factor of a phase ph	-
δ	Dirac delta function	-
$\delta\mathbf{u}$	test function	-
Δc_{max}	maximum increase of cohesion due to suction effects	Pa
$\Delta c'$	effective cohesion drop (dimensionless)	-
ΔP	prescribed increment of liquid pressure	Pa
Δt	time increment	s
Δt_{crit}	critical time step	s
$\Delta\varphi'$	effective friction angle drop (dimensionless)	-
ε^p_{eq}	equivalent plastic strain invariant	-
ε_{vol}	volumetric strain	-
$\bar{\dot{\varepsilon}}_{vol}$	averaged volumetric strain rate	-
$\boldsymbol{\varepsilon}$	total strain	-
$\boldsymbol{\varepsilon}^p$	plastic strain vector	-
$\boldsymbol{\varepsilon}^{el}$	elastic strain vector	-
$\boldsymbol{\varepsilon}^{el}_s$	elastic strain vector due to suction changes	-
η	shape factor controlling the rate of strenght decrease	-
κ	stiffness coefficient per unit volume	Pa/m^2

κ_m	stiffness coefficient of a mixture per unit volume	$\mathrm{Pa/m^2}$
κ_{ph}	stiffness coefficient of a phase ph per unit volume	$\mathrm{Pa/m^2}$
κ_s^{el}	elastic swell index corresponding to a change of suction	Pa
Λ	plastic multiplier	-
λ	parameter in Van Genuchten retention curve	-
λ_e	eigenvalue	-
μ_f	viscosity of a fluid phase f	kg/sm
ν	Poisson ratio	-
ξ	hardening/softening parameter	-
ρ	density	$\mathrm{kg/m^3}$
ρ_c	density of a component c	$\mathrm{kg/m^3}$
ρ_{l0}	liquid density reference value	$\mathrm{kg/m^3}$
ρ_m	density of mixture	$\mathrm{kg/m^3}$
ρ_{ph}	density of a phase ph	$\mathrm{kg/m^3}$
ρ_v	vapour density	$\mathrm{kg/m^3}$
ϱ	spectral radius	-
σ'_n	effective stress normal to a reference plane	Pa
$\boldsymbol{\sigma}$	total stress vector	Pa
$\boldsymbol{\sigma}_{av}$	averaged stress stress vector	Pa
$\boldsymbol{\sigma'}$	effective stress vector	Pa
$\overline{\boldsymbol{\sigma}}$	net stress vector	Pa
τ	shear strength	Pa
τ_p	peak shear strength	Pa
τ_r	residual shear strength	Pa
φ	friction angle	rad
φ_s	increase of friction angle due to suction	rad
φ'	effective friction angle (in saturated conditions)	rad
φ'_b	effective friction angle of a basal sliding surface	rad
φ'_p	peack effective friction angle (in saturated conditions)	rad
φ'_r	residual effective friction angle (in saturated conditions)	rad
$\widehat{\varphi}'$	mobilised friction angle	rad
ω	angular frequency	rad^-1
ω^c_{ph}	mass fraction of a component c in a phase ph	-
Ω	total domain	$\mathrm{m^3}$
∇	vector differential operator	-
$\partial\Omega$	partial domain	$\mathrm{m^2}$
$\frac{\partial(\cdot)}{\partial t}$	partial derivative	-

Bibliography

Abbo, A. J. and S. W. Sloan
1995. A smooth hyperbolic approximation to the Mohr-Coulomb yield criterion. *Computers & structures*, 54(3):427–441.

Abe, K., K. Soga, and S. Bandara
2014. Material point method for coupled hydromechanical problems. *Journal of Geotechnical and Geoenvironmental Engineering*, 140(3):1–16.

Al-Kafaji, I. K. J.
2013. *Formulation of a Dynamic Material Point Method (MPM) for Geomechanical Problems*. PhD thesis, Universität Stuttgart.

Alonso, E. and A. Lloret
1983. Evolution in time of the reliability of slopes in partially saturated soils. In *Fourth International Conference on Applications of Statistics and Probability in Soil and Structural Engineering*, P. Editrice, ed., Firenze (Italy).

Alonso, E. E. and A. Gens
2006. Aznalcóllar dam failure. Part 1: Field observations and material properties. *Geotechnique*, 56(3):165–183.

Alonso, E. E., A. Gens, and A. Josa
1990. A constitutive model for partially saturated soils. *Géotechnique*, 40(3):405–430.

Alonso, E. E., N. M. Pinyol, and A. M. Puzrin
2010a. Catastrophic Slide: Vaiont Landslide, Italy. In *Geomechanics of Failures. Advanced Topics*. Springer.

Alonso, E. E., N. M. Pinyol, and A. M. Puzrin
2010b. *Geomechanics of Failures. Advanced Topics*. Springer.

Alonso, E. E., A. Zervos, and N. M. Pinyol
2015. Thermo-poro-mechanical analysis of landslides: from creeping behaviour to catastrophic failure. *Accepted for publication in Geotechnique*.

Andersen, S. and L. Andersen
2008. Modeling of Landslides with the Material Point Method. In *Sixth International Conference on Engineering Computational Technology*.

Andersen, S. and L. Andersen
2010. Modelling of landslides with the material-point method. *Computational Geosciences*, 14(1):137–147.

Andersen, S. M.
2009. *Material-Point Analysis of Large-Strain Problems: Modelling of Landslides*. PhD thesis, AALBORG University.

Armero, F. and E. Love
2003. An Arbitrary Lagrangian-Eulerian Finite Element Method for finite strain plasticity. *International Journal for Numerical Methods in Engineering*, 57:471–508.

Aubry, R., S. R. Idelsohn, and E. Oñate
2005. Particle finite element method in fluid mechanics including thermal convection-diffusion. *Computers & Structures*, 83(17-18):1459–1475.

Bandara, S. and K. Soga
2015. Coupling of soil deformation and pore fluid flow using material point method. *Computers and Geotechnics*, 63(1):199–214.

Bandara, S. S.
2013. *Material point method to simulate large deformation problems in fluid-saturated granular medium*. PhD thesis, University of Cambridge.

Banerjee, B.
2004. Material point method simulations of fragmenting cylinders. In *17th ASCE Engineering Mechanics Conference*, volume 1.

Banerjee, B., J. E. Guilkey, T. B. Harman, J. A. Schmidt, and P. A. Mcmurtry
2012. Simulation of impact and fragmentation with the material point method. *Computational Physics*, Pp. 1–6.

Bardenhagen, S. G.
2002. Energy Conservation Error in the Material Point Method for Solid Mechanics. *Journal of Computational Physics*, 180(1):383–403.

Bardenhagen, S. G., J. U. Brackbill, and D. Sulsky
2000. The material-point method for granular materials. *Computer Methods in Applied Mechanics and Engineering*, 187(3-4):529–541.

Bardenhagen, S. G., J. E. Guilkey, K. M. Roessig, J. U. Brackbill, and W. M. Witzel
2001. An Improved Contact Algorithm for the Material Point Method and Application to Stress Propagation in Granular Material. *Computer Modeling in Engineering and Sciences*, 2(4):509–522.

Bardenhagen, S. G. and E. M. Kober
2004. The generalized interpolation material point method. *Computer Modeling in Engineering and Sciences*, 5(6):477–495.

Bardenhagen, S. G., J. A. Nairn, and H. Lu
2011. Simulation of dynamic fracture with the Material Point Method using a mixed J-integral and cohesive law approach. *International Journal of Fracture*, 170(1):49–66.

Beuth, L.
2012. *Formulation and application of a quasi-static material point method.* PhD thesis, Universität Stuttgart.

Beuth, L., T. Benz, P. A. Vermeer, C. J. Coetzee, P. Bonnier, and P. Van Den Berg
2007. Formulation and validation of a quasi-static material point method. In *Proceedings of the 10th International Symposium on Numerical Methods in Geomechanics*, volume 10, Pp. 189–195, Rhodes, Greece.

Biot, M. A.
1941. General theory of three-dimensional consolidation. *Journal of Applied Physics*, 12(2):155–164.

Bishop, A. W.
1967. Progressive failure-with special reference to the mechanism causing it. In *Proceedings of the Geotechnical Conference*, volume 2, Pp. 142–150, Oslo.

Bishop, A. W.
1971. The influence of progressive failure on the choice of the method of stability analysis. *Geotechnique*, 21:168–172.

Bjerrum, L.
1967. Progressive failure in slopes in overconsolidated plastic clays and clay shales. *Journal of Soil Mechanics & Foundations Div*, 93(5):3–49.

Brackbill, J. U., D. B. Kothe, and H. M. Ruppel
1988. FLIP: a low-dissipation, particle-in-cell method for fluid flow. *Computer Physics Communications*, 48:25–38.

Bromhead, E. N., M. R. Cooper, and D. J. Petley
1998. The Selborne cutting slope stability experiment (CD-ROM The Selborne data collection CD).

Brydon, A. D., S. G. Bardenhagen, E. A. Miller, and G. T. Seidler
2005. Simulation of the densification of real open-celled foam microstructures. *Journal of the Mechanics and Physics of Solids*, 53(12):2638–2660.

Bui, H. H. and R. Fukagawa
2008. Lagrangian meshfree particles method (SPH) for large deformation and failure flows of geomaterial using elastic-plastic soil constitutive model. *International Journal for Numerical and Analytical Methods in Geomechanics*, 32:1537–1570.

Bui, H. H. and R. Fukagawa
2013. An improved SPH method for saturated soils and its application to investigate the mechanisms of embankment failure: Case of hydrostatic pore-water pressure. *International Journal for Numerical and Analytical Methods in Geomechanics*, 37(1):31–50.

Bui, H. H., R. Fukagawa, K. Sako, and J. C. Wells
2011. Slope stability analysis and discontinuous slope failure simulation by elasto-plastic smoothed particle hydrodynamics (SPH). *Géotechnique*, 61(7):565–574.

Buzzi, O., D. M. Pedroso, and A. Giacomini
2008. Caveats on the Implementation of the Generalized Material Point Method. *Computer Modeling in Engineering and Sciences*, 31(2):85–106.

Cascini, L., S. Cuomo, M. Pastor, and G. Sorbino
2010. Modeling of rainfall-induced shallow landslides of the flow-type. *Journal of geotechnical . . .*, Pp. 85–98.

Ceccato, F.
2014. *Study of large deformation geomechanical problems with the Material Point Method*. PhD thesis, Universita degli Studi de Podova.

Cecinato, F. and A. Zervos
2012. Influence of thermomechanics in the catastrophic collapse of planar landslides. *Canadian Geotechnical Journal*, 49(2):207–225.

Cecinato, F., A. Zervos, and E. Veveakis
2011. A thermo-mechanical model for the catastrophic collapse of large landslides. *International Journal for Numerical and Analytical Methods in Geomechanics*, 35:1507–1535.

Coetzee, C. J., A. H. Basson, and P. A. Vermeer
2007. Discrete and continuum modelling of excavator bucket filling. *Journal of Terramechanics*, 44(2):177–186.

Coetzee, C. J., P. A. Vermeer, and A. H. Basson
2005. The modelling of anchors using the material point method. *International Journal for Numerical and Analytical Methods in Geomechanics*, 29(9):879–895.

Collatz, L.
1955. *Numerische Behandlung von Differentialgbeichungen*. Berlin: Springer.

Cooper, A. H.
1998. Subsidence hazards caused by the dissolution of Permian gypsum in England: geology, investigation and remediation. *Geological Society, London, Engineering Geology Special Publications*, 15(1):265–275.

Cooper, M. R.
1996. The progressive development of a failure slip surface in over-consolidated clay at Selborne, UK. In *Proc. 7th Int. Symp. on Landslides, Trondheim, Norway, Vol 2*, K. Senneset, ed., volume 2, Pp. 683–688, Rotterdam. Balkema, Rotterdam.

Cooper, M. R., E. N. Bromhead, D. J. Petley, and D. I. Grant
1998. The Selborne cutting stability experiment. *Geotechnique*, 48(1):83–101.

Courant, R., K. Friedrichs, and H. Lewy
1967. On the partial difference equations of mathematical physics. *IBM Journal of Research and Development*, 11:215–234.

Crosta, G. B., S. Imposimato, and D. Roddeman
2015. Landslide Spreading, Impulse Water Waves and Modelling of the Vajont Rockslide. *Rock Mechanics and Rock Engineering*.

Cummins, S. J. and J. U. Brackbill
2002. An Implicit Particle-in-Cell Method for Granular Materials. *Journal of Computational Physics*, 180(2):506–548.

Cundall, P. A.
1987. Distinct element models of rock and soil structure. In *In Analytical and Conlputational Methods in Engineering Rock Mechanics*, E. T. Brown, ed., Pp. 129–163. London: Allen and Unwin.

Cundall, P. A. and O. D. L. Strack
1979. A discrete numerical model for gran ular assemblies. *Géotechnique*, 29(1):47–65.

Cuomo, S., N. Prime, A. Iannone, F. Dufour, L. Cascini, and F. Darve
2013. Large deformation FEMLIP drained analysis of a vertical cut. *Acta Geotechnica*, 8(2):125–136.

Del Ventisette, C., G. Gigli, M. Bonini, G. Corti, D. Montanari, S. Santoro, F. Sani, R. Fanti, and N. Casagli
2015. Insights from analogue modelling into the deformation mechanism of the landslide. *Geomorphology*, 228:52–59.

Delage, P. and J. Graham
1996. Mechanical behaviour of unsaturated soils. In *Int. Conference on Unsaturated Soils UNSAT '95*, E. E. Alonso and P. Delage, eds., Pp. 1223–1256.

Detournay, C. and E. Dzik
2006. Nodal Mixed Discretization for tetrahedral elements. In *4th international FLAC symposium, numerical modeling in geomechanics. Minnesota Itasca Consulting Group, Inc. Paper*, Hart and Varona, eds., Pp. Paper. No. 07–02.

Di Toro, G., T. Hirose, S. Nielsen, G. Pennacchioni, and T. Shimamoto
2006. Natural and experimental evidence of melt lubrication of faults during earthquakes. *Science*, 311(February):647–649.

Donea, J., P. Fasoli-Stella, and S. Giuliani
1977. Lagrangian and Eulerian Finite element techniques for transient fluid- structure interaction problems. In *Transactions of the 4th International Conference on Structural Mechanics in Reactor Technology*, volume B, Pp. 1–12, San Francisco.

Donea, J., A. Huerta, J. P. Ponthot, and A. Rodríguez-Ferran
2004. Arbitrary Lagrangian-Eulerian methods. In *Encyclopedia of Computational Mechanics*, E. Stein, R. de Borst, and T. J. R. Hughes, eds. Jhon Wiley & Sons, Ltd.

Dufour, F., H. B. Muhlhaus, and L. Moresi
2001. A particle-in-cell formulation for large deformation in cosserat continua. In *Bifurcation and Localisation Theory in Geomechanics*, A. V. Dyskin, H.-B. Muhlhaus, and E. Pasternak, eds., Pp. 133–138. Lisse: Swets & Zeitlinger.

Edlefson, N. E. and A. B. C. Anderson
1943. Thermodynamics of soil moisture. *Hilgardia*, 15(2):31–298.

Escario, V. and F. Juca
1989. strength and deformation of partly saturated soils. In *12th Int. Conf. Soil Mech and Found. Eng.*, Pp. 43–46.

Esch, J. M. V., D. Stolle, and I. Jassim
2011. Finite element method for coupled dynamic flow-deformation simulation. In *Proceedings of the 2nd International Symposium on Computational Geomechanics (COMGEO II)*, Pp. 415–524, Cavtat-Dubrovnik, Croatia.

Eymard, R., T. Gallouët, and R. Herbin
2000. The finite volume method. In *Handbook of Numerical Analysis*, P. Ciarlet and J. Lions, eds., volume VII, Pp. 713–1020.

Fell, R., J. Glastonbury, and G. Hunter
2007. Rapid landslides: The importance of understanding mechanisms and rupture surface mechanics. *Quarterly Journal of Engineering Geology and Hydrogeology*, 40:9–27.

Ferri, F., G. Di Toro, T. Hirose, and T. Shimamoto
2010. Evidence of thermal pressurization in high-velocity friction experiments on smectite-rich gouges. *Terra Nova*, 22(5):347–353.

Finlayson, B. A.
1972. *The method of weighted residuals and variational principles, with application in fluid mechanics, heat and mass transfer*, Mathematics in Science and Engineering. Elsevier Science.

Finlayson, B. A. and L. E. Scriven
1966. The Method of Weighted Residuals. A Review. *Applied Mechanics Reviews*, 19(6):735–748.

Forsyth, G. E. and W. R. Wasow
1960. *Finite Difference Methods for Partial Differential Equations*. New York: Wiley.

Fredlund, D. G., N. R. Morgensten, and R. A. Widger
1978. The shear strength of unsaturated soils. *Canadian Geotechnical Journal*, 15(3):313–321.

Galerkin, B. G.
1915. Rods and Plates: Series in some questions of elastic equilibrium of rods and plates. *Vestnik Inzhenerov Tekhnikov*, 19:897–908.

Gan, J. K. M., D. G. Fredlund, and H. Rahardjo
1988. Determination of the shear strength parameters of an unsaturated soil using the direct shear test. *Canadian Geotechnical Journal*, 25(3):500–510.

Gens, A. and E. E. Alonso
2006. Aznalcóllar dam failure. Part 2: Stability conditions and failure. *Geotechnique*, 56(3):185–201.

Gingold, R. A. and J. J. Monaghan
1977. Smoothed particle hydrodynamics: theory and application to non-spherical stars. *Monthly Notices of the Royal Astronomical Society*, 181:375–389.

Glastonbury, J. and R. Fell
2008a. A decision analysis framework for the assessment of likely post-failure velocity of translational and compound natural rock slope landslides. *Canadian Geotechnical Journal*, 45(3):329–350.

Glastonbury, J. and R. Fell
2008b. Geotechnical characteristics of large slow , very slow , and extremely slow landslides. *Canadian Geotechnical Journal*, 45:984–1005.

Glastonbury, J. and R. Fell
2010. Geotechnical characteristics of large rapid rock slides. *Canadian Geotechnical Journal*, 47:116–132.

Goren, L. and E. Aharonov
2009. On the stability of landslides: A thermo-poro-elastic approach. *Earth and Planetary Science Letters*, 277(3-4):365–372.

Grant, D.
1996. *Instrumentation systems for and failure mechanisms of an induced slope failure project*. PhD thesis, University of Southampton.

Guilkey, J. and J. Weiss
2001. An implicit time integration strategy for use with the material point method. In *Proceedings from the First MIT Conference on Computational Fluid and Solid Mechanics*, K. J. Bathe, ed., Pp. 216–219, Cambridge. Elsevier.

Guilkey, J. E., T. B. Harman, and B. Banerjee
2007. An Eulerian-Lagrangian approach for simulating explosions of energetic devices. *Computers & Structures*, 85(11-14):660–674.

Guilkey, J. E., J. B. Hoying, and J. A. Weiss
2006. Computational modeling of multicellular constructs with the material point method. *Journal of biomechanics*, 39(11):2074–2086.

Guilkey, J. E. and J. A. Weiss
2003. Implicit time integration for the material point method: Quantitative and algorithmic comparisons with the finite element method. *International Journal for Numerical Methods in Engineering*, 57(9):1323–1338.

Guo, Y. and J. A. Nairn
2004. Calculation of J-integral and stress intensity factors using the material point method. *Computer Modeling in Engineering and Sciences*, 6:295–308.

Guo, Y. J. and J. A. Nairn
2006. Three-Dimensional Dynamic Fracture Analysis Using the Material Point Method. *Computer Modeling in Engineering and Sciences*, 16(3):141.

Han, K. K., H. Rahardjo, and B. B. Broms
1995. Effect of hysteresis on the shear strength of a residual soil. In *Proceedings of the First International Conference on Unsaturated Soils. UNSAT'95. Vol 2*, Pp. 499–504, Paris, France.

Han, R. and T. Hirose
2012. Clay-clast aggregates in fault gouge: An unequivocal indicator of seismic faulting at shallow depths? *Journal of Structural Geology*, 43(October):92–99.

Harlow, F. H.
1964. The particle-in-cell computing method for fluid dynamics. *Computer Methods in Physics*, 3:319–343.

Harlow, F. H., M. A. Ellison, and J. H. Reid
1964. The particle-in-cell computing method for fluid dynamics. *Methods in computational physics*, 3(3):319–343.

Hendron, A. J. and F. D. Patton
1985. The Vajont slide, a geotechnical analysis based on new geologic observations of the failure surface. Technical report, Department of the Army US Army Corps of Engineers, Washington, D C.

Hendron, A. J. and F. D. Patton
1987. The Vaiont slide. A geotechnical analysis basedon new geologic observations of the failure surface. *Engineering Geology*, 24:475–491.

Hillel, D.
1971. *Soil and Water-Physical Principles and Processes.* New York: Academic Press.

Hoek, E.
2007. *Practical Rock Engineering.* http://www.rocscience.com.

Hsü, K. J.
1975. Catastrophic debris streams generated by rockfalls. *Geological Society of America Bulletin*, 86(1):129–140.

Hu, W. and Z. Chen
2003. A multi-mesh MPM for simulating the meshing process of spur gears. *Computers & Structures*, 81(20):1991–2002.

Hu, W. and Z. Chen
2006. Model-based simulation of the synergistic effects of blast and fragmentation on a concrete wall using the MPM. *International Journal of Impact Engineering*, 32(12):2066–2096.

Huang, P., X. Zhang, S. Ma, and X. Huang
2011. Contact algorithms for the material point method in impact and penetration simulation. *International Journal for Numerical Methods in Engineering*, 85(4):498–517.

Hungr, O., S. Leroueil, and L. Picarelli
2014. The Varnes classification of landslide types, an update. *Landslides*, 11(April):167–194.

Hutchinson, J. N.
1987. Mechanisms producing large displacements in landslides on pre-existing shears. *Memoir of the Geological Society of China*, 9:175–200.

Hutchinson, J. N.
1994. Some aspects of the morphological parameters of landslides, with example drawn from Italy and elsewhere. *Geologica Romana*, 30:1–12.

Ionescu, I., J. Guilkey, M. Berzins, R. M. Kirby, and J. Weiss
2005. Computational simulation of penetrating trauma in biological soft tissues using the material point method. *Studies in health technology and informatics*, 111:213–218.

Jassim, I., D. Stolle, and P. Vermeer
2013. Two-phase dynamic analysis by material point method. *International Journal for Numerical and Analytical Methods in Geomechanics*, 37(15):2502–2522.

Kamojjala, K., R. Brannon, A. Sadeghirad, and J. Guilkey
2013. Verification tests in solid mechanics. *Engineering with Computers*, 31:193–213.

Kenney, T. C.
1967. Stability of the Vajont valley, discussion of a paper by L. Müller (1964) on the rock slide in the Vajont valley. *Rock Mechanics and Engineering Geology*, 5:10–16.

Leroueil, S.
2001. Natural slopes and cuts: movement and failure mechanisms. *Géotechnique*, 51(3):197–243.

Li, S. and W. K. Liu
2002. Meshfree and particle methods and their applications. *Applied Mechanics Reviews*, 55(1):1–34.

Li, W. C., H. J. Li, F. C. Dai, and L. M. Lee
2012. Discrete element modeling of a rainfall-induced flowslide. *Engineering Geology*, 149-150:22–34.

Li, X., S. He, Y. Luo, and Y. Wu
2011. Simulation of the sliding process of Donghekou landslide triggered by the Wenchuan earthquake using a distinct element method. *Environmental Earth Sciences*, 65(4):1049–1054.

Lian, Y. P., X. Zhang, X. Zhou, S. Ma, and Y. L. Zhao
2011. Numerical simulation of explosively driven metal by material point method. *International Journal of Impact Engineering*, 38(4):238–246.

Liao, C. J., D. H. Lee, J. H. Wu, and C. Z. Lai
2011. A new ring-shear device for testing rocks under high normal stress and dynamic conditions. *Engineering Geology*, 122(1-2):93–105.

Ling, H. I., M.-H. Wu, D. Leshchinsky, and B. Leshchinsky
2009. Centrifuge Modeling of Slope Instability. *Journal of Geotechnical and Geoenvironmental Engineering*, 135(6):758–767.

Liu, Z. and H. A. Koyi
2012. Kinematics and internal deformation of granular slopes: insights from discrete element modeling. *Landslides*, 10(2):139–160.

Love, E. and D. L. Sulsky
2006a. An energy-consistent material-point method for dynamic finite deformation plasticity. *International Journal for Numerical Methods in Engineering*, 65(10):1608–1638.

Love, E. and D. L. Sulsky
2006b. An unconditionally stable, energy-momentum consistent implementation of the material-point method. *Computer Methods in Applied Mechanics and Engineering*, 195(33-36):3903–3925.

Lucy, L. B.
1977. A numerical approach to the testing of the fission hypothesis. *The astronomical journal*, 82:1013–1024.

Lysmer, J. and R. L. Kuhlmeyer
1969. Finite dynamic model for infinite media. *Journal of the Engineering Mechanics Division*, 3:859–977.

Mackay, D. and W. Y. Shiu
1981. A critical review of Henry's law constants for chemicals of environmental interest. *Journal of Physical and Chemical Reference Data*, 10(4):1175–1199.

Mackenzie-Helnwein, P., P. Arduino, W. Shin, J. A. Moore, and G. R. Miller
2010. Modeling strategies for multiphase drag interactions using the material point method. *International journal for numerical methods in engineering*, 83(3):295–322.

Malvern, L. W.
1969. *Introduction to the Mechanics of a Continuous Medium*. Englewood Cliffs, New Jersey, USA: Prentice-Hall, Inc.

Mandal, S. and R. Maiti
2015. *Semi-quantitative Approaches for Landslide Assessment and Prediction*. London: Springer.

Mast, C. M.
2013. *Modeling Landslide-Induced Flow Interactions with Structures using the Material Point Method*. PhD thesis, University of Washington.

Mast, C. M., P. Mackenzie-Helnwein, P. Arduino, G. R. Miller, and W. Shin
2012. Mitigating kinematic locking in the material point method. *Journal of Computational Physics*, 231(16):5351–5373.

Mencl, V.
1966. Mechanics on landslides with non-circular slip surfaces with special reference to the Vaiont Slide. *Géotechnique*, 19(4):329–337.

Mieremet, M. M. J.
2015. *Numerical stability for velocity-based 2-phase formulation for geotechnical dynamic analysis.* PhD thesis, Delft University of Technology.

Mizoguchi, K., T. Hirose, T. Shimamoto, and E. Fukuyama
2007. Reconstruction of seismic faulting by high-velocity friction experiments: An example of the 1995 Kobe earthquake. *Geophysical Research Letters*, 34(August):2–4.

Moresi, L., F. Dufour, and H.-B. Muhlhous
2003. A Lagrangian integration point finite element method for large deformation modelling of viscoelastic geomaterials. *Journal in Computational Physics*, 184:476–497.

Moresi, L., H. Muhlhous, and F. Dufour
2001. An overview of numerical methods for Earth simulations. In *Exploration Geodynamics Chapman Conference*, Pp. 113–119, Dunsborough.

Mostazo, R. C.
2004. *Meso-scale Simulation of Texture Development Due to Elastic Loading Using a Hybrid Monte Carlo Kinetics in a Material Point Method Algorithm.* Colorado School of Mines.

Muller, A. L. and E. A. Vargas
2014. The Material Point Method for Analysis of Closure Mechanisms in Openings and Impact in Saturated Porous Media. In *48th American Rock Mechanics Association.*, Pp. 1–4, Minneapolis, Minnesota.

Müller, L.
1964. The rock slide in the Vajont Valley. *Rock Mechanics and Engineering Geology*, 2:148–212.

Nairn, J. A.
2003. Material point method calculations with explicit cracks. *Computer Modeling in Engineering and Sciences*, 4(6):649–663.

Nairn, J. A. and Y. J. Guo
2005. Material point method calculations with explicit cracks, fracture parameters, and crack propagation. *11th Int. Conf. Fracture, Turin, Italy.*

Nairn, J. A. and N. Matsumoto
2009. Fracture Modeling of Crack Propagation in Wood and Wood Composites Including Crack Tip Processes and Fiber Bridging Mechanics. In *Proceedings of the 12th International Conference on Fracture*, Pp. 12–17.

Nonveiller, E.
1987. The Vajont reservoir slope failure. *Engineering Geology*, 24:493–512.

Oñate, E., M. A. Celigueta, S. R. Idelsohn, F. Salazar, and B. Suárez
2011. Possibilities of the particle finite element method for fluid-soil-structure interaction problems. *Computational Mechanics*, 48(3):307–318.

Okura, Y., H. Kitahara, and T. Sammori
2000. Fluidization in dry landslides. *Engineering Geology*, 56(3-4):347–360.

Oliver, J. and A. E. Huespe
2004. Continuum approach to material failure in strong discontinuity settings. *Computer Methods in Applied Mechanics and Engineering*, 193(30-32):3195–3220.

Palmer, C. and J. R. Rice
1973. The growth of slip surfaces in the progressive failure of overconsolidated clay. *Proc. R. Soc. A*, 332:527–548.

Peterson, K.
2008. *Modeling Arctic sea ice using the material-point method and an elastic-decohesive rheology*. PhD thesis, University of New Mexico.

Pinyol, N. M. and E. E. Alonso
2010a. Criteria for rapid sliding II. Thermo-hydro-mechanical and scale effects in Vaiont case. *Engineering Geology*, 114(3-4):211–227.

Pinyol, N. M. and E. E. Alonso
2010b. Fast planar slides. A closed-form thermo-hydro-mechanical solution. *International journal for numerical and analytical methods in geomechanics*, 34(1):27–52.

Potts, D. M., G. T. Dounias, and V. P. R
1990. Finite element analysis of progressive failure of Carsington embankment. *Géotechnique*, 40(1):79–101.

Potts, D. M. and A. Gens
1985. A critical assessment of methods of correcting for drift from the yield surface in elasto-plastic finite element analysis. *Numerical and Analytical Methods in Geomechanics*, 9(2):149–159.

Potts, D. M., N. Kovacevic, and P. R. Vaughan
1997. Delayed collapse of cut slopes in stiff clay. *Géotechnique*, 47(5):953–982.

Potts, D. M. and L. Zdravković
2001. *Finite Element Analysis in Geotechnical Engineering: Theory & Application*. Thomas Telford.

Prime, N., F. Dufour, and F. Darve
2014. Solid-fluid transition modelling in geomaterials and application to a mudflow interacting with an obstacle. *International Journal for Numerical and Analytical Methods in Geomechanics*, 38:1341–1361.

Puzrin, A. M. and L. N. Germanovich
2005. The growth of shear bands in the catastrophic failure of soils. *Proceedings of the Royal Society A: Mathematical, Physical and Engineering Sciences*, 461(2056):1199–1228.

Radjaï, F. and F. Dubais, eds.
2011. *Discrete-element modelling of granular materials*. London: Wiley-ISTE.

Richards, L. A.
1931. Capillary conduction of liquids in porous mediums. *Physics*, 1(5):318–333.

Richtmyer, R. D. and K. W. Morton
1967. *Difference Methods for Initial-Value Problems*. New York: Interscience.

Rots, J., P. Nauta, G. Kuster, and J. Blaauwendraad
1985. Smeared Crack Approach and Fracture Localization in Concrete. *Heron*, 30(1):1–48.

Sadeghirad, A., R. M. Brannon, and J. Burghardt
2011. A convected particle domain interpolation technique to extend applicability of the material point method for problems involving massive deformations. *International Journal for Numerical Methods in Engineering*, 86(12):1435–1456.

Sadeghirad, A., R. M. Brannon, and J. E. Guilkey
2013. Second-order convected particle domain interpolation (CPDI2) with enrichment for weak discontinuities at material interfaces. *International Journal for Numerical Methods in Engineering*, 95(11):928–952.

Santamarina, J., A. Klein, and M. A. Fam
2001. *Soils and Waves*. John Wiley & Sons, Inc.

Sassa, K.
1988. Special lecture: Geotechnical model for the motion of landslides. In *Proc. of 5th Symposium on Landslides*, C. Bonnard, ed., volume 1, Pp. 37–55, Rotterdam. Balkema.

Scheidegger, A. E.
1973. On the prediction of the reach and velocity of catastrophic landslides. *Rock Mechanics*, 5(4):231–236.

Schreyer, H. L., D. L. Sulsky, L. B. Munday, M. D. Coon, and R. Kwok
2006. Elastic-decohesive constitutive model for sea ice. *Journal of Geophysical Research: Oceans*, 111(C11).

Schreyer, H. L., D. L. Sulsky, and S.-J. Zhou
2002. Modeling delamination as a strong discontinuity with the material point method. *Computer Methods in Applied Mechanics and Engineering*, 191(23-24):2483–2507.

Semenza, E.
2001. *La Storia del Vaiont Raccontata del Geologo che ha Scoperto la Frana*. Tecomproject Editore Multimediale.

Shin, W., G. R. Miller, P. Arduino, and P. Mackenzie-Helnwein
2010. Dynamic meshing for material point method computations. *Engineering and Technology*, 48(9):84–92.

Skempton, A. W.
1964. Fourth Rankine Lecture: Long-term stability of clay slopes. *Géotechnique*, 14(2):77–102.

Skempton, A. W.
1966. Bedding-plane slip, residual strength and the Vaiont landslide. *Correspondence to Géotechnique*, 16(2):82–84.

Sloan, S. W., A. J. Abbo, and D. Sheng
2001. Refined explicit integration of elastoplastic models with automatic error control. *Engineering Computations*, 18(1/2):121–194.

Stark, T. D. and H. T. Eid
1994. Slope stability analyses in stiff fissured clays. *J. Geotech. Geoenv. Engng*, 123(4):335–343.

Steffen, M., R. M. Kirby, and M. Berzins
2008a. Analysis and reduction of quadrature errors in the material point method (MPM). *International Journal for Numerical Methods in Engineering*, 76(6):922–948.

Steffen, M., P. C. Wallstedt, and J. E. Guilkey
2008b. Examination and analysis of implementation choices within the material point method (MPM). *Computer Modeling in Engineering and Sciences*, 32(2):107–127.

Stomakhin, A., C. Schroeder, L. Chai, J. Teran, and A. Selle
2013. A material point method for snow simulation. *ACM Transactions on Graphics*, 32(4):102.

Sulsky, D., Z. Chen, and H. Schreyer
1994. A particle method for history-dependent materials. *Computer Methods in Applied Mechanics and Engineering*, 118(1-2):179–196.

Sulsky, D. and A. Kaul
2004. Implicit dynamics in the material-point method. *Computer Methods in Applied Mechanics and Engineering*, 193(12-14):1137–1170.

Sulsky, D., H. Schreyer, K. Peterson, R. Kwok, and M. Coon
2007. Using the material-point method to model sea ice dynamics. *Journal of Geophysical Research: Oceans*, 112(C2):1–18.

Sulsky, D. and H. L. Schreyer
1996. Axisymmetric form of the material point method with applications to upsetting and Taylor impact problems. *Computer Methods in Applied Mechanics and Engineering*, 139(1-4):409–429.

Sulsky, D. and L. Schreyer
2004. MPM simulation of dynamic material failure with a decohesion constitutive model. *European Journal of Mechanics - A/Solids*, 23:423–445.

Sulsky, D., S.-J. Zhou, and H. L. Schreyer
1995. Application of a particle-in-cell method to solid mechanics. *Computer Physics Communications*, 87(1-2):236–252.

Superchi, L.
2012. *The Vajont rockslide: new techniques and traditional methods to re-evaluate the catastrophic event.* PhD thesis, Padova University.

Taylor, D. W.
1948. *Fundamentals of soil mechanics.* New York: Wiley.

Terzaghi, K.
1925. *Erdbaumechanik auf bodenphysikalischer Grundlage.* Wien, Deuticke: [publisher unknown].

Terzaghi, K.
1943. *Theoretical soil mechanics.* New York: Wiley.

Terzaghi, K. and R. Peck
1948. *Soil mechanics in engineering practice.* New York: Wiley.

Thomson, W.
1871. On the equilibrium of vapour at a curved surface of liquid. *Philosophical Magazine Series 4*, 4(42):448–452.

Tika, T. E. and J. N. Hutchinson
1999. Ring shear tests on soil from the Vaiont slide slip surface. *Géotechnique*, 49(1):59–74.

Tran, L. T., J. Kim, and M. Berzins
2010. Solving time-dependent PDEs using the material point method , a case study from gas dynamics. *International Journal for Numerical methods in Fluids*, 62(2010):709–732.

Troncone, A.
2005. Numerical analysis of a landslide in soils with strain-softening behaviour. *Geotechnique*, 55(8):585–596.

Troncone, A., E. Conte, and A. Donato
2014. Two and three-dimensional numerical analysis of the progressive failure that occurred in an excavation-induced landslide. *Engineering Geology*, 183:265–275.

Truesdell, C. and R. A. Toupin
1960. The classical field theories of mechanics. In *Handbook of physics (Vol. III-1)*, S. Flügge, ed. New York: Springer.

Uriel Romero, S. and R. Molinia
1977. Kinematic aspects of Vaiont slide. In *Proceedings of the 3th International Conference of the ISRMR*, National Academy of Sciences, ed., volume 2B, Pp. 865–870, Denver, USA.

Van Genuchten, M. T.
1980. A closed-form equation for predicting the hydraulic conductivity of unsaturated soils. *Soil Science Society of America Journal*, 44(5):892–898.

Vardoulakis, I.
2002. Dynamic thermo-poro-mechanical analysis of catastrophic landslides. Geotechnique. *Geotechnique*, 52(3):157–171.

Vaunat, J., E. Romero, C. Marchi, and C. Jommi
2002. Modelling of the shear strength of unsaturated soils. In *Proceedings of the 3rd International conference of Unsaturated Soils, UNSAT 2002*, J. F. T. Jucá, T. M. P. de Campos, and F. A. M. Marinho, eds., Pp. 245–251. Swets & Zeitinger.

Vermeer, P. A., L. Beuth, and T. Benz
2008. A quasi-static method for large deformation problems in geomechanics. In *The 12th International Conference of International Association for Computer Methods and Advances in Geomechanics*, Pp. 55–63, Goa, India.

Verruijt, A.
2010. *An Introduction to Soil Dynamics*, volume 24 edition. Springer.

Veveakis, E., I. Vardoulakis, and G. Di Toro
2007. Thermoporomechanics of creeping landslides: The 1963 slide, northern Italy. *Journal of Geophysical Research*, 112(F3):2156–2202.

Voight, B. and C. Faust
1982. Frictional heat and strength loss in same rapid slides. *Geotechnique*, 32(1):43–54.

Wallstedt, P. C. and J. E. Guilkey
2008. An evaluation of explicit time integration schemes for use with the generalized interpolation material point method. *Journal of Computational Physics*, 227(22):9628–9642.

Wang, H. K., Y. Liu, and X. Zhang
2012. The carbon nanotube composite simulation by material point method. *Computational Materials Science*, 57:23–29.

Wieckowski, Z.
2004. The material point method in large strain engineering problems. *Computer Methods in Applied Mechanics and Engineering*, 193(39-41):4417–4438.

Wieckowski, Z., S. K. Youn, and J. H. Yeon
1999. A particle-in-cell solution to the silo discharging problem. *International Journal for Numerical Methods in Engineering*, 45(9):1203–1225.

Xiao-Fei, P., X. Ai-Guo, Z. Guang-Cai, Z. Ping, Z. Jian-Shi, M. Shang, and Z. Xiong
2008. Three-Dimensional Multi-mesh Material Point Method for Solving Collision Problems. *Communications in Theoretical Physics*, 49(5):1129–1138.

Xikui, L. and O. C. Zienkiewicz
1992. Multiphase flow in deforming porous media and finite element solutions. *Computers & Structures*, 45(2):211–227.

Yamaguchi, H., T. Kimura, and N. Fuji-I
1976. On the influence of pregressive failures on the bearing capacity of shallow foundations in dense sand. *Soils and Foundations*, 16(4):11–22.

Yang, C. M., W. L. Yu, J. J. Dong, C. Y. Kuo, Shimamoto, C. T. Lee, T. Togo, and Y. Miyamoto
2014. Initiation, movement, and run-out of the giant Tsaoling landslide. What can we learn from a simple rigid block model and a velocity-displacement dependent friction law? *Engineering Geology*, 182 Part B(November):158–181.

Yerro, A., E. Alonso, and N. Pinyol
2013. The Material Point Method : A promising computational tool in Geotechnics. In *Proceedings of the 18th International Conference on Soil Mechanics and Geotechnical Engineering, Paris 2013*, Pp. 853–856.

Yerro, A., E. Alonso, and N. Pinyol
2014a. Modelling progressive failure with MPM. In *Numerical Methods in Geotechnical Engineering*, M. Hicks, R. B. J. Brinkgreve, and A. Rohe, eds., Pp. 319–323. 214 Taylor & Francis Group.

Yerro, A., E. E. Alonso, and N. M. Pinyol
2014b. Run-out of landslides in brittle soils. A MPM analysis. In *Geomechanics from Micro to Macro*, K. Soga, K. Kumar, G. Biscontin, and M. Kuo, eds., volume 1, Pp. 977–982, London. Taylor & Francis.

York II, A. R.
1997. *Development of modifications to the material point method for the simulation of thin membranes, compressible fluids, and their interactions.* PhD thesis, Sandia National Laboratories.

York II, A. R., D. Sulsky, and H. L. Schreyer
1999. The material point method for simulation of thin membranes. *International Journal for Numerical Methods in Engineering*, 44(10):1429–1456.

Zabala, F.
2010. *Modelación de problemas geotécnicos hidromecánicos utilizando el método del punto material.* PhD thesis, Universitat Politècnica de Catalunya.

Zabala, F. and E. E. Alonso
2011. Progressive failure of Aznalcóllar dam using the material point method. *Géotechnique*, 61(9):795–808.

Zabala, F. and E. E. Alonso
2012. The Material Point Method and the analyisis of dams and dam failures. In *Innovative Numerical Modelling in Geomechanics*, A. Roberto, ed., chapter 8, Pp. 171–177.

Zhang, H. W., K. P. Wang, and Z. Chen
2009. Material point method for dynamic analysis of saturated porous media under external contact/impact of solid bodies. *Computer Methods in Applied Mechanics and Engineering*, 198(17-20):1456–1472.

Zhao, T., S. Utili, and G. B. Crosta
2015. Rockslide and Impulse Wave Modelling in the Vajont Reservoir by DEM-CFD Analyses. *Rock Mechanics and Rock Engineering.*

Zhou, S., J. Stormont, and Z. Chen
1999. Simulation of geomembrane response to settlement in landfills by using the material point method. *International Journal for Numerical and Analytical Methods in Geomechanics*, 23(15):1977–1994.

Zhou, S., X. Zhang, and H. Ma
2013. Numerical simulation of human head impact using the material point method. *International Journal of Computational Methods*, 10(4).

Zienkiewicz, O.
1977. *The Finite Element Method in Engineering Science*. London: McGraw-Hill.

Zienkiewicz, O. C. and T. Shiomi
1984. Dynamic behaviour of saturated porous media; the generalized Biot formulation and its numerical solution. *International Journal for Numerical and Analytical Methods in Geomechanics*, 8(1):78–96.

Zou, Q. and D. Z. Zhang
2004. Application of a FLIP-MPM-MFM Method for Simulating Weapon-Target Interaction. In *75th Shock & Vibration Symposium, Virginia Beach, VA*, volume 836.

List of publications

At indexed journals

The material point method for unsaturated soils (2015)
Authors: **Yerro A.**, Alonso E., Pinyol N.
Journal: Géotechnique, 65(3), pp. 201-217, DOI: 10.1680/geot.14.P.163

Trends in large deformation analysis of landslide mass movement (2015)
Authors: Soga K., Alonso E., **Yerro A.**, Kumar K., Bandara S.
Journal: Géotechnique, DOI: 10.1680/geot./15-LM-005

Mathematical modelling of slopes (2014)
Authors: Alonso E.E., Pinyol N.M., **Yerro A.**
Journal: Procedia Earth and Planetary Science, 9, pp. 64-73

At conferences

Recent developments of the Material point Method for the simulation/prediction of landslides (2015)
Authors: Alonso E.E., **Yerro A.**, Pinyol N.M.
In: (Key note lecture) International Symposium on Geohazards and Geomechanics. September 2015, Warwick, UK

Run-out of landslides in brittle soils: An MPM analysis (2014)
Authors: **Yerro A.**, Alonso E., Pinyol N.
In: Geomechanics from micro to macro, K. Soga et al. (eds.), London, UK, Taylor and Francis, pp. 977-982

Modelling progressive failure in MPM (2014)
Authors: **Yerro A.**, Alonso E., Pinyol N.
In: 8th European Conference on Numerical Methods in Geotechnical Engineering (NUMGE), M. Hicks et al. (eds.), Delft, The Netherlands, pp. 319-323

The Material Point Method: a promising computational tool in Geotechnics (2013)
Authors: **Yerro A.**, Alonso E., Pinyol N.
In: Proc. 18th International Conference for Soil Mechanics and Geotechnical Engineering, Paris, Vol. 1, pp. 853-856

Solving hydro-mechanical problems with the material point method (2011)
Authors: **Yerro, A.**
In: Proc. 21st European Young Geotechnical Engineers Conference, Rotterdam, The Netherlands, pp. 318-323

Under review at indexed journals

Internal progressive failure in deep seated landslides
Authors: **Yerro A.**, Pinyol N., Alonso E.
Journal: Rock Mechanics and Rock Engineering

Failure initiation and post-failure response in brittle materials. An MPM analysis
Authors: **Yerro A.**, Alonso E., Pinyol N.
Journal: Computers and Geotechnics